Load-Pull Techniques with Applications to Power Amplifier Design

The Springer Series in Advanced Microelectronics provides systematic information on all the topics relevant for the design, processing, and manufacturing of microelectronic devices. The books, each prepared by leading researchers or engineers in their fields, cover the basic and advanced aspects of topics such as wafer processing, materials, device design, device technologies, circuit design, VLSI implementation, and subsystem technology. The series forms a bridge between physics and engineering and the volumes will appeal to practicing engineers as well as research scientists.

Series Editors:

Dr. Kiyoo Itoh Hitachi Ltd., Central Research Laboratory, 1-280 Higashi-Koigakubo, Kokubunji-shi, Tokyo 185-8601, Japan

Professor Thomas H. Lee Department of Electrical Engineering, Stanford University, 420 Via Palou Mall, CIS-205 Stanford, CA 94305-4070, USA

Professor Takayasu Sakurai Center for Collaborative Research, University of Tokyo, 7-22-1 Roppongi, Minato-ku, Tokyo 106-8558, Japan

Professor Willy Sansen ESAT-MICAS, Katholieke Universiteit Leuven, Kasteelpark Arenberg 10, 3001 Leuven, Belgium

Professor Doris Schmitt-Landsiedel Lehrstuhl für Technische Elektronik, Technische Universität München, Theresienstrasse 90, Gebäude N3, 80290 Munich, Germany

For further volumes:

www.springer.com/series/4076

Load-Pull
Techniques
with Applications
to Power Amplifier
Design



Fadhel M. Ghannouchi Electrical and Computer Engineering, Intelligent RF Radio Laboratory University of Calgary Calgary, Alberta Canada Mohammad S. Hashmi Electrical and Computer Engineering, Intelligent RF Radio Laboratory University of Calgary Calgary, Alberta Canada

ISSN 1437-0387 Springer Series in Advanced Microelectronics ISBN 978-94-007-4460-8 ISBN 978-94-007-4461-5 (eBook) DOI 10.1007/978-94-007-4461-5 Springer Dordrecht Heidelberg New York London

Library of Congress Control Number: 2012939475

© Springer Science+Business Media Dordrecht 2013

This work is subject to copyright. All rights are reserved by the Publisher, whether the whole or part of the material is concerned, specifically the rights of translation, reprinting, reuse of illustrations, recitation, broadcasting, reproduction on microfilms or in any other physical way, and transmission or information storage and retrieval, electronic adaptation, computer software, or by similar or dissimilar methodology now known or hereafter developed. Exempted from this legal reservation are brief excerpts in connection with reviews or scholarly analysis or material supplied specifically for the purpose of being entered and executed on a computer system, for exclusive use by the purchaser of the work. Duplication of this publication or parts thereof is permitted only under the provisions of the Copyright Law of the Publisher's location, in its current version, and permission for use must always be obtained from Springer. Permissions for use may be obtained through RightsLink at the Copyright Clearance Center. Violations are liable to prosecution under the respective Copyright Law.

The use of general descriptive names, registered names, trademarks, service marks, etc. in this publication does not imply, even in the absence of a specific statement, that such names are exempt from the relevant protective laws and regulations and therefore free for general use.

While the advice and information in this book are believed to be true and accurate at the date of publication, neither the authors nor the editors nor the publisher can accept any legal responsibility for any errors or omissions that may be made. The publisher makes no warranty, express or implied, with respect to the material contained herein.

Printed on acid-free paper

Springer is part of Springer Science+Business Media (www.springer.com)

Fadhel M. Ghannouchi dedicates this book to his wife Asma, and daughters Layla and Nadia

Mohammad S. Hashmi dedicates this book to his wife Rabeya, and son Jafar

Preface

For the purpose of identifying the large-signal behavior of the transistor devices, the use of linear S-parameter is often inadequate. Large-signal characterization, therefore, is essential for the estimation and determination of the device performance in the nonlinear domain. The load-pull approach is one recommended approach for the large-signal characterization, optimization, and design of transistor devices and radio frequency (RF), microwave and mm-wave power amplifiers (PAs).

The load-pull technique was first reported almost four decades ago. This pioneering work brought a paradigm shift in the characterization, measurement, and optimization of transistor devices and PAs. The first load-pull setup can be considered rudimentary but has definitely helped in advancing the state-of-the-art in load-pull techniques.

This book describes the principles of operation, calibration, design and realization approaches and application of load-pull techniques in the context of PAs. It explores the topic from the basic principles of load-pull techniques through to their many interesting advancements, including passive and active techniques, high power load-pull and envelope load-pull setups with applications to amplifier, mixer and noise measurements. In addition, the book also covers waveform engineering systems, their calibration techniques and applications.

The book can be used by graduate students, researchers and design engineers in microwave and wireless design areas. It is assumed that the readers have already acquired a basic knowledge of RF and microwave circuit design. A solid background in transmission line theory and basic communication concepts is required. The book may also be used as a textbook for a graduate course on large signal device measurement and characterization.

Chapter 1 is a brief reminder of the basic concepts related to PA characteristics, figures of merits of PA, power amplifier classes of operation, PA design methodologies, and introduction to load-pull systems along with their important features.

Chapter 2 is dedicated to passive load-pull techniques. It explains the fundamentals of passive load tuning techniques and elaborates on the two most common techniques, namely electronic tuner (ETS) and electromechanical tuner (EMT), employed to achieve impedance tuning using passing approach. Measurement and

viii Preface

calibration procedure applied in a load-pull measurement setup is then discussed in detail. The chapter also provides extensive details on various passive harmonic load-pull architectures along with their respective advantages and limitations. Subsequently, common techniques used to enhance the tuning range of passive load-pull setups are discussed.

Chapter 3 provides extensive details on active load-pull techniques and systems. It starts with closed-loop active load-pull technique and its realization methods. Adequate details have been included for the design of application specific closed-loop load-pull system. It then covers feed-forward active load-pull and various methods to develop hybrid setup, for enhancing the tuning range and achieving highly reflective load-pull systems. Active open-loop load-pull requires iterative operation of the system for converging on optimal impedance solution. The last section is dedicated to an algorithm for high speed convergence in active open-loop load-pull systems.

Chapter 4 presents the theory, techniques and principles behind using six-port reflectometer in reverse and forward configurations to characterize transistors operated in large signal conditions, and the issues related to the implementation of these techniques are discussed. Source-pull characterization using six-port reflectometer for transistor noise measurement, mixer testing and design, as well as oscillator device line measurement purposes are explained and discussed. AM/AM and AM/PM distortion measurement and passive and active load-pull large signal characterization of transistors using the six-port reflectometer technique are also presented and discussed.

Chapter 5 deals with the issues involved in the characterization of high power microwave transistor devices. There are multiple aspects that need to be addressed in order to overcome those issues. All these have been discussed in detail in this chapter. The techniques adopted in customizing the load-pull setup for high power device measurements and characterization applications have been elaborated and explained in detail. Finally, emerging solutions catering to large periphery high power microwave devices are presented.

Chapter 6 presents the theory of active envelope load pull (ELP) and the associated design and calibration techniques of active envelope load-pull. Thereafter harmonic envelope load-pull is explained in detail which is followed by some unique measurement applications of envelope load-pull system.

Chapter 7 is dedicated to theory and calibration approaches adopted in developing error corrected nonlinear time-domain waveform measurements systems. Subsequently the concept of waveform engineering is presented. Finally, a number of applications of waveform engineering system are discussed.

Chapter 8 presents some advanced applications and configurations of load-pull setups. The first part of this chapter primarily discusses the concept of load-pull systems for multi-tone and modulated excitations. It experimentally demonstrates that such systems are extremely useful for real life practical applications. Then the use of load-pull and source-pull systems in noise characterization is described in detail. Finally application of load-pull systems in mixer characterization and measurements in presented.

Acknowledgements

We would like to gratefully acknowledge the help and support received from friends, colleagues, support staff and students, both past and present at iRadio Laboratory, University of Calgary, Calgary; Poly-grames Research Center, Ecole Polytechnique, Montreal; and Cardiff University, UK. We are grateful to our great students and researchers; this book could not have been completed without their fruitful research. In particular, we would like to thank Dr. R.G. Bosisio and Dr. P.J. Tasker for their useful comments, discussions, collaboration and for their help in producing many of the results presented in this book over the years. In addition, we would like to thank C. Heys for her help in proofreading and formatting the manuscript and Ivana d'Adamo for her administrative support. The authors would also like to thank IEEE and Focus Microwaves for their permission and courtesy to reproduce several figures and illustrations published in their journals and/or application notes.

Dr. M. Hashmi acknowledges Alberta Innovates Technology Futures (AITF), Alberta, Canada for the financial contribution to support the post-doctoral fellowship at iRadio Laboratory, University of Calgary, which helped the completion of this work. Dr Ghannouchi acknowledges the main sponsors and financial supporters of the Intelligent Radio Laboratory (iRadio Lab), Alberta Innovates Technology Futures (AITF), Alberta, Canada, the Canada Research Chairs (CRC) program and Natural Science and Engineering council of Canada (NSERC).

Finally we would like to profoundly thank our respective spouses Asma and Rabeya, and children Layla Ghannouchi, Nadia Ghannouchi and Jafar Talal Hashmi for their understanding and patience throughout the many evenings and weekends taken to prepare this book. We are also thankful to our respective patents for their encouragement and valuable support in our early professional years as graduate students and young researchers.

Contents

1	Fun	dament	rals			
	1.1	Introd	uction			
	1.2		wer Amplifier Characteristics			
	1.3		s of Merit			
		1.3.1	Drain Efficiency and Power Added Efficiency 5			
		1.3.2	Intermodulation and Harmonic Distortions 6			
		1.3.3	Adjacent Channel Power Ratio			
		1.3.4	Error Vector Magnitude			
	1.4	Power	Amplifier			
	1.5		Amplifier Design Methodologies			
		1.5.1	CAD-Based Design Methods			
		1.5.2	Measurement-Based Design Methods			
	1.6	Nonlir	near Microwave Measurement System			
		1.6.1	What Is Load-Pull?			
		1.6.2	Why Load-Pull?			
	1.7	Impor	tant Load-Pull Features			
		1.7.1	Repeatability of Reflection Coefficients			
		1.7.2	Tuning Range and Its Distribution			
		1.7.3	Tuning Speed			
		1.7.4	Power Handling Capability			
		1.7.5	Tuner Resolution			
		1.7.6	Tuner Bandwidth			
		1.7.7	Tuner Size			
	1.8	Comm	on Load-Pull Systems			
	Refe					
2	Pass	sive Loa	nd-Pull Systems			
	2.1	·				
	2.2	e Load-Pull System				
		2.2.1	Electromechanical Tuner (EMT)			
		2.2.2	Electronic Tuner (ETS)			

xii Contents

		2.2.3 ETS and EMT Comparisons	34
	2.3	Load-Pull Measurement	35
		2.3.1 Load-Pull Setup	36
		2.3.2 System Calibration	38
	2.4	Harmonic Load-Pull System	42
		2.4.1 Triplexer Based Harmonic Load-Pull Setup	44
		2.4.2 Harmonic Rejection Tuner Based Harmonic Load-Pull Setup	45
		2.4.3 Single Tuner Harmonic Load-Pull Setup	46
		2.4.4 Harmonic Load-Pull Comparisons	47
	2.5	Tuning Range Enhancement	49
		2.5.1 Enhanced Loop Architecture	50
		2.5.2 Cascaded Tuner	51
	Refe	rences	52
•			
3		ve Load-Pull Systems	55
	3.1	Introduction	55
	3.2	Closed-Loop Load-Pull System	56
		3.2.1 System Realization	56
		3.2.2 Analysis of Closed-Loop System	57
	3.3	Closed-Loop Load-Pull Architectures	62
	3.4	Optimized Closed-Loop Load-Pull System	64
	3.5	Feed-Forward Load-Pull System	68
	3.6	Optimized Feed-Forward Load-Pull System	71
	3.7	Harmonic Feed-Forward Load-Pull System	74
	3.8	Open-Loop Load-Pull System	76
	3.9	Convergence Algorithm for Open-Loop and Feed-Forward	
		Load-Pull Techniques	78
	3.10	Comparison of Active Load-Pull Techniques	83
	Refe	rences	84
4	Civ_I	Port Based Load-Pull System	87
•	4.1	Introduction	87
	4.2	Impedance and Power Flow Measurement	88
	4.3	SP in Reverse Configuration	89
	4.3	e e	89
		4.3.2 Error Box Calculation	93
	4.4	4.3.3 Discussion	94
	4.4	SP Based Source-Pull Configuration	95
	4.5	SP Based Load-Pull Configuration	96
		4.5.1 Passive Load-Pull System	96
		4.5.2 Active Branch Load-Pull System	97
		4.5.3 Active Loop Load-Pull System	99
	4.6	On-Wafer Load-Pull Measurements	99
	4.7	11	101
		ı	102
		4.7.2 Mixer Characterization	103

Contents xiii

		4.7.3 Power Amplifier Characterization 104		
	4.8	Oscillator Measurements		
	4.9	AM/AM and AM/PM Measurements		
		4.9.1 Principles of Operation		
		4.9.2 Measurement Procedure		
	Refe	rences		
5	High	n-Power Load-Pull Systems		
	5.1	Introduction		
	5.2	Limitations of Existing Load-Pull Systems		
		5.2.1 Problems Due to High Standing Waves		
		5.2.2 Problem of Large Load-Pull Power		
	5.3	High-Power Load-Pull		
		5.3.1 Pre-matching Technique		
		5.3.2 Enhanced Loop Architecture		
		5.3.3 Quarter Wave Transformer Technique		
		5.3.4 Broadband Impedance Transformer Technique 126		
	5.4	Impact of a Transformation Network on P_{LP} and VSWR 127		
	5.5	Hybrid Load-Pull System		
	5.6	Calibration and Data Extraction		
	Refe	rences		
6	Enve	elope Load-Pull System		
	6.1	Introduction		
	6.2	Envelope Load-Pull Concept		
		6.2.1 Mathematical Formulation		
	6.3	Practical Realization		
		6.3.1 Design of Control Unit		
	6.4	ELP Calibration		
		6.4.1 Error Flow Model Formulation		
		6.4.2 Simplification of the Error Flow Model 146		
		6.4.3 Calibration Technique		
		6.4.4 Evaluation of the Calibration Technique 150		
	6.5	Stability Analysis		
	6.6	T		
	6.7	Harmonic Envelope Load-Pull System		
	6.8	Unique Measurement Applications		
	Refe	rences		
7	Wav	eform Measurement and Engineering		
	7.1	Introduction		
	7.2	Theoretical Formulation		
	7.3	Historical Perspectives		
	7.4	Practical Waveform Measurement System 169		
	7.5	System Calibration		
		7.5.1 First Step: Power Flow Calibration		

xiv Contents

		7.5.2	Second Step: S-Parameter Calibration	2
		7.5.3	Third Step: Enhanced Calibration	4
		7.5.4	Calibration Evaluation	5
	7.6	Six-Po	rt Based Waveform Measurement System 17	7
		7.6.1	Multi-harmonic Reference Generator	8
		7.6.2	SP Reflectometer Principle	8
		7.6.3	Multi-harmonic SP Reflectometer Architecture 17	9
		7.6.4	Multi-harmonic SP Reflectometer Calibration 18	
		7.6.5	Calibration Verification	2
	7.7		orm Engineering	
	7.8	Applic	ations of Waveform Engineering	4
		7.8.1	Transistor Characterization	4
		7.8.2	CAD Incorporation	
		7.8.3	Power Amplifier Design	
	Refe	rences		7
8	Adva	anced C	Configurations and Applications	1
	8.1		action	
	8.2	Multi-t	one Load-Pull Technique	1
	8.3	Real-T	ime Multi-harmonic Load-Pull Technique 19	7
	8.4	Modul	ated Signal Load-Pull Technique	1
	8.5	Multi-t	one Envelope Load-Pull Technique	4
	8.6	Wideba	and Load-Pull Technique	8
		8.6.1	Wideband Load-Pull Approach	9
		8.6.2	Setup Description	0
	8.7	Noise (Characterization	2
		8.7.1	Noise Parameter Measurement	2
		8.7.2	Noise Parameter Test Setup	5
	8.8	Mixer	Characterization	7
		8.8.1	Measurement Setup	7
		8.8.2	Experimental Procedure	0
	Refe	rences		1
Autl	nors			5
Abo	ut the	Book		7
Inda	N W 7		22	0

Chapter 1 Fundamentals

This chapter presents the fundamentals of three aspects, namely radio frequency (RF) power amplifiers, approaches adopted for the optimal design of these amplifiers, and load-pull measurement systems.

1.1 Introduction

The key component in any wireless communication system is the RF power amplifier (RFPA). RFPAs convert the DC power into RF power, which enables the transmission of the RF signal containing digital information from the transmitter to the receiver via wireless environments. The quality of RFPAs, in terms of efficiency and linearity, has a significant impact on the cost, reliability, size and performance of wireless communication systems.

Achievement of both high efficiency and linearity in RFPAs is a complex process, as the power amplifier (PA) has to be designed to operate closer to saturation. Operation of the PA at saturation increases the efficiency, but also increases the distortion. Therefore, the RFPA design process requires a trade-off between two important metrics, namely efficiency and linearity. Here, efficiency refers to the capability of the PA in converting DC power into RF power, which is extremely important as any PA exhibiting low efficiency will consume much more DC power than an efficient one when delivering the same amount of RF power.

For a handheld application that uses a battery as the primary power source, poor efficiency means shorter talk and standby times. This can seriously limit the competency of the final product in the market. Moreover, poor efficiency leads to a large amount of heat dissipation, which requires additional effort and money for high-capacity cooling facilities.

In the context of the PA, linearity refers to a measure of how faithfully a PA can amplify the input signal. PAs always demonstrate certain levels of nonlinearities. The tolerance for nonlinearity really depends on the applications. For example, CDMA (code division multiple access) and WCDMA (wideband code division multiple access) based wireless systems require, apart from the usual high efficiency,

1

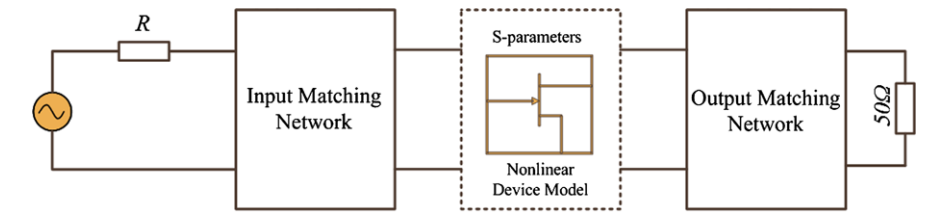


Fig. 1.1 Generic block diagram of a single-stage RF amplifier

a high linearity over a large dynamic power range. In contrast, the linearity is a relatively less serious issue for PAs based on the GSM (global system for mobile applications) standards, due to the constant envelope characteristics of the GSM signal.

It is not possible for the efficiency and linearity to reach their optimal levels simultaneously on a stand-alone power device. Various types of advanced PA architectures, such as Doherty, Kahn and LINC (linear amplification using nonlinear components), have been proposed to achieve good efficiency and linearity at the same time [1–10]. These architectures provide promising results, but inevitably increase the complexity of the communication systems, thereby contributing to higher costs with decreasing reliability. Therefore, it is always a challenge for PA designers to adopt an appropriate optimization solution with which a good compromise in specifications can be reached.

1.2 RF Power Amplifier Characteristics

Before getting into the description of RFPAs, it is prudent to understand the characteristics of RF amplifiers. For this purpose, a generic block diagram of a single-stage RF amplifier is depicted in Fig. 1.1. It consists of input and output matching networks, and a transistor device. Ideally, this configuration is generic both for small-or large-signal power amplifiers.

Matching networks are application specific and are appropriately designed. For example, matching networks can be customized for amplifying extremely small signals with very low noise at the output (i.e., a low noise amplifier), can be designed such that maximum gain is realized, or can be intended for maximum output power (i.e., a power amplifier). Irrespective of the applications, the matching networks are realized using lumped components, distributed elements (transmission lines) or a combination of both. They are basically characterized by intrinsic linear elements and, therefore, are considered linear time-invariant networks.

An active device can, however, be thought as either a linear or nonlinear network, depending on the electrical power range of the signals involved in the process [11]. If the power level of the input signal is so small that the output is just the amplified version of input, as depicted in Fig. 1.2, the device is considered to be operating in linear mode. On the contrary, if the power level of the input is large enough to

Fig. 1.2 Depiction of linear and nonlinear behavior of an amplifier

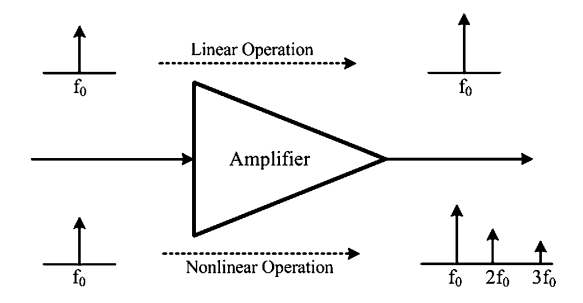
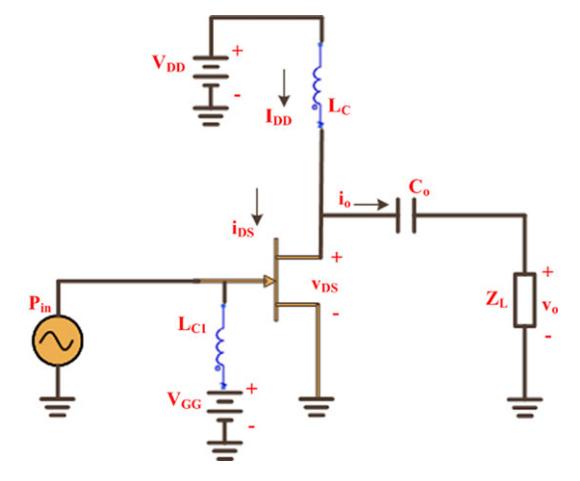


Fig. 1.3 Schematic of an amplifier for definition of load line



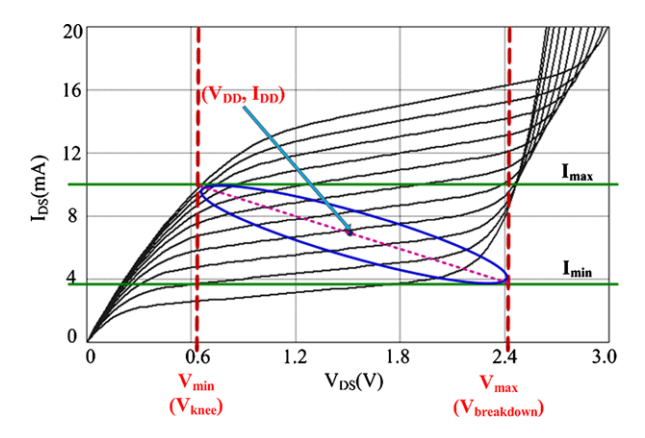
generate harmonics in the output signal, as also depicted in Fig. 1.2, the device is said to be operating in nonlinear mode.

The linear mode of operation is modeled in terms of scattering parameters (S-parameters). The S-parameters are frequency dependent, described for a specific biasing condition and independent of the power level of the stimulus. These parameters are inadequate for describing the characteristics of devices operating in nonlinear mode. In order to address this problem, there have been proposals of complex large-signal models [12–15] to describe the nonlinear characteristics of devices.

In an alternative context, it is a common practice to link the performance characteristics of a power amplifier to the load line, as it identifies the capabilities of devices for maximum output power application. The load line represents the trajectory of all the instantaneous values of current (i_{DS}) and voltage (v_{DS}) of a device when it is operated under a specific load and at a given bias point.

For the purposes of the explanation of a load line, let us consider the typical schematic of an amplifier, as given in Fig. 1.3. The amplifier is biased through an RF choke inductor, L_C , with a bias voltage, V_{DD} , and drain bias current, I_{DD} . The DC blocking capacitor, C_0 , is selected to be large enough to keep a steady-state voltage, V_{DD} , during the entire RF cycle. During a steady state, this schematic can

Fig. 1.4 Typical load line of an amplifier (*dashed straight line*: resistive load, *solid elliptic line*: complex load)



be solved to determine the expression between the instantaneous current (i_{DS}) and instantaneous voltage (v_{DS}) given in Eq. (1.1).

$$i_{DS} = I_{DD} - \frac{v_{DS} - V_{DD}}{Z_L} \tag{1.1}$$

Equation (1.1), known as the load line equation, defines the trajectory of all the combination of values (i_{DS}, v_{DS}) of the device under specific operating conditions of a device for specific quiescent points (I_{DD}, V_{DD}) and load impedance (Z_L) . For the real value of Z_L , the load line equation represents a straight line; whereas a complex Z_L converts the load line equation into the equation of a shifted and rotated ellipse [78], as shown in Fig. 1.4.

In theory, v_{DS} could be any value and, therefore, can produce any value of i_{DS} . In practice, however, this is not the case, as the load line is regulated by the device DCIV characteristic, as can be seen in Fig. 1.4. It is evident that the trajectory is limited by the knee voltage (V_{min} or V_{knee}), the breakdown voltage (V_{max} or $V_{breakdown}$), the device's maximum current (I_{max}), and the zero value current (I_{min}).

The load line is considered a very effective tool, as it can provide information about the load impedance (real or complex) just by visual inspection. However, it is imperative to understand that if an RF transistor is loaded with 50 Ω impedance without a matching circuit, the load line is an ellipse instead of a straight line. It is due to the presence of intrinsic device output capacitance that combines with the real 50 Ω impedance to form a complex load. In addition, load line trajectories also help in the design of optimal matching circuit by determining the condition when the device output capacitance is canceled out by the matching circuit i.e., the situation when the device sees only real load impedance at its terminals.

1.3 Figures of Merit

Evaluation of an RF power amplifier for any particular application is carried out using established figures of merit, such as drain efficiency (η_D), power-added efficiency (PAE), harmonic distortion, intermodulation distortion, Adjacent Channel

1.3 Figures of Merit 5

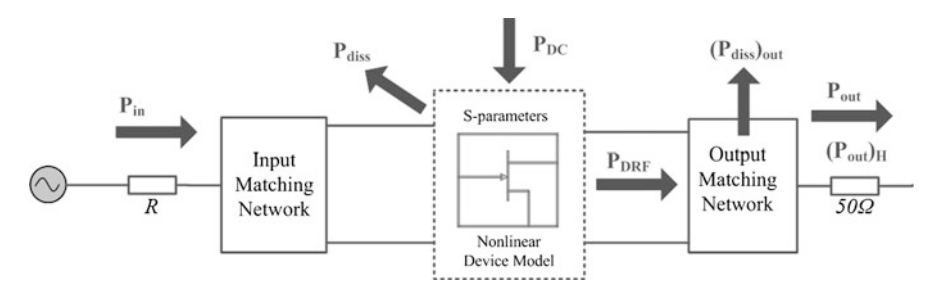


Fig. 1.5 Power flow depiction in a power amplifier

Power Ratio (ACPR), and Error Vector Magnitude (EVM). The values of these figures of merit are the reference values for comparison with other amplifiers using other design techniques or technologies.

1.3.1 Drain Efficiency and Power Added Efficiency

Several forms of the definition of efficiency have been adopted previously, but the most commonly used are drain efficiency (η_D) and the power-added efficiency (PAE). For defining the efficiency metrics, let us look to the power flow in a power amplifier, as depicted in Fig. 1.5. Power P_{in} is the power flowing into the amplifier input over a specified frequency range; whereas P_{out} is the power flowing out of the amplifier over a specified frequency. If P_{in} is only contained in one harmonic component (i.e., the fundamental frequency), then P_{out} is the corresponding power at the fundamental frequency and $(P_{out})_H$ is the output power of the harmonic components generated by nonlinear characteristics of the power amplifier.

The dc power, P_{DC} , is supplied to the active device for the operation of the power amplifier. The active device also receives the input ac power, P_{in} , and dissipates a portion of the combined P_{DC} and P_{in} as heat, while it converts the remaining into ac power, P_{DRF} , which gets delivered to the output matching network. The output network dissipates a portion of P_{DRF} and then delivers the remainder in the form of P_{out} and $(P_{out})_H$. The optimal design of a power amplifier requires minimization of these power losses at various stages and maximization of power transfer to the load with minimal distortion.

The drain efficiency (η_D) is defined as the ratio between the output power (P_{out}) and the dc power (P_{DC}) .

$$\eta_D = \frac{P_{out}}{P_{DC}} \tag{1.2}$$

The drain efficiency is good for amplifiers that possess high gain or where the input power comes at no cost. It is a very useful metric in the evaluation of conduction loss independent from the input power dissipation. As the drain efficiency

ignores the effect of input power, it helps measure the effectiveness of the amplifier in avoiding the dissipation on the controlled resistance of the output port [79].

An alternative efficiency metric called total efficiency (η_T), although rarely used but more physically significant, is defined as the ratio of the output power and the sum of all powers fed to the amplifier. From Fig. 1.5, the expression of η_T can be deduced as:

$$\eta_T = \frac{P_{out}}{P_{DC} + P_{in}} \tag{1.3}$$

The total efficiency can be used to measure the effectiveness of an amplifier in reducing the need for heat removal, as can be seen in Eq. (1.4), which relates the total dissipated power, $(P_{diss})_T$, and the total efficiency, η_T [79].

$$(P_{diss})_T = P_{DC} + P_{in} - P_{out} = \left(\frac{1}{\eta_T} - 1\right) P_{out}$$
 (1.4)

The most commonly used efficiency metric is called PAE which is defined as the (RF) power added by the amplifier, $(P_{out} - P_{in})$, divided by the dc power consumption, P_{DC} .

$$PAE = \frac{P_{out} - P_{in}}{P_{DC}} = \frac{P_{out}}{P_{DC}} \left(1 - \frac{P_{in}}{P_{out}} \right) = \eta_D \left(1 - \frac{1}{G} \right)$$
 (1.5)

The PAE carries more information than the drain efficiency, as it also depends on the gain of the amplifier (G). While the drain efficiency increases monotonically with the input power, the PAE reaches a maximum and then its value decreases until reaching zero and could even have a negative value.

1.3.2 Intermodulation and Harmonic Distortions

A power amplifier is a nonlinear system that generates harmonic components in addition to the frequency corresponding to the excitation signal. Intermodulation and harmonic distortions quantify the impact of distortion associated with the harmonic components and provide a measure of linearity performance of a power amplifier.

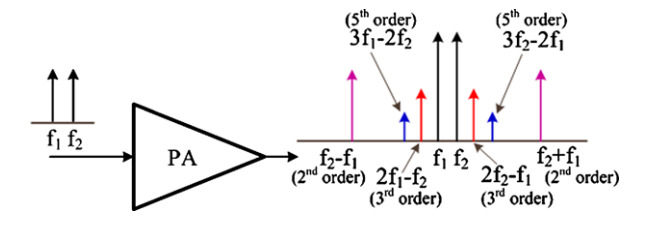
Harmonic distortion is measured when the amplifier is excited with a single-tone test signal and harmonic distortion components are generated at the output, as depicted in Fig. 1.2. Usually the second and third harmonics carry most of the energy; therefore, the harmonic distortions are defined for these harmonic components.

$$HD_{2,dBc} = 10\log\left(\frac{P_{out}(2f_0)}{P_{out}(f_0)}\right)$$
 (1.6)

$$HD_{3,dBc} = 10 \log \left(\frac{P_{out}(3f_0)}{P_{out}(f_0)} \right)$$
 (1.7)

The harmonic distortions are expressed in dBc relative to the fundamental frequency power. The power level of the harmonics changes with the input power; therefore, the corresponding harmonic distortion figures in dBc change as well.

Fig. 1.6 Illustration of the intermodulation products and the associated frequencies with two-tone excitation



Another harmonic distortion term that is very commonly used is called total harmonic distortion (THD) which is given in Eq. (1.8). It includes all the harmonic distortion components in one figure of merit.

$$THD_{dBc} = 10\log\left(\frac{\sum_{n\geq 2} P_{out}(nf_0)}{P_{out}(f_0)}\right)$$
(1.8)

Intermodulation distortion (IMD) is more realistic for the actual wireless communication system. It is the result of two or more signals interacting in a power amplifier to produce additional unwanted signals. For example, the additional unwanted signals (intermodulation products) for two input signals occur at the sum and difference of integer multiples of the original frequencies given by Eq. (1.17) and as depicted in Fig. 1.6.

$$(IMD)_{products} = mf_1 \pm nf_2 \tag{1.9}$$

where m and n are integers and define the order of intermodulation products as a sum of m + n.

It is evident from Fig. 1.6 that the two-tone third-order components $(2f_1 - f_2)$ and $2f_2 - f_1$ are most relevant, as they are very close to the fundamental components and, therefore, cannot be easily filtered. Higher order intermodulation products generally do not affect the performance of PAs significantly, as these components either possess very low amplitudes or are far from the fundamental components [11].

Equation (1.10) corresponds to third-order intermodulation product (IMD3) when the fundamental components f_1 and f_2 are very close.

$$IMD_{3,dBc} = 10\log_{10}\left(\frac{P_{out}(2f_2 - f_1)}{P_{out}(f_2)}\right) \approx 10\log_{10}\left(\frac{P_{out}(2f_1 - f_2)}{P_{out}(f_1)}\right)$$
(1.10)

Another metric to describe the linearity performance of a power amplifier is known as the intercept point. For third-order products, it is known as the third-order intercept point (IP3), as shown in Fig. 1.7. IP3 is an important parameter and helps in the estimation of spurious free dynamic range (DR_{SF}) [80].

It is important to understand that THD, IMD3, and IP3 are good metrics for describing the performance of PAs exhibiting weak memory effects [16]. However, these are insufficient for the situations when the PAs exhibit strong nonlinearity.

Fig. 1.7 Representation of third-order intercepts point

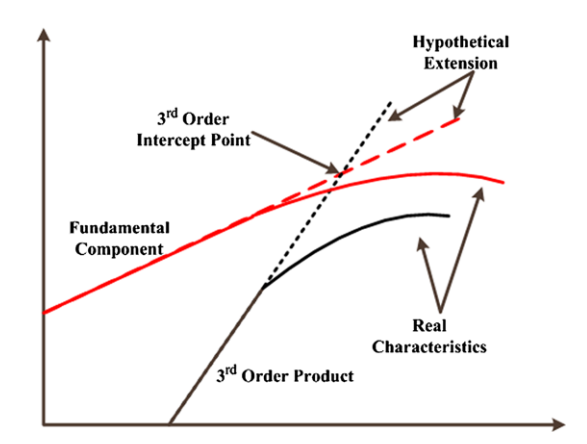
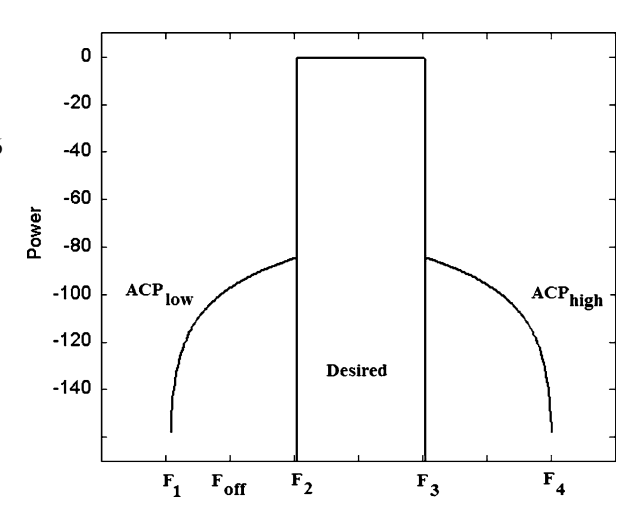


Fig. 1.8 Ideal representation of main and adjacent channel power spectra and their respective frequency band definitions [81], © IEEE 2006



1.3.3 Adjacent Channel Power Ratio

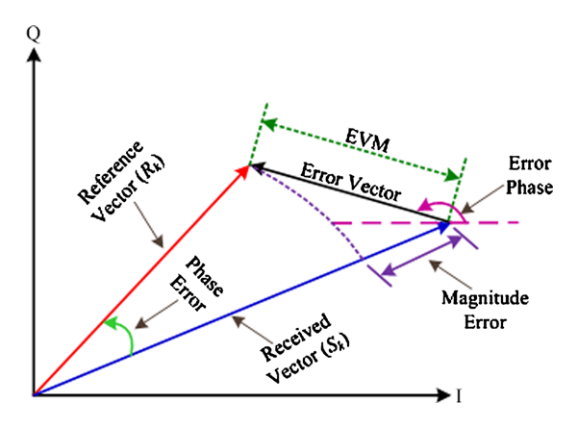
For amplifiers exhibiting strong nonlinearity or for digitally modulated excitations, adjacent channel power ratio (ACPR) is more relevant considering that harmonic distortion is applicable for single tone excitation and the usefulness of intermodulation distortion is limited to excitations with specified number of tones (usually 2).

ACPR describes the level of spectral regrowth and is often expressed in dB below the main carrier power (dBc) as depicted in Fig. 1.8 and is expressed as the ratio of the power leaking into the adjacent channel to the power in the main channel given by Eq. (1.11) [17].

$$ACPR_{dBc} = 10\log\left(\frac{\int_{F_2}^{F_3} P(F)dF}{\int_{F_1}^{F_2} P(F)dF}\right)$$
(1.11)

1.3 Figures of Merit 9

Fig. 1.9 Illustration of error vector magnitude (EVM) and its components



The plot shows a representative power spectrum showing the driving signal (between frequencies F_2 and F_3) and the adjacent channel power (ACP) resulting from third order interactions only. In an ideal system, ACPR should be as high as possible as it conveys that the leakage from the main channel to the side channel is low.

Alternatively, a measure of ACPR is the distortion level at a given frequency offset F_{off} from the lowest desired frequency (F_2) [81].

1.3.4 Error Vector Magnitude

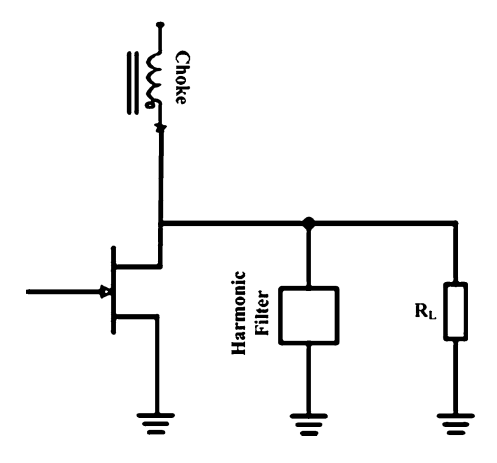
According to 3GPP standards, EVM is a measure of the difference between the reference waveform and the measured waveform [82]. The difference is called error vector, illustrated in Fig. 1.9, and the EVM, usually mentioned in percentage, is defined as the square root of the ratio of the mean error vector power to the mean reference power expressed in Eq. (1.12).

$$EVM_{RMS} = \sqrt{\frac{\sum_{k \in K} |S_k - R_k|^2}{\sum_{k \in K} |R_k|^2}}$$
 (1.12)

where S_k is the received (measured) vector, R_K is the reference symbol vector, and K is the total number of symbols.

The ACPR provides information about the out-of-band distortion, the error vector magnitude (EVM) estimates the in-band distortion caused by the amplifier nonlinearities. EVM possesses a direct relation with the signal to noise ratio and can be used to determine the physical error introduced at different stages of communication system and thus serves as an easily tool for designers in troubleshooting specific problems. One of the advantages of EVM is the simplicity in their measurement as it does not require an entire communication system, instead EVM can be calculated from the measured down-converted digitally modulated radio signal [17].

Fig. 1.10 A generic topology of transconductance amplifier



1.4 Power Amplifier

Transconductance amplifiers, in which the transistor device is operated as a current source and whose current is dependent on the voltage presented to its input, are the most common types of power amplifiers. In these amplifiers, the transistor devices drive a controlled current into a load network which consists of a harmonic filter and resistive load as depicted in Fig. 1.10. The harmonic filters are designed in such a way that it possesses high impedance at fundamental frequency and extremely low impedance at the harmonics. This ensures that the impedance presented to the device at the fundamental frequency is simply the load resistance, R_L , whereas the harmonics are presented with virtually open circuit. As a result, the voltage across the device output port remains sinusoidal for any current driven by the device.

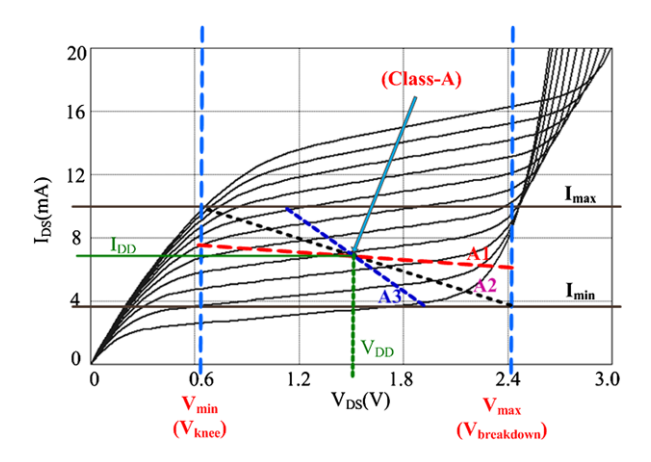
It is imperative to understand that performance, such as efficiency, of transconductance amplifiers can be varied by varying the shape of current waveform considering that these amplifiers are utilize transistor devices as current source. The modification or shaping of current waveforms leads to operating classes of power amplifiers namely class-A, class-B, class-AB, class-C, and class-F.

In class-A, the transistor device is biased in such a way that it conducts current all the time. In theory, the current through the device should exactly replicate the shape of the input voltage signal; and, the dc bias current should be sufficient to ensure that the device remains in conductance region at all times [79]. To satisfy this requirement and to obtain the optimal performance of the amplifier in class-A mode, the biasing point (I_{DD} , V_{DD}) shown in Fig. 1.11 is chosen according to Eqs. (1.13) and (1.14). This biasing provides plenty of room for the output signal swing, and hence the chances of reaching cut-off and saturation regions are small. It is primarily due to this reason that class-A amplifier exhibits very low distortion in its output.

$$I_{DD} = \frac{I_{max}}{2} \tag{1.13}$$

$$V_{DD} = V_{knee} + \frac{V_{max} - V_{knee}}{2} = \frac{V_{max} + V_{knee}}{2}$$
(1.14)

Fig. 1.11 Load lines for different loading conditions



The bias point defined by Eqs. (1.13) and (1.14) are also applicable for small-signal amplifiers. However there is significant difference in the operation of large-signal (power) amplifier and the small-signal amplifier. In the case of small-signal, the appropriate matching involves the termination of device output with its complex conjugate. Under this type of matching the device load line, plotted using Eq. (1.1), is represented by A1 in Fig. 1.11 [83]. It is apparent that in such a situation the current swing is less than the maximum device current (I_{max}). Similarly for load impedance with a smaller resistance than the device output resistance, the load line is the one indicated as A3 in Fig. 1.11 and this leads to a condition where the voltage swing is smaller as compared to the maximum voltage rating (V_{max}).

In the cases of both A1 and A3, the maximum achievable output power is not reached, as these load lines do not utilize the full current and voltage swings. However, for a power amplifier, the goal is to obtain maximum output power from the device; therefore, the load line must correspond to the one marked as A2 in Fig. 1.11. For load line A2, the real part of load impedance given by Eq. (1.15) is dependent on the maximum current and voltage ratings of the device, while the imaginary part of load impedance is selected in such a way that it cancels the output reactance of the device. However, this optimal value of load impedance for maximum output power creates a mismatch between the device and load impedance and has the potential to cause a high voltage standing wave ratio (VSWR) at the output of the device [18].

$$Re(Z_L)_{opt-classA} = (R_{opt})_{classA} = \frac{V_{max} - V_{knee}}{I_{max}}$$
(1.15)

The voltage and current at the device output in the class-A operation mode are sinusoidal and swing between the minimum and maximum values, which are dependent on the device's technology. In such a situation, expressions for the dc power delivered to the device, the power at the output of device, and the drain efficiency are given as:

$$P_{DC} = V_{DD}I_{DD} = \left(\frac{I_{max}}{2}\right)\left(\frac{V_{max} + V_{knee}}{2}\right)$$
(1.16)

$$(P_{out})_{classA} = \frac{I_{out}^2(R_{opt})_{classA}}{2} = \frac{(I_{max}/2)^2}{2} \left(\frac{V_{max} - V_{knee}}{I_{max}}\right)$$
$$= \frac{I_{max}(V_{max} - V_{knee})}{8} = \frac{I_{max}(V_{DD} - V_{knee})}{4}$$
(1.17)

$$(\eta_D)_{classA} = \frac{(P_{out})_{classA}}{P_{DC}} = \frac{V_{max} - V_{knee}}{2(V_{max} + V_{knee})} = \frac{V_{DD} - V_{knee}}{2V_{DD}}$$
(1.18)

It is apparent from Eqs. (1.16), (1.17), (1.18) that output power and drain efficiency of class-A PA increases with the square of the output current I_{out} ; whereas the consumed dc power is constant. For class-A, the optimum values of P_{out} and efficiency occurs for the situation when the current I_{out} reaches its maximum value ($I_{max}/2$).

The theoretical maximum drain efficiency of class-A PA reaches 50 % when the knee voltage (V_{knee}) is very small. This low value is contributed by the continuous consumption of dc power. In order to overcome this issue, and to improve the efficiency of PAs, bias current (I_{DD}) is reduced while keeping the same maximum voltage and current swing. The reduction in the bias current is achieved by reducing the conduction angle, which forms the basis of reduced conductions angle power amplifiers [83].

In order to enhance the efficiency of transconductance amplifier, it is essential to have at least one of the waveforms to be non-sinusoidal. For the replication of this condition, the voltage waveform is kept same as in class-A while the current waveforms are altered such that there are periods in which the device does not conduct. The PAs in such a situation are called reduced conduction angle power amplifiers with the assigned terminology of classes AB, B, and C; as summarized in Table 1.1. The conduction angle (α) is determined by the quiescent gate voltage (V_{GSQ}) , which is a function of the device pinch-off voltage (V_p) as well as the device built-in voltage (V_{bi}) .

It is also important to understand that the linearity of PA is affected by the reduction in the conduction angle. It is essentially due to the fact that the output current and voltage has smaller swing in the linear region when the conduction angle is reduced. The most linear amplifier is obtained for class-A operation and the linearity worsens while moving from class-A to class-C. An amplifier operating in class-A or class-B exhibits similar linearity performance if the transconductance of the device (g_m) remains constant [21]. However, in practical situations this is not normally the case and as a consequence class-A power amplifier exhibits better linearity.

Even with all the advantages, the reduced conduction angle power amplifiers with shorted harmonics have some limitations. The main problem of such power amplifiers lies in the fact that it involves increase in the input RF signal with the reduction in the conduction angle if the peak current is to be maintained constant. As a consequence, the gains of such amplifiers get reduced which limit the usefulness of these techniques in the design of amplifiers with devices possessing high gain.

An alternative solution to overcome the problems caused by harmonics present in the output of the PA is to provide either an open circuit condition at all harmonics except the fundamental frequency for achieving class-E and class-D operation modes [19, 20, 22, 23] or drain current and voltage shaping for achieving class-F, class-F⁻¹,

Class	Conduction angle (α)	Bias voltage (V_{GSQ})	Bias current (I_Q)
A	2π	$V_p + 0.5 * (V_{bi} - V_p)$	$0.5*I_{max}$
AB	π –2 π	$V_p + (0 \to 0.5) * (V_{bi} - V_p)$	$(0 \rightarrow 0.5) * I_{max}$
B	π	V_p	0
C	0–π	< <i>V</i> _p	0

Table 1.1 PA classes based on conduction angle

class-J, and class-J * [23–27] operation modes, in order to obtain increased output power and drain efficiency.

The concepts of class-F amplifiers and class-B amplifiers are the same with the only difference being the addition of odd harmonics in the class-F voltage waveform. The addition of odd harmonics pushes the class-F voltage waveforms closer to square shapes. In this mode of operation, the odd harmonics are open-circuited which allows the harmonic voltages to exist without harmonic currents. The result of such an exercise is that the presence of odd harmonics flattens the bottom of the voltage waveform due to abrupt change in the incremental conductivity between the triode and transconductance regions [79]. In addition, the flattening of the bottom of the voltage waveforms also flattens the top of the voltage waveforms due to the symmetry of the odd harmonics [79].

The main advantage of the class-F amplifiers lies in the fact that, in theory, they can achieve efficiency up to 100 % for the case when all the odd harmonics are open-circuited to obtain perfect square voltage waveform. In such a situation the amplifier works like a switch and for this reason class-F amplifiers are termed as switched mode power amplifiers. Another advantage of class-F is the increased output power, by almost 27 %, without increasing the peak voltage or peak current considering that the amplitude of square wave is $4/\pi$ times that of the sinusoidal wave [59, 79].

Complexity of class-F power amplifiers is the major limitation due to the fact that the number of resonators required increases with each harmonics. Keeping this in the perspective it is rare to see design of class-F amplifiers with more than three harmonics terminations considering the complexity involved in their designs even with the availability of synthesized load-pull data. Nevertheless even only three harmonic tuning is sufficient to obtain high efficiency Class-F and its dual class-F⁻¹ power amplifiers [22, 84].

Switched-mode power amplifiers, such as class-F, operate on the principle that the transistor device remains out of the transconductance region of simultaneous high voltage and high current. However, there is always some overlap between the current and voltage, because only a limited number of harmonics are taken into account. Switching amplifiers overcome this issue by employing the transistor device as a switch in such a way that it is either in the high impedance region or in the high conductivity triode region. The operation of switch (device) in one direction or the other with load impedance or inverted load impedance regulates the power amplifiers, namely class-D, inverse class-D, class-E, and inverse class-E [85, 86].

As there is no overlap between the current and voltage waveforms in the switching amplifiers, the theoretical maximum achievable drain efficiency is 100 %.

1.5 Power Amplifier Design Methodologies

Power amplifier (PA) design techniques, which are driven by the availability of measurement systems, modeling approaches and choice of simulation programs, are commonly categorized into two types. The first category is computer-aided design (CAD) based methods, which predict the behavior of the PA through the use of device models; and, the other type is measurement-based methods, where the device is characterized a priori for relevant design parameters, such as gain, output power and power-added efficiency, which are then used in the PA design process.

1.5.1 CAD-Based Design Methods

The design of linear microwave passive and active circuits/systems using CAD tools has become standard design process; whereas, the design of nonlinear microwave components, such as PAs, are still evolving. Nonetheless, CAD-based PA design is gaining popularity due to the availability of powerful CAD tools, such as Advanced Design System (ADS) and Microwave Office (MWO) [28, 29].

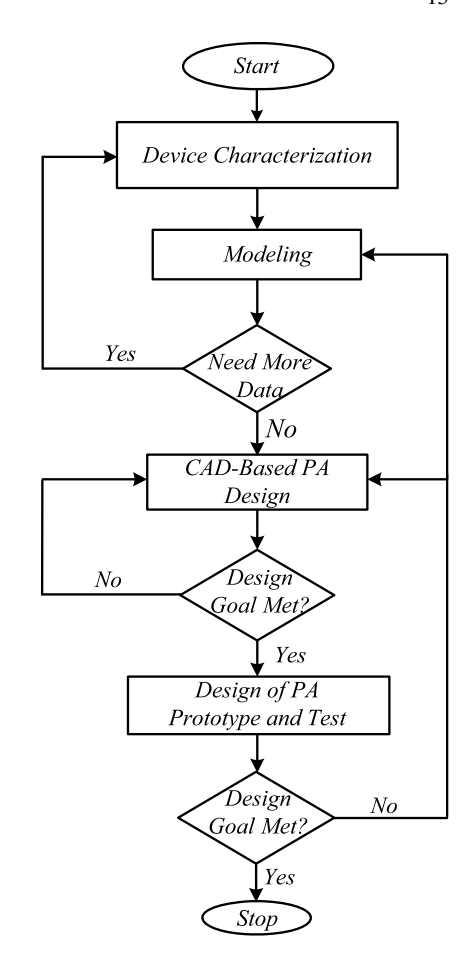
In this type of technique, as shown in Fig. 1.12, a model for the specified device is developed in theory; and, the model extraction procedure is initially identified [30, 31]. Subsequently, experimental characterization of the specified device is carried out, using large-signal measurement techniques, such as vectorial large-signal measurement [32], in order to obtain the necessary measurement data required for model extraction.

By following the selected extraction procedure, the model is extracted and preferably implemented in a CAD environment [33–36]. The accuracy and reliability of the model is tested, for which an iterative process is usually needed. The model can be relied upon once the requisite accuracy in the desired performance is achieved. PA designers can start CAD-based design by using the model; and, the designed PA is finalized, if all the design specifications are met at the PA performance testing stage.

The main advantage of this approach lies in the fact that nonlinear circuits and systems can be built via models using CAD tools. The CAD tools assist the designers in tackling complex design problems at the outset. For example, nonlinear simulation algorithms, such as harmonic balance, allow the designers to design the necessary circuitries around the nonlinear model and test the overall performance of the system prior to the manufacturing of expensive prototypes.

Furthermore, CAD tools also give the designers a quick, easy and inexpensive option to go back and restart the design, if a big design flaw is spotted during the simulation. The use of CAD tools in design and testing stages, therefore, significantly increase the chance of a first-pass design.

Fig. 1.12 Flow-chart of CAD-based PA design methods



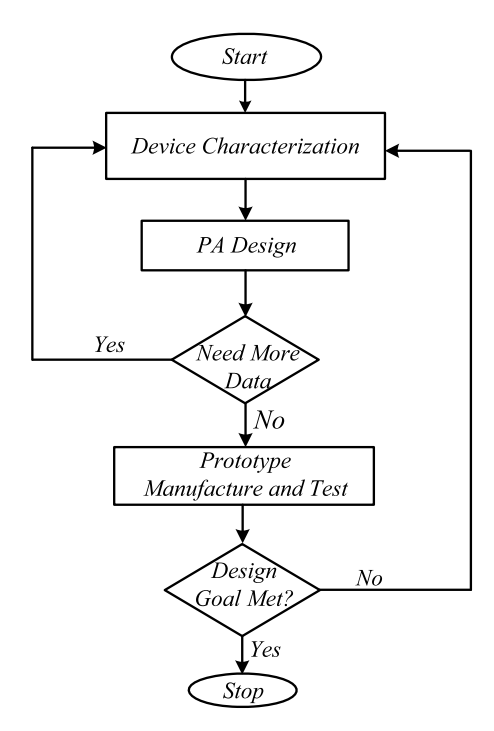
1.5.2 Measurement-Based Design Methods

In these methods, the specified transistor device is first characterized, in order to obtain key design parameters of the device, such as the gain, efficiency and load-pull contours. A generic design flow for measurement-based PA is given in Fig. 1.13.

In this type of technique, the measured data forms the primary basis of design; and, these data are used to build PA prototypes along with the auxiliary circuitries, such as matching and biasing circuits. The design process is finalized once the designed PA successfully passes the test. The major advantage of this approach is the time saved by discarding the time-consuming development of device modeling. This type of design method relies on the accuracy of the measurement system in generating the data.

This technique used to be extremely risky, but the emergence of accurate large-signal measurement systems [37–43] has greatly improved the effectiveness of this design strategy. These measurement systems allow for the capture of detailed key

Fig. 1.13 Flow-chart of measurement-based PA design methods

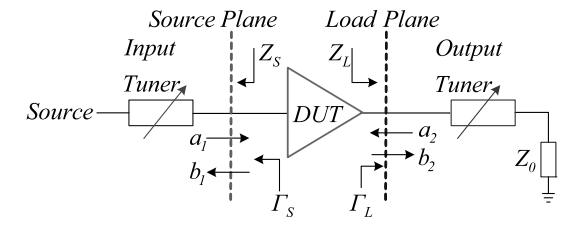


characteristics of transistor devices with improved accuracy when the device under test is driven in realistic working conditions. For example, the large-signal waveform measurement systems provide the ability to monitor, control and alter the current and voltage waveforms at device ports, in order to collect the required measurement data for the design of high-efficiency power amplifiers [44, 45]. Such measurement systems, therefore, enable first-pass PA design considering that the design is based on measured data under required operating conditions.

1.6 Nonlinear Microwave Measurement System

The increased demand for enhanced performance from the transistor devices requires them to be commonly operated nearer to compression, firmly in their nonlinear regions. The measurement of devices operating in nonlinear operation requires large-signal measurement systems (also called nonlinear measurement systems). For PA applications, large-signal measurement systems [37–43], along with load-pull test benches [46–52], are essential for accurate measurements of device characteristics under realistic operating conditions.

Fig. 1.14 Block diagram defining load reflection coefficient, Γ_L , generated using an output tuner at the load plane [46], diagram © IEEE 2011



1.6.1 What Is Load-Pull?

In generic terms, load-pull refers specifically to presenting a priori impedance to a device under test (DUT) in a precisely controlled fashion, in order to extract the optimal performance from the DUT [47]. In load-pull measurements, optimal performance is found by varying terminal impedances, along with frequency and bias, so as to rapidly and accurately establish conditions under which optimal performances from the specified DUT can be obtained.

For PAs, the optimal loading conditions primarily depend on the nonlinearities exhibited by transistors. These are significantly different from linear cases, where the optimal loading conditions are directly identified from S-parameters [18, 19]. In the nonlinear case, load-pull systems determine the appropriate impedance values experimentally through impedance tuners, while physically the changing load reflection coefficient, Γ_L , as shown in Fig. 1.14, for the extraction of desired design parameters from transistor devices.

The desired matching impedance, Z_L , the incident and reflected traveling waves, a_2 and b_2 , at the output port and reflection coefficient, Γ_L , are related by expressions in Eqs. (1.19) and (1.20).

$$\Gamma_L = \frac{a_2}{b_2} \tag{1.19}$$

$$\Gamma_L = \frac{Z_L - Z_0}{Z_L + Z_0} \tag{1.20}$$

where Z_0 is the characteristic impedance of the system in which the DUT is going to be used (normally 50 Ω).

In summary, a load-pull system includes an active or passive impedance-tuner [46–52], the controlling mechanism to precisely set the tuner impedance to achieve desired impedance, and equipment and test set to measure the traveling waves at the DUT ports.

1.6.2 Why Load-Pull?

There are various ways to identify the reasons for using load-pull based measurements and characterization of high-frequency power transistors. The high-frequency

active and passive design requires accurate measurements. Passive elements are assumed linear and, therefore, can be fully defined through frequency dependent S-parameters [18]; however, the active elements, such as power transistors, are usually considered nonlinear and cannot be accurately defined through linear S-parameters.

For example, the output current and voltages are nonlinearly related in the case of active components. The nonlinear dependence gives rise to unwanted spectral components, harmonics or intermodulation products that were not present in the excitations.

In the design of PAs, the appropriate terminations at the input and output are extremely important, as they help in the estimation and determination of the amplifier behavior and performances. For this reason, it is important to assess the impact of input and output terminations in the design of PAs. The correct choice of input and output terminations can optimize the performance of PAs in terms of parameters, such as the output power, PAE and gain.

Load-pull systems enable rapid, accurate and reliable determination of performance parameters of the PAs, as they allow precise and controlled setting of the terminal impedances. In addition, these systems allow for measurements and characterization of transistor devices, in order to test the linearity of PAs under varying loading conditions, while subjected to modulated excitation signals [53].

There is significant benefit in using load-pull systems for the determination of optimal loading conditions of a microwave device operating in nonlinear mode, such as mixers [54] and oscillators [55, 56]. In many applications, the terminal loading conditions at harmonic frequencies may also significantly affect the device performance, as proven by both theory [57–59] and experiments [60–70]. In such situations, harmonic load-pull systems are very effective, as they allow for changing Γ_L values at a discrete set of frequencies (typically two or three) [47, 48].

Another significant application of load-pull systems is in the generation of measurement data that can be utilized in CAD platforms for the development and validation of nonlinear device models [33–36], which is extremely important for right-the-first-time PA design.

1.7 Important Load-Pull Features

How does one choose between various types of load-pull tuners [46–52]? What is most significant factor in choosing a load-pull tuner? The answer is simple, while tuner repeatability and resolution are important characteristics for all load-pull systems, the priority of other features depends on how specific tuner characteristics meet the needs of a desired measurement application.

For example, a passive solid-state load-pull system [71] may be a better choice for high-speed on-wafer device characterization because of the absence of mechanical vibrations; whereas a passive mechanical load-pull system [72] can be used both for noise and power characterization of a packaged device, and active load-pull systems [49–51] can be more appropriate for high-power applications considering their

ability to synthesize high reflection coefficients. Therefore, several aspects need to be looked into before deciding the appropriate tuner for a specified application.

1.7.1 Repeatability of Reflection Coefficients

Measurements using an automated tuner-based load-pull system require precalibrated tuners, and, therefore ability of the tuners to repeat impedance states is extremely important. Any discrepancy in the synthesized impedance translates to discrepancy in synthesized matching network or developed nonlinear device model. The repeatability of the tuner ensures that data obtained from automated load-pull system could be fully trusted and therefore utilized in the development of accurate application specific device models and matching circuit design.

Repeatability of the impedance tuner is the difference in the reflection coefficient between two or more repeated settings of the tuner to the same horizontal and vertical positions and is measured by a calibrated vector network analyzer (VNA). The repeatability of impedance can be tested by setting the tuner to a number of positions around the Smith Chart twice: once to save the measured data in the VNA memory; and, repeated to retrieve the data from the VNA and compare it with the memory data. The error in repeatability is computed using the following expression [73]:

$$(S_{11})_{repeatability} = 20.\log \left| (S_{11})_{measured} - (S_{11})_{memory} \right| \tag{1.21}$$

where $(S_{11})_{measured}$ stands for the last measured S-parameter, and $(S_{11})_{memory}$ stands for the S-parameter in memory.

The repeatability is mentioned in terms of dB. For example, commercially available passive-mechanical tuners and passive solid-state tuners typically exhibit better than -60 dB and -70 dB repeatability, up to 50 GHz, respectively [74]. Active load-pull systems [49–51] generally do not exhibit good repeatability with the exception of the active envelope load-pull system, which possesses good repeatability around -55 dB [75].

1.7.2 Tuning Range and Its Distribution

The tuning range of the tuner, often called the ability to establish a reflection environment, refers to the range of reflection factors that a tuner can present. In principle, this aspect is more relevant for the characterization of high-power devices, where extremely low output impedances are often encountered. Usually, passive tuners are very good for low- or medium-power devices where the desired reflection factor is closer to the center of the Smith chart. However, passive tuners possess limited ability to synthesize reflection coefficients close to the border of the Smith chart [47, 48] and, therefore, find limited usefulness in applications, such as high-power device characterization or harmonic load-pull measurements.

On the other hand, active load tuners do not suffer from tuning range limitations and, thus, are more appropriate for the measurement and characterization of high-power devices and harmonic load-pull applications [46]. Active tuners can also synthesize reflection coefficients outside the Smith chart boundary and, as a result, find applications in the design of oscillators.

The tuning range distribution refers to coverage of the generated reflection factors over the Smith chart and the control of these reflection points in a precise manner within the desired region of the Smith chart [74]. The pre-matched load-tuners [47, 48] and active envelope load-pull [75] systems can be precisely controlled and employed in applications where an accurate reflection environment is required in a particular region of the Smith chart.

1.7.3 Tuning Speed

Tuning speed is the time taken by a tuner to move from one impedance state to the next. This feature is very important for applications where high measurement throughput is required. In addition to the tuner's speed, the total measurement time also includes time taken by the measurement equipments at each impedance position while the measurements are being made [74]. Passive tuners are good for high yield and fast measurement throughput applications.

1.7.4 Power Handling Capability

Power handling is an extremely important feature of any load-pull setup. It is described as the maximum root mean square (rms) or peak power that can be delivered to a tuner without any appreciable change in tuner impedance or any damage to the tuner [74]. In practical applications, a high tuner insertion loss causes heating of tuner elements which can lead to variation in the calibrated impedance seen by the DUT; whereas an improperly designed tuner can exhibit corona discharge which has the potential to damage the tuner or the DUT [76]. A passive tuner with high power handling capability overcomes these problems [73, 74], and carefully configured active load-pull setups with high power handling ability can often meat application requirements [76].

1.7.5 Tuner Resolution

Tuner resolution, which refers to the resolution of impedance points synthesizable by the tuner, is an important parameter for power transistor characterization as parameters such as PAE and output power of these devices are highly sensitive to even

Fig. 1.15 A single probe tuner, photo © Focus Microwaves Inc.



slight variation in impedance states. Therefore a tuner exhibiting high resolution is considered extremely important in precision measurements. Any standard passive-mechanical tuners typically synthesize 10,000 points, which can be enhanced to millions of points using cascaded tuners or interpolation [77]. However, in such cases, the tuning accuracy is fully dependent on the accuracy of interpolation [77]. Furthermore, high resolution tuners increase the measurement time considering the time required in covering all the impedance states.

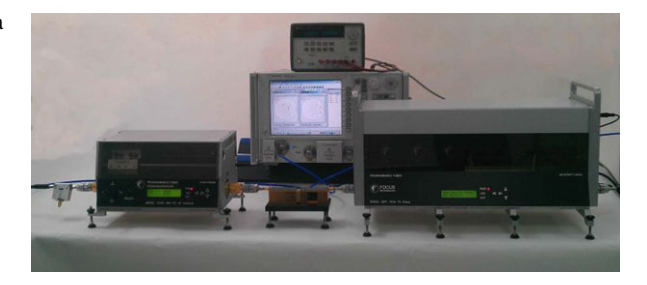
1.7.6 Tuner Bandwidth

Tuner bandwidth is often interchangeably referred to both the frequency range of the tuner and the instantaneous bandwidth of the tuner. The bandwidth of the tuner is the frequency range over which the tuner is able to synthesize the specified impedances, whereas the instantaneous bandwidth, or the modulation bandwidth, of the tuner is the frequency range over which the group delay is constant. The standard passive tuners are able to operate successfully from low MHz to 40 GHz, but are unable to synthesize constant reflection coefficients under modulated excitations. Active load-pull systems have potential to provide constant reflection coefficients over a modulation bandwidth.

1.7.7 Tuner Size

Tuner size is extremely important in on-wafer high-speed device characterization where in situ calibration is used; smaller size in such situations are required in order to avoid acoustic vibrations and mechanical vibrations [72]. It is a standard practice to perform a vibration test on the load-pull systems, even if utilizing small sized tuners, in such on-wafer high-speed environments.

Fig. 1.16 Setup diagram of a fully functional passive load-pull system, photo © Focus Microwayes Inc.



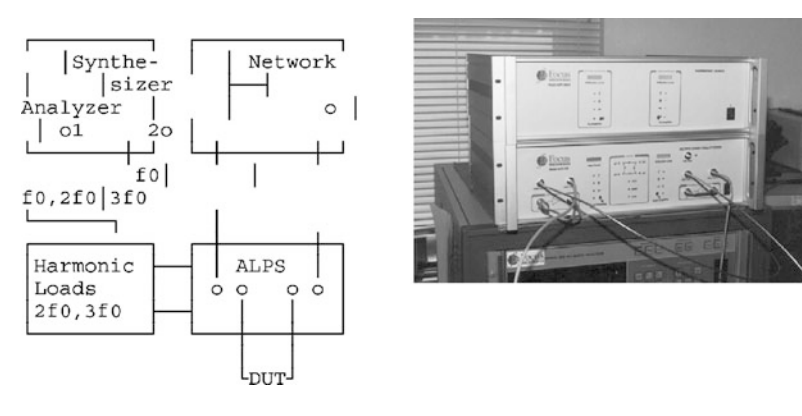


Fig. 1.17 An active load-pull setup (ALPS) for high frequency device characterization, photo © Focus Microwaves Inc.

1.8 Common Load-Pull Systems

Over the years, the configurations of load-pull systems have evolved; however, they still fall into two categories, namely passive and active load-pull systems. They are categorized and distinguished based on the fashion in which they synthesize the load impedance.

In passive techniques, the desired impedance is synthesized by varying the reflection coefficient of the impedance controlling element, such as the single probe tuner as depicted in Fig. 1.15; and, the measurement is carried out using a typical setup, as shown in Fig. 1.16.

As mentioned earlier, in the passive technique, the reflection coefficient is changed through the setting of the tuner, whereas the active load-pull approach synthesizes the impedance environment by injecting a signal at the DUT port. A typical setup of an active load-pull setup is depicted in Fig. 1.17. Once again, it is important to mention that both active and passive techniques have unique benefits and, therefore, have advantages in specific measurement applications. Passive load-pull techniques are mostly needed for swept drive, frequency and bias applications; and, active load-pull systems are more appropriate for applications requiring highly reflective environments.

References 23

References

 H. Chireix, High power outphasing modulation. Proc. Inst. Radio Eng. 23(II), 1370–1392 (1935)

- W.H. Doherty, A new high efficiency power amplifier for modulated waves. Proc. Inst. Radio Eng. 24, 1163–1182 (1936)
- 3. L. Kahn, Single sideband transmission by envelope elimination and restoration. Proc. Inst. Radio Eng. 40, 803–806 (1952)
- D.C. Cox, Linear amplification with nonlinear components, IEEE Trans. Commun. 22, 1942– 1945 (1974)
- F.H. Raab, Efficiency of Doherty RF power amplifier system. IEEE Trans. Broadcast. BC-33(3), 77–83 (1983)
- S. Bousnina, F.M. Ghannouchi, Analysis and experimental study of an L-band new topology Doherty amplifier. in 2001 IEEE Microwave Theory and Techniques Society's International Microwave Symposium Digest, Phoenix, USA, vol. 2 (May 2001), pp. 935–938
- B. Kim, J. Kim, I. Kim, J. Cha, The Doherty amplifier. IEEE Microw. Mag. 7(5), 42–50 (2006)
- 8. M. Helaoui, F.M. Ghannouchi, Linearization of power amplifiers using the reverse Mm-linc technique. IEEE Trans. Circuits Syst. II, Express Briefs **57**(1), 6–10 (2010)
- S.C. Jung, O. Hammi, F.M. Ghannouchi, Design optimization and DPD linearization of GaN based unsymmetrical Doherty power amplifiers for 3G multi-carrier applications. IEEE Trans. Microw. Theory Tech. 57(9), 2105–2113 (2009)
- R. Darraji, F.M. Ghannouchi, O. Hammi, A dual-input digitally driven Doherty amplifier architecture for performance enhancement of Doherty transmitters. IEEE Trans. Microw. Theory Tech. 59(5), 1284–1293 (2011)
- 11. S.A. Maas, Nonlinear Microwave and RF Circuits, 2nd edn. (Artech House, Norwood, 2003)
- 12. J. Wood, D.E. Root (eds.), Fundamentals of Nonlinear Behavioural Modelling for RF and Microwave Design (Artech House, Norwood, 2005)
- D.E. Root, J. Verspecht, D. Sharritt, J. Wood, A. Cognata, Broad-band poly-harmonic distortion behavioral models from fast automated simulations and large-signal vectorial network measurements. IEEE Trans. Microw. Theory Tech. 53(11), 3656–3664 (2005)
- J. Verspecht, D.E. Root, Poly-harmonic distortion modeling. IEEE Microw. Mag. 7(3), 44–57 (2006)
- 15. J. Verspecht, M. Vanden Bossche, F. Verbeyst, Characterizing components under large signal excitation: defining sensible 'large signal S-parameters, in *49th IEEE ARFTG Conference*, Denver, USA (June 1997), pp. 109–117
- S.C. Cripps, RF Power Amplifiers for Wireless Communications, 2nd edn. (Artech House, Norwood, 2006)
- 17. R. Gilmore, L. Besser, *Practical RF Circuit Design for Modern Wireless Systems*, vol. II (Artech House, Norwood, 2003)
- D.M. Pozar, Microwave Engineering, 3rd edn. (Wiley, New York, 2005). ISBN 0-471-17096-
- 19. G. Gonzalez, Microwave Amplifier Design, 2nd edn. (Prentice Hall, New York, 1996)
- L.J. Kushner, Output performance of idealized microwave power amplifiers. Microw. J. 32(10), 103–116 (1989)
- P. Colantonio, J.A. Garcia, F. Giannini, E. Limiti, E. Malaver, J.C. Pedro, High linearity and efficiency microwave PAs, in *European Gallium Arsenide and Other Semiconductor Applica*tion Symposium (2004), pp. 183–186
- F.H. Raab, Class E, class C, and class F power amplifiers based upon a finite number of harmonics. IEEE Trans. Microw. Theory Tech. 49(8), 1462–1468 (2001)
- 23. J.H. Jeong, H.H. Seong, J.H. Yi, G.H. Cho, A class D switching power amplifier with high efficiency and wide bandwidth by dual feedback loops, in *International Conference on Consumer Electronics*, Rosemont, USA (June 1995), pp. 428–429

 J. Staudinger, Multiharmonic load termination effects on GaAs power amplifiers. Microw. J., 60–77 (1996)

- 25. F.H. Raab, Maximum efficiency and output of class-F power amplifiers. IEEE Trans. Microw. Theory Tech. **49**(6), 1162–1166 (2001)
- H. Kim, G. Choi, J. Choi, A high efficiency inverse class-F power amplifier using GaN HEMT. Microw. Opt. Technol. Lett. 50(9), 2420–2422 (2008)
- A. Ramadan, T. Reveyrand, A. Martin, J.-M. Nebus, P. Bouysse, L. Lapierre, J.-F. Villemazet, S. Forestier, Two-stage GaN HEMT amplifier with gate-source voltage shaping for efficiency versus bandwidth enhancements. IEEE Trans. Microw. Theory Tech. 59(3), 699–706 (2011)
- Advanced Design System (ADS), Version 2009, Agilent Technologies: http://www.agilent.com
- 29. Microwave Wave Office (MWO), Version 2010, AWR Corp: http://www.awrcorp.com
- 30. Y. Tsividis, Operation and Modeling of the MOS Transistor (McGraw-Hill, New York, 1987)
- 31. C.M. Snowden, Nonlinear modelling of power FETs and HBTs, in *3rd International Workshop on Integrated Nonlinear Microwave and Millimeterwave Circuits*, Duisberg, Germany (Oct. 1994), pp. 11–25
- 32. J. Verspecht, P. Van Esch, Accurately characterizing hard nonlinear behavior of microwave components with the nonlinear network measurement system: introducing 'nonlinear scattering functions', in 5th International Workshop on Integrated Nonlinear Microwave and Millimeterwave Circuits, Duisberg, Germany (Oct. 1998), pp. 17–26
- 33. D. Schreurs, J. Verspecht, S. Vandenberghe, G. Carchon, K. van der Zanden, B. Nauwelaers, Easy and accurate empirical transistor model parameter estimation from vectorial large-signal measurements, in *IEEE Microwave Theory and Techniques Society's International Microwave Symposium Digest*, Anaheim, USA (June 1999), pp. 753–756
- A. Issaoun, R. Barrak, A.B. Kouki, F.M. Ghannouchi, C. Akyel, Enhanced empirical largesignal model for HBTs with performance comparable with physics-based models. IEE Proc. Sci. Meas. Technol. 151(3), 142–150 (2004)
- 35. M. Prigent, J.C. Nallatamby, M. Camiade, J.M. Nebur, E. Ngoya, R. Quere, J. Obregon, Comprehensive approach to the nonlinear design and modelling of microwave circuits, in *IEEE Signals, Systems, and Electronics Conference*, Pisa, Italy (Oct. 1998), pp. 450–455
- H. Qi, J. Benedikt, P. Tasker, A novel approach for effective import of nonlinear device characteristics into CAD for large signal power amplifier design, in *IEEE Microwave Theory and Techniques Society's International Microwave Symposium Digest*, San Francisco, USA (June 2006), pp. 477–480
- J.G. Lecky, A.D. Patterson, J.A.C. Stewart, A vector corrected waveform and load line measurement system for large signal transistor characterization, in *IEEE Microwave Theory and Techniques Society's International Microwave Symposium Digest*, Orlando, USA (May 1995), pp. 1243–1246
- 38. D.J. Williams, P.J. Tasker, An automated active source- and load-pull measurement system, in 6th IEEE High Frequency Student Colloquium, Cardiff, UK (Sept. 2001), pp. 7–12
- 39. S. Bensmida, P. Poire, F.M. Ghannouchi, Source-pull/load-pull measurement system based on RF and baseband coherent active branches using broadband six-port reflectometers, in *37th European Microwave Conference*, Munich, Germany (Oct. 2007), pp. 953–956
- W.S. El-Deeb, M.S. Hashmi, N. Boulejfen, F.M. Ghannouchi, Small-signal, complex distortion and waveform measurement system for multiport microwave devices. IEEE Instrum. Meas. Mag. 14(3), 28–33 (2011)
- 41. J. Benedikt, R. Gaddi, P.J. Tasker, M. Goss, High-power time-domain measurement system with active harmonic load-pull for high-efficiency base-station amplifier design. IEEE Trans. Microw. Theory Tech. **48**(12), 2617–2624 (2000)
- 42. D. Barataud, C. Arnaud, B. Thibaud, M. Campovecchio, J.-M. Nebus, J.P. Villotte, Measurements of time-domain voltage/current waveforms at RF and microwave frequencies based on the use of a vector network analyzer for the characterization of nonlinear devices application to high-efficiency power amplifiers and frequency multipliers. IEEE Trans. Instrum. Meas. 47(5), 1259–1264 (1998)

References 25

43. F. van Raay, G. Kompa, A new on-wafer large signal waveform measurement system with 40 GHz harmonic bandwidth, in *IEEE Microwave Theory and Techniques Society's International Microwave Symposium Digest*, Albuquerque, USA (June 1992), pp. 1435–1438

- 44. H.M. Nemati, A.L. Clarke, S.C. Cripps, J. Benedikt, P.J. Tasker, C. Fager, J. Grahn, H. Zirath, Evaluation of a GaN HEMT transistor for load- and supply-modulation applications using intrinsic waveform measurements, in *IEEE Microwave Theory and Techniques Society's International Microwave Symposium Digest*, Anaheim, USA (May 2010), pp. 509–512
- 45. Y.Y. Woo, Y. Yang, B. Kim, Analysis and experiments for high efficiency class-F and inverse class-F power amplifiers. IEEE Trans. Microw. Theory Tech. **54**(5), 1969–1974 (2006)
- 46. M.S. Hashmi, F.M. Ghannouchi, P.J. Tasker, K. Rawat, Highly reflective load-pull. IEEE Microw. Mag. 11(4), 96–107 (2011)
- Maury Microwave Corporation, Device characterization with harmonic load and source pull, Application Note: 5C-044, Dec. 2000
- Focus Microwave, Load pull measurements on transistors with harmonic impedance control, Technical Note, Aug. 1999
- G.P. Bava, U. Pisani, V. Pozzolo, Active load technique for load-pull characterization at microwave frequencies. IEE Electron. Lett. 18(4), 178–180 (1982)
- 50. Y. Takayama, A new load pull characterization method for microwave power transistors, in *IEEE Microwave Theory and Techniques Society's International Microwave Symposium Digest*, New Jersey, USA (June 1976), pp. 218–220
- 51. F.M. Ghannouchi, F. Beauregard, A.B. Kouki, Power added efficiency and gain improvement in MESFETs amplifiers using an active harmonic loading technique. Microw. Opt. Technol. Lett. **7**(13), 625–627 (1994)
- F.M. Ghannouchi, M.S. Hashmi, S. Bensmida, M. Helaoui, Enhanced loop passive sourceand load-pull architecture for high reflection factor synthesis. IEEE Trans. Microw. Theory Tech. 58(11), 2952–2959 (2010)
- B. Noori, P. Hart, J. Wood, P.H. Aaen, M. Guyonnet, M. Lefevre, J.A. Pla, J. Jones, Load-pull measurements using modulated signals, in 36th European Microwave Conference, Manchester, UK (Sept. 2006), pp. 1594

 –1597
- D.-L. Le, F.M. Ghannouchi, Multitone characterization and design of fet resistive mixers based on combined active source-pull/load-pull techniques. IEEE Trans. Microw. Theory Tech. 46(9), 1201–1208 (1998)
- F.M. Ghannouchi, Device line simulation of high-speed oscillators using harmonic-balance techniques. Arab. J. Sci. Eng. 19(4B), 805–812 (1994)
- P. Berini, M. Desgagne, F.M. Ghannouchi, R.G. Bosisio, An experimental study of the effects of harmonic loading on microwave mesfet oscillators and amplifiers. IEEE Trans. Microw. Theory Tech. 42(6), 943–950 (1994)
- 57. D.M. Snider, A theoretical analysis and experimental confirmation of the optimally loaded and overdriven RF power amplifier. IEEE Trans. Electron Devices 14(12), 851–857 (1967)
- 58. J.D. Rhodes, Output universality in maximum efficiency linear power amplifiers. Int. J. Circuit Theory Appl. **31**, 385–405 (2003)
- 59. F.H. Raab, Class-F power amplifiers with maximally flat waveforms. IEEE Trans. Microw. Theory Tech. **31**(11), 2007–2012 (1997)
- R. Negra, F.M. Ghannouchi, W. Bachtold, Analysis and evaluation of harmonic suppression of lumped-element networks suitable for high-frequency class-E operation condition approximation. IET Microw. Antennas Propag. 2(8), 794

 –800 (2008)
- 61. M. Helaoui, F.M. Ghannouchi, Optimizing losses in distributed multiharmonic matching networks applied to the design of an RF GaN power amplifier with higher than 80 % power-added efficiency. IEEE Trans. Microw. Theory Tech. **57**(2), 314–322 (2009)
- F.M. Ghannouchi, M.S. Hashmi, Experimental investigation of the uncontrolled higher harmonic impedances effect on the performance of high-power microwave devices. Microw. Opt. Technol. Lett. 52(11), 2480–2482 (2010)

26 1 Fundamentals

63. G. Zhao, S. El-Rabaie, F.M. Ghannouchi, The effects of biasing and harmonic loading on MESFET tripler performance. Microw. Opt. Technol. Lett. **9**(4), 189–194 (1995)

- 64. F.M. Ghannouchi, F. Beauregard, A.B. Kouki, Power added efficiency and gain improvement in MESFETs amplifiers using an active harmonic loading technique. Microw. Opt. Technol. Lett. **7**(13), 625–627 (1994)
- P. Wright, J. Lees, J. Benedikt, P.J. Tasker, S.C. Cripps, A methodology for realizing high efficiency class-J in a linear and broadband PA. IEEE Trans. Microw. Theory Tech. 57(12), 3196–3204 (2009)
- M.S. Hashmi, A.L. Clarke, S.P. Woodington, J. Lees, J. Benedikt, P.J. Tasker, Electronic multiharmonic load-pull system for experimentally driven power amplifier design optimization, in *IEEE Microwave Theory and Techniques Society's International Microwave Symposium Digest*, Boston, USA, vols. 1–3 (June 2009), pp. 1549–1552
- 67. E. Bergeault, O. Gibrat, S. Bensmida, B. Huyart, Multiharmonic source-pull/load-pull active setup based on six-port reflectometers: influence of the second harmonic source impedance on RF performances of power transistors. IEEE Trans. Microw. Theory Tech. **52**(4), 1118–1124 (2004)
- 68. G.R. Simpson, M. Vassar, Importance of 2nd harmonic tuning for power amplifier design, in 48th Automatic Radio Frequency Techniques Group Conference, Florida, USA (Dec. 1996), pp. 1–6
- 69. P. Butterworth, S. Gao, S.F. Ooi, A. Sambell, High-efficiency class-F power amplifier with broadband performance. Microw. Opt. Technol. Lett. **44**(3), 243–247 (2005)
- G. Collinson, C.W. Suckling, Effects of harmonic terminations on power and efficiency of GaAs HBT power amplifiers at 900 MHz, in *IEE Colloquium on Solid-State Power Amplifiers* (Dec. 1991), pp. 12/1–12/5
- Maury Microwave Corporation, LP series electronic tuner system, Technical Data, 4T-081, 2002
- Focus Microwave, Mechanical vibrations of CCMT tuners used in on-wafer load-pull testing, Application Note AN-46, Oct. 2001
- 73. Focus Microwave, Comparing tuner repeatability, Application Note AN-49, March 2002
- Maury Microwave Corporation, Introduction to tuner-based measurement and characterization, Technical Data, 5C-054, Aug. 2004
- M.S. Hashmi, A.L. Clarke, S.P. Wooding, J. Lees, J. Benedikt, P.J. Tasker, An accurate calibrate-able multi-harmonic active load-pull system based on the envelope load-pull concept. IEEE Trans. Microw. Theory Tech. 58(3), 656–664 (2010)
- Z. Aboush, J. Lees, J. Benedikt, P. Tasker, Active harmonic load-pull system for characterizing highly mismatched high power transistors, in *IEEE Microwave Theory and Techniques Society's International Microwave Symposium Digest*, Long Beach, USA (June 2005), pp. 1311– 1314
- Focus Microwave, High resolution tuners eliminate load-pull performance errors, Application Note AN-15, Jan. 1995
- 78. M. Salib, D. Dawson, H. Hahn, Load-line analysis in the frequency domain with distributed amplifier design examples, in *IEEE Microwave Theory and Techniques Society's International Microwave Symposium Digest*, Palo Alto, USA (June 1987), pp. 575–578
- 79. S. Kee, The class E/F family of harmonic-tuned switching power amplifiers, PhD Thesis, California Institute of Technology, 2002
- Anritsu, Intermodulation distortion measurements using the 37300 series vector network analyzer, Application Note-11410-00213, Sept. 2000
- 81. R.H. Caverly, J.C.P. Jones, Contributions to adjacent channel power in microwave and wireless systems by PIN diodes, in *IEEE Microwave Theory and Techniques Society's International Microwave Symposium Digest*, San Francisco, USA (June 2006), pp. 910–913
- 82. 3GPP Technical Specification 25141, Base Station Conformance Testing (FDD)
- 83. M.A.Y. Medina, RF power amplifiers for wireless communications, PhD Thesis, Katholieke Universiteit Leuven, 2008

References 27

84. B. Ingruber, J. Baumgartner, D. Smely, M. Wachutka, G. Magerl, F.A. Petz, Rectangularly driven class-A harmonic-control amplifier. IEEE Trans. Microw. Theory Tech. **46**(11), 1667–1672 (1998)

- 85. S. El-Hamamsy, Design of high efficiency RF class-D power amplifier. IEEE Trans. Power Electron. 9(3), 297–308 (1994)
- 86. M.J. Chudobiak, The use of parasitic nonlinear capacitors in class-E amplifiers. IEEE Trans. Circuits Syst. I, Fundam. Theory Appl. **14**(12), 941–944 (1994)

Chapter 2 Passive Load-Pull Systems

In general, a passive load-pull system is built around a passive tuner. The tuner is used in combination with peripheral equipment and components, such as a vector network analyzer (VNA), signal generators, power meters, bias tees, isolators, for achieving the load-pull functionality. Primarily two types of passive tuners, namely the electromechanical tuner (EMT) and the electronic tuner (ETS), are employed in load-pull systems. It is imperative to understand the limitations of both these tuners so that the best solution can be employed for any specified application. The initial sections of this chapter are focused on the explanation and comparison of EMT and ETS based passive load-pull systems.

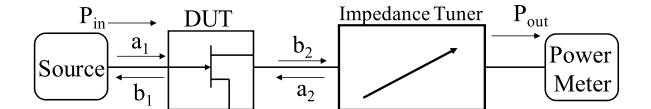
The major challenge in setting up a passive load-pull setup involves calibration, which is carried out to remove errors arising from mismatches, dispersions and imperfections in the cables and system components. A second aspect of calibration involves shifting of the measurement planes, considering that the actual measurement takes place away from the device under test (DUT) ports. Later sections of this chapter address the calibration aspect in detail.

2.1 Introduction

An impedance tuner is the main engine of any passive load-pull system [1–4]. The tuner is placed between the DUT and power meter, as shown in Fig. 2.1, for the search of optimal matching conditions for given targeted performance. The synthesis of optimal impedance involves changing of the tuner setting and then measuring subsequently the output power, P_{out} , using the power meter. The optimal impedance synthesized by the impedance tuner corresponds to the maximum reading of P_{out} by the power meter, according to the maximum power transfer theorem [5]. A separate power meter measures the power injected, P_{in} , by the source at the input of DUT.

Overall, setting of the impedance tuner directly provides the matching reflection coefficient, as given in Eq. (2.1), while readings of the power meters at the input and output relates the incident and reflected traveling waves, as given in Eqs. (2.2) and (2.3), at the respective DUT ports.

Fig. 2.1 Typical representation of a passive load-pull system



$$\Gamma_{out} = \frac{a_2}{b_2} \tag{2.1}$$

$$P_{in} = |a_1|^2 - |b_1|^2 = |a_1|^2 (1 - |\Gamma_{in}|^2)$$
(2.2)

$$P_{out} = |b_2|^2 - |a_2|^2 = |b_2|^2 (1 - |\Gamma_{out}|^2)$$
(2.3)

where, Γ_{out} and Γ_{in} are the reflection coefficients at the output and input ports of the DUT, respectively; and, a and b with subscripts represent the incident and reflected waves at the respective ports.

The optimal values of Eqs. (2.1), (2.2), (2.3) enable the determination of design parameters such as gain, efficiency and power-added efficiency (PAE). The determination of the optimal values and, subsequently, the design parameters is an iterative process and requires numerous changes in the configuration of the load-pull tuner.

2.2 Passive Load-Pull System

A passive load-pull system typically employs either electromechanical tuners (EMTs) that rely on horizontal and vertical movement of probes along a transmission line [6] or electronic tuners (ETSs), which rely on the appropriate electronic circuits with electronically changing matching properties [7]. EMTs are stub, slug or slide screw type [8, 9], whereas ETSs are mostly solid state and employ PIN diodes [10, 11].

2.2.1 Electromechanical Tuner (EMT)

These tuners allow precise positioning of probes/stubs/slugs in a slotted transmission line, in order to generate repeatable complex microwave reflection factors. Movement of the probes changes the impedance by changing the parallel susceptance. The probes are called mismatched elements and introduce mismatch through their movement in the horizontal and vertical directions. The movement of a probe in the vertical direction alters mainly the magnitude of the mismatch, while its movement in the horizontal direction alters mainly the phase of the mismatch.

A pictorial presentation of working principle of single-stub EMT is depicted in Fig. 2.2 [12]. In Fig. 2.2(a), the stub is outside the electric fields of the traveling wave propagating in the central conductor (transmission line) and, therefore, does not affect the impedance at the reference plane (usually set at 50 Ω). However, as soon as the probe moves vertically downward towards the central conductor (transmission line) the magnitude of the reflection factor at the reference plane increases, as can

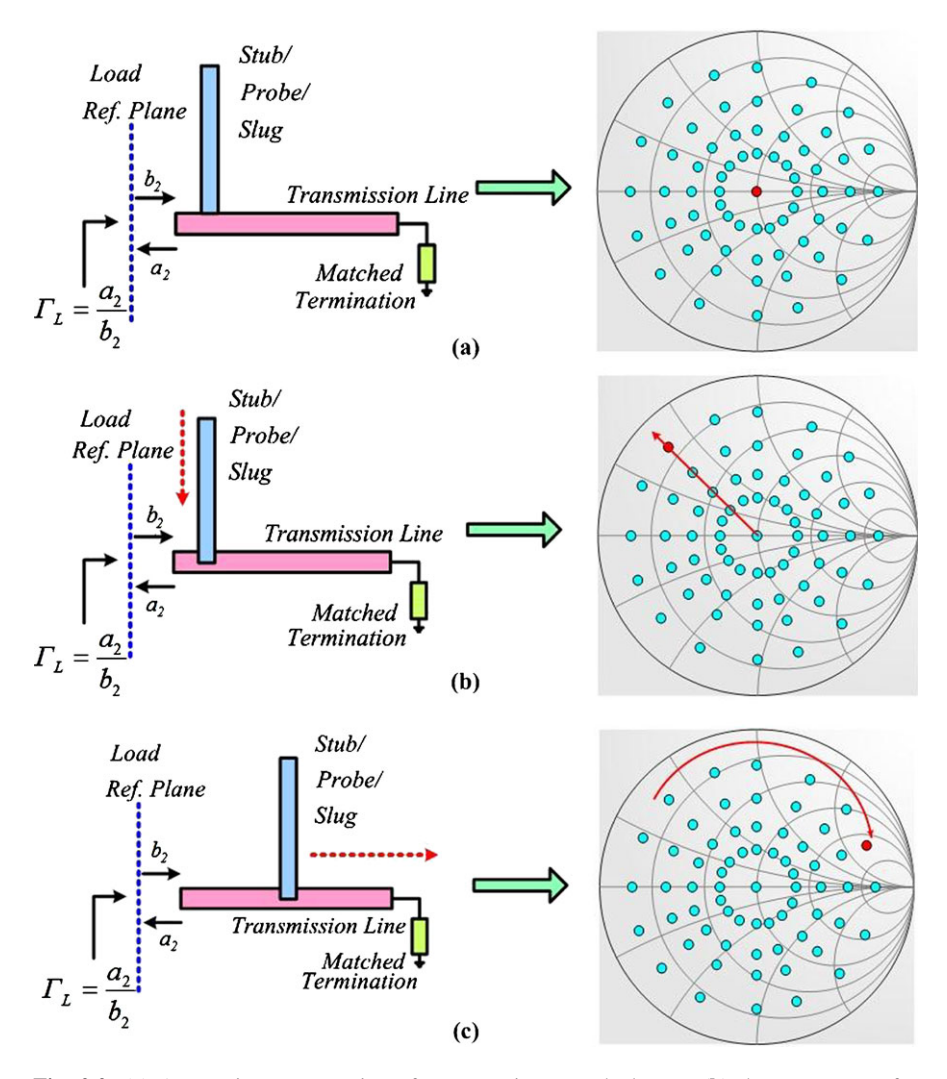
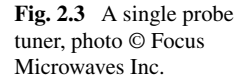


Fig. 2.2 (a) A generic representation of an EMT in a matched state, (b) the movement of a stub/probe/slug in the vertical direction changes the magnitude of the reflection factor, (c) the movement of a stub/probe/slug in the horizontal direction alters the phase of the reflection factor [12]; © IEEE 2011

be seen in Fig. 2.2(b). The movement of the probe in the horizontal direction along the central conductor varies the phase of the reflection coefficient, as evident in Fig. 2.2(c).

In principle, in any EMT, the magnitude of the impedance mismatch at the reference plane is determined by the probe position (depth); and, the phase of the impedance mismatch at the reference plane is determined by the carriage position across the length of the tuner length. An EMT is considered good if the resolution





of the movements of the stub/slug/probe in the horizontal and vertical directions is incrementally small in range of tens of microns [13]. A good EMT ensures that the desired reflection coefficient can be synthesized on a dense grid. An example of a commercial EMT (in this case, a single probe tuner) is given in Fig. 2.3.

The slide screw type of EMT consists of a 50 Ω coax- or slab-line with a probe with a nominal minimum length of $\lambda/4$ at its lowest frequency of operation and has two degrees of freedom [14, 15]. One movement is up and down towards the center conductor. This way the probe forms an adjustable shunt discontinuity with the 50 Ω transmission line. The other movement is the traveling of the probe along the 50 Ω mainline.

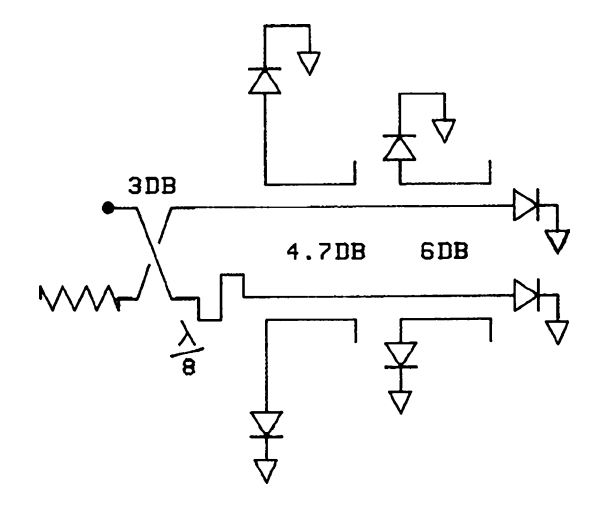
In stub tuners, two or more parallel sliding shorts (stubs) are placed on a 50 Ω line. When one is placed at the DUT reference plane and another $\lambda/8$ away from it, they independently control the real and imaginary parts of the admittance [6]. For a reflection factor (Γ_L) setting of 0, each stub has to be set to precisely $n\lambda/8$. A very high voltage standing wave ratio (VSWR) can be reached with a stub tuner.

The slug tuner is a construction with a 50 Ω coax- or slab-line, where two movable slugs can slide over the center conductor. The slug reduces the characteristic impedance locally to typically 10–15 Ω , while an electrical length of $\lambda/8$ for the transmission line gives maximum tuning range. In slug tuners, setting maximum $\Gamma_L(|\Gamma_L|)$ is easier, and losses tend to be constant over the tuning range, compared to other EMT types [6].

Overall, in a coaxial environment, the frequencies at which EMT can be used are around 200 MHz to 50 GHz in different multi-octave bands and tuner types. EMTs that use waveguides cover standard WR bands from 26.5 to 110 GHz [13].

In any automatic load-pull system based around an EMT, the movements of the probes in the horizontal and vertical directions are achieved through stepper motors; and, the actual positioning of the probe are monitored and controlled by timing belts. The use of timing belt to control axis positioning minimizes the vibrations translated from the stepper motors to the axis and then the probes [3] and, thus, makes these systems useful for on-wafer applications. In most cases, EMTs use the same vertical anti-backlash mechanism with a resolution of 0.75 or 1.5 µm per motor step; and,

Fig. 2.4 A generic diagram of a 6-diode based electronic tuner [10], © IEEE 1982



the horizontal step size varies between 1.25 and 25 µm, depending on the frequency of operation, in order to obtain an optimal tuning speed/resolution ratio [13].

2.2.2 Electronic Tuner (ETS)

An ETS is an electronic circuit with the ability to electronically change matching properties. These electronic circuits can be based on either varactor or PIN diodes. The latter is more common for load-pull applications, due to the ability to handle higher power compared to varactor-based ETS. The diode-based ETS synthesize reflection coefficient by varying the impedance state of a number of PIN diodes connected in parallel and placed in a precise manner along a transmission line, an example of which is shown in Fig. 2.4.

In such a configuration, each diode is capable of generating a continuous discontinuity as a spoke of a wheel of increasing $|\Gamma_L|$, while other diodes can subsequently change the angle of Γ_L discretely. The ETS in Fig. 2.4 consists of directional couplers, six PIN diodes, and external loads. This six-diode ETS can produce a total of sixty-four (2⁶) impedance states, corresponding to two states of each diode independently. Depending on the design, the diode impedance state can be varied continuously or toggled discretely between on and off states [10].

Essentially, a single ETS is limited in tuning resolution; therefore, a number of ETSs are cascaded together for applications requiring higher tuning resolution. The cascaded configuration is transparent to the user and, therefore, behaves as one tuner unit. Passive ETSs are generally quite lossy and, therefore, can usually achieve VSWRs up to 10 [7]. However, their miniature size and light weight make them appropriate for on-wafer measurements.

Characteristics	ETS	EMT
Reflection Factor, Γ	Noise: O Load Pull: -	++
Number of Impedances	O	++
Insertion Loss	-	+/++
Tuning Resolution	Noise: O Load Pull: –	++
Maximum Power	O / - / – Depending on DUT	++
Frequency Bandwidth	O	++
Spurious Oscillations	O / -	++
On Wafer Operation	++	O
Tuner Size	++	On Wafer: - Test Fixture: ++
Tuner Speed	++	-
Test Total Speed	+	+
Tuner Linearity	O / - Depending on DUT	++
DSB Noise Measurement	_	+
Temperature Drift	-	++

Table 2.1 Comparison between ETS and EMT [16]

Legend: ++ Excellent; + Good; O Acceptable; - Poor; - Unacceptable for certain tasks

2.2.3 ETS and EMT Comparisons

Load-pull systems are employed in diverse applications, such as the design of power amplifiers and oscillators and noise measurements,. As a consequence it is imperative to understand the features and limitations of ETSs and EMTs. Table 2.1 provides a comparison between EMT and ETS based on the most common load-pull parameters and applications [16].

ETSs consist of sets of PIN diodes, mounted in microstrip circuits, having only two states, i.e., on and off. Due to the physical distribution along microstrip lines, ETSs generate irregular shapes of reflection factors with values up to 0.8 over a limited frequency range [16]. An EMT can generate a reflection factor (Γ) of 0.75 in standard form and up to 0.92 in a pre-matched or cascaded state from low frequencies up to millimeter waves [17, 18].

ETSs are faster and can change states from impedance to impedance within milliseconds, whereas EMTs take at least a few seconds to tune from one state to another. However, it should be noted that ETS can save only around 10 % of the measurement time compared to that of EMT during the complete load-pull measurements, due to the time needed to read the instrumental setup via general purpose interface bus (GPIB) [16]. ETSs are also miniature, compact and substantially

smaller compared to EMTs, making the ETS more suitable for applications prone to mechanical vibrations, such as on-wafer device characterization and measurement.

The insertion loss of an ETS at the operating reflection factor is very high, due to lossy microstrip lines. This requires high-power driver amplifiers at the source side of the setup, which in turn raises the question of linearity of the PIN diodes and the temperature drift in the ETS. An ETS operating loss of 12 dB at $\Gamma=0.8$ is a common observable fact, this results in raising the cost of the setup considerably, whereas an EMT has only a few tenths of a dB at this Γ level [16].

The ETS has unpredictable impedance behavior at low frequencies, whereas the EMT is low pass and presents 50 Ω to the DUT. The ETS behavior is a high risk factor for uncontrollable spurious oscillations outside the test band. An EMT does not create parasitic oscillations, in principle, at low frequencies.

The tuning repeatability accuracy of ETS is around -70 to -80 dB, and the tuning accuracy of a modern EMT is around -60 dB. However, for accurate noise and load-pull measurements, tuning accuracies of -40 dB are sufficient [16].

In terms of tuning resolution, EMTs possess high resolution, thereby allowing fine-tuning to the optimal performance of the DUT; whereas an ETS exhibits irregular impedance patterns with the points jumping unpredictably when the diodes are switched on and off and, therefore, is not able to fine-tune to the optimal performance of the DUT. In noise measurements, the unpredictable jumping of impedance states for small frequency changes prohibits the use of ETSs in double sideband setups. This necessitates either YIG (yttrium iron garnet) filters or other expensive single sideband noise receivers. They do not allow direct measurement of the minimum noise figure, NF_{min} , by tuning to the optimal reflection factor Γ_{opt} ; whereas EMT allows fine-tuning and can, therefore, directly measure NF_{min} .

ETS is favored for on-wafer applications; however, EMT has been used in on-wafer applications below 0.8 GHz, after performing appropriate vibration tests [3].

2.3 Load-Pull Measurement

The load-pull measurement procedure primarily involves the following three steps:

- Assembly of the system components to establish a load-pull measurement setup.
- Calibration of the load-pull measurement setup for correction of errors arising from imperfect system components, dispersions, and mismatches. Calibration for setting the appropriate calibrated reference planes.
- Measurement of relevant data at the calibrated reference planes and then the deembedding of these data, in order to refer them to the device planes so that the behavior of the DUT can be accurately predicted.

It is imperative to understand the typical setup of a load-pull system, as shown in Fig. 2.5, before getting into the details. As depicted, a standard load-pull system consists of various equipments, such as a directional coupler, impedance tuners, power meters, and a computer for automating and controlling the overall measurement process.

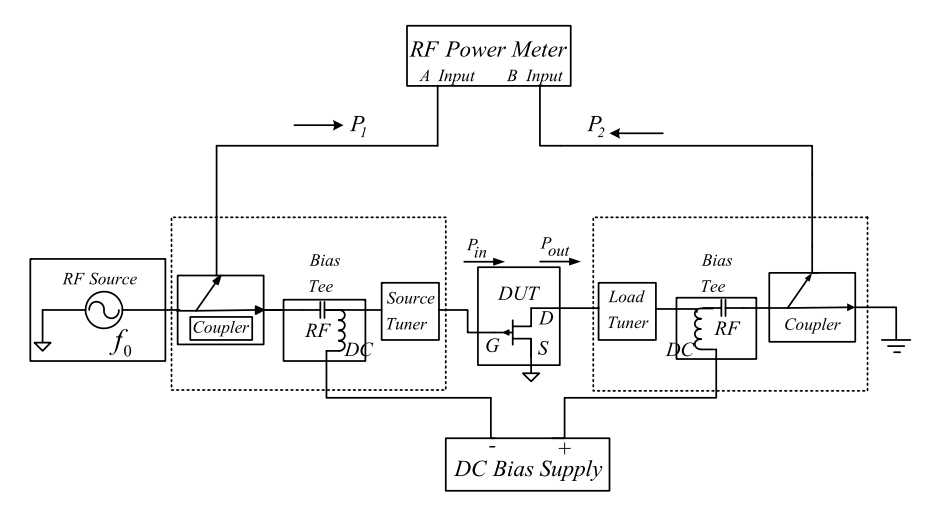


Fig. 2.5 Block diagram of a typical setup that depicts standard components required for carrying out automated load-pull measurements

In the block diagram of Fig. 2.5, the tuners are shown to be close to the DUT ports, ensuring that maximum possible reflection coefficients synthesized by the tuners are directly seen by the DUTs. However, this is a non-real time setup, as all variables must be fixed a priori and then de-embedding procedures must then be applied before measurements are made [19, 20]. Such systems are slow in terms of speeds as compared to real-time load-pull systems [21–24].

In real-time systems, the incident and reflected waves are directly collected from the DUT ports; thus, the measurements are instantaneous with every change in the DUT operating conditions [22–24]. Nonetheless, a non-real-time passive load-pull system is frequently used to utilize maximum synthesizable reflection coefficients from passive tuners [25]. However, with the advancements in passive tuner technologies [9, 18], real-time passive load-pull systems are also possible and will obviously provide better performance in terms of speed, accuracy, flexibility, ease and deployment of the type of tuners.

2.3.1 Load-Pull Setup

Essentially, a complete load-pull measurement setup consists of at least two fundamental tuners (one each at the output and input of the DUT), one signal source, a test fixture or probe station, two power meters or a dual channel power meter, a power supply, a spectrum analyzer, an RF test set (including bias tees, cables, attenuators, couplers, power combiners and dividers), and access to a vector network analyzer (VNA). A generic block diagram of a real-time passive load-pull measurement setup is given in Fig. 2.6 [26].

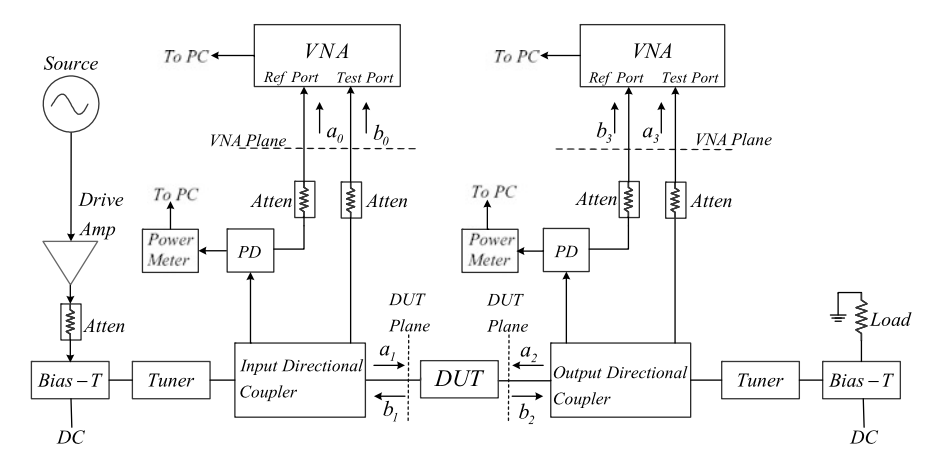


Fig. 2.6 Generic block diagram of a real-time passive load-pull setup [26], © IEEE 1984

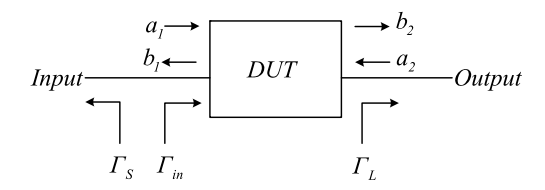
The DUT is fed from a high-power microwave source, and its source and load impedances are controlled by adjustable impedance tuners at the input and output. If the DUT is an oscillator, only the output part of the system is needed. Uncorrected large-signal reflection coefficients at the input and output of the DUT are monitored using dual directional couplers and RF network analyzers. Attenuators ensure that the signal levels at the inputs of the harmonic frequency converters are within the safe operating range. If only one network analyzer is available, coaxial switches can be used to connect it back and forth between the input and output circuits.

The power meters are used for the monitoring of the uncorrected power incident on the input port of the DUT and the uncorrected power generated at the output port of the DUT. Only one power meter at each port is required, because the reflection coefficients generated by the tuners are known [27], given that the tuners are precharacterized using tuner calibration techniques [28–32]. The pre-characterization of tuners ensures that all the imperfections associated with the stub movement in the impedance tuners, central conductor of the tuners and the connectors at the tuner ports are compensated. This step also helps in speeding up the overall measurement, as it enables synthesis of the required reflection coefficient using interpolation instead of multiple actual movements of stubs in the horizontal and vertical directions [13].

The power dividers create reference signals for the respective network analyzers. In principle, in an alternate configuration, the power divider and power meter can be connected to other coupled ports of the respective directional couplers. However, such a configuration results into reduced accuracy in the measurements for the condition when the reflection coefficients at the DUT ports are close to zero and giving very small power meter readings [26, 27].

An interfacing computer (not shown in the figure) is used for controlling the instrument and acquiring and processing the measured data, and for error correction.

Fig. 2.7 Power waves and the reflection coefficients of interest at the DUT reference planes [26], © IEEE 1984



2.3.2 System Calibration

The main objective behind the load-pull characterization of DUTs is the accurate prediction of device performance under realistic conditions, but the errors due to imperfect system components, such as inherent directivity, mismatch and cross-coupling errors associated with the network analyzer, cause uncertainty in the reflection coefficients and RF power at the specified reference planes, thereby defeating the primary objective.

It is, therefore, extremely important to calibrate the load-pull setup, in order to accurately set and measure the reflection coefficients and, hence, the design parameters, such as PAE, drain efficiency, and gain. The calibration, in principle, serves a dual purpose, by removing the systematic errors arising from imperfections and system components, as well as by shifting the reference plane from the network analyzer measuring planes to the DUT reference planes. In essence, after calibration, the system performs three functionalities, which are critical for achieving accurate load-pull measurement results and can be summarized as:

- Setting a particular impedance value (reflection coefficients).
- Measuring the load reflection coefficients (impedances).
- Measuring the required device performance at the particular impedance.

In practical load-pull measurements, the input and output powers, P_{in} and P_{out} , at the DUT plane, as shown in Fig. 2.7, are given by:

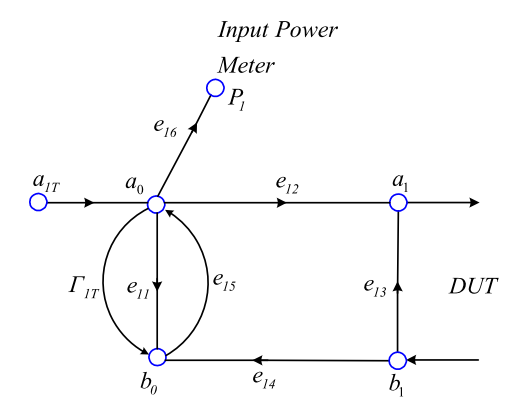
$$P_{in} = |a_1|^2 - |b_1|^2 = |a_1|^2 (1 - |\Gamma_{in}|^2)$$
(2.4)

$$P_{out} = |b_2|^2 - |a_2|^2 = |b_2|^2 (1 - |\Gamma_L|^2)$$
 (2.5)

where Γ_{in} and Γ_{L} are the reflection coefficients at the input and port of the DUT and the load seen by the DUT, respectively. The traveling waves a_1 , b_1 , a_2 and b_2 are the incident and reflected waves at the DUT ports as shown in Fig. 2.7.

During load-pull measurement, the impedance tuners set the desired reflection coefficients, whereas the vector network analyzers (VNAs) and power meters in Fig. 2.6 give direct (but uncorrected) measurements of Γ_{in} , Γ_L , $|a_1|^2$ and $|b_2|^2$. The errors introduced by the VNA and the hardware configuration in the measured reflection coefficients significantly affect the accuracy in the measurements of input and output RF power. The accuracy in the measured reflection coefficients and, hence, the RF power is limited, due to the inherent directivity, mismatch, and cross-coupling errors associated with the network analyzer components. These errors impact the performance of the load-pull setup and, in turn, put a question mark on the reliability of the measured data.

Fig. 2.8 Signal flow error model for the input port incorporating the imperfections contributed by directional coupler, power meter and network analyzer [26], © IEEE 1984



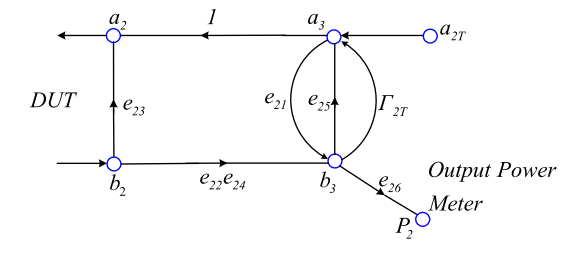
For example, unknown tuner losses add uncertainty in the measured data, if the output power meter is farther from the DUT [1, 33], with tuner losses as large as several decibels [34]. On the other hand, finite coupler directivity and connector mismatches can result in significant errors in the measured RF power in systems where the RF power levels are determined using directional couplers at the input and/or output of the DUT [35, 36]. With 25 dB directivity, errors in the measured power can be as large as 1 dB [26]; and, these errors significantly affect the measurement data, if the VSWR in the directional coupler is high.

Error correction in the measurement can be carried out using the error flow model of the complete measurement system given in Fig. 2.6. The respective error flow models of the input and output ports (as given in Figs. 2.8 and 2.9) incorporate all the errors, such as the finite coupler directivity, connector mismatches, and cross-coupling between the reference and VNA's measuring ports. The models have been simplified using the flow graph reduction technique [5]. The major assumption considered in this simplification is that the reflection coefficients of the power meter sensor heads and the reference and VNA inputs are constant and independent of RF power level. These models form the basis of a unified approach to the vector error correction of RF power and reflection coefficient measurements. These error models are analogous to the error models commonly used for error correction in VNA systems [37], but include some additional terms.

In the error flow model of the input side shown in Fig. 2.8, a_{1T} represents the input signal from the high-power microwave source, Γ_{1T} is the reflection coefficient presented to the input directional coupler by the input tuner, e_{16} represents coupling to the input power meter, and e_{11} represents directivity errors in the reference channel of the input network analyzer. The term e_{13} represents the source mismatch, $e_{12}e_{14}$ denotes the transmission tracking, and e_{15} indicates the error occurring in the measuring port of the VNA. The incident and reflected traveling waves at the input VNA ports are a_0 and b_0 , whereas the actual incident and reflected traveling waves at the input ports of DUT are represented by a_1 and b_1 , respectively. The VNA measures the uncorrected reflection coefficient, Γ_{in}^U , as given in Eq. (2.6):

$$\Gamma_{in}^{U} = \frac{b_0}{a_0} \tag{2.6}$$

Fig. 2.9 Signal flow error model for the output port incorporating the imperfections contributed by directional coupler, power meter and network analyzer [26], © IEEE 1984



The quantity of interest is, however, the input reflection coefficient, Γ_{in} , expressed in Eq. (2.7), which relates the error terms and the input uncorrected reflection coefficient measured at the input VNA plane in Fig. 2.7.

$$\Gamma_{in} = \frac{b_1}{a_1} = \frac{\Gamma_{in}^U - e_{11}}{e_{12}e_{14} - e_{11}e_{13} + e_{13}\Gamma_{in}^U}$$
(2.7)

There are three unknowns in Eq. (2.6), namely e_{13} , e_{11} and $e_{12}e_{14}$. These unknowns can be determined by carrying out measurements on calibration standards, such as open-short-load (OSL), by connecting these standards to the input DUT plane in Fig. 2.6. The measurements on the calibration standard provide a system of three equations (2.8) that relate the error terms and the reflection coefficients, which can be solved to determine the error terms of e_{11} , e_{13} and $e_{12}e_{14}$ [38].

$$\begin{bmatrix} e_{11} \\ e_{13} \\ \Delta e \end{bmatrix} = \begin{bmatrix} 1 & (\Gamma_{in})_{open} (\Gamma_{in}^{U})_{open} & -(\Gamma_{in})_{open} \\ 1 & (\Gamma_{in})_{short} (\Gamma_{in}^{U})_{short} & -(\Gamma_{in})_{short} \\ 1 & (\Gamma_{in})_{load} (\Gamma_{in}^{U})_{load} & -(\Gamma_{in})_{load} \end{bmatrix}^{-1} \begin{bmatrix} (\Gamma_{in}^{U})_{open} \\ (\Gamma_{in}^{U})_{short} \\ (\Gamma_{in}^{U})_{load} \end{bmatrix}$$
(2.8)

where $\Delta e = e_{12}e_{14} - e_{11}e_{13}$. Terms Γ_{in} with subscripts open, load and short refer to the actual reflection coefficients of the OSL standards at the DUT plane; whereas terms Γ_{in}^U with subscripts open, load and short are the corresponding measurements at the VNA plane.

The determination of error terms using Eq. (2.8) enables the calibration of the input port for the measurement of an accurate reflection coefficient at the input DUT plane, as given by Eq. (2.7).

For the error model of the output network in Fig. 2.9, e_{26} represents coupling to the power meter, e_{25} denotes directivity errors in the test channel of the network analyzer, and Γ_{2T} and a_{2T} indicate the tuner and node, respectively. This is a general form that can describe any passive or active tuner. A passive tuner has a non-zero Γ_{2T} term and zero a_{2T} , while active tuners have a non-zero a_{2T} . One step in the calibration procedure, which is described in the following paragraphs, requires that a test signal is injected from the right of the output coupler. In this case, a_{2T} is non-zero.

The simplification of signal flow model in Fig. 2.9 gives the error corrected reflection coefficients at the output reference plane, in terms of the uncorrected reading, Γ_L^U , given in Eq. (2.10).

$$\Gamma_L^U = \frac{a_3}{b_3} \tag{2.9}$$

$$\Gamma_L = e_{23} + \frac{e_{22}e_{24}\Gamma_L^U}{1 - e_{21}\Gamma_L^U} \tag{2.10}$$

The simplifications of Figs. 2.8 and 2.9 also provide error corrected input and output power, as per Eqs. (2.11) and (2.12).

$$P_{in} = |P_1|^2 \left| \frac{e_{12}}{e_{16}} \right|^2 \frac{(1 - |\Gamma_{in}|^2)}{|1 - \Gamma_{in}e_{13}|^2}$$
 (2.11)

$$P_{out} = \frac{|P_2|^2}{|e_{24}e_{26}|^2} |1 - e_{21}\Gamma_L|^2 (1 - |\Gamma_L|^2)$$
 (2.12)

where $|P_1|^2$ and $|P_2|^2$ are the input and output power meter readings, respectively. It is important to note that the equations are independent of the tuner reflection coefficients, Γ_{1T} and Γ_{2T} , and the directivity terms, e_{15} and e_{25} . Therefore, it is not necessary to obtain explicit values for these four terms.

The measurement of input power requires the determination of the error terms of e_{13} , e_{11} and $e_{12}e_{14}$, which can be obtained by standard one-port VNA calibration techniques in which the DUT is replaced by a series of calibration standards such as a short circuit, an offset short circuit, and an open circuit [39]. The error term $|e_{12}/e_{16}|^2$ in Eq. (2.11) is obtained by connecting a matched power meter in place of the DUT. The ratio of the power meter reading to the input power meter reading is $|e_{12}/e_{16}|^2$.

For the measurement of output power, once again one-port VNA calibration [39] can be performed to determine the error terms e_{21} , e_{23} , and $e_{22}e_{24}$. The input signal for this stage of the calibration, a_{2T} , is injected from the right in Fig. 2.6, with the signal generator and an amplifier connected in place of the load. To determine the error term, $|e_{24}e_{26}|^2$, the magnitude of the insertion loss of the output coupler and power divider, between the DUT output reference plane and the output power meter, is measured. If the test signal injected into the coupler at the DUT reference plane is supplied from a matched source and if the output tuner is replaced by a matched load, the power insertion loss, I_P , is given by:

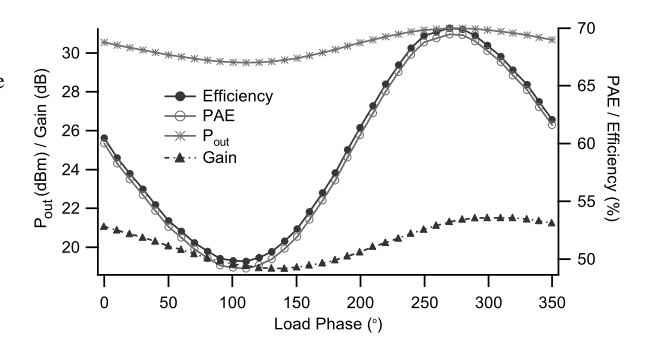
$$I_P = \frac{|e_{24}e_{26}|^2}{|1 - e_{21}e_{25}|^2} \tag{2.13}$$

Since e_{21} and e_{25} are usually small, the insertion loss measurement gives $|e_{24}e_{26}|^2$ directly.

As a guideline, for maximum accuracy, the system should be calibrated at coaxial (APC-7 or APC-3.5) reference planes close to the test fixture. Then, appropriate deembedding using coaxial-to-microstrip transition [40] needs to be carried out to transfer the reference plane into the microstrip test fixture.

The available signal power, P_a , at the output of the driver amplifier, in Fig. 2.6 is measured using a matched power meter. The driver amplifier is then connected at the input port of the output directional coupler, in place of the DUT. The corrected output power is obtained for a range of different output tuner settings across the load plane. These power measurements are compared with the calculated output

Fig. 2.10 The performance of a 1 W GaAs FET for $|\Gamma_L(2f_0)| = 1$ with a variable phase of the second harmonic, while maintaining optimal fundamental and third harmonic terminations [41], © IOP Journal of Measurement Science and Technology 2010



power, $P_a(1 - |\Gamma_L|^2)$, which is obtained using the measured P_a and the corrected Γ_L . A maximum tolerance of around 0.15 dB between the corrected measured and calculated output power values provides confidence in the calibration process [26].

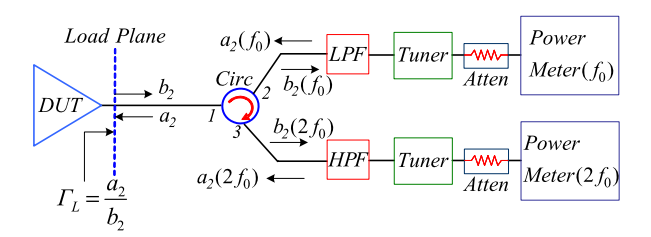
2.4 Harmonic Load-Pull System

The terminal loading conditions at harmonic frequencies significantly affect device performance. In principle, during the characterization and optimization of transistor devices, the harmonic power generated by the device needs to be fully reflected back at a given phase, in order to extract the best possible efficiency. In an ideal scenario, all the harmonic power can be reflected back; however, this is not possible in practical load-pull systems, due to lossy transition between the tuner and the device. During the characterization of devices, it is a common practice to vary the phase and magnitude of the harmonic reflection coefficients, while keeping the fundamental reflection coefficient constant, in order to obtain optimal efficiency.

Figure 2.10 illustrates an example of the effect of phase variation of $\Gamma_L(2f_0)$ on the performance of a 1 W GaAs (gallium arsenide) FET (field effect transistor) device, while keeping the reflection coefficients at the fundamental frequency and third harmonic fixed [41]. It is apparent that, in this case, the variation of phase of the second harmonic reflection coefficient can swing the efficiency by more than 20 %. Similar effects can be observed when the phase of the third harmonic reflection coefficient or the magnitudes of the second or third harmonic coefficients are varied [42]. Improvements to the tune of over 15 % in efficiency can be achieved in the final designed PA, while terminating the harmonic impedances in optimal terminations, compared to 50 Ω [43]. In addition to the harmonically tuned PAs, the harmonic terminations play a key role in the design of switching-mode PAs [44].

Device characterization for the optimal design of either harmonically tuned PAs or switching-mode PAs is carried out using a harmonic load-pull system [45–47]. One of the first reported passive harmonic load-pull setups [33], which is shown in Fig. 2.11, was based around a circulator. The architecture used standard slide screw tuners, filters and power meters to monitor and control the magnitude and phase of the reflected signal components at the fundamental and second harmonic frequencies. This setup, although very basic when compared to current developments, did

Fig. 2.11 This architecture was one of the first passive harmonic load-pull setups [33], © IEEE 1979



achieve tuning of impedances for fundamental and second harmonic frequencies. In this setup, the transmitted wave, b_2 , enters the circulator via port 1; and, the fundamental and second harmonic components exit through the appropriate low-pass and high-pass filters at ports 2 and 3, respectively. The respective tuners reflect the traveling waves, $a_2(f_0)$ and $a_2(2f_0)$, and subsequently synthesize the respective fundamental and second harmonic reflection factors at the load plane given by Eqs. (2.14) and (2.15).

$$\Gamma_L(f_0) = \frac{a_2(f_0)}{b_2(f_0)} \tag{2.14}$$

$$\Gamma_L(2f_0) = \frac{a_2(2f_0)}{b_2(2f_0)} \tag{2.15}$$

The reflected traveling waves, $a_2(f_0) = \Gamma_L(f_0)b_2(f_0)$ and $a_2(2f_0) = \Gamma_L(2f_0) \times b_2(2f_0)$, then combine at port 1 of the circulator to form the overall reflected traveling wave, a_2 , as given in Eq. (2.16):

$$a_2 = a_2(f_0) + a_2(2f_0) = \Gamma_L(f_0)b_2(f_0) + \Gamma_L(2f_0)b_2(2f_0)$$
 (2.16)

In theory, an n-port wideband circulator with appropriate band-pass filters can be employed to extend this setup to n-1 harmonics. However, in practice, it is not feasible, considering the bandwidth limitation and substantial losses associated with circulators beyond the second harmonic. Usually, high harmonic reflection coefficients are required, and the losses render the circulator based harmonic load-pull system inappropriate in practical applications. In addition, the poor isolation of circulators also affects the system's ability to synthesize harmonically independent reflection coefficients and, therefore, limits the overall usefulness of this harmonic load-pull setup.

Over the years, passive harmonic load-pull architectures and setups have evolved to address the two major issues of high reflection factor synthesis at harmonic frequencies and harmonically independent reflection factor emulation [17, 18]. These developments in the harmonic load-pull architectures can be grouped in three distinct categories, namely triplexer based harmonic load-pull, harmonic rejection tuner harmonic load-pull and multipurpose single tuner harmonic load-pull [17].

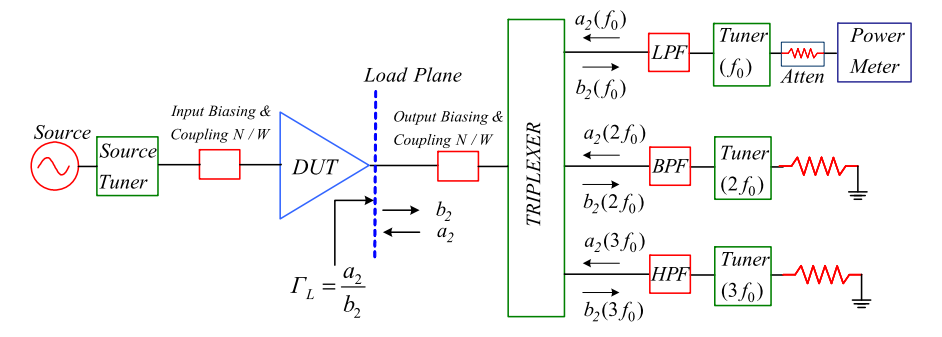


Fig. 2.12 Block diagram of triplexer based three-harmonic load-pull system

2.4.1 Triplexer Based Harmonic Load-Pull Setup

A block diagram of a typical three-harmonic triplexer based load-pull architecture is shown in Fig. 2.12. It is apparent that an appropriate triplexer and tuners corresponding to carrier and harmonic frequencies are required to build a triplexer based harmonic load-pull system. The input and output biasing networks provide for the biasing at the gate and source, respectively and, the input and output coupling networks are needed for capturing the transmitted and reflected traveling waves at the input and output ports, respectively. The optional source tuner is used for matching at the input port. The triplexer, which acts like filters for the respective harmonic components, separates the harmonic components from the output generated by the DUT. The subsequent filters at the output of the triplexer further improve the rejection of the out-of-band frequency components.

The respective load-tuners for harmonic components f_0 , $2f_0$, and $3f_0$ tune the reflection environment as per specific requirements and reflect the respective $a_2(f_0)$, $a_2(2f_0)$, and $a_2(3f_0)$ and, in the process, synthesize the harmonically independent reflection factors by interacting with the respective components, $b_2(f_0)$, $b_2(2f_0)$ and $b_2(3f_0)$, of the traveling wave, b_2 . The reflected traveling wave components, having different weighting factors, contributed by the tuners, then combine to form the overall a_2 given in Eq. (2.17).

$$a_2 = a_2(f_0) + a_2(2f_0) + a_2(3f_0)$$
 (2.17)

The primary benefit of such a technique is that the reflection factors at different harmonic frequencies can be set independently, i.e., the harmonic reflection factors are independent of each other. It can thus be inferred that this method gives full magnitude and phase control of all three harmonic frequencies, f_0 , $2f_0$, and $3f_0$. The drawback of this technique is the limited tuning coverage at the harmonics, as shown in Fig. 2.13, due to the losses inherent in the triplexer. This is a serious limitation for applications requiring high harmonic terminations, such as class-F and inverse class-F mode PAs [48].

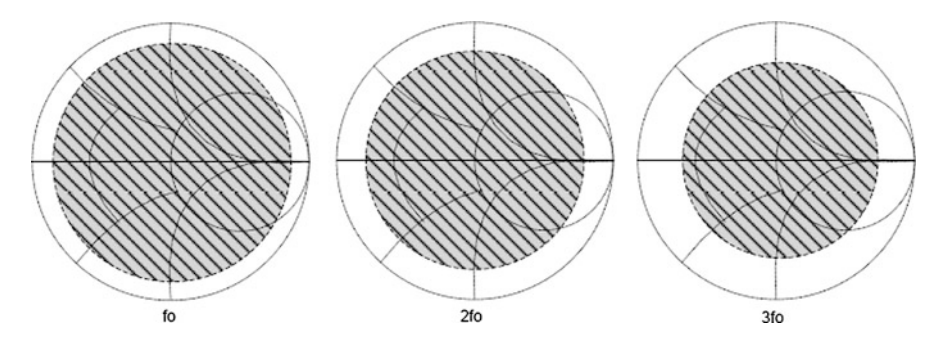


Fig. 2.13 Depiction of tuning coverage at f_0 , $2f_0$ and $3f_0$ for the triplexer based three-harmonic load-pull system [17]

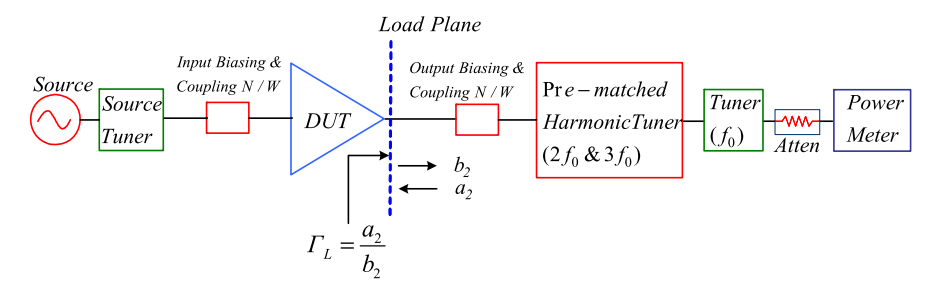


Fig. 2.14 The harmonic rejection tuner based three-harmonic load-pull architecture

2.4.2 Harmonic Rejection Tuner Based Harmonic Load-Pull Setup

The harmonic rejection tuner (HRT) based harmonic load-pull architecture incorporates an HRT in addition to a fundamental tuner, as shown in Fig. 2.14. In a standard HRT based harmonic load-pull setup, pre-matched type harmonic tuners, as explained in Chap. 5, such as passive harmonic tuners (PHT) [17] are used.

The fundamental tuner, possessing full magnitude and phase control for the reflection coefficient at the fundamental frequency, f_0 , is placed farther from the DUT output port, as the reflection coefficient required at the fundamental frequency is smaller than those of the harmonic frequencies. The HRT, which is capable of full phase control at harmonic frequencies $2f_0$ and $3f_0$, is placed nearer to the DUT port, in order to minimize the impact of the loss associated with the cables and connectors. This helps in the synthesis of higher reflection coefficients at the harmonic frequencies.

Furthermore, this technique overcomes the loss associated with the triplexer; therefore, the reflection coefficient can cover a larger region on the Smith chart, as shown in Fig. 2.15. The harmonic rejection tuners are low loss, which also contributes to the synthesis of reflection coefficient with increased magnitude. It is also evident that the HRTs, although are capable of providing higher reflection coefficients, do preclude a large portion of Smith chart. This limitation, however, does not

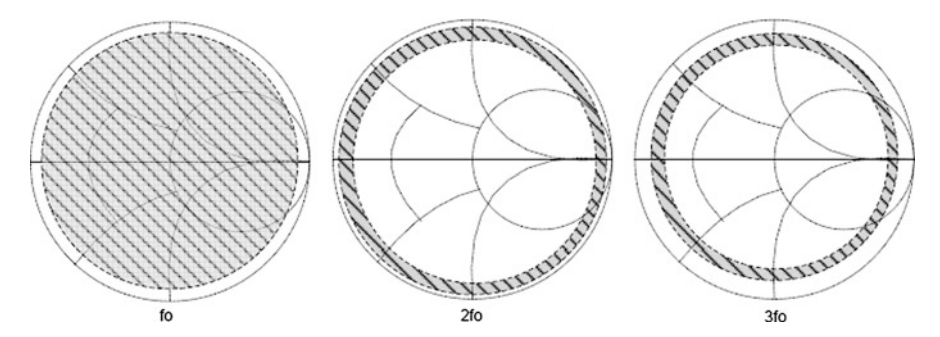


Fig. 2.15 Depiction of tuning coverage at f_0 , $2f_0$ and $3f_0$ for the HRT based three-harmonic load-pull system [17]

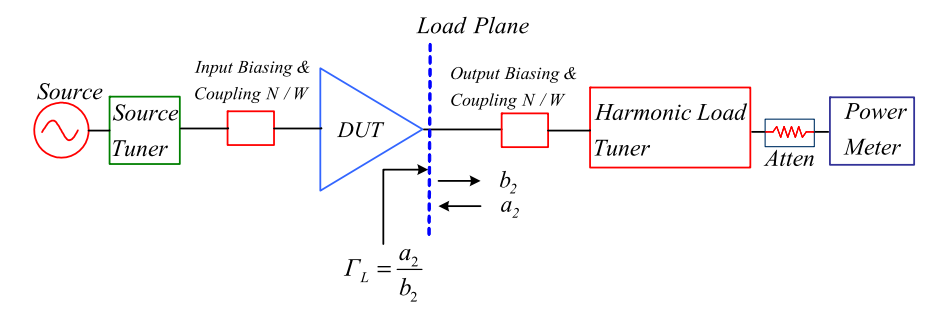


Fig. 2.16 The multipurpose tuner based harmonic load-pull architecture

affect the usefulness in practical applications considering that the required harmonic reflection coefficients usually fall nearer the boundary of the Smith chart.

The primary limitation of this technique is the poor isolation between the synthesized reflection coefficients at the fundamental and harmonic frequencies. This is due to the fact that the tuners are cascaded; therefore, setting of the tuner state at one frequency affects the tuner state at the other frequencies. As a consequence, this technique becomes impractical for more than three harmonic frequencies.

2.4.3 Single Tuner Harmonic Load-Pull Setup

Figure 2.16 shows a typical block diagram of a single tuner harmonic load-pull setup, which also includes a source tuner and peripheral biasing and measuring network. In this architecture, a multipurpose load tuner that covers the fundamental frequency and the range of all of the relevant harmonic frequencies is employed for the synthesis of harmonically independent fundamental and harmonic reflection coefficients [17].

For example, a three-harmonic multipurpose tuner uses three independent wideband probes for the control of the magnitude and phase of the reflection coefficients

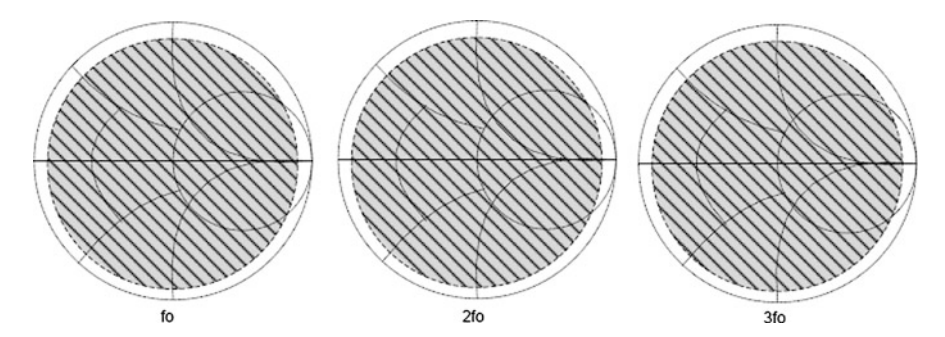


Fig. 2.17 Depiction of tuning coverage at f_0 , $2f_0$ and $3f_0$ for the single multipurpose tuner based three-harmonic load-pull system [17]

at the three harmonic frequencies of f_0 , $2f_0$, and $3f_0$. The proper positioning and movement of the three probes in the horizontal and vertical directions allow independent tuning at the three harmonic frequencies [17]. A multipurpose tuner gives full magnitude and phase control for all three harmonic frequencies, as shown in Fig. 2.17.

Since this setup utilizes only one tuner, the overall system loss associated with biasing and measuring networks, cables and connectors is less; hence, the achievable magnitude of the reflection coefficient is higher than other harmonic load-pull architectures. This setup is compact and smaller in size compared to the types of other setups. A major limitation of this technique includes the requirement for very powerful computing facility to monitor and control the movement of the tuner probes. In addition, this technique also suffers from inherent limited isolation, due to the series configuration of all the probes. The limited isolation prevents this setup from synthesizing harmonically independent harmonic reflection coefficients at all frequencies and in all parts of the Smith chart.

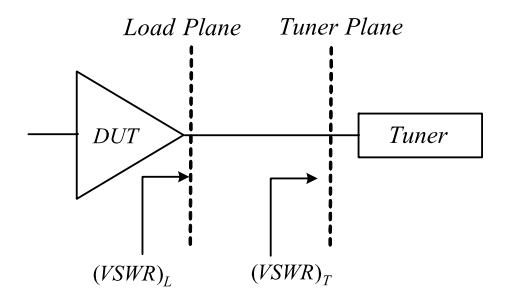
2.4.4 Harmonic Load-Pull Comparisons

The harmonic tuning methods can be compared primarily in two aspects, namely the tuning isolation and the effective Smith chart coverage.

An important factor of any load-pull device characterization system is the accuracy at which the impedance seen by the DUT at the fundamental frequency can be controlled. If the impedance changes without the user's knowledge or if it cannot be kept constant for varying harmonic impedances, the measurement results obtained are invalid. Hence, when considering harmonic load-pull systems, it is essential to know the isolation across frequencies.

The triplexer based harmonic load-pull architecture relies on the isolation inherent within the isolator to mitigate the effects of variation in the setting of one tuner from setting of another. Triplexers typically possess 50–60 dB of isolation at the fundamental and harmonic frequencies; therefore, this technique can practically

Fig. 2.18 Definition of VSWR at load and tuner planes for a fundamental load-pull tuning setup



tune harmonic impedances independent of each other. In some applications, poor isolation outside the fundamental and harmonic frequency band can cause spurious oscillations, especially at low frequencies, due to high out-of-band reflections.

In the HRT based harmonic load-pull setup, the frequency isolation between the harmonic resonators is around 30 dB. The poor frequency isolation is the result of the sum of vectors generated by the reflections at f_0 , $2f_0$, and $3f_0$, as well as the residual reflection of the slab-line [17]. This makes setting of harmonically independent impedances extremely difficult.

In the case of the multipurpose tuner, the fundamental and harmonic probes reposition themselves for each desired reflection factor for the combination of f_0 , $2f_0$, and $3f_0$, which helps in achieving very good tuning isolation. However, the measurement using multipurpose based harmonic load-pull is relatively slow, due to physical movement of probes for each set of harmonic impedances.

For tuning range, it is the effective voltage standing wave ratio (VSWR) at the load plane that matters and not the tuner's ability to synthesize the VSWR at the tuner plane. The VSWR at the load plane depends on the interface between the tuner and the DUT and gets reduced accordingly. Figure 2.18 provides a simple relationship of the VSWR at the load and tuner planes. It is important to note that there are always a passive measurement network and transition between the DUT and the tuner, which reduce the achievable VSWR at the load plane compared to the tuner plane.

In a triplexer based harmonic load-pull setup, as shown in Fig. 2.12, there is loss due to the insertion loss of the triplexer, which is responsible for the reduced Smith charge coverage shown in Fig. 2.13. The coverage gets further reduced at harmonic frequencies, as the triplexer loss at harmonic frequencies is higher.

In the case of HRT based harmonic load-pull architecture, there are only measuring passive networks between the tuner and the DUT, as shown in Fig. 2.14; therefore, the reduction in the Smith chart coverage is smaller. However, there is a transition between the fundamental and harmonic tuners, causing reduction in the VSWR and further reducing the Smith chart coverage at the fundamental frequency, f_0 , as shown in Fig. 2.15, compared to the harmonic frequencies.

In a single multipurpose tuner, the reduction in the VSWR at the harmonic and fundamental frequencies is almost similar, as all the tuning probes are contained in a single casing. The reductions in the VSWR at the fundamental and harmonic frequencies are caused only by the passive measuring network between the tuner and the DUT.

Tuning method	Advantages	Disadvantages
Triplexer based	– High tuning isolation	- Unsuitable for on-wafer applications
	 Simple extension of existing setup 	 Insertion loss of the triplexer at all frequencies causes a reduced tuning range
	 Very good amplitude and phase control at all the harmonic frequencies 	 Out-of-band reflections in the triplexer can cause spurious oscillations
Harmonic rejection tuner based	 High tuning range 	 Very poor tuning isolation
	 High power handling capability 	 Unsuitable for broadband applications
	 Low insertion loss at fundamental frequency 	Limited to only three harmonics
Multipurpose single tuner based	- High tuning range	 Slow measurement time and throughput
	- High tuning isolation	 Requires powerful computing resource
	 Ideal for on-wafer applications 	

Table 2.2 Features of harmonic tuning methods [17]

Table 2.2 summarizes the major features of the described three different harmonic load-pull techniques.

Appropriate for broadband

applications

2.5 Tuning Range Enhancement

The tuning range in a passive load-pull system is limited, due to the inherent losses in the biasing and measuring network, connectors, cables, fixture and the tuner itself [30]. Therefore, depending on the load-pull system architecture, a substantial part of the Smith chart is precluded; and, as a consequence, not all relevant impedances can be synthesized

Most of the low-power device characterization and PA design requirements are met by standard passive load-pull setups. However, limitations of such systems are apparent during high-power device characterization and PA design or harmonic load-pull measurements, as these situations require highly reflective impedance environments. To address this issue, several solutions have been proposed [12].

The enhanced loop [49] and cascaded tuner architectures [18] are recent developments in passive load-pull architectures that have the ability to synthesize high reflection coefficients. In both of these systems, the idea is the enhancement of the

Fig. 2.19 The enhanced loop load-pull architecture for synthesizing a high reflection coefficient [49], © IEEE 2010

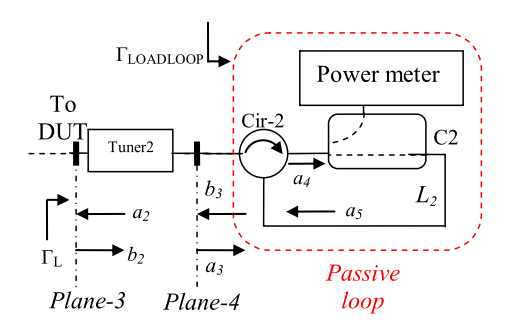
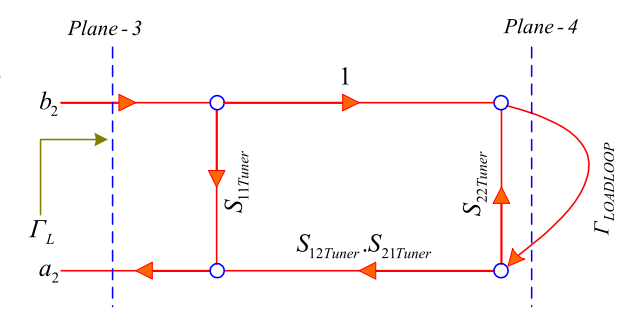


Fig. 2.20 The signal flow model depicting the generation of reflection factor using enhanced loop load-pull architecture [49], © IEEE 2010



tuning range by reflecting back the transmitted signal that is transmitted through the main tuner.

2.5.1 Enhanced Loop Architecture

In order to achieve high reflection factors, this technique combines a passive tuner and a passive loop, as shown in Fig. 2.19. It employs a low-loss circulator, Cir-2, with very high directivity, so that the loss incurred in the setup is smaller and that there is good isolation between signals a_4 and b_3 . The employed coupler, C2, and the loop cable, L_2 , are low loss. The coupling port of the coupler is connected to a power meter, in order to monitor and measure the DUT performances, in terms of output power or linearity, during load-pull characterization. The passive loop at the output of Tuner2 generates reflection coefficient $\Gamma_{LOADLOOP}$ at plane-4 and augments the overall reflection coefficient Γ_L at plane-3. The flow model in Fig. 2.20 depicts the generation of reflection factor Γ_L at plane-3.

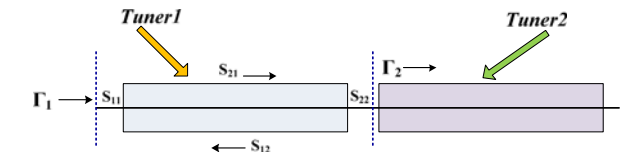
The following expressions relate the traveling waves in the enhanced loop load-pull architecture of Fig. 2.19:

$$a_4 = k_4 a_3$$
 (2.18)

$$a_5 = k_5 a_4 \tag{2.19}$$

$$b_3 = k_6 a_5 \tag{2.20}$$

Fig. 2.21 Two tuners cascaded in series to obtain higher reflection factor [18], © Maury Microwave Corporation



where k_4 , k_5 and k_6 are the complex factors dependent on the S-parameters of the circulator, Cir-2, and the directional coupler, C2.

The mismatch between *Tuner2* and the passive loop plane, *Plane-4*, is related by the following expression:

$$\Gamma_{LOADLOOP} = K_L = \frac{b_3}{a_3} = |K_L|e^{-2j\beta L_2}$$
(2.21)

where the parameter $K_L(=k_4k_5k_6)$ is a complex factor that depends on the passive loop structure characteristics, i.e., the transmission factors of coupler C2 and circulator Cir-2.

It is clear from Eq. (2.21) that the reflection coefficient generated by the passive loop is also dependent on the phase velocity, β , of the traveling waves and the length of cable in the passive loop, L_2 . The simplification of the flow model in Fig. 2.20 results in the following expression for the overall reflection coefficient at *plane-3*.

$$\Gamma_L = \frac{b_2}{a_2} = S_{11TUNER2} + \frac{S_{12TUNER2}S_{21TUNER2}K_L}{1 - S_{22TUNER2}K_L}$$
 (2.22)

Equation (2.16) demonstrates that the total load reflection coefficient, Γ_L , at *plane-3* gets enhanced by the contribution from the passive loop. If the loop does not contribute anything to the overall reflection coefficient, then S_{11} of Tuner2 is the total reflection coefficient.

2.5.2 Cascaded Tuner

Figure 2.21 depicts the cascading of two passive tuners in series. The cascaded tuners are capable of generating reflection factor, Γ_1 , at the DUT plane, which is governed by Eq. (2.23) [18].

$$\Gamma_1 = S_{11} + \frac{S_{12}S_{21}\Gamma_2}{1 - S_{22}\Gamma_2} \tag{2.23}$$

where S_{11} , S_{21} , S_{12} , and S_{22} are the S-parameters of *Tuner1* (closest to the DUT). Γ_2 is S_{11} looking into *Tuner2* at a particular termination.

The overall reflection looking into the cascaded tuner combination is equal to the complex reflection of the first tuner added to the complex reflection of the second tuner and multiplied by some insertion/reflection factor. It is important to notice that the effect of the second tuner is highly influenced by the $S_{21}S_{12}$ product of the first tuner. There are two extreme cases that best describe this effect [18]:

- If Tuner1 is at a physical short circuit, i.e., $S_{21}S_{12} = 0$, Tuner2 would be completely masked.
- If *Tuner1* is at initialized at 50 Ω , i.e., $S_{11} \sim 0$ and $S_{21}S_{12} \sim 1$, *Tuner2* would be all that is seen.

References

- J.M. Cusack, S.M. Perlow, B.S. Perlman, Automatic load contour mapping for microwave power transistors. IEEE Trans. Microw. Theory Tech. 22, 1146–1152 (1974)
- F. Secchi, R. Paglione, B. Perlman, J. Brown, A computer controlled microwave tuner for automated load pull. RCA Rev. 44(4), 566–583 (1983)
- Focus Microwave, Mechanical vibrations of CCMT tuners used in on-wafer load-pull testing, Application Note AN-46, Oct. 2001
- J. Sevic, Introduction to tuner-based measurement and characterization, Technical Note, Maury Microwave Corporation, 5C-054
- D.M. Pozar, Microwave Engineering, 3rd edn. (Wiley, New York, 2005). ISBN 0-471-17096-
- 6. Microlab, Mechanical tuners, Application Note, Oct. 2000
- R. Tuijtelaars, Overview of device noise parameter measurement system, in VDE/ITG-23.10.01 (2001), pp. 1–5
- Maury Microwave Corporation, Device characterization with harmonic load and source pull, Application Note: 5C-044, Dec. 2000
- Focus Microwave, Load pull measurements on transistors with harmonic impedance control, Technical Note, Aug. 1999
- B.W. Leake, A programmable load for power and noise characterization, in *IEEE Microwave Theory and Techniques Society's International Microwave Symposium Digest*, Dallas, USA (June 1982), pp. 348–350
- Maury Microwave Corporation, LP series electronic tuner system, Technical Data, 4T-081, 2002
- M.S. Hashmi, F.M. Ghannouchi, P.J. Tasker, K. Rawat, Highly reflective load-pull. IEEE Microw. Mag. 11(4), 96–107 (2011)
- Focus Microwave, Computer controlled microwave tuner—CCMT, Product Note 41, Jan. 1998
- 14. Maury Microwave Corporation, Slide screw tuners, Technical Data, 2G-035A, Feb. 1998
- 15. Focus Microwaves, Algorithms for automatic high precision residual tuning to 50 Ω using programmable tuners, Application Note 45, May 2001
- Focus Microwave, Electronic tuners (ETS) and electromechanical tuners (EMT)—a critical comparison, Technical Note, Aug. 1998
- Focus Microwave, Comparing harmonic load-pull techniques with regards to power-added efficiency (PAE), Application Note 58, May 2007
- Maury Microwave Corporatio, Cascading tuners for high-VSWR and harmonic applications, Application Note 5C-081, Jan. 2009
- F. Deshours, E. Bergeault, F. Blache, J.-P. Villotte, B. Villeforceix, Experimental comparison of load-pull measurement systems for nonlinear power transistor characterization. IEEE Trans. Instrum. Meas. 57(11), 1251–1255 (1997)
- A. Ferrero, V. Teppati, Experimental comparison of active and passive load-pull measurement technologies, in 30th European Microwave Conference Proceedings, Paris, France (Oct. 2000), pp. 1–4
- C. Arnaud, J.L. Carbonero, J.M. Nebus, J.P. Teyssier, Comparison of active and passive loadpull test benches, in 57th ARFTG Conference, vol. 39 (May 2001), pp. 1–4

References 53

 M.S. Hashmi, A.L. Clarke, S.P. Woodington, J. Lees, J. Benedikt, P.J. Tasker, An accurate calibrate-able multiharmonic active load-pull system based on the envelope load-pull concept. IEEE Trans. Microw. Theory Tech. 58(3), 656–664 (2010)

- W.S. El-Deeb, N. Boulejfen, F.M. Ghannouchi, A multiport measurement system for complex distortion measurements of nonlinear microwave systems. IEEE Trans. Instrum. Meas. 59(5), 1406–1413 (2010)
- 24. D. Barataud, F. Blache, A. Mallet, P. Bouysse, J.-M. Nebus, J. Villotte, J. Obregon, J. Verspecht, P. Auxemery, Measurement and control of current/voltage waveforms of microwave transistors using a harmonic load-pull system for the optimum design of high efficiency power amplifiers. IEEE Trans. Instrum. Meas. 48(4), 835–842 (1999)
- J.E. Mueller, B. Gyselinckx, Comparison of active versus passive on-wafer load-pull characterization of microwave MMwave power devices, in *IEEE Microwave Theory and Techniques Society's International Microwave Symposium Digest*, San Diego, USA (June 1994), pp. 1077–1080
- R.S. Tucker, P.D. Bradley, Computer-aided error correction of large-signal load-pull measurements. IEEE Trans. Microw. Theory Tech. 32(3), 296–300 (1984)
- P.D. Bradley, R.S. Tucker, Computer-corrected load-pull characterization of power MES-FETs, in *IEEE Microwave Theory and Techniques Society's International Microwave Sym*posium Digest, Boston, USA (June 1983), pp. 224–226
- 28. C. Tsironis, Adaptable pre-matched tuner system and method, US Patent No. 6674293
- 29. G.R. Simpson, Impedance tuner systems and probes, US Patent No. 7589601
- 30. J. Sirois, B. Noori, Tuning range analysis of load-pull measurement systems and impedance transforming networks, in 69th ARFTG Conference, Honolulu, USA (June 2007), pp. 1–5
- 31. C. Roff, J. Graham, J. Sirois, B. Noori, A new technique for decreasing the characterization time of passive load-pull tuners to maximize measurement throughput, in 72nd ARFTG Conference, Portland, USA (Dec. 2008), pp. 92–96
- 32. P. Hart, J. Wood, B. Noori, P. Aaen, Improving loadpull measurement time by intelligent measurement interpolation and surface modeling techniques, in *67th ARFTG Conference*, San Francisco, USA (June 2006), pp. 69–72
- R.B. Stancliff, D.B. Poulin, Harmonic load-pull, in *IEEE Microwave Theory and Techniques Society's International Microwave Symposium Digest*, Florida, USA (Apr. 1979), pp. 185–187
- 34. E.W. Strid, Measurement of losses in noise-matching networks. IEEE Trans. Microw. Theory Tech. 29(3), 247–252 (1981)
- G.P. Bava, U. Pisani, V. Pozzolo, Active load technique for load-pull characterization at microwave frequencies. IEE Electron. Lett. 18(4), 178–180 (1982)
- 36. Y. Takayama, A new load pull characterization method for microwave power transistors, in *IEEE Microwave Theory and Techniques Society's International Microwave Symposium Digest*, New Jersey, USA (June 1976), pp. 218–220
- 37. R.A. Hackborn, An automatic network analyzer system. Microw. J. May, 45–52 (1968)
- 38. W.S. El-Deeb, M.S. Hashmi, S. Bensmida, N. Boulejfen, F.M. Ghannouchi, Thru-less calibration algorithm and measurement system for on-wafer large-signal characterization of microwave devices, IET J. Microw. Antenna Propag. **4**(11), 1773–1781 (2010)
- E.F. DaSilva, M.K. McPhun, Calibration technique for one-port measurements. Microw. J. June, 97–100 (1978)
- J.R. Souza, E.C. Talboys, S-parameter characterization of coaxial to microstrip transition. IEE Proc. 129(Part H), 37–40 (1982)
- 41. M.S. Hashmi, A.L. Clarke, J. Lees, M. Helaoui, P.J. Tasker, F.M. Ghannouchi, Agile harmonic envelope load-pull system enabling reliable and rapid device characterization. IOP J. Meas. Sci. Technol. **21**(055109), 1–9 (2010)
- M.S. Hashmi, A.L. Clarke, S.P. Woodington, J. Lees, J. Benedikt, P.J. Tasker, Electronic multiharmonic load-pull system for experimentally driven power amplifier design optimization, in *IEEE Microwave Theory and Techniques Society's International Microwave Symposium Digest*, Boston, USA, vols. 1–3 (June 2009), pp. 1549–1552

- F. Blache, J.-M. Nebus, P. Bouysse, L. Jallet, A novel computerized multiharmonic active load-pull system for the optimization of high-efficiency operating classes in power transistor, in *IEEE International Microwave Symposium Digest*, Orlando, USA (June 1995), pp. 1037– 1040
- 44. A. Grebennikov, N.O. Sokal, Switch Mode RF Power Amplifiers (Elsevier, Oxford, 2007)
- 45. F.M. Ghannouchi, F. Beauregard, A.B. Kouki, Power added efficiency and gain improvement in MESFETs amplifiers using an active harmonic loading technique. Microw. Opt. Technol. Lett. **7**(13), 625–627 (1994)
- R. Hajji, F.M. Ghannouchi, R.G. Bosisio, Large-signal microwave transistor modeling using multiharmonic load-pull measurements. Microw. Opt. Technol. Lett. 5(11), 580–585 (1992)
- 47. F.M. Ghannouchi, R. Larose, R.G. Bosisio, A new multiharmonic loading method for large-signal microwave and millimeter-wave transistor characterization. IEEE Trans. Microw. Theory Tech. **39**(6), 986–992 (1991)
- 48. Y.Y. Woo, Y. Yang, B. Kim, Analysis and experiments for high efficiency class-F and inverse class-F power amplifiers. IEEE Trans. Microw. Theory Tech. **54**(5), 1969–1974 (2006)
- F.M. Ghannouchi, M.S. Hashmi, S. Bensmida, M. Helaoui, Enhanced loop passive sourceand load-pull architecture for high reflection factor synthesis. IEEE Trans. Microw. Theory Tech. 58(11), 2952–2959 (2010)

Chapter 3 Active Load-Pull Systems

This chapter describes active load-pull techniques, their design issues, and important characteristics. The description involves two aspects namely the theoretical postulations of various active load-pull methods and then the respective designs, features, and practical issues encountered in realizations. The peripheral equipments used for measurement of traveling waves at the device under test (DUT) ports have not been included, as their configuration and calibration is similar to the description provided previously.

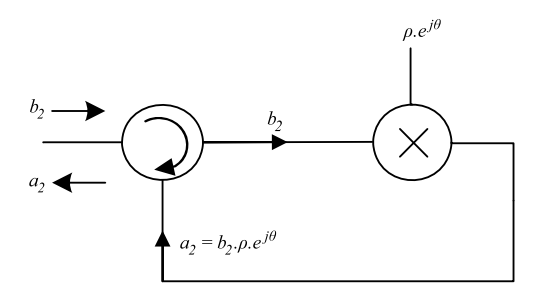
3.1 Introduction

Passive load-pull systems, although provide direct characteristic impedance transformation through passive tuners, are unable to synthesize high reflection coefficients due to inherent losses in the measurement network between DUTs and tuner [1]. This drawback has a serious repercussion in the characterization of either high power transistor devices or devices under harmonic terminations, where the required reflection coefficients lie mostly on or near the border of the Smith chart [2, 3].

Active load-pull systems, which are based on injection of signals at the DUT plane, possess the ability to synthesize high reflection coefficients by overcoming the inherent losses in the passive technique, and therefore can provide full Smith chart coverage [4, 5].

Closed-loop, feed-forward, and open-loop are the three broad categories of active load-pull technique [6–8]. For the emulation of desired reflection coefficients at the DUT plane the closed-loop, also known as feedback, load-pull modifies the DUT output appropriately before feeding it back as reflected traveling wave [4, 6]. Feedforward or split signal load-pull uses a part of the input signal to generate coherent modified signal to be reflected at the DUT plane [5, 7], whereas the open-loop load-pull generates coherent modified reflected wave from external signal source [8], for synthesis of reflection coefficients at the DUT plane.

Fig. 3.1 Diagram depicting the concept of reflection coefficient synthesis in an ideal closed-loop active load-pull system



3.2 Closed-Loop Load-Pull System

Figure 3.1 depicts block diagram of an ideal closed-loop active load-pull system. It can be observed that it requires a three-port component, e.g. circulator, for forwarding the incident traveling wave, b_2 , and reflected traveling wave, a_2 , in the respective directions. A complex variable $\rho e^{j\theta}$ modifies the phase and magnitude of the incident traveling wave, b_2 , before injecting it back into the form of reflected traveling wave, a_2 , so as to synthesize reflection coefficient given below in Eq. (3.1).

$$\Gamma_{Load} = \frac{a_2}{b_2} = \frac{b_2 \rho e^{j\theta}}{b_2} = \rho e^{j\theta} \tag{3.1}$$

where, ρ is the magnitude and θ is the phase of the desired reflection coefficient, Γ_{Load} , at the DUT plane.

3.2.1 System Realization

Realization of the closed-loop load-pull system requires a variable attenuator, a phase shifter, and a loop amplifier as shown in Fig. 3.2. The attenuator/loop amplifier combined together allows adjustment in the magnitude of reflected traveling wave a_2 , and the phase shifter modifies its phase, in order to emulate Γ_{Load} at the DUT plane. The circulator directs the traveling waves b_2 and a_2 in their respective direction. A directional coupler in place of circulator can also be employed, and will be described in a later section, for a load-pull system requiring superior stability.

In an ideal situation, when the circulator is assumed ideal and the losses in the system are ignored, the modified wave generated by the feedback loop can be given by Eq. (3.2) and the reflection coefficient at the DUT plane by Eq. (3.3).

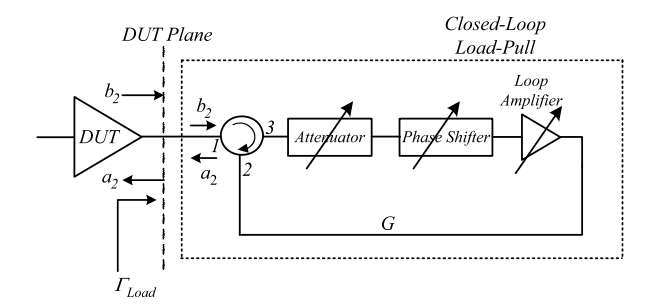
$$a_2 = Gb_2 \tag{3.2}$$

$$\Gamma_{Load} = \frac{a_2}{b_2} = G \tag{3.3}$$

where, G is complex gain of the feedback loop and represents the overall change in magnitude and phase of the incident traveling wave, b_2 .

It is, thus, safe to assume that the magnitude of Γ_{Load} is proportional to G, established through the settings of attenuator and loop amplifier, while the phase of Γ_{Load}

Fig. 3.2 Block diagram of a realized closed-loop active load-pull system



is completely dependent on the setting of the phase shifter. Therefore, in principle, the reflection coefficient, Γ_{Load} , at the DUT plane, given by Eq. (3.3), can be set to any value, even larger than unity, by choosing an appropriate loop gain G. However, the simplicity of Eq. (3.3) is slightly misleading considering that a high value of G can create oscillating closed-loop load-pull [1, 4]. This is an unwanted situation as it has the potential to damage either the DUT being characterized or the measurement system itself.

The oscillation in the load-pull system can be eliminated by keeping the loop gain G below one (G < 1). In order to keep G < 1, the amplifier gain should not exceed the isolation of the circulator [6]. In theory, an ideal circulator has infinite isolation and therefore the amplifier gain can be set to any value. However, for all practical purposes, standard circulators possess isolation of the order of 30 dB and therefore the loop amplifier must be set below this level in order to avoid instability in the loop. In practical situations a narrow band filter, preferably waveguide type selected on purposes to prevent oscillation at all frequencies lower than its cut-off frequency, is inserted in the loop. The filter also helps in the mitigation of oscillation at higher frequencies outside the band of characterization.

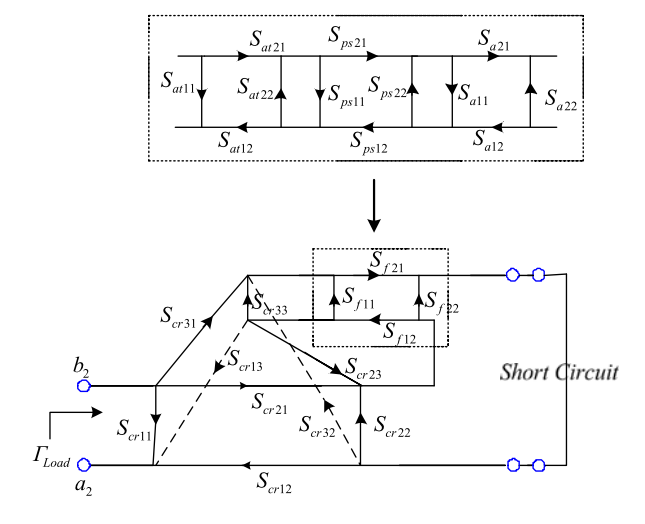
3.2.2 Analysis of Closed-Loop System

In a normal circumstance the closed-loop load-pull system, Fig. 3.2, must synthesize high reflection coefficient, at the DUT plane, without encountering any difficulty. However, experimental investigations have shown the following problem of such a system during the characterization and measurement applications [4, 6, 9].

- A strong inter-dependency of magnitude, $|\Gamma_{Load}|$, and phase, φ_{Load} , of the reflection coefficient, Γ_{Load} , on both the phase shifter and attenuator settings.
- A limited tuning range while synthesizing small magnitude, |Γ_{Load}|, of reflection coefficient.
- Occurrence of oscillation in case of a broadband loop amplifier.

To gain better assessment on how these undesired effects occur and affect the performance of the closed-loop active load-pull system, the analysis of the system using signal flow model shown in Fig. 3.3 is carried out. The S-parameters depend

Fig. 3.3 Signal flow model and the associated S-parameter description of the closed-loop active load-pull system [1], © IEEE 1994



solely on the characteristics of the components used in the feedback loop. The circulator is described by three port S-parameters S_{cr} . The feedback network is described by two-port S-parameters S_f , which are obtained from the cascade connection of the S-parameter sets for the attenuator, S_{at} , phase shifter, S_{ps} , and loop amplifier, S_a .

The reflection coefficient at the DUT plane, for linear operation of loop amplifier, deduced from Fig. 3.3 is given in Eq. (3.4).

$$\Gamma_{Load} = S_{11} + \frac{S_{12}S_{21}}{1 - S_{22}} \tag{3.4}$$

where,

$$S_{11} = \frac{S_{f11}S_{cr13}S_{cr31} - S_{f11}S_{cr33}S_{cr11} + S_{f12}S_{cr13}S_{cr21} - S_{f12}S_{cr23}S_{cr11} + S_{cr11}}{1 - S_{f11}S_{cr23} - S_{f12}S_{cr23}}$$
(3.5)

$$S_{12} = \frac{S_{f11}S_{cr13}S_{cr32} - S_{f11}S_{cr33}S_{cr12} + S_{f12}S_{cr13}S_{cr22} - S_{f12}S_{cr23}S_{cr12} + S_{cr12}}{1 - S_{f11}S_{cr23} - S_{f12}S_{cr23}}$$
(3.6)

$$S_{11} = \frac{S_{f11}S_{cr13}S_{cr31} - S_{f11}S_{cr33}S_{cr11} + S_{f12}S_{cr13}S_{cr21} - S_{f12}S_{cr23}S_{cr11} + S_{cr11}}{1 - S_{f11}S_{cr23} - S_{f12}S_{cr23}}$$
(3.5)

$$S_{12} = \frac{S_{f11}S_{cr13}S_{cr32} - S_{f11}S_{cr33}S_{cr12} + S_{f12}S_{cr13}S_{cr22} - S_{f12}S_{cr23}S_{cr12} + S_{cr12}}{1 - S_{f11}S_{cr23} - S_{f12}S_{cr23}}$$
(3.6)

$$S_{21} = S_{f21}\gamma + S_{f22}\alpha + S_{11}\frac{S_{f21}S_{cr33} + S_{f22}S_{cr23}}{S_{cr13}}$$
(3.7)

$$S_{cr13}$$

$$S_{22} = S_{f21}\delta + S_{f22}\beta + S_{12}\frac{S_{f21}S_{cr33} + S_{f22}S_{cr23}}{S_{cr13}}$$
(3.8)

The parameters α , β , γ , and δ in the above equations are variables defined in Eqs. (3.9)–(3.12) [1].

$$\alpha = S_{cr21} - \frac{S_{cr11}S_{cr23}}{S_{cr13}} \tag{3.9}$$

$$\beta = S_{cr22} - \frac{S_{cr12}S_{cr23}}{S_{cr13}} \tag{3.10}$$

$$\gamma = S_{cr31} - \frac{S_{cr13}}{S_{cr13}}$$

$$S_{cr13}$$

$$S_{cr13}$$
(3.11)

$$\delta = S_{cr32} - \frac{S_{cr33}S_{cr12}}{S_{cr13}} \tag{3.12}$$

It can be ascertained from Eqs. (3.4)–(3.12) that the non-ideal components employed in the design of the active closed-loop load-pull system plays key role in the reflection coefficient synthesis ability of the system. The degree of the undesired effects, due to the non-ideal components, obviously depends on the characteristics of the respective circulator, attenuator, phase shifter, and the loop amplifier. For example, typical S-parameters given in Eqs. (3.13)–(3.16) have been inserted into the expressions (3.4)-(3.12) to determine the impact of imperfection in the loop components on reflection coefficient Γ_{Load} [1].

$$S_{cr} = \begin{bmatrix} 0.09 & 0.9 & 0.1 \\ 0.9 & 0.09 & 0.01 \\ 0.1 & 0.01 & 0.09 \end{bmatrix}$$

$$S_{at} = \begin{bmatrix} 0.25 & 0.01 \\ 0.01 & 0.25 \end{bmatrix}$$

$$S_{ps} = \begin{bmatrix} 0.11 & 0.91 \\ 0.91 & 0.11 \end{bmatrix}$$

$$(3.13)$$

$$(3.14)$$

$$S_{at} = \begin{bmatrix} 0.25 & 0.01 \\ 0.01 & 0.25 \end{bmatrix} \tag{3.14}$$

$$S_{ps} = \begin{bmatrix} 0.11 & 0.91 \\ 0.91 & 0.11 \end{bmatrix} \tag{3.15}$$

$$S_a = \begin{bmatrix} 0.3 & 25.1\\ 0.25 & 0.3 \end{bmatrix} \tag{3.16}$$

Figure 3.4 illustrates the dependence of magnitude and phase of Γ_{Load} on the variations in the $|S_{at21}|$, and $Arg(S_{ps21})$. For example, at an attenuator setting $|S_{at21}| = -22$ dB, a change of the phase shifter setting Arg (S_{ps21}) from 0° to 180° results in no phase change, $\Delta \varphi_{Load}$, at all but in a magnitude change, $\Delta \Gamma_{Load}$, of 0.7 in the reflection coefficient, Γ_{Load} .

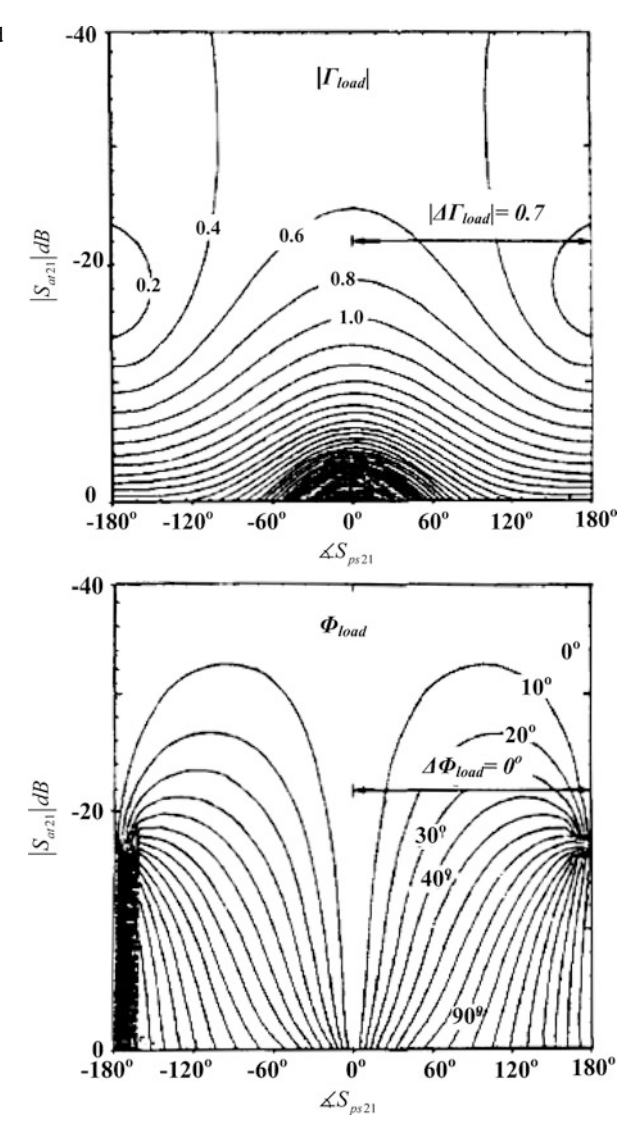
It can also be observed from Fig. 3.4 that the synthesizable reflection coefficients using closed-loop active load-pull are restricted. For example, in this case the system cannot synthesize reflection coefficient smaller than 0.5 for the phase shifter setting at $Arg(S_{ps21}) = 0^{\circ}$ irrespective of the variation in the attenuator setting $|S_{at21}|$. Reflection coefficient smaller than 0.5 can be synthesized using the active load-pull system if loop components have lesser imperfections than Eqs. (3.13)–(3.16).

It is easier to comprehend the two problems through Eqs. (3.4)–(3.12), i.e., the limitation of the system to synthesize smaller reflection coefficient and the strong dependence of synthesized reflection coefficient on the attenuator and phase shifter settings, but these equations are too abstract for interpreting the oscillation conditions in the system. In order for comprehending the equations easily, first the ideal situation is considered where all components are assumed to have matched input and output ports and the circulator is assumed to have infinite directivity. The amplifier is also assumed to possess infinite reverse isolation. With these assumptions the flow model of Fig. 3.4 greatly simplifies, and gives the expression, Eq. (3.17), for synthesized reflection coefficient at the DUT plane.

$$\Gamma_{Load} = \Gamma_{Load}^{o} = S_{cr31} S_{at21} S_{ps21} S_{a21} S_{cr12}$$
(3.17)

where Γ^o_{Load} is the synthesized reflection coefficient, when all the components in the system are ideal, whose magnitude is directly determined by the setting of the attenuator and the phase by the setting of the phase shifter.

Fig. 3.4 Magnitude (top) and phase (bottom) contours of the reflection coefficient as a function of the attenuator and phase shifter settings [1], © IEEE 1994



Next Eqs. (3.4)–(3.12) are used as a basis for a perturbation analysis. Cumulative Step-by-step approach where only one non-ideal effect of the components used in the feedback network is considered (e.g. poor input match S_{a11} of amplifier (effect (1) in Table 3.1)), leading to a set of expressions for Γ_{Load} which can be analyzed simply.

Table 3.1 summarizes the results of perturbation analysis for the closed-loop active load-pull system. The non-ideal effects (2), (5), and (7) can be neglected if an isolator is used at the output of the loop amplifier. The input mismatch (8) of the circulator S_{cr11} directly adds to Γ_{Load}^o and hence must be kept small. The effects

Table 3.1 Results of perturbation analysis for closed-loop active load-pull system [1], © IEEE 1994

Effects	Importance	$\Gamma_{Load} - \Gamma^o_{Load}$
(1) S_{a11}	Minor, damped by coupling factor	$S_{cr31}S_{at21}S_{ps21}S_{a11}S_{at12}S_{ps12}S_{cr13}$
(2) S_{a22}	Major, isolator behind amplifier helpful	$S_{cr21}S_{a22}S_{cr12}$
(3) S_{a12}	Minor	$S_{cr21}S_{a12}S_{at12}S_{ps12}S_{cr13}$
$(4) S_{at11}$	Minor, damped by coupling factor	$S_{cr31}S_{at11}S_{cr13}$
(5) S_{at22}	Major, isolator behind amplifier helpful	$S_{cr21}S_{a12}S_{ps12}S_{at22}S_{ps21}S_{a21}S_{cr12}$
(6) S_{ps11}	Minor, damped by coupling factor	$S_{cr31}S_{at11}S_{cr13}$
(7) S_{ps22}	Major, isolator behind amplifier helpful	$S_{cr21}S_{a12}S_{ps22}S_{a21}S_{cr12}$
(8) S_{cr11}	Major, matched input needed	S_{cr11}
$(9) S_{cr22}$	Minor, damped by coupling factor	$S_{cr31}S_{at21}S_{ps21}S_{a21}S_{cr22}S_{a12}S_{ps12}S_{at12}S_{cr13}$
(10) S_{cr33}	Minor, damped by coupling factor	$S_{cr21}S_{at21}S_{ps21}S_{a21}S_{cr33}S_{a12}S_{ps12}S_{at12}S_{cr12}$
(11) S_{cr23}	Major, high directivity is a must	$\frac{S_{cr21}S_{at12}S_{ps12}S_{at2}S_{cr13}}{1 - S_{a12}S_{ps12}S_{at12}S_{cr23}}$
(12) S_{cr32}	Major, high directivity is a must. Avoid oscillations: $ S_{a21} S_{cr32} < 1$	$\frac{S_{cr31}S_{at21}S_{ps21}S_{a21}S_{cr12}}{1 - S_{a21}S_{ps21}S_{at21}S_{cr32}}$

(1), (4), (6), (9), and (10) mainly concern the active closed-loop load-pull system utilizing directional coupler as a three-port component. A high coupling factor will dampen all these effects. In case of circulator, high isolation between the ports can eliminate all these effects.

Effects (11) and (12) create condition of oscillations, when the forward gain of the feedback loop gets higher than 1, and can be suppressed through the use of high directivity circulator or directional coupler. A sufficient condition to avoid oscillations under all attenuator and phase shifter settings ($|S_{at21}| < 1$, $|S_{ps21}| < 1$) is given in Eq. (3.18), which conveys that the amplifier gain has to be smaller than the circulator directivity at all frequencies.

$$|S_{at21}||S_{cr32}| < 1 (3.18)$$

Further, Fig. 3.5 gives another condition, Eq. (3.19), which, if not satisfied, can create instability in the load-pull system.

$$|\Gamma_{Load}||\Gamma_{DUT}| < 1 \tag{3.19}$$

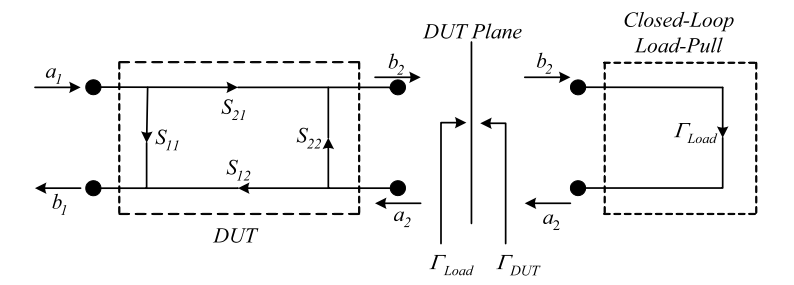


Fig. 3.5 A simplified signal flow graph for the closed-loop load pull

In practical applications $|\Gamma_{DUT}|$ is normally smaller than 1, $\Gamma_{DUT} < 1$, consequently active load-pull with the ability to synthesize $|\Gamma_{Load}|$ higher than 1, $\Gamma_{Load} > 1$, has the potential to nullify Eq. (3.19) and create unwanted oscillations according to the basic stability theory [10]. This may happen if a broadband loop amplifier with large gain ripple is used in the feedback loop. For example, a high reflection coefficient synthesized by reducing attenuation in the loop at a specific frequency f_1 might create oscillation at another frequency f_2 if the amplifier gain at f_2 is higher. It is also important to note that the stability condition, Eq. (3.19), also affects the DUT, as both the load-pull and the DUT are coupled with each other through their reflection coefficients and therefore any oscillation in the system easily transfers to the DUT [10].

Simplification of Eqs. (3.3) and (3.19) suggests that the active load-pull loopgain G must be smaller than the return loss of the output of the DUT in order to maintain stability in the measurement setup as expressed in Eq. (3.20).

$$G < 20\log|S_{22}| \text{ dB} \tag{3.20}$$

Equation (3.20) also identifies that a perfect match at the DUT output allows an infinite gain G without any oscillations in the system. In practice, though, the gain G is limited by the finite directivity of the circulator and therefore in order to avoid oscillations, the loop gain G must be smaller than the directivity of the circulator so as to fulfill the stability criterion in Eqs. (3.18) and (3.20).

3.3 Closed-Loop Load-Pull Architectures

Analysis of closed-loop system provides a suggestion that in its simplest form, it is capable, in principles, of synthesizing high reflection coefficient, despite the fact that it suffers from instability issues. In order to overcome the oscillation problem, an isolator is required at the output of loop amplifier as shown in Fig. 3.6. The incorporation of isolator is extremely useful, in particular, during characterization and measurement of high power DUTs where the signal powers are extremely high and slight mismatches condition at the circulator ports have the potential to cause loop oscillation and damage the measurement system and/or the DUT.

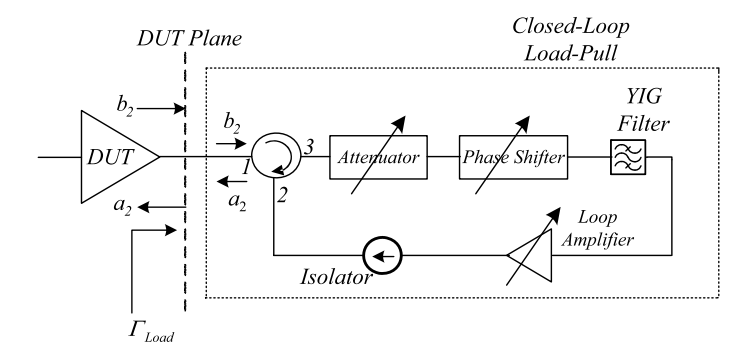


Fig. 3.6 Block diagram of closed-loop active load pull incorporating isolator and narrow band filter in order to eliminate oscillation problem [11], © IEEE 2007

Oscillations in closed-loop load-pull system, due to large gain ripple in the characteristics of the loop amplifier, can be eliminated by inserting a highly selective bandpass filter, such as yttrium iron garnet (YIG) filter, in the feedback loop as shown in Fig. 3.6. The YIG filters possess flat gain over a specified bandwidth; therefore eliminate the effects of large gain ripple in the response of loop amplifier. The downside of the YIG filter insertion in the loop, however, is the resulting limited bandwidth of the load-pull system.

Applications such as characterization and measurement of transistor devices for high efficiency PA design require harmonic terminations on the border of Smith chart [12–15]. The active closed-loop system can be easily extended to multi-harmonic configurations, as shown in Fig. 3.7 for three-harmonic frequencies system. Three-harmonic load-pull system requires a triplexer for separating the harmonic components of the incident traveling wave, b_2 , given in Eq. (3.21). The respective harmonic components are modified in the feedback loop and then combined by the other triplexer to create reflected traveling wave, a_2 , given in Eq. (3.22). The ratio of Eq. (3.21) and (3.22) give the reflection coefficients, at the respective harmonic frequencies, according to Eq. (3.23).

$$b_2 = b_2(f_0) + b_2(2f_0) + b_2(3f_0)$$
(3.21)

$$a_2 = a_2(f_0) + a_2(2f_0) + a_2(3f_0)$$
 (3.22)

$$\Gamma_{Load}(nf_0) = \frac{a_2(nf_0)}{b_2(nf_0)} \tag{3.23}$$

where, n = 1, 2, 3.

The harmonic load-pull shown in Fig. 3.7 is capable of synthesizing any desired reflection coefficient at various harmonic components, by enhancing power level of reflected traveling wave a_2 of specific harmonic component. The constraint on loop amplifier, however, is the major bottleneck considering that it might go into compression in order to raise the power level of the reflected traveling wave. Successful operation of system, however, requires that the loop amplifier must be linear which necessitates an appropriate corrective steps described in next section.

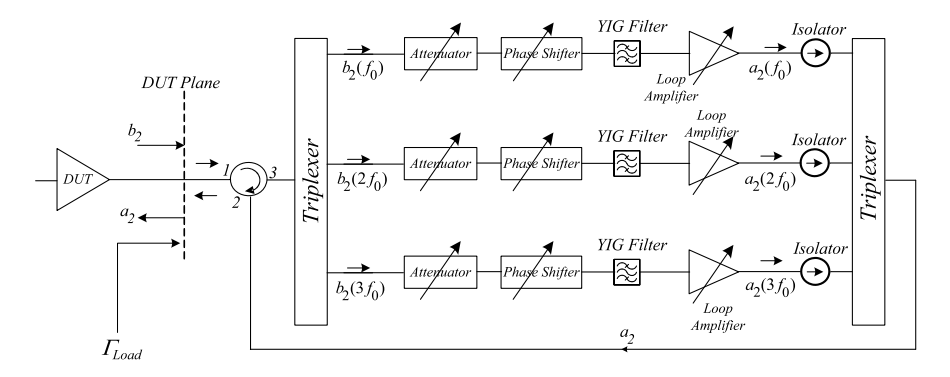


Fig. 3.7 Generic architecture of three-harmonic load-pull system based on active closed-loop technique

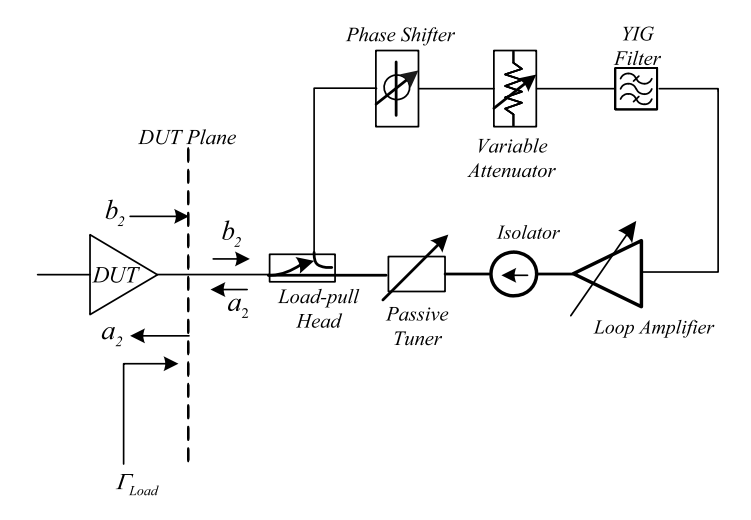


Fig. 3.8 Block diagram of load-pull system combining active closed-loop and passive tuner [6], © IEEE 2008

3.4 Optimized Closed-Loop Load-Pull System

In particular, the losses in the measuring network and the active load-pull loop have dual impact: enhanced risk of oscillations [16] and increased output power requirement from the loop amplifier for the synthesis of a given Γ_{Load} . A simple technique to address these problems is to replace the circulator with a low-loss three-port component, such as load-pull head [17], as shown in Fig. 3.8. Note that the presence of isolator in the loop is necessary to protect the loop amplifier, and to attain a stable feedback loop.

Inclusion of a passive tuner in the loop, further, helps in reducing the output power demand from the loop amplifier for the synthesis of low impedances. The tuner in the loop could be two-port slug tuner (with one or more slugs) [18] so that

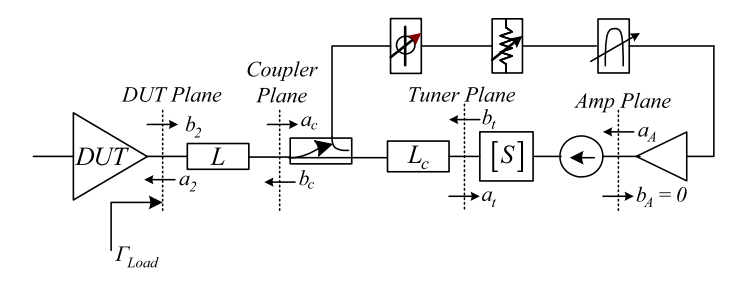


Fig. 3.9 Simplified schematic of load-pull system combining active closed-loop and passive tuner [6], © IEEE 2008

when the slugs are completely raised up, the tuner does not provide any contributions to Γ_{Load} and therefore is completely set by only the active loop. Under this condition the power required from the loop amplifier is maximal. On the other hand when the slugs are fully inserted, the loop is cut off, and the loop amplifier does not contribute to Γ_{Load} regardless of its output power. As a conclusion, between these two extreme cases, there must be an optimal situation (i.e., an optimal tuner slug setting), where the required output power from loop amplifier reaches a minimum. This aspect can be analyzed using the simplified schematic in Fig. 3.9, which depicts the unavoidable losses due to cables in the loop by L_c and losses in the measuring network by L. The schematic also includes the respective incident and reflected traveling waves at various planes, and the scattering matrix (S-matrix), S, of the passive tuner.

Following quantities are defined and/or assumed for simplification of the analysis of closed-loop load-pull system schematic given in Fig. 3.9 [6].

- G = the overall loop gain (including the coupling factor of load-pull head, amplifier gain, and overall loop losses).
- The isolator is ideal and therefore $b_A = 0$.
- Γ_{Lo} = the desired reflection coefficient at the DUT plane.
- Γ_{Lt} = the maximum reflection coefficient synthesized by only passive tuner at the DUT plane (i.e., when the active loop is completely shut down (i.e., $a_A = 0$).
- P_{out} = the power delivered by the DUT when $\Gamma_{Load} = \Gamma_{Lo}$.

Now the output power, P_A , from loop amplifier can be expressed by Eq. (3.24).

$$P_A = |a_A|^2 \tag{3.24}$$

where,

$$a_A = Ga_C = GLb_2 \tag{3.25}$$

Equations (3.24) and (3.25), when combined, give the expression for loop amplifier output power in terms of the incident traveling wave, b_2 , at the DUT plane and the losses in the measuring network, L, given in Eq. (3.26).

$$P_A = |G|^2 |L|^2 |b_2|^2 (3.26)$$

The incident traveling wave, b_2 , when $\Gamma_{Load} = \Gamma_{Lo}$ is related to the DUT output, P_{out} , by the expression given in Eq. (3.27).

$$|b_2^2| = \frac{P_{out}}{1 - |\Gamma_{Io}|^2} \tag{3.27}$$

Simplification of Eqs. (3.26) and (3.27) gives the loop amplifier output power, P_A , Eq. (3.28), in terms of the feedback loop gain, G, power delivered by the DUT, P_{out} , and loss in the measuring network, L.

$$P_A = |G|^2 |L|^2 \frac{P_{out}}{1 - |\Gamma_{Lo}|^2}$$
(3.28)

At the tuner plane, S-parameter of the loop tuner, represented as S_{ij} (i, j = 1, 2), is related to the reflected traveling wave at the amplifier plane, a_A , by Eq. (3.29).

$$b_t = S_{11}a_t + S_{12}a_A \tag{3.29}$$

For load-pull head, with low coupling factor (< 20 dB), following assumptions relating the losses in the measuring network, losses in the feedback loop, and the traveling waves at the tuner reference plane can be made [6, 19]:

$$b_t = \frac{a_2}{LL_c} \tag{3.30}$$

$$a_t = LL_c b_2 (3.31)$$

Substitution of Eqs. (3.25), (3.30) and (3.31) into Eq. (3.29) and followed by a simplification provides the expression for the loop gain, G, given in Eq. (3.32).

$$G = \frac{\Gamma_{Lo} - S_{11}(LL_c)^2}{S_{12}L(LL_c)}$$
 (3.32)

Moreover, for a reciprocal lossless tuner S_{11} and S_{12} are related by Eq. (3.33) [19].

$$|S_{11}|^2 + |S_{21}|^2 = |S_{11}|^2 + |S_{12}|^2 = 1$$
 (3.33)

In case of reciprocal low loss passive tuner in the loop, therefore, following assumptions can be made:

$$|S_{11}|^2 + |S_{12}|^2 = |\gamma|^2 \tag{3.34}$$

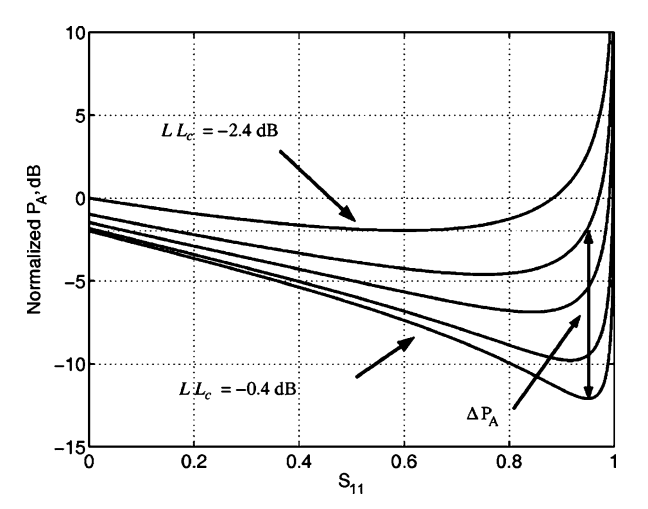
where, $|\gamma|$ is the maximum value that $|S_{11}|$ can reach and should not be confused with the propagation constant.

Equations (3.28), (3.32) and (3.34) can be solved to deduce the expression for the output power from loop amplifier given in Eq. (3.35) [6].

$$P_A = \frac{|\Gamma_{Lo} - S_{11}(LL_c)^2|^2}{(|\gamma|^2 - |S_{11}|^2|(LL_c)|^2)} \frac{P_{out}}{1 - |\Gamma_{Lo}|^2}$$
(3.35)

Equation (3.35) gives insights on the behavior of the amplifier output power with respect to the desired reflection coefficient, Γ_{Lo} , the pre-tuning provided by the loop tuner, S_{11} , and overall losses, LL_c , in the measurement setup. This equation can be further analyzed by plotting P_A versus S_{11} for different values of LL_c , at a fixed Γ_{Lo} , with the purpose of identifying the impact of loop tuner and load-pull head on

Fig. 3.10 Normalized loop amplifier output power P_A versus tuner S_{11} for different values of overall losses. ΔP_A is the difference between the minimum P_A and its value for $S_{11} = 0$ [6], © IEEE 2008



 P_A . For example, Fig. 3.10 shows a plot of P_A versus S_{11} when $\Gamma_{Lo} = 0.96$ and $\gamma = 1$. In this case S_{11} has been assumed purely real and S_{11} continuously varies between zero and γ .

The plot contains information about P_A for several values of LL_c , from -2.4 dB (typical for measurement setups with standard couplers) to -0.4 dB (setup with load-pull head). The P_A in this plot has been normalized with respect to its value corresponding to $LL_c = -2.4$ dB and $S_{11} = 0$.

It can be observed that the use of load-pull head in the active load-pull setup reduces the requirements on loop amplifier power output by reducing the attenuation terms LL_c . For $S_{11}=0$, i.e. when the tuner is not present in the loop, the required P_A to obtain $\Gamma_{Lo}=0.96$ is 2 dB lower for $LL_c=-0.4$ dB, with respect to the value of the required power when $LL_c=-2.4$ dB.

Furthermore, Fig. 3.10 also shows the effect of loop tuner as a prematching device in active closed-loop load-pull system. It is evident that the minimum required P_A show strong dependence on the loop tuner setting S_{11} . If term ΔP_A is the difference between the minimum value of the P_A and its value for $S_{11} = 0$, then it can be deduced that ΔP_A is 2 dB for $LL_c = -2.4$ dB and is 10 dB for $LL_c = -0.4$ dB. This clearly demonstrates the advantage of using loop tuner and load-pull head in the closed-loop active load-pull system.

The determination of the best tuner setting for the minimum P_A requires zeroing of the first derivative of (3.35) on the real axis, which results into Eq. (3.36).

$$S_{11min} = \frac{|\gamma|^2 (LL_c)^2}{\Gamma_{Lo}}$$
 (3.36)

where, S_{11min} is one of the tuner setting for minimum P_A .

If the active loop is shut down, i.e., $a_A = 0$, and the tuner S_{11} is set to S_{11min} , the reflection coefficient synthesized at the DUT Plane, Γ_{Load} , is smallest, Γ_{Lmin} , and is given by Eq. (3.37) [6].

$$\Gamma_{Lmin} = \frac{|\gamma|^2 (LL_c)^4}{\Gamma_{Lo}} \tag{3.37}$$

However, when $a_A = 0$, the maximum $|\Gamma_{Load}|$ obtainable with the tuner, $|\Gamma_{Lt}|$, is given in Eq. (3.38) according to the initial definition/assumption [6].

$$|\Gamma_{Lt}| = |\gamma|(LL_c)^2 \tag{3.38}$$

This means that by setting the tuner to $|S_{11min}|$, the magnitude of reflection coefficient synthesized at the DUT plane will be given by Eq. (3.39).

$$|\Gamma_{Load}| = \frac{|\Gamma_{Lt}|^2}{|\Gamma_{Lo}|} \tag{3.39}$$

With these considerations, a practical procedure to find the best tuner position, which minimizes P_A , and to obtain the desired Γ_{Lo} is given below [6].

- Measure the maximum $|\Gamma_{Lt}|$ obtainable with the tuner when the loop is shut down.
- If the desired $|\Gamma_{Lo}| < |\Gamma_{Lt}|$, there is no need for active closed-loop load-pull.
- Otherwise, set the tuner, when the loop is shut down, so that $|\Gamma_{Load}| = (|\Gamma_{Lt}|^2/|\Gamma_{Lo}|)$ and $\arg(\Gamma_{Load}) = \arg(\Gamma_{Lo})$; this corresponds to setting the S_{11} of the tuner equal to the S_{11min} .
- Finally, synthesize the desired Γ_{Lo} by properly setting the active-loop attenuator and phase shifter.

3.5 Feed-Forward Load-Pull System

This technique involves splitting of source signal into two parts, with one forwarded to the DUT to be measured while the other gets modified by attenuator, phase shifter, and loop amplifier before being fed at the output of the DUT output port for achieving the load-pull functionality, as shown in Fig. 3.11. Because of high isolation provided by the power splitter and the additional isolator at the loop amplifier output, there is only minor risk of oscillations in this load-pull technique as evident from the ensuing analysis.

If the components of the load-pull are assumed ideal, i.e. power splitter with no insertion or return loss and an infinite isolation between both of its output ports and the connectors exhibiting no loss, then the modified traveling wave generated by it is given by Eq. (3.40).

$$a_2 = Ga_1 \tag{3.40}$$

where factor G represents the overall complex gain introduced by the feed-forward load-pull components. Additionally Eq. (3.40) assumes a perfectly matched loop amplifier; a condition provided by the isolator at the loop amplifier output.

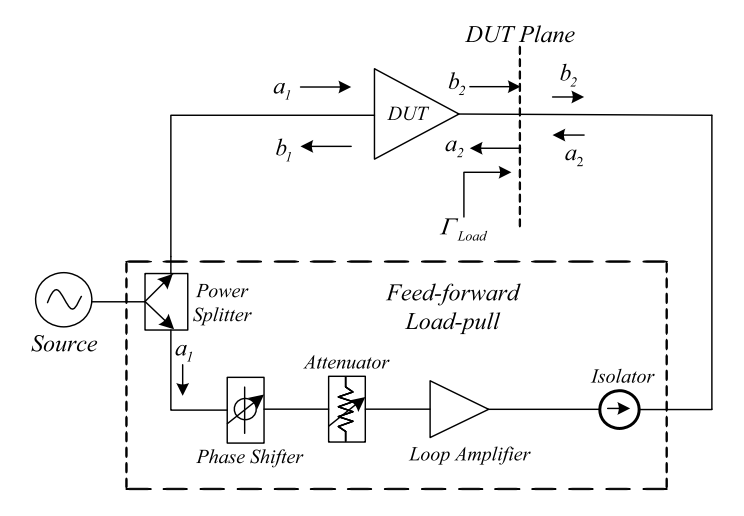


Fig. 3.11 A generic schematic of feed-forward active load-pull architecture

The incident traveling wave at the DUT plane, b_2 , is related to the excitation, a_1 , and the reflected traveling wave at the DUT plane, a_2 , by the expression in Eq. (3.41).

$$b_2 = S_{21}a_1 + S_{22}a_2 \tag{3.41}$$

where S_{21} and S_{22} are the large-signal S-parameters of the DUT at the fundamental frequency [21, 22].

Equations (3.41) and (3.42), when simplified, provide the expression for the synthesized load reflection coefficient, Γ_{Load} , Eq. (3.42), at the DUT plane.

$$\Gamma_{Load} = \frac{a_2}{b_2} = \frac{1}{(\frac{S_{21}}{G} + S_{22})}$$
(3.42)

It can be inferred from Eq. (3.42) that the synthesized reflection coefficients, Γ_{Load} , are dependent not only on the load-pull gain, G, but also on the DUT large signal S-parameters S_{21} and S_{22} . The synthesized Γ_{Load} will be zero when G=0, i.e. when the load-pull is not operated, and will be maximum when $G=1/S_{22}$, i.e. when the load-pull is in operation and very high power is injected at the DUT output port by the feed-forward load-pull. The DUT operating in stable condition always possess $S_{22} \leq 1$ and therefore the maximum Γ_{Load} obtained from the feed-forward load-pull system, according to Eq. (3.42), can cover the entire Smith chart.

However, the synthesis of Γ_{Load} by the feed-forward load-pull is unpredictable due to its dependence on the large signal S-parameters S_{21} and S_{22} of an unknown DUT. For example, in order to synthesize a specific Γ_{Load} the load-pull gain, G, can be calculated, from Eq. (3.42), using the values S_{21} and S_{22} from previous set of measurements. The large-signal S-parameters depend largely on the port impedances at the DUT, and the changing DUT parameters such as drive power and bias. It is, therefore, likely that both terms S_{21} and S_{22} will change with any

Fig. 3.12 Measurement flow graph of feed-forward load-pull system [20], © IEEE 1994

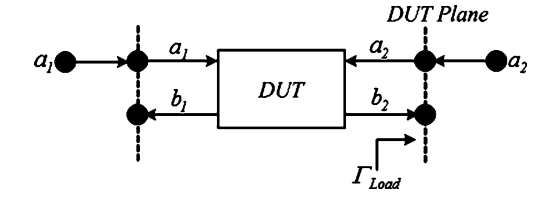
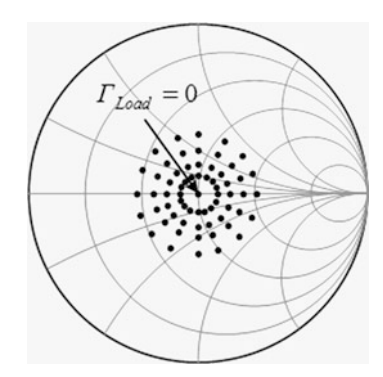


Fig. 3.13 Loci of the synthesizable reflection coefficients by the feed-forward load-pull system [20], © IEEE 1994

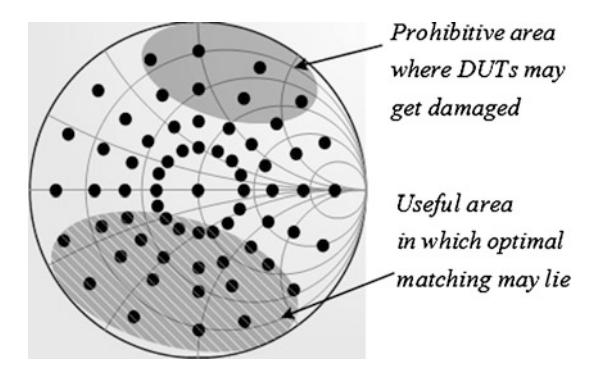


variation in the setting of the load-pull components, drive power or bias, thereby necessitating the calculation of new value for G. Thus the dependence of the large signal S-parameters on port impedances, drive power, and bias level makes the reflection coefficient synthesis an iterative process. In principle the feed-forward load-pull system requires convergence technique, described in a later section, in order to achieve precision in the synthesized reflection coefficient.

The feed-forward load-pull system, although slow in synthesizing desired reflection coefficient due to iterative nature, exhibits increased stability as compared to closed-loop active load-pull system. It remains stable as long as the complex gain, G, remains less than the combined reverse transmission coefficient, S_{12} , of the DUT and the isolation of the power splitter. In practical situations, a standard power splitter provides an isolation of more than 20 dB [23] and the reverse transmission coefficient, S_{12} , readily adds another 20 dB, consequently provides plenty of room to the feed-forward load-pull gain, G. Furthermore, the output and input of the active feed-forward loop are completely isolated and, as a result, its stability is independent of the reflection coefficient S_{22} of the DUT. Consequently the condition for the stable operation of the active feed-forward load-pull is decoupled from the stability criterion for the DUT, therefore discards the need of loop amplifier with constant magnitude and phase frequency response.

It can, additionally, be inferred from Eq. (3.42) that, although, the feed-forward load-pull remains stable for majority of practical applications but can oscillate when complex loop gain approaches extremely high value, which might be the case during high power DUT measurements and characterization. As a result unconditional stability of the DUT can't be guaranteed; thereby necessitating fulfillment of an additional condition at the DUT input so as to achieve stability.

Fig. 3.14 A graphical illustration of problems encountered by the feed-forward load-pull technique [20], © IEEE 1994



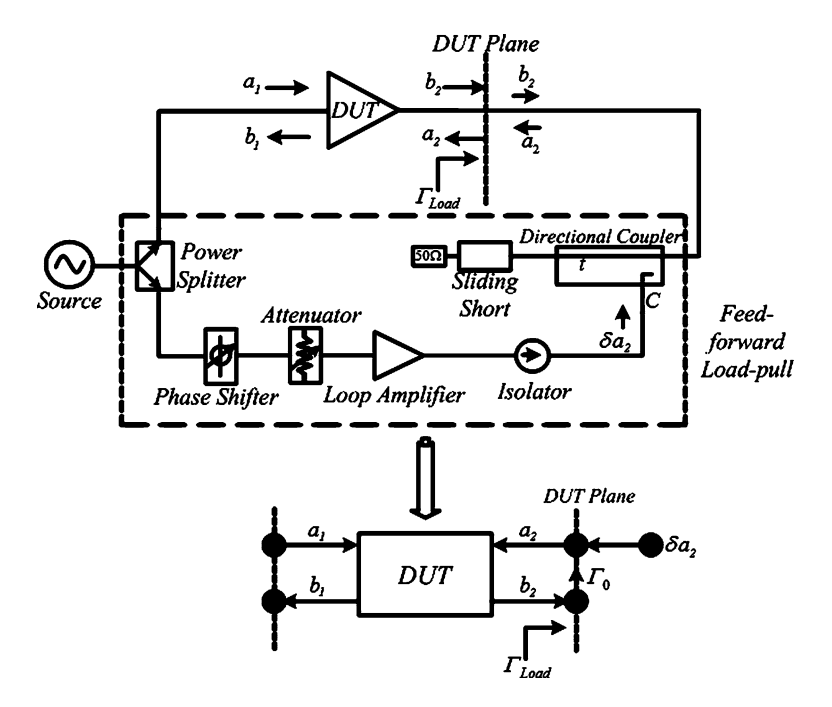


Fig. 3.15 Modified schematic of feed-forward active load-pull system (*top*) and the associated signal flow model (*bottom*) [26], © IEEE 1993

3.6 Optimized Feed-Forward Load-Pull System

The expression for reflection coefficient synthesized by a typical feed-forward loadpull, given in Fig. 3.11 and whose measurement flow graph is illustrated in Fig. 3.12, in term of its loop components is given by Eq. (3.43) [24]. In the flow graph, the stimulus is represented by power source a_1 , while the load-pull is represented by a_2 .

$$\Gamma_{Load} = \frac{a_2}{b_2} = L_1 G e^{j\varphi} \tag{3.43}$$

where.

 L_1 = losses in the feed-forward loop $Ge^{j\varphi}$ = complex gain of the feed-forward loop

A feed-forward load-pull system output is normally matched to $50~\Omega$ and as a result Γ_{Load} at the initialization is zero. Consequently, reflection coefficients synthesized by it makes locus around the $50~\Omega$ impedance as shown in Fig. 3.13 [25]. This pattern of synthesized reflection coefficient is useful for weakly mismatched DUTs, but may encounter three following major problems for highly mismatched DUTs [20].

- The distribution of reflection coefficients may yield poor concentration, therefore
 may not allow fine scan, of reflection coefficients in Smith chart regions where
 the DUTs achieve their best matching conditions, Fig. 3.14. It has been found
 that more than half of the experimental data determined from this system is not
 useful in the case of highly mismatched DUTs [25], leading to a load-pull system
 providing extremely poor measurement throughput.
- The required high mismatches result in reflection coefficients of large magnitude and in such conditions slight error in their phase adjustments may result into damage of the DUTs, as shown in Fig. 3.14.
- Large power sources are required to drive the output port of the DUT in order to generate high reflection coefficients. For example, 8-watt DUT requires at least 40-watt power from the feed-forward load-pull source in order to synthesize required reflection coefficients, for accurate optimization and characterization [20].

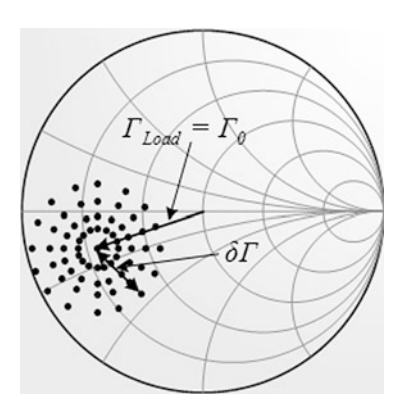
To improve and overcome the three major problems of feed-forward load-pull system, the output can be deliberately mismatched and moved away from 50 Ω by using an assembly of sliding-short circuit and a directional coupler as shown in Fig. 3.15 [26]. The load-pull component is then connected to the coupled port of the directional coupler, with coupling factor C, to synthesize the required reflection coefficient at the DUT plane. Signal flow graph of the modified feed-forward load-pull, depicted in Fig. 3.15, which also includes term Γ_0 , the prematch established by sliding-short circuit, and δa_2 , the signal injected by the feed-forward load-pull, can be analyzed to derive expression for synthesized reflection coefficients in Eqs. (3.44) and (3.45).

$$a_2 = \Gamma_0 b_2 + C \delta a_2 \tag{3.44}$$

$$\frac{a_2}{b_2} = \Gamma_{Load} = \Gamma_0 + C \frac{\delta a_2}{b_2} = \Gamma_0 + \delta \Gamma \tag{3.45}$$

It can be deduced from Eq. (3.45) that the reflection coefficient will be equal to Γ_0 , the value set by the sliding-short circuit, if the power from the feed-forward load-pull is turned off. It is therefore a standard practice, in such a system, to load-pull any DUT using the sliding-short circuit to first identify the Smith chart region where the probable optimal reflection coefficient could lie, and then synthesize it using the sliding-short circuit itself. Later the active component of feed-forward load-pull injects δa_2 to trace the locus of synthesized reflection coefficients around

Fig. 3.16 Loci of the synthesizable reflection coefficient by the modified feed-forward load-pull architecture [20], © IEEE 1994



it, for example shown in Fig. 3.16. In other words, when feed-forward load-pull is turned on, the reflected power, δa_2 , generate reflection coefficients which act as perturbations $\delta \Gamma$ on the initial setting Γ_0 of the sliding-short circuit as depicted in Fig. 3.16.

Only small δa_2 are required to generate perturbations $\delta \Gamma$, in a particular chosen area of Smith chart, and therefore extremely small possibility exists for the modified system to generate reflection coefficients beyond the safe region of Smith chart. As a result, the incorporation of a sliding-short circuit in the feed-forward load-pull allows a very safe load-pull operation resulting in reduced risk of damage to DUTs.

Moreover, modification in the feed-forward load-pull system results into substantially reduced output power from the loop amplifier as it only need to provide the additional perturbations $\delta\Gamma$ on top of Γ_0 . For example, if vector perturbation $\delta\vec{\Gamma}$ is assumed in phase with the vector $\vec{\Gamma}_0$ then Eq. (3.45) can be simplified to obtain the expression for the power reflected by the load-pull source, $\frac{1}{2}\delta a_2^2$, given in Eq. (3.46).

$$\frac{1}{2}|\delta a_2|^2 = \frac{1}{|C|^2}|b_2|^2|\Gamma_{Load} - \Gamma_0|^2$$
(3.46)

The power reflected by the load-pull source in standard feed-forward load-pull, Fig. 3.11, can be given by expression:

$$\frac{1}{2}|a_2|^2 = \frac{1}{|C|^2}|b_2|^2|\Gamma_{Load}|^2 \tag{3.47}$$

The ratio, *R*, of the power reflected by the active feed-forward load-pull system in the modified, Fig. 3.15, and original, Fig. 3.11, setup is given by:

$$R = \frac{1}{|C|^2} \frac{|\Gamma_{Load} - \Gamma_0|^2}{|\Gamma_{Load}|^2}$$
 (3.48)

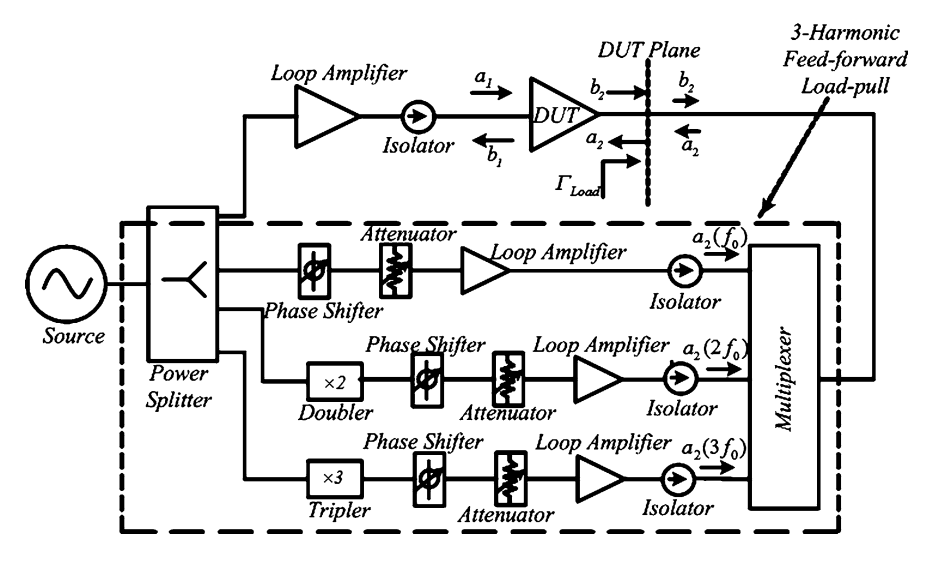


Fig. 3.17 A generic architecture of three-harmonic load-pull system based on feed-forward method

If a perfect lossless 6 dB coupler is assumed, i.e., $\Gamma_0 = 0.75$ and $|C|^2 = 0.25$, then following can be derived from Eq. (3.48) [20]:

$$\Gamma_{Load} = 0.9 \to R = 11 \%$$

$$\Gamma_{Load} = 0.95 \to R = 17 \%$$

$$\Gamma_{Load} = 0.99 \to R = 23.5 \%$$
(3.49)

It is evident from Eq. (3.49) that the incorporation of sliding-short circuit and a perfect 6 dB coupler in the standard feed-forward load-pull system results in the reduction of required reflected power to the tune of almost 75 % while synthesizing reflection coefficients between 0.9 to 0.99.

3.7 Harmonic Feed-Forward Load-Pull System

Extension of feed-forward load-pull to harmonic setup is simple, for example the three-harmonic setup depicted in Fig. 3.17. The feed-forward active loop requires frequency doubler and tripler to generate respective harmonic frequencies considering that the input signal has little or no power at the harmonics. Attenuators, phase shifters, and loop amplifiers appropriately modify the harmonic components of reflected traveling wave, a_2 , in order to synthesize the desired reflection coefficients at the respective harmonics according to Eq. (3.23).

The modified components $a_2(f_0)$, $a_2(2f_0)$, and $a_2(3f_0)$ are then combined together to formulate a_2 , according to Eq. (3.22), by the multiplexer placed at the

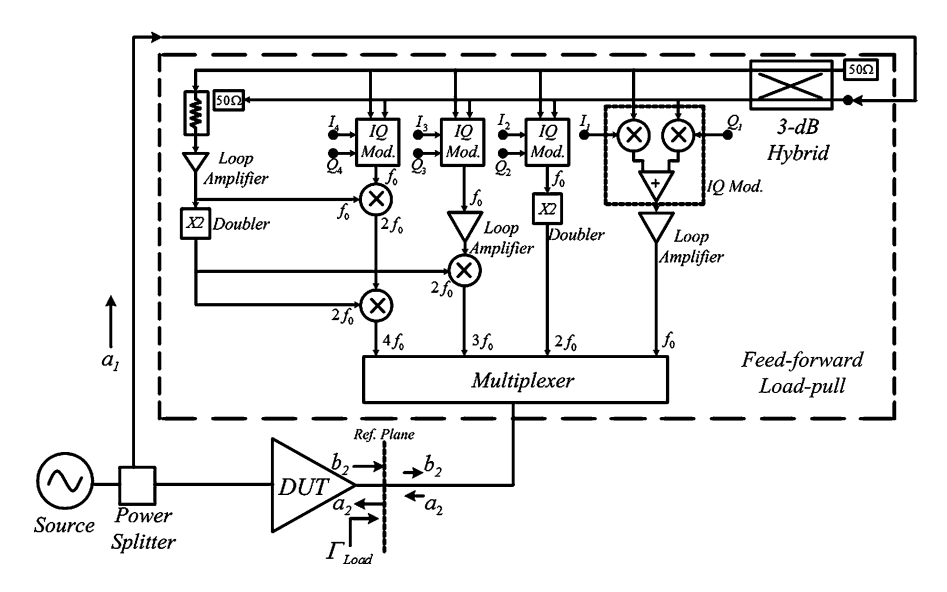


Fig. 3.18 Block diagram of 4-harmonic feed-forward active load-pull technique [27], © IEEE 2000

output of the feed-forward loop. The major limitation of this technique, however, is the escalating requirement of higher power loop amplifiers with the increase in number of harmonic components to be load-pulled. To minimize required output power from the loop amplifiers, vector generator based electronic load-module (ELM) can be employed for the realization of feed-forward load-pull system, for example as shown in Fig. 3.18.

ELM comprises a chain of IQ modulator (made up of double-balanced mixer) for the fundamental frequency, and frequency multipliers for the harmonic components. In this setup configuration, the source signal directed to the load-pull loop, a_1 , first gets divided into quadrature signals by a 3-dB hybrid which then get multiplied with I and Q modulation signals by two double-balanced mixers, see Fig. 3.18, and summed up to formulate reflected traveling wave, a_2 , according to Eq. (3.22). Suppose I and Q signals are DC voltages V_I and V_Q with positive or negative polarity, the resulting harmonic components from each ELM is the output signal, $V_{OUI}(t)$, given in Eq. (3.50).

$$V_{out}(t)^n = a_2(nf_0) = cst \hat{V}_{in} \left(V_I^n \cos \omega_0 t + V_Q^n \sin \omega_0 t \right)$$
(3.50)

where n refers to the harmonic index, \hat{V}_{in} is the input signal amplitude, and cst the conversion gain of the multipliers. V_I controls the real part and V_Q the imaginary part of the output phasor in the complex plane. As a result the IQ modulator enables the adjustment of the RF output voltage, i.e. magnitude and phase of the reflected traveling wave, with arbitrary amplitude and phase relation to the input signal. The multipliers and the control signals also provide gain, dependent on the input voltage range of ELM, to respective harmonic components of a_2 and consequently reduce the required output power from loop amplifiers.

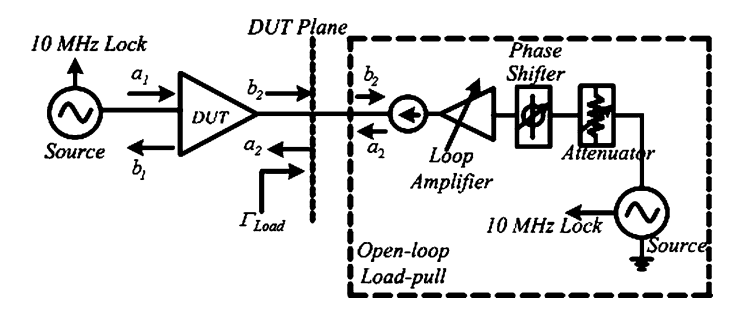


Fig. 3.19 A generic block diagram of active open-loop load-pull technique

The harmonic feed-forward load-pull, in addition to its slow reflection coefficient synthesis ability, is also not capable of emulating harmonically independent reflection coefficients. This is due to the fact that the search for convergence of any specific harmonic reflection coefficient involves inherent interactions between the traveling wave components of other harmonics, which consequently leads to the interaction among the reflection coefficients at harmonic frequencies.

3.8 Open-Loop Load-Pull System

Active open-loop and feed-forward load-pull techniques are almost similar, with the only difference between the two being the source of reflected traveling wave, a_2 . The feed-forward load-pull utilizes same source for excitation and reflected wave, whereas the open-loop system employs two separate sources for the excitation and reflected wave as shown in Fig. 3.19. The sources are locked to a common reference signal, such as 10 MHz locking signal, in order to maintain phase coherence between the transmitted and reflected waves at the DUT plane. Isolator prevents and discards any potential damage to the loop amplifier, whereas attenuator and phase shifter modifies the phase and magnitude of reflected wave.

The reflection coefficient, at the DUT plane, synthesized by an open-loop load-pull is expressed as:

$$\Gamma_{Load} = \frac{a_2}{b_2} = \frac{a_2}{S_{21}a_1 + S_{22}a_2} = \frac{1}{(S_{21}\frac{a_1}{a_2} + S_{22})}$$
(3.51)

where S_{21} and S_{22} are the large-signal S-parameters of the DUT at the fundamental frequency [21, 22], and G represents the overall complex gain generated by the open-loop active load-pull.

It is evident, from Eq. (3.51), that open-loop load-pull can synthesize Γ_{Load} from 0 to ∞ just by changing the magnitude of reflected traveling wave, a_2 . Reflection coefficient, Γ_{Load} , will be zero when the load-pull source is switched off resulting into no reflected wave, a_2 , while it will increase with the increasing a_2 and will reach a maximum of $1/S_{22}$, exactly same as the feed-forward load-pull, usually

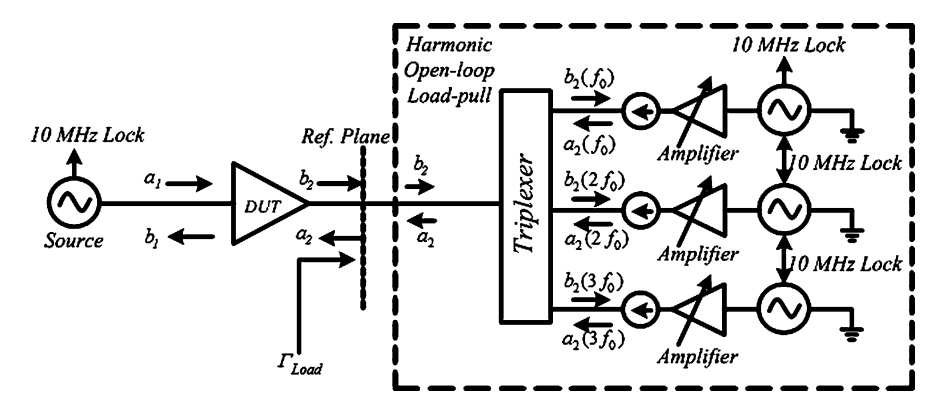


Fig. 3.20 Block diagram of a 3-harmonic active open-loop load-pull setup [8], © IEEE 2000

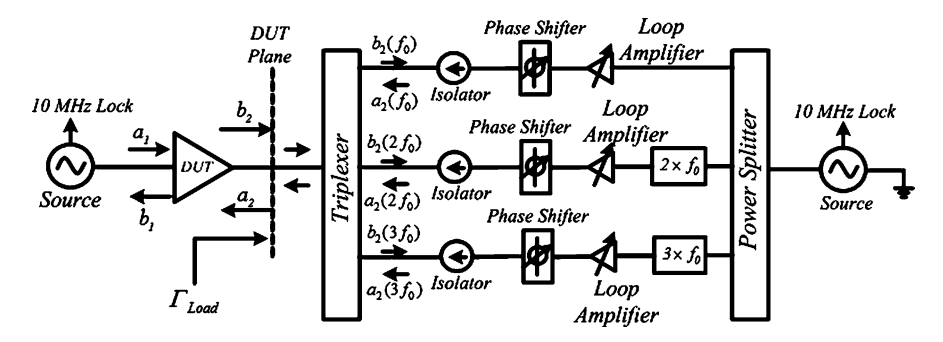


Fig. 3.21 Active open loop harmonic load-pull architecture employing doubler, tripler and just one load-pull source

required for practical applications. Furthermore, synthesis of reflection coefficient using open-loop load-pull being dependent on large signal S-parameters of the DUT, which change with excitation, bias, and impedance environment at the ports, is an iterative and slow process which necessitates convergence algorithm, described in next section, for its precise setting.

The advantage of the open-loop load-pull, though, is its absolute stability, due to the fact that it makes no loop when attached to the DUT and as a result eliminates any possibility of loop oscillations. The absolute stability makes it suitable for high power or harmonic measurements of DUTs; the applications requiring high reflection environments. The higher reflections can be obtained simply by increasing the output power from the loop amplifier. As a further consequence of the absolute stability there are no constraints on the magnitude and phase response of the amplifier as it is the case for closed-loop load-pull system.

Active open-loop load-pull is easily extendible to multi-harmonic setup, for example the 3-harmonic load-pull depicted in Fig. 3.20. The sources used for generating the respective harmonic components of a_2 need to be locked to a common reference in order to maintain coherence between them. Triplexer combines the

fundamental, $a_2(f_0)$, second and third harmonic, $a_2(2f_0)$ and $a_2(3f_0)$, components generated by the respective load-pull sources. In this architecture, the appropriate changes in magnitude and phase of the harmonic components of reflected wave, a_2 , is carried out through the in-built function in the respective load-pull sources. If load-pull sources are devoid of in-built functions for the control of magnitude and phase, separate attenuators and phase shifters can be utilized for achieving the amplitude and phase tuning functionality.

The serious drawback of open-loop active harmonic load-pull setup lies in the practical limitations for scaling it to higher harmonics due to the exorbitantly high costs of the load-pull sources. In order to avoid this limitation one must, either employ single load-pull source capable of generating multi-harmonic components from their distinct ports or, use doublers and triplers in conjunction with a power divider as shown in Fig. 3.21. However, in such a configuration, the required output power from the loop amplifiers increases due to the power division by the divider.

Additionally, the harmonic open-loop active load-pull can't synthesize harmonically independent reflection coefficients due to interactions of different harmonic components of a_2 . The interactions between the harmonic components disturb the settings of all the other reflection coefficients while searching for the convergence of any specific harmonic reflection coefficient. The deflections in the established harmonic reflection coefficients can be minimized through the use of high speed algorithm which reduces the number of required iterations for convergence [28], consequently resulting into reduced interactions between the harmonic frequency components.

3.9 Convergence Algorithm for Open-Loop and Feed-Forward Load-Pull Techniques

According to the active feed-forward and open-loop load-pull concept, reflection coefficients synthesis in these systems is achieved by solving (3.52) for a_{2h} , with h indicating the harmonic index [28].

$$a_{2,h} - \Gamma_h b_{2,h}(a_{2,1}, a_{2,2}, \dots, a_{2,h}) = 0$$
 (3.52)

Therefore, with no prior knowledge of the function $b_{2,h}(.)$, the solution to Eq. (3.52) is often found using a numerical technique such as Newton-Raphson [29]. This is an iterative process and often requires up to 5–10 iterations to converge to a solution for the fundamental harmonic tone [30]. In the case of harmonic load-pull, the number of iterations further increases due to change in the fundamental tone causing distortions in higher harmonics. The problem is further compounded by the fact that the numerical techniques present their own disadvantages such as multiple roots and numerical oscillations [29].

Alternatively, Poly Harmonic Distortion Modeling (PHD) based framework [31, 32] is utilized in the determination of solutions to Eq. (3.52) [28]. The PHD models contain magnitude and phase of spectral components of the input signal and also

introduce harmonic cross product information, which give the relationships between harmonic frequencies for a given drive level and frequency. These information and relationships are then used for achieving solution of Eq. (3.52) in lesser number of iterations as compared to the numerical techniques.

The PHD modeling technique explained in [31] can be used to describe the output $b_{2,h}$ of a non-linear DUT as a function of the respective components of reflected traveling wave, $a_{2,h}$, at the DUT plane, expressed in Eq. (3.53). Equations (3.52) and (3.53), when combined, allow for the formulation of a new convergence algorithm, which is much improved in terms of speed and convergence as compare to numerical method, for the emulation of reflection coefficient in the feed-forward and open-loop load-pull.

$$b_{2,h} = S_{21}(|a_{1,1}|)|a_{1,1}| + \sum_{h} S_{22}(|a_{1,1}|)a_{2,h} + \sum_{h} T_{22,h}(|a_{1,1}|)(a_{2,h}^{*})$$
(3.53)

where, S and T coefficients are functions only of the magnitudes of the stimulus a-wave, a_1 and a_2 , fundamental components [33].

The formulation in Eq. (3.53) can be modified, as illustrated in [33], by describing P and Q as input and output a-wave harmonic phase operators, as shown in Eqs. (3.54) and (3.55). This expression, a third order model, when generalized provides the formulation given in Eqs. (3.56) and (3.57) [28].

$$b_{2,h} = S_{21}|a_{1,1}| \left(\frac{Q}{P}\right)^0 P + \sum_h S_{22}|a_{2,h}| \left(\frac{Q}{P}\right)^1 P$$
$$+ \sum_h T_{22,h}|a_{2,h}| \left(\frac{Q}{P}\right)^{-1} P \tag{3.54}$$

$$P = \frac{a_{1,1}}{|a_{1,1}|} \qquad Q = \frac{a_{2,1}}{|a_{2,1}|} \tag{3.55}$$

$$b_{2,h} = P \sum_{n=-1}^{n=1} \left\{ R_{2,h,n} \left(\frac{Q}{P} \right)^n \right\}$$
 (3.56)

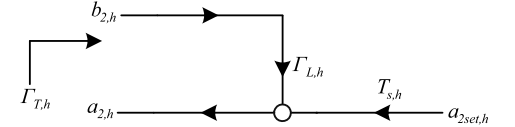
$$R_{2,h,n} = G_{h,n}(|a_{1,1}|, |a_{2,1}|, \dots)$$
(3.57)

Adapting this generalized formulation and assuming that the magnitude of the input signal, $|a_{1,1}|$, during this process is held constant; one can simplify it to Eq. (3.58) by considering only the linear third order mixing terms. This is analogous to X-parameter formulation described in [32].

$$b_{2,h} = G_{2,0,h} + G_{2,1,h}|a_{2,h}| \left(\frac{Q}{P}\right) + G_{2,-1,h}|a_{2,h}| \left(\frac{P}{Q}\right)$$
(3.58)

In a measurement scenario, $G_{2,0,h}$ can be deduced from the output response of $|a_{1,1}|$ at the harmonic being load-pulled. Parameters $G_{2,1,h}$ and $G_{2,-1,h}$ are extracted by applying a perturbation signal to the incident $a_{2,1}$ wave, first of all with a zero degree phase and then followed by the same signal with a 90 degree shift while keeping $|a_{1,1}|$ constant in both cases [31]. By utilizing the measured values of $a_{2,h}$ and $b_{2,h}$

Fig. 3.22 Flow graph showing the losses in the active open-loop load-pull system and the amplifier gain [28], © IEEE 2010



at the center and the offset points, indicated by subscripts 0, 1 and 2, one can then calculate the G parameters using the equation set (3.59)–(3.62).

$$\Delta_1 = a_{2,h,1} - a_{2,h,0}$$
 $\Delta_2 = a_{2,h,2} - a_{2,h,0}$ (3.59)

$$G_{2,1,h} = \frac{(\Delta_2^*)(b_{2,h,1} - b_{2,h,0}) + (\Delta_1^*)(b_{2,h,2} - b_{2,h,0})}{(\Delta_1)(\Delta_2^*) - (\Delta_1^*)(\Delta_2)}$$
(3.60)

$$G_{2,-1,h} = \frac{b_{2,h,1} - b_{2,h,0} - G_{2,1,h}(\Delta_1)}{(\Delta_1^*)}$$
(3.61)

$$G_{2,0,h} = b_{2,h,0} - G_{2,1,h}(a_{2,h,0}) - G_{2,-1,h}(a_{2,h,0}^*)$$
(3.62)

The estimation of $b_{2,h}$, from Eqs. (3.58)–(3.62), and the knowledge of target reflection coefficient, Γ_h , enables the computation of reflected signal, $a_{2,h}$, from Eq. (3.52). If the resulting value of $a_{2,h}$ doesn't bring sufficient accuracy in the target reflection coefficient, the process represented by Eqs. (3.53)–(3.62) can be repeated.

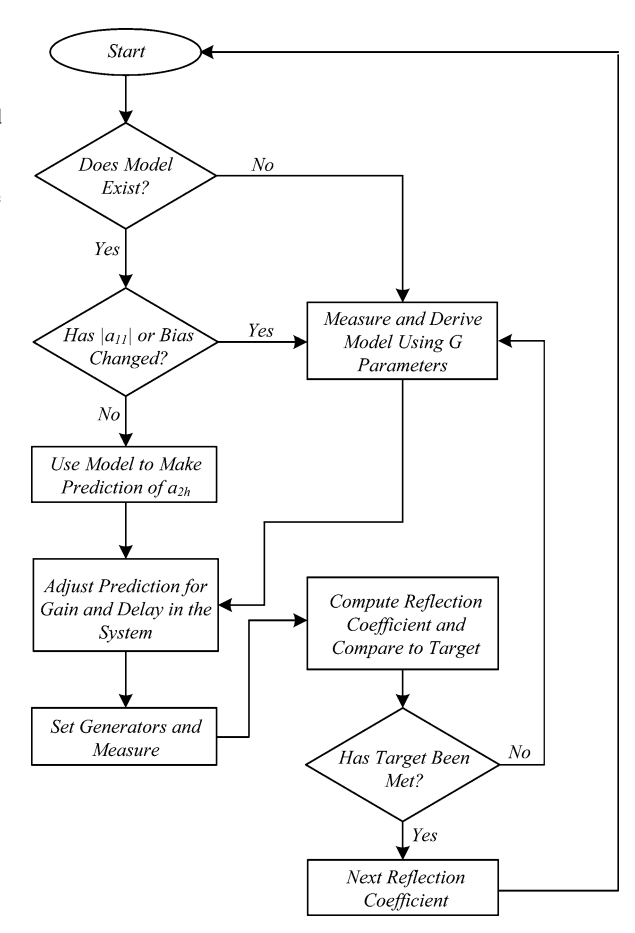
In order to implement this algorithm for the feed-forward or open-loop load-pull system, one has to include the following practical considerations.

Firstly, the reflected wave predicted using (3.47) does not take into account the non-ideal behaviors of the load-pull realization. This is best described by the error model illustrated in Fig. 3.22; where $T_{s,h}$ accounts for the insertion gain/loss of the load-pull amplifiers and couplers etc., while $\Gamma_{L,h}$ accounts for the impedance mismatch of the measurement system, both of which can be dependent on $a_{2set,h}$. It is therefore imperative to re-adjust the reflected wave from calculated value of $a_{2,h}$ to the compensated value of $a_{2set,h}$ in order to account for the physical state of the system. To correctly achieve the target reflection coefficient, $\Gamma_{T,h}$, the characterized system reflection coefficient at the harmonic being load-pulled, $\Gamma_{L,h}$, and amplifier gain, $T_{s,h}$, must be incorporated into (3.52) according to Eq. (3.63).

$$a_{2set,h} = \frac{b_{2,h}(\Gamma_{T,h} - \Gamma_{Load,h})}{T_{s,h}}$$
(3.63)

Two distinct set of measurements are required, to compute the local model, so as to solve Eq. (3.52) for prediction of reflected wave, $a_{2,h}$. As a result, an optimization is necessary to maximize the use of an existing set of G parameters, provided the input drive, $|a_{1,1}|$, or biasing conditions remain unchanged. If the computed reflection coefficient is found to be within the acceptable tolerance of the target reflection coefficient, the existing model would have converged without requiring an update; this is beneficial during load-pull of a reflection coefficient grid. The efficiency of this algorithm can be calculated by comparing the number of useful to redundant measurements.

Fig. 3.23 Flow chart illustrating the implementation of convergence algorithm, based on PHD modeling approach, for the determination of reflection coefficient in active feed-forward and open-loop load-pull systems [28], © IEEE 2010



Finally, according to Eq. (3.52), any adjustments in the fundamental reflected wave, $a_{2,1}$, distorts higher harmonic components, thereby requiring additional iterations, if they were of interest. This effect can be compensated by utilizing harmonic cross-product information from the local model generated by the fundamental tone. For example, during load-pull of the fundamental, the second harmonic may be required to stay at constant impedance. In this case, the measured output response of the second harmonic, $b_{2,2}$, can be used to calculate the adjustments required in the reflected wave, $a_{2,2}$, to achieve constant reflection coefficient using the process described above and the equation set (3.59)–(3.62).

The flow chart in Fig. 3.23 summarizes the implementation of the convergence algorithm, including the optimization and adjustment steps, based on PHD modeling approach, for the determination of reflection coefficient in active feed-forward and open-loop load-pull systems. In order to illustrate how this algorithm works, a single target was considered for emulation using active open-loop load-pull system [28]. This was followed by carrying out measurements to attain multiple targets on a

Fig. 3.24 Path taken by the convergence algorithm, based on PHD modeling approach, for the emulation of target impedance in an active open-loop load-pull systems [28], © IEEE 2010

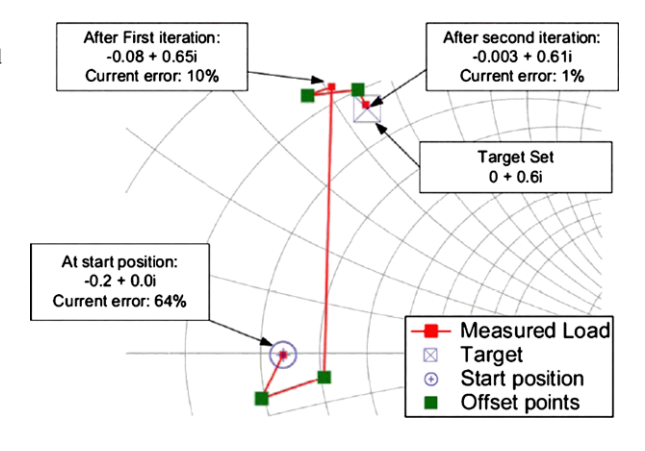
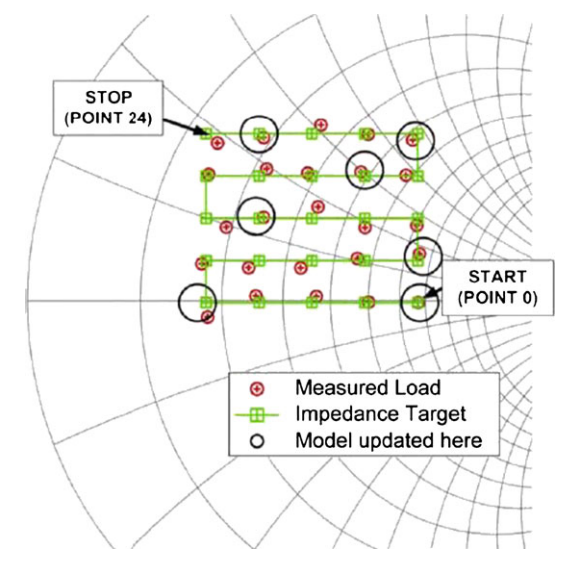


Fig. 3.25 Convergence results on a 5 × 5 square grid of target impedances emulated using active open-loop load-pull system [28], © IEEE 2010



square grid. The measurements were carried out on a $10 \times 75~\mu m$ GaAs HEMT, operating at 3 GHz in Class-B biasing conditions.

Figure 3.24 illustrates the path taken by the algorithm to achieve the target impedance, while Fig. 3.25 shows the convergence results on a 5×5 square grid of target impedances, and also highlights the points at which the algorithm required the model to be updated. At the starting point, -0.2 + i0, two perturbations are made to the $a_{2,1}$ wave; thereby creating the two offset points, which allow the calculation of a local model. The local model is then used to compute a value of $a_{2set,h}$ which moves the load to a new position, -0.08 + i0.65, which in this case is not within the tolerance range, set at 5 %, of the algorithm. The algorithm therefore requires the model to update itself at this stage, hence the additional set of offset points. The position of the load now obtained, -0.003 + i0.61, is within 1 % of the target, 0 + 0.6i; implying the algorithm has now converged to a solution.

Characteristics	Closed-loop	Feed-forward	Open-loop
Dynamic range limitation	Low	Medium	High
$(\Gamma_{Load})_{min}$	Limited	No limitation	No limitation
$(\Gamma_{Load})_{max}$	1	1	1
Adjustment of Γ_{Load}	Fast	Slow	Slow
Oscillations possibility	High	Low	None
Costs	Low	Medium	High
Harmonic tuning	Independent	Dependent	Dependent

Table 3.2 Comparison of the three types of active load-pull systems

The performance of this convergence algorithm can be quantified in terms of its efficient use of the load-pull system. An ideal system, 100% efficient, would require only one measurement per impedance point. The efficiency of the algorithm, based on PHD modeling, to converge to a solution is 44% for the emulated 5×5 square impedance grid considered in this case, averaging 2.26 measurements per impedance point. It is significantly better as compared to Newton-Raphson convergence algorithm whose typical efficiency is 5% to 10% [30].

3.10 Comparison of Active Load-Pull Techniques

The characteristics of the three types of active load-pull systems are summarized in Table 3.2.

The dynamic range of the closed-loop system is limited by the requirement of flat gain from loop amplifier in order to avoid loop oscillations. The feed-forward and open-loop systems are not constrained by flat gain loop amplifier and therefore possess higher dynamic range. The feed-forward load-pull might get into oscillations under some conditions and therefore open-loop has advantage while comparing the dynamic range of these two.

In the closed-loop system, synthesis of smaller magnitude of reflection coefficients strongly depends on the resolution of phase shifter and attenuator settings. The feed-forward and open-loop systems are not limited by this drawback and can, therefore, synthesize any smallest required reflection coefficient. Ideally the maximum synthesizable reflection coefficient can be higher than one, but in practical applications (Γ_{Load})_{max} equal to one is sufficient.

Reflection coefficient synthesis in closed-loop system is fast, whereas in the other systems is slow due to iterative nature of synthesis process. Oscillations in closed-loop system are inherent and therefore special measures are needed to prevent or mitigate them. The feed-forward system has slight possibility of occurrence of oscillations during the characterization of high power DUTs, while the open-loop system is completely free from loop oscillations.

Harmonic reflection coefficients are dependent on each other in the feed-forward and open-loop systems, whereas they are independent in closed-loop system.

References

- J.-E. Muller, B. Gyselinckx, Comparison of active versus passive on-wafer load-pull characterization of microwave and MM-wave power devices, in *IEEE MTT-S International Microwave Symposium Digest* (June 1994), pp. 1077–1080
- 2. Maury Microwave Corporation, Pulsed-bias pulsed-RF harmonic load-pull for gallium nitride (GaN) and wide band gap (WBG), Application Note: 5A-043, Nov. 2009
- C. Roff, J. Benedikt, P.J. Tasker, Design approach for realization of very high efficiency power amplifiers, in *IEEE MTT-S International Microwave Symposium Digest* (June 2007), pp. 143– 146
- G.P. Bava, U. Pisani, V. Pozzolo, Active load technique for load-pull characterization at microwave frequencies. IEE Electron. Lett. 18(4), 178–180 (1982)
- Y. Takayama, A new load pull characterization method for microwave power transistors, in *IEEE/MTT-S International Microwave Symposium*, New Jersey, USA (June 1976), pp. 218– 220
- V. Teppati, A. Ferrero, U. Pisani, Recent advances in real-time load-pull systems. IEEE Trans. Instrum. Meas. 57, 11 (2008)
- M. Spirito, L.C.N. de Vreede, M. de Kok, M. Pelk, D. Hartskeerl, H.F.F. Jos, J.E. Mueller, J. Burghartz, A novel active harmonic load-pull setup for on-wafer device characterization, in IEEE/MTT-S International Microwave Symposium (June 1994), pp. 1217–1220
- 8. J. Benedikt, R. Gaddi, P.J. Tasker, M. Goss, M. Zadeh, High power time domain measurement system with active harmonic load-pull for high efficiency base station amplifier design, in *IEEE/MTT-S International Microwave Symposium*. Boston, USA (2000), pp. 1459–1462
- D.D. Poulin, J.R. Mahon, J.-P. Lanterri, A high power on-wafer pulsed active load-pull system. IEEE Trans. Microw. Theory Tech. 40(12), 2412–2417 (1992)
- G.D. Vendelin, A.M. Pavio, U.L. Rohde, Microwave Circuit Design Using Linear and Nonlinear Techniques (Wiley, New York, 1990), p. 400
- 11. V. Camarchia, V. Teppati, S. Corbellini, M. Pirola, Microwave measurements part II—non-linear measurements. IEEE Instrum. Meas. Mag. 10, 34–39 (2007)
- 12. Y.Y. Woo, Y. Yang, B. Kim, Analysis and experiments for high efficiency class-F and inverse class-F power amplifiers. IEEE Trans. Microw. Theory Tech. **54**(5), 2006 (1969–1974)
- P. Colantonio, F. Giannini, R. Giofre, E. Limiti, A. Serino, M. Peroni, P. Romanini, C. Proietti, A C-band high efficiency second harmonic tuned power amplifier in GaN technology. IEEE Trans. Microw. Theory Tech. 54(6), 2713–2722 (2006)
- M. Helaoui, F.M. Ghannouchi, Optimizing losses in distributed multi-harmonic matching networks applied to the design of an RF GaN power amplifier with higher than 80 % power-added efficiency. IEEE Trans. Microw. Theory Tech. 57(2), 314–322 (2009)
- F.M. Ghannouchi, M.S. Hashmi, Experimental investigation of the uncontrolled higher harmonic impedances effect on the performance of high-power microwave devices. Microw. Opt. Technol. Lett. 52(11), 2480–2482 (2010)
- A. Ferrero, Active load or source impedance synthesis apparatus for measurement test set of microwave components and systems, U.S. Patent 6 509 743, Jan. 21, 2003
- 17. V. Teppati, A. Ferrero, A new class of non-uniform, broadband, nonsymmetrical rectangular coaxial-to-microstrip directional couplers for high power applications. IEEE Microw. Wirel. Compon. Lett. **13**(4), 152–154 (2003)
- S. Dudkiewics, R. Meierer, Cascading tuners for high-VSWR and harmonic load-pull, Maury Microwave Corporation, Application Note: 5C-081, Jan 2009
- D.M. Pozar, Microwave Engineering, 3rd edn. (Wiley, New York, 2005). ISBN 0-471-17096-
- P. Bouysse, J.M. Nebus, J.M. Coupat, J.P. Villotte, A novel, accurate load-pull setup allowing the characterisation of highly mismatched power transistors. IEEE Trans. Microw. Theory Tech. 42(2), 327–332 (1994)

References 85

21. J. Verspecht, F. Verbeyst, M.V. Bossche, Network analysis beyond S-parameters: characterizing and modeling component behavior under modulated large-signal operating conditions, in *56th ARFTG Conference Digest* (Nov. 2000), pp. 1–4

- 22. J. Verspecht, Large-signal network analysis. IEEE Microw. Mag. 6(4), 82–92 (2005)
- 23. K. Rawat, F.M. Ghannouchi, A design methodology for miniaturized power dividers using periodically loaded slow wave structure with dual-band applications. IEEE Trans. Microw. Theory Tech. **57**(12), 3380–3388 (2009)
- F. Blache, J.M. Nebus, P. Bouysse, J.-P. Villotte, A novel computerized multiharmonic active load-pull system for the optimization of high efficiency operating classes in power transistors, in *IEEE/MTT-S International Microwave Symposium*. USA (1995), pp. 1037–1040
- J.-M. Nebus, P. Bouysse, J.-P. Villotte, J. Obregon, Improvement of active load-pull technique for the optimization of high power communication SSPAs. Int. J. Microw. Millimeter-wave Computer-Aided Eng. 5(3), 149–160 (1995)
- J.-M. Nebus, P. Bouysse, J.M. Coupat, J.-P. Villotte, An active load-pull setup for the large signal characterization of highly mismatched microwave power transistors, in *IEEE Instru*mentation and Measurement Technology Conference, Irvine, USA (1993), pp. 2–5
- F.V. Raay, G. Kompa, Waveform measurements—the load-pull concept, in 55th ARFTG Conference, Boston, USA (2000), pp. 1–8
- R.S. Saini, S. Woodington, J. Lees, J. Benedikt, P.J. Tasker, An intelligence driven active loadpull system, in 75th ARFTG Microwave Measurement Conference, Anaheim, USA (2010), pp. 1–4
- 29. S.C. Chapra, Numerical Methods for Engineers, 6th edn. (McGraw Hill, New York, 2009)
- 30. D.J. Williams, P.J. Tasker, An automated active source and load pull measurement system, in *Proceedings of 6th IEEE High Frequency Postgraduate Colloquium*, Cardiff, UK (2001), pp. 7–12
- 31. J. Verspecht, D.E. Root, Poly-harmonic distortion modeling. IEEE Microw. Mag. **7**(3), 44–57 (2006)
- 32. J. Horn, D. Gunyan, L. Betts, J. Verspecht, D.E. Root, Measurement-based large-signal simulation of active components from automated nonlinear vector network analyzer data via X-parameters, in *IEEE International Conference on Microwaves, Communications, Antenna and Electronic Systems* (May 2008), pp. 1–6
- S. Woodington, T. Williams, H. Qi, D. Williams, L. Pattison, A. Patterson, J. Lees, J. Benedikt,
 P.J. Tasker, A novel measurement based method enabling rapid extraction of a RF waveform look-up table based behavioral model, in *IEEE/MTT-S International Microwave Symposium*,
 Boston, USA (June 2008), pp. 1453–1456

Chapter 4 Six-Port Based Load-Pull System

The previous couple of chapters explain the theory, concept and measurement techniques of active and passive load-pull systems. This chapter provides detailed treatment of six-port based setups for passive and active load/source-pull measurements, as well as a description of six-port based harmonic load/source-pull measurements. The load-pull measurements for on-wafer devices require special attention; therefore, an alternative approach for impedance and power flow calibration using a reflection based technique is described.

4.1 Introduction

As mentioned in previous chapters, the load/source-pull systems experimentally determine the performances of a device in large-signal operations and identify the optimal loading conditions that yield the desired performance, in terms of power, power efficiency or linearity or a trade-off among them. Numerous active and passive load/source-pull setups have been developed and used in the past for such measurements. Six-port (SP) junctions, extensively used for load-/source-pull configurations [1–9], have been very flexible in their usage and applications.

In theory, any load-pull system should be able to measure the input impedance of a device under test (DUT), the load impedance seen by the DUT at its output (Z_L) , the source impedance presented to the DUT at its input (Z_S) , the input power absorbed by the DUT (P_{in}) , and the power delivered to load (P_L) . In addition, the load-pull system also monitors the voltages and currents across both the input and output of the DUT for any pair of (Z_S, Z_L) , in order to plot the power-added efficiency (PAE) in the Smith chart.

In some circumstances, measurement and monitoring of the linearity of the device is also required. Several metrics of linearity are used depending on the application, such as amplitude dependent amplitude distortion (AM/AM), amplitude dependent phase distortion (AM/PM), carrier to third-order intermodulation products (C/IMD3), the adjacent channel power ratio (ACPR) and the error vector magnitude

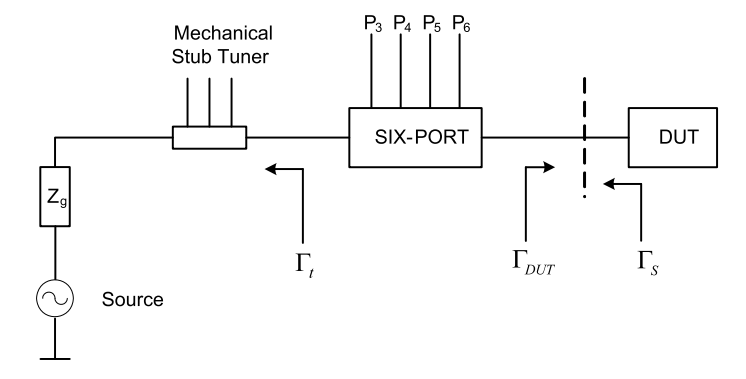


Fig. 4.1 A typical SP based reflectometer with variable test port impedance

(EVM). An SP based load-pull setup enables all these measurements and, therefore, possesses an appropriate and attractive position in the load/source-pull domain.

4.2 Impedance and Power Flow Measurement

Measurements of scattering parameters (S-parameters) using an SP based reflectometer, such as shown in Fig. 4.1, were reported almost three decades ago [10, 11].

The measurements of complex S-parameters of an N-port network require 4 N power readings [11, 12]. The phases of the S-parameters are directly obtained from radio frequency (RF) signals. In addition, it has been shown that the calibration and measurement calculations are not functions of the source impedance presented to the input port of the SP reflectometer; therefore, one could change the source impedance by using a passive tuner inserted before the input port of the SP reflectometer [12].

The power flow exciting the DUT connected to the measuring port of the SP junction, as shown in Fig. 4.1, can be calculated using the following expressions [12]:

$$\Gamma_{DUT}(f) = \frac{w(f) - e(f)}{-c(f)w(f) + d(f)}$$

$$\tag{4.1}$$

$$P_{DUT}(f) = \frac{k(f)P_{Ref}(f)}{|1 + c(f)\Gamma_{DUT}(f)|^2}$$
(4.2)

where c(f), d(f) and e(f) are the error box parameters, w(f) is the embedded reflection coefficient, k(f) is the power calibration parameter that has to be determined at each measurement's frequency, $P_{Ref}(f)$ is the power reading measured by the reference port of the SP junction, and $\Gamma_{DUT}(f)$ is the reflection coefficient measured by the SP reflectometer.

In Fig. 4.1, $\Gamma_S(f)$ is the source impedance seen by the DUT. The complex value of $\Gamma_S(f)$ is related to the tuner impedance, $\Gamma_t(f)$, and the S-parameters, s_{ij} , of the two-port network delimited by the input and output ports of the SP junction when

the remaining ports of the SP junction are terminated by the 50 Ω power sensors [12].

$$\Gamma_S(f) = s_{22}(f) + \frac{s_{12}(f)s_{21}(f)\Gamma_t}{1 - s_{11}(f)\Gamma_t} = \frac{\alpha(f)\Gamma_t + \beta(f)}{\mu(f)\Gamma_t + 1}$$
(4.3)

where $\alpha(f)$, $\beta(f)$ and $\mu(f)$ are directly related to the two-port network delimited by the input and output reference planes of the SP junction.

If the SP junction is designed to be "transparent" in such a way that the input and measuring port of the SP junction are both situated in the direct line of the 50 Ω ($|s_{12}| = |s_{21}| \cong 1$; $|s_{11}| \cong |s_{22}| \cong 0$), a good approximation of the $\Gamma_S(f)$ is given by [12]:

$$|\Gamma_{\mathcal{S}}(f)| \cong |\Gamma_{t}(f)|$$
 (4.4)

It is thus evident from Eqs. (4.2), (4.3), (4.4) that the SP configuration can facilitate impedance and power flow measurements on the fly for arbitrarily changing the impedance presented to the DUT. This assumes that the tuner is pre-calibrated and that the impedance corresponding to Γ_t is known for any position of the stubs of the used tuner.

4.3 SP in Reverse Configuration

An SP junction is usually built with physically assigned input, output and power reference ports and three other power detection ports. The normal use of an SP reflectometer requires the connection of the signal generator at the input port and the DUT to the output port of the SP junction, as shown in Fig. 4.2(a) [13]. In such a configuration, microwave signals are injected from the input to the output; and, the SP reflectometer measures the reflection coefficient of the DUT and the power flow at the output port according to Eqs. (4.1) and (4.2). In this measurement setup, also known as a direct configuration, the signal generator impedance can be arbitrary and has no effect on the SP calibration and measurement calculations [11].

Alternatively, if the signal generator is connected to the output and the DUT to the input of the SP reflectometer, the SP junction is considered to be in a reverse configuration, as shown in Fig. 4.2(b) [13]. In a reverse configuration, the microwave signal is injected from the output port to the input port. In this configuration, the SP measures the reflection coefficient of the DUT, seen at the reference plane located at the output port (port 2) of the SP junction.

4.3.1 SP Calibration in Reverse Configuration

The calibration procedure of the SP reflectometer used in a reverse configuration is divided into the following two steps [13]:

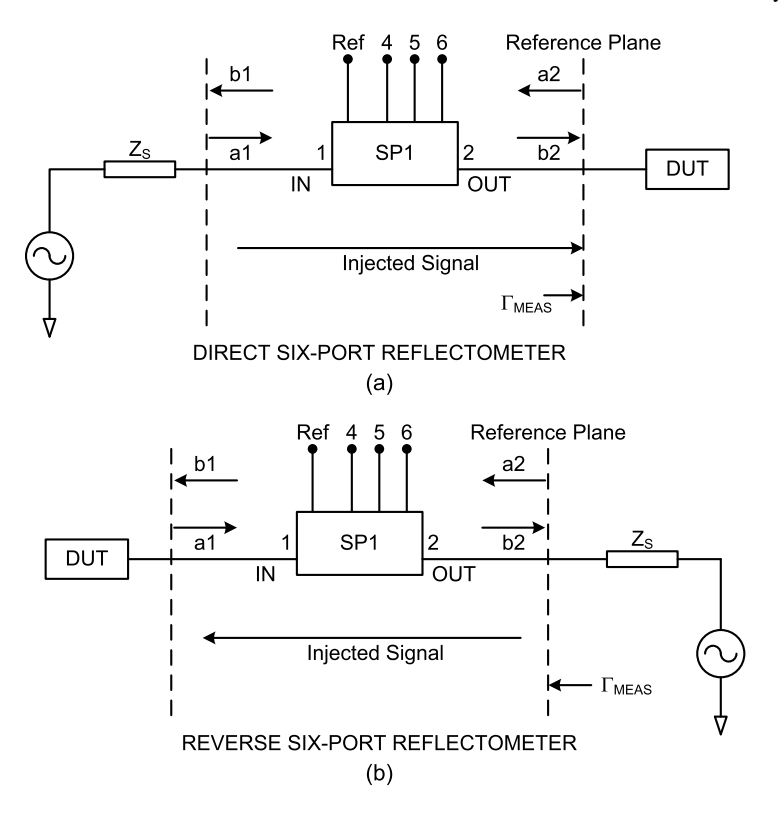


Fig. 4.2 SP reflectometers: (a) direct, (b) reverse configuration [13]; © IEEE 1994

- The common SP to four-port reduction technique using thirteen unknown and well-distributed loads
- A new error box procedure using three well-known standards

The determination of the error box parameters are based on those obtained in the direct configuration and on some analytical manipulations [12]. Figure 4.3 depicts the different steps required for the calibration, de-embedding and measurement procedures of the reverse SP reflectometer. The calibration and de-embedding procedures characterize the SP junction and fix the reference plane for the measurements shown in Figs. 4.3(a) and 4.3(b). A self-calibration approach [14, 15], contrary to an explicit calibration method [11], can be used in this situation.

It is important to note that a -10 dB directional coupler is added to the output in the de-embedding procedure. This coupler allows the use of the SP junction in the reverse configuration, as shown in Fig. 4.3(c). This reverse configuration consists of a generator connected to the output port of the SP reflectometer via the -10 dB directional coupler. The SP junction measures the reflection coefficient of the tuner, which is shifted from the input port (port 1) to the reference plane at the output port (port 2).

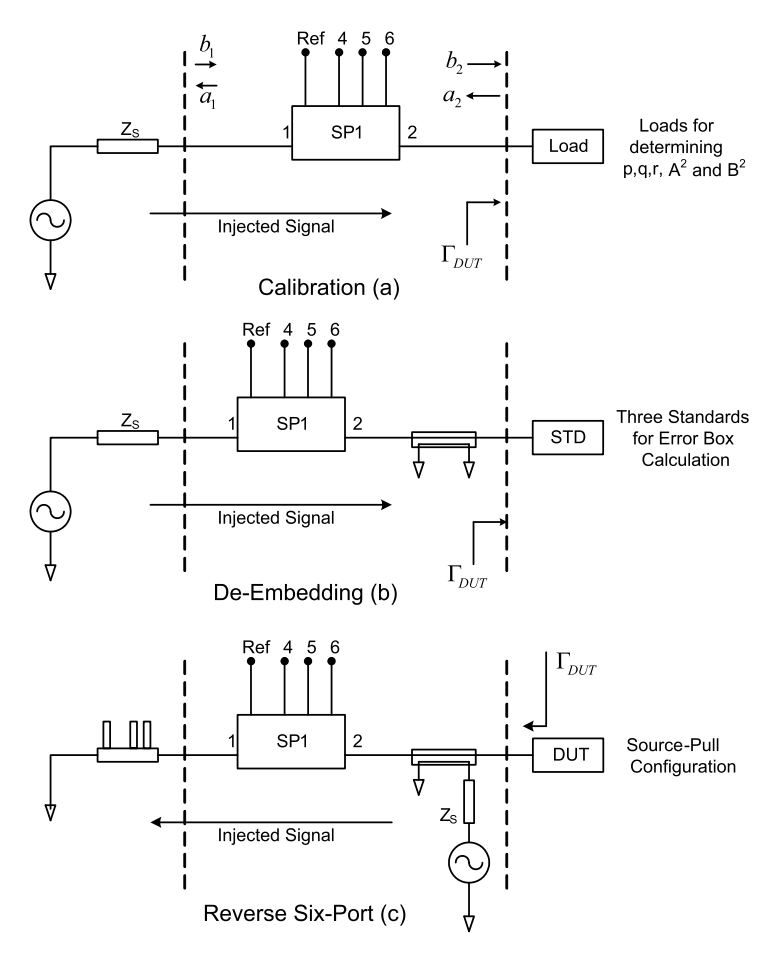


Fig. 4.3 Reverse SP reflectometer measurements: (a) calibration in the direct configuration, (b) de-embedding in direct configuration, (c) measuring in the reverse configuration [13]; ◎ IEEE 1994

The microwave signal injected through the coupler excites the DUT. A part of this signal is reflected toward the SP junction, enabling it to measure the reflection coefficient of the tuner connected to the input port. It is assumed that the SP junction is transparent ($|s_{12}| = |s_{21}| \cong 1$; $|s_{11}| \cong |s_{22}| \cong 0$), in order to minimize the insertion loss and allow the tuner to cover a wider area on the Smith chart. The measured tuner reflection coefficient is shifted to the reference plane defined by the de-embedding procedure at the right-hand side of the SP junction and directional coupler. As the use of an SP reflectometer in a reverse configuration requires calibration of SP reflectometer in a direct configuration, it is essential to establish a relation between the calibration and the de-embedding of the direct and reverse SP junctions.

The power readings at the SP junctions are given by following expressions:

$$P_{Ref} = P_3 = \beta_3 |1 + \xi_3 \Gamma_{DUT}|^2 |b_2|^2 \tag{4.5}$$

$$P_i = \beta_i |1 + \xi_i \Gamma_{DUT}|^2 |b_2|^2, \quad i = 4, 5, 6$$
 (4.6)

where β_i are real constants, ξ_i are complex constants that characterize the SP junction, b_2 is the outgoing wave at the output port (port 2, Fig. 4.3), and Γ_{DUT} is the reflection coefficient of the DUT.

The ratio of P_i/P_3 can be written as [15]:

$$\frac{P_4}{P_{ref}} = \alpha_4 |\Gamma_{DUT} - Q_4|^2 \tag{4.7}$$

$$\frac{P_5}{P_{ref}} = \alpha_5 |\Gamma_{DUT} - Q_5|^2 \tag{4.8}$$

$$\frac{P_6}{P_{ref}} = \alpha_6 |\Gamma_{DUT} - Q_6|^2 \tag{4.9}$$

where α_i and Q_i are complex constants.

The reflection coefficient Γ_{DUT} of the load is determined by the intersection of three circles using the six-to-four port reduction technique [12]:

$$\begin{bmatrix} |\Gamma_{DUT}|^2 \\ \Gamma_{DUT}^* \\ \Gamma_{DUT} \end{bmatrix} = \begin{bmatrix} \alpha_4 & -\alpha_4 Q_4^* & -\alpha_5 Q_4 \\ \alpha_5 & -\alpha_5 Q_5^* & -\alpha_5 Q_5 \\ \alpha_6 & -\alpha_6 Q_6^* & -\alpha_6 Q_6 \end{bmatrix}^{-1} \begin{bmatrix} \frac{P_4}{P_{ref}} - \alpha_4 |Q_4|^2 \\ \frac{P_5}{P_{ref}} - \alpha_5 |Q_5|^2 \\ \frac{P_6}{P_{ref}} - \alpha_6 |Q_6|^2 \end{bmatrix}$$
(4.10)

In Eq. (4.10), the product of rows two and three is equal to row one. Therefore, after simplification of Eq. (4.10), one can obtain the expression given in (4.11):

$$p\left[\frac{P_{4}}{P_{ref}}\right]^{2} + q\left(A^{2}\right)^{2}\left[\frac{P_{5}}{P_{ref}}\right]^{2} + r\left(B^{2}\right)^{2}\left[\frac{P_{6}}{P_{ref}}\right]^{2} + (r - p - q)A^{2}\left[\frac{P_{4}}{P_{ref}}\right]\left[\frac{P_{5}}{P_{ref}}\right]$$

$$+ (q - p - r)B^{2}\left[\frac{P_{4}}{P_{ref}}\right]\left[\frac{P_{6}}{P_{ref}}\right] + (p - q - r)A^{2}B^{2}\left[\frac{P_{5}}{P_{ref}}\right]\left[\frac{P_{6}}{P_{ref}}\right]$$

$$+ p(p - q - r)\left[\frac{P_{4}}{P_{ref}}\right] + q(q - p - r)A^{2}\left[\frac{P_{5}}{P_{ref}}\right]$$

$$+ r(r - p - q)B^{2}\left[\frac{P_{6}}{P_{ref}}\right] + pqr = 0$$
(4.11)

where the real quantities of p, q, r, A^2 and B^2 are the calibration constants related to α_i and Q_i and associated with the physical structure of the SP junction [14]. These parameters are determined by the six-port to four-port reduction formulation.

For each specified frequency, at least five measurements for different distributed loads, leading to a set of five nonlinear equations, are needed to solve this set of equations [14, 15]. The explicit knowledge of the impedance values of these distributed loads is not required in the calculations of p, q, r, A^2 and B^2 .

As mentioned earlier, in practice, thirteen loads are employed to improve the accuracy of the calibration over the entire Smith chart [12]. Furthermore, the elimination of $|b_2|^2$ from the expression makes the quantities of p, q, r, A^2 and B^2 completely independent of the choice of port 1 or port 2 for the test port of the SP junction. Hence, if the power reference and the remaining detection ports are fixed, the calibration of the SP junction, which is aimed at the determination of p, q, r, A^2 and B^2 , normally gives the same value of these parameters for an SP reflectometer used in either a direct or reverse configuration.

4.3.2 Error Box Calculation

Once the calibration constants are determined, the SP reflectometer can measure an embedded reflection coefficient, $w = g(P_i/P_{ref}, p, q, r, A^2, B^2)$, given in Eq. (4.1) at an unknown reference plane [14]. The error box calculation (or de-embedding procedure) determines the three complex constants (c, d and e), which relate w to the reflection coefficient, Γ , at a chosen reference plane with the following relation:

$$w = \frac{d\Gamma + e}{c\Gamma + 1} \tag{4.12}$$

With three well-known standards and their measured embedded reflection coefficients, w_i , given by the SP reflectometer, one can easily find c, d and e by solving the following system of linear equations:

$$w_1 \Gamma_1^{std} c - \Gamma_1^{std} d - e = -w_1$$

$$w_2 \Gamma_2^{std} c - \Gamma_2^{std} d - e = -w_2$$

$$w_3 \Gamma_3^{std} c - \Gamma_3^{std} d - e = -w_3$$

$$(4.13)$$

Referring to Fig. 4.3(c), for a reverse SP configuration, the microwave signal must be injected from the output port (port 2) to the input port (port 1); and, there is a need for three de-embedding standards at the left side of the reference plane, which is physically impossible. To overcome this difficulty, a direct SP error box, as shown in Fig. 4.3(b), with the three standards connected successively to the measuring port at the right side of the reference plane is used. For the reverse SP error box calculation, Eq. (4.13) changes to the following set of equations:

$$w_{1} \frac{c'}{\Gamma_{1}^{std}} - \frac{d'}{\Gamma_{1}^{std}} - e' = -w_{1}$$

$$w_{2} \frac{c'}{\Gamma_{2}^{std}} - \frac{d'}{\Gamma_{2}^{std}} - e' = -w_{2}$$

$$w_{3} \frac{c'}{\Gamma_{3}^{std}} - \frac{d'}{\Gamma_{3}^{std}} - e' = -w_{3}$$

$$(4.14)$$

where the value Γ_i^{std} of the three standards in (4.13) are replaced by $1/\Gamma_i^{std}$ in (4.14), since it is equivalent to using Γ_i^{std} on the left side of the reference plane, which is valid when Γ is referred to the same characteristic impedance (50 Ω).

In practice, it is usually convenient to use a short circuit, an open circuit and a matched load of 50 Ω ($\Gamma=0$) as the three de-embedding standards. Unfortunately, for a reverse SP error box procedure, the matched load needs to be replaced by another standard to avoid the l/Γ singularity. To circumvent this difficulty, one can determine the reverse SP error box by first finding coefficients c,d and e of the conventional error box procedure and then deducing coefficients c',d' and e' of the reverse SP error box using the following relations [12], which are derived by comparing (4.13) and (4.14):

$$c' = 1/c;$$
 $d' = 1/d;$ $e' = 1/e$ (4.15)

Measurement results obtained by a reverse SP calibrated and de-embedded according to the above procedures confirm the validity of this technique [13]. The reverse SP reflectometer is suitable to perform source-pull measurements at the input of the DUT. The measurement technique consists of a signal injected into the DUT via the directional coupler. The reflected signal from the input port of the DUT allows the SP reflectometer to perform measurements in the opposite direction. It should be mentioned that, when the DUT is well matched, the SP reflectometer is not powered and will not operate. However, source-pull measurements are only useful when the DUT input is mismatched.

4.3.3 Discussion

Considering Eqs. (4.12) and (4.15), it can be seen that $\Gamma' = 1/\Gamma$, where Γ' and Γ are the reflection coefficients measured by an SP reflectometer in the reverse and direct configurations, respectively. It may seem that this relation can be equally obtained by just taking $\Gamma = b/a$ and $\Gamma' = a/b$ (where a and b are the incident and reflected waves, respectively), which is not true. For example, in the case of a direct SP measurement, $1/\Gamma_{meas}$ does not lead to the impedance of the generator and has no physical significance. In a direct SP configuration, the DUT is connected to port 2 of the SP reflectometer, which measures the ratio of a_2/b_2 , i.e., the incoming and outgoing waves at the output of the junction (port 2, Fig. 4.2). This ratio represents the reflection coefficient of the DUT seen from the left side of the reference plane. In a reverse SP configuration, the reference plane is always located at port 2, but the output port of the reflectometer becomes port 1.

The reverse SP junction, therefore, measures the ratio of a_1/b_1 rather than that of a_2/b_2 . Ratio a_1/b_1 , which is shifted to port 2 of the SP junction by the deembedding procedure, then represents the reflection coefficient of the test port of the SP reflectometer seen from the load side of the reference plane. Therefore, the inverse value of a_1/b_1 cannot yield the reflection coefficient of the DUT connected to port 2.

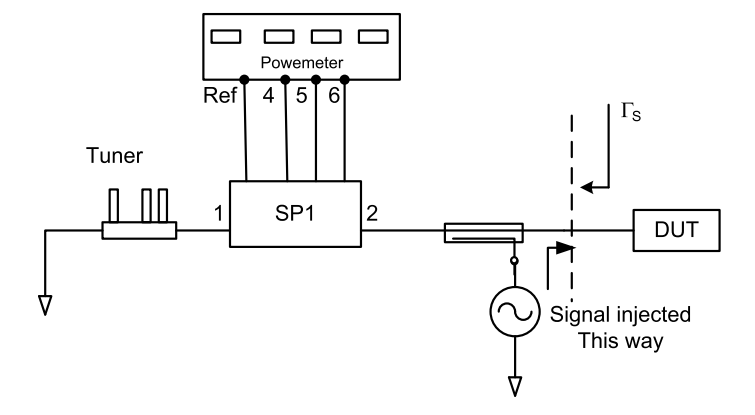


Fig. 4.4 A passive source-pull measurement system based on an SP reflectometer

In summary, reverse SP reflectometer measurements require a conventional calibration procedure to characterize the SP junction and a special error box to fix the reference plane. This error box can be obtained either by using the relations given in Eq. (4.15) or by inverting the actual reflection coefficient, Γ , of the standards used to calculate parameters c, d and e of the direct error box [12].

4.4 SP Based Source-Pull Configuration

The source-pull measurement is aimed at evaluating the linear and nonlinear device performances as functions of source impedance [8]. In source-pull measurement, the input impedance is varied, in order to determine the DUT behavior as a function of source impedance. The source-pull measurement can be carried out using an SP technique, in both passive and active systems.

Figure 4.4 presents a typical passive source-pull system based on an SP reflectometer. In this setup, the input signal is injected to the DUT via a directional coupler, and the source impedance is varied with the help of a stub tuner. The SP reflectometer in such an arrangement is operated in reverse configuration and measures the source impedance seen at the reference plane.

The setup in Fig. 4.5 depicts a typical setup of an active source-pull measurement system based on an SP reflectometer. This setup utilizes a variable attenuator and a variable phase shifter for varying the magnitude and phase of the reflection coefficient being synthesized. The settings of the attenuator and phase shifter can be altered during measurement applications. The SP reflectometer in this setup is used in reverse configuration, allowing for the measurement of the source impedance seen at the reference plane.

It is important to note that the active source-pull configuration has more flexibility and greater accuracy in generating synthesized reflection coefficients, as it is dependent on the settings of the phase shifter and attenuator. The development of

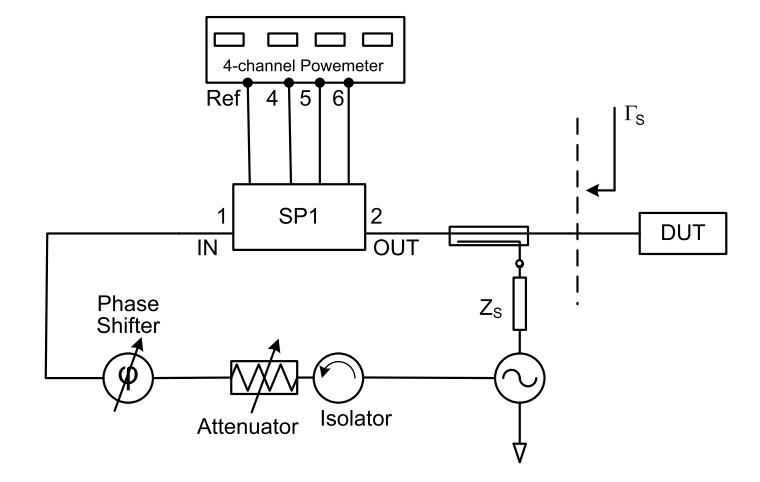


Fig. 4.5 A typical setup of active source-pull measurement system based on an SP reflectometer

more accurate and automated passive tuners, however, has made passive load-pull equally flexible and accurate.

4.5 SP Based Load-Pull Configuration

Both passive and active load-pull measurement setups can be realized using an SP technique. The concept of active and passive load-pull measurements is similar to the more conventional methods described in Chaps. 2 and 3. The only difference lies in the measurement of the reflection coefficient. The more conventional load-pull systems capture the traveling waves directly, whereas the SP based load-pull depends on the ability of the SP reflectometer to measure the de-embedded reflection coefficients.

4.5.1 Passive Load-Pull System

The SP based passive load-pull configuration, as shown in Fig. 4.6, includes two SP junctions, SP1 and SP2, and two tuners, T1 and T2. This configuration allows for the determination of the large-signal input impedance, $\Gamma_{in}(f)$, of the DUT and the power delivered to it, $P_{in}(f)$, by means of SP1, according to Eqs. (4.16) and (4.17). The source impedance seen by the DUT at its input can be changed by varying the stub positions of T1.

$$\Gamma_{in}(f) = b_1/a_1 = \Gamma_1(f) \tag{4.16}$$

$$P_{in}(f) = \frac{1}{2} (|a_1|^2 - |b_1|^2) = \frac{k_1(f) P_{Ref1}(f) (1 - |\Gamma_{in}(f)|^2)}{|1 + c_1(f) \Gamma_{in}(f)|^2}$$
(4.17)

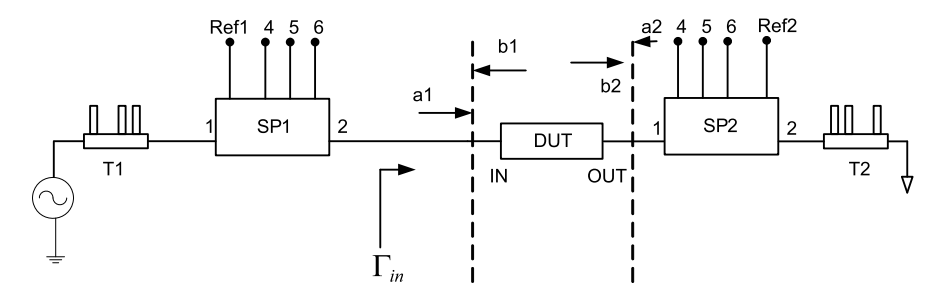


Fig. 4.6 SP based passive load-pull measurement configuration

The determination of source impedance, $\Gamma_s(f)$, is not directly possible using conventional SP calibration and measurement approaches in either a direct or reverse configuration. Therefore a straightforward technique to solve this problem is the pre-calibration of T1 using a vector network analyzer (VNA), which provides the impedance of the tuner's port connected to the DUT as a function of the tuner's stub positions. This technique requires a repeatable and high-quality computer-driven tuner [12].

The reflection coefficient associated with the load impedance and the power absorbed by the load are measured with SP2 operated in direct configuration, where port 1 is connected to the DUT and port 2 to the tuner T2, and can be calculated as follows:

$$\Gamma_{DUT}(f) = a_2(f)/b_2(f) \tag{4.18}$$

$$P_{DUT}(f) = \frac{1}{2} (|b_2|^2 - |a_2|^2) = \frac{k_2(f) P_{Ref2}(f) (1 - |\Gamma_{DUT}(f)|^2)}{|1 + c_2(f) \Gamma_{DUT}(f)|^2}$$
(4.19)

SP2 operated in a direct configuration enables the determination of Γ_{DUT} according to the following expression:

$$\Gamma_{DUT} = \frac{\alpha \Gamma_2 + \beta}{\delta \Gamma_2 + 1} \tag{4.20}$$

where α , β and δ are complex coefficients modeling the two-port network delimited by the reference planes where Γ_{DUT} and Γ_2 are defined and measured.

Coefficients α , β and δ can be determined beforehand using the short, open and load de-embedding technique [12]. Section 4.6 of this chapter provides the necessary equations to de-embed both the reflection coefficient and the power flow measurements between different reference planes and through different error networks.

4.5.2 Active Branch Load-Pull System

The active branch load-pull measurement system is basically an SP network analyzer that also includes two SP junctions, including phase and amplitude signal

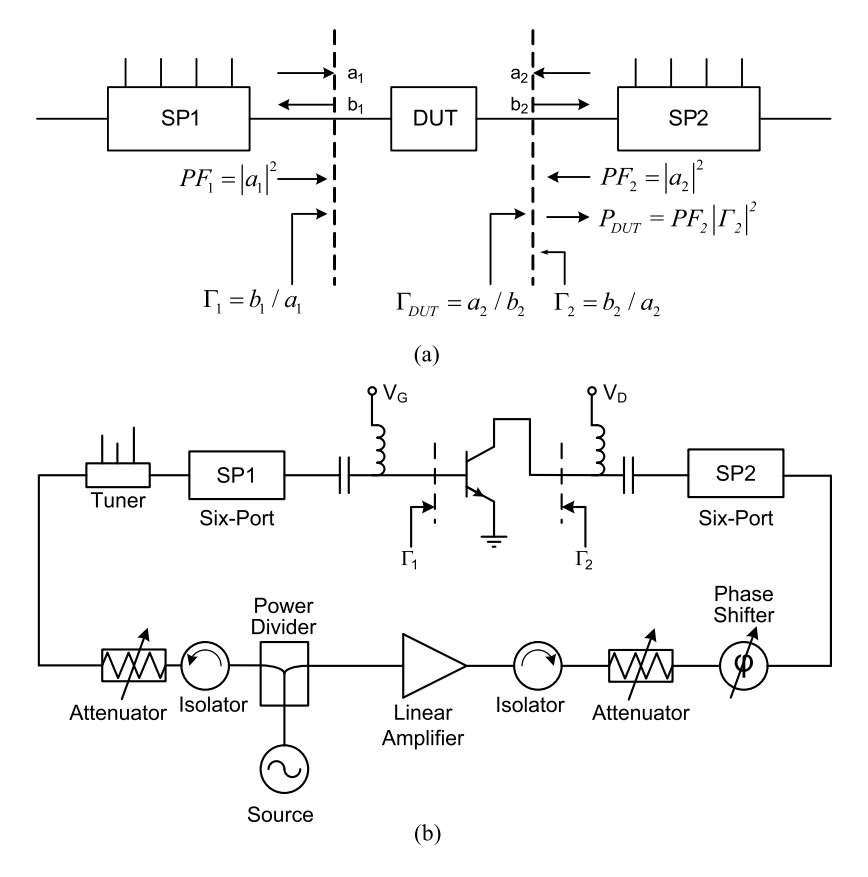


Fig. 4.7 SP based active load-pull (a) measurement configuration and (b) measurement system

controllers inserted in one branch as shown in Fig. 4.7(a). The two SP junctions are calibrated independently for impedance and power flow measurements in a reverse configuration. The active load presented to the DUT, $Z_{DUT}(f)$, can be varied by changing the phase and amplitude of the injected signal, $a_2(f)$, at the output of the DUT.

Equations (4.21) and (4.22) are used to determine the complex value of $Z_{DUT}(f)$ from the measured reflection coefficient, $\Gamma_2(f)$, obtained from the second SP reflectometer, SP2 [12].

$$Z_{DUT}(f) = Z_0 \frac{1 + \Gamma_{DUT}(f)}{1 - \Gamma_{DUT}(f)}$$
(4.21)

$$Z_{DUT}(f) = Z_0 \frac{1 + \Gamma_{DUT}(f)}{1 - \Gamma_{DUT}(f)}$$

$$\Gamma_{DUT}(f) = \frac{1}{\Gamma_2(f)}$$
(4.22)

The power absorbed by the active load-pull setup and presented to the DUT can be calculated using the following expression:

$$P_{DUT}(f) = PF_2(f) |\Gamma_2(f)|^2$$
 (4.23)

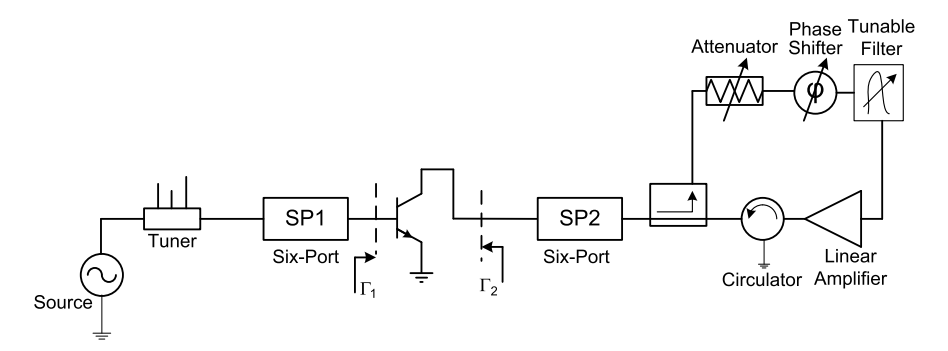


Fig. 4.8 SP active loop load-pull measurement system

4.5.3 Active Loop Load-Pull System

An alternative technique for realizing an SP based active load-pull setup is the active loop method, as shown in Fig. 4.8.

In this technique, a directional coupler, called a loop coupler, is placed at the output of the DUT and takes part of the output signal and sends it to a variable attenuator, a phase shifter, a tunable filter and an amplifier. The loop also uses a circulator to re-inject the amplified signal back to the DUT output. In this configuration, the reflection coefficient provided to the DUT does not change with the device output power if the loop amplifier is in the linear region and has a constant gain [16].

4.6 On-Wafer Load-Pull Measurements

An absolute de-embedding technique for simultaneous impedance and power measurements suitable for on-wafer load-pull measurements of microwave transistors is required [6–9, 17]. This allows extraction of the impedance and power calibration of a network analyzer directly from the embedded reflection coefficient measurements. The de-embedding technique requires two sets of open-short-load (OSL) calibration standards, one coaxial and one non-coaxial, such as a coplanar waveguide (CPW).

An absolute power calibration performed at the coaxial reference planes using a standard power meter are also required for accurate power flow measurement purposes at the coplanar reference planes of the microwave probes needed for on-wafer measurements.

A general formulation of the on-wafer de-embedding problem is illustrated in Fig. 4.9, where (A, B) two error box networks are delimited by the network analyzer reference planes and the coaxial reference planes, and (A', B') are two error box networks delimited by the coaxial reference planes and the coplanar references planes at the tips of the microwave probes. These error boxes are represented by transmission matrices ([A], [B]) and ([A'], [B']).

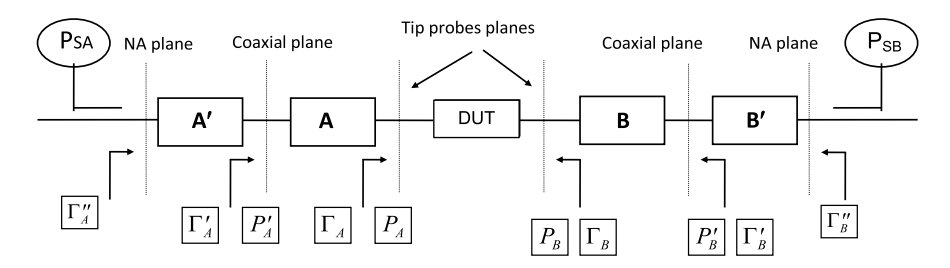


Fig. 4.9 On-wafer impedance and absolute power calibration procedure

In Fig. 4.9, the reflection coefficients at both the coaxial and coplanar reference planes are related to the reflection coefficients at the network analyzer reference planes and coaxial reference planes, respectively, as follows [12]:

$$\Gamma_A' = \frac{\alpha_1 \Gamma_A + \alpha_2}{\alpha_3 \Gamma_A + 1} \tag{4.24}$$

$$\Gamma_A'' = \frac{\alpha_1' \Gamma_A' + \alpha_2'}{\alpha_3' \Gamma_A' + 1} \tag{4.25}$$

$$\Gamma_B' = \frac{\beta_1 \Gamma_B + \beta_2}{\beta_3 \Gamma_B + 1} \tag{4.26}$$

$$\Gamma_B'' = \frac{\beta_1' \Gamma_B' + \beta_2'}{\beta_3' \Gamma_B' + 1} \tag{4.27}$$

where α_i , α_i' , β_i and β_i' are the error box parameters that can be calculated using four OSL calibrations, two at the coaxial references planes and two at the coplanar references planes.

The two power flows at the coaxial reference planes can be calculated as follows [6]:

$$P_A' = \frac{k_A' P_{SA}}{|1 + \alpha_3' \Gamma_A'|^2} \tag{4.28}$$

$$P_B' = \frac{k_B' P_{SB}}{|1 + \beta_3' \Gamma_B'|^2} \tag{4.29}$$

where P_{SA} and P_{SB} are two power readings sampled by directional couplers at coaxial reference planes. These directional couplers can be placed within the network analyzer or can be inserted between the coaxial reference planes and the coplanar reference planes. Power calibration factors k'_A and k'_B can be calculated by connecting an absolute power meter successively at both coaxial reference planes as follows [12]:

$$k_A' = \frac{P_{APM} |1 + \alpha_3' \Gamma_{APM}'|^2}{P_{SAPM} (1 - |\Gamma_{APM}'|^2)}$$
(4.30)

$$k_B' = \frac{P_{BPM}|1 + \beta' \Gamma_{BPM}'|^2}{P_{SBPM}(1 - |\Gamma_{RPM}'|^2)}$$
(4.31)

where P_{APM} and P_{BPM} are the power readings of a standard power meter when it is connected successively to the coaxial references planes, P_{SAPM} and P_{SBPM} are the two sampled power readings, and Γ'_{APM} and Γ'_{BPM} are the measured reflection coefficients when the standard power meter is connected successively to the coaxial reference planes.

The power flows at the coplanar reference planes can be calculated from [12]:

$$P_A = \frac{k_A P_{SA}}{|1 + \alpha'' \Gamma_A|^2} \tag{4.32}$$

$$P_B = \frac{k_B P_{SB}}{|1 + \beta'' \Gamma_B|^2} \tag{4.33}$$

where the value of k_A , k_B , α'' and β'' can be calculated using the following expressions and without any need to perform extra power calibration at the coplanar reference planes [12]:

$$k_A = \frac{|\alpha_1 - \alpha_2 \alpha_3| k_A'}{|1 + \alpha_3' \Gamma_A|^2} \tag{4.34}$$

$$\alpha'' = \frac{\alpha_3 + \alpha_3' \alpha_1}{\alpha_3' \alpha_2 + 1} \tag{4.35}$$

$$k_B = \frac{|\beta_1 - \beta_2 \beta_3| k_B'}{|1 + \beta_2' \Gamma_B|^2} \tag{4.36}$$

$$\beta'' = \frac{\beta_3 + \beta_3' \beta_1}{\beta_3' \beta_2 + 1} \tag{4.37}$$

It is evident that this technique requires two OSL calibration standards, one coaxial and one coplanar, for on-wafer de-embedding. A coaxial power detector is also needed for power flow calibration purposes. The main advantage of this technique is that a second power calibration at the tips of the coplanar probes is not necessary. Such power calibration is almost impossible to perform, because there is no accurate coplanar power sensor that can be connected to the tip of the probes to calculate k_A and k_B .

4.7 Applications of Source-Pull Setup

In certain situations, such as in the characterization of mixers, oscillators or noise measurements, it is more desirable to vary the generator impedance and measure its reflection coefficient than to measure the reflection coefficient of the DUT. These applications cannot be carried out using either an automatic VNA or the conventional SP configuration.

This section contains measurement applications that specifically require an SP reflectometer in reverse configuration. In such a configuration, the microwave source and DUT are placed at the output of the SP junction; and, the measurement reference plane also lies at the output of the SP junction. A tuner is connected at the input of

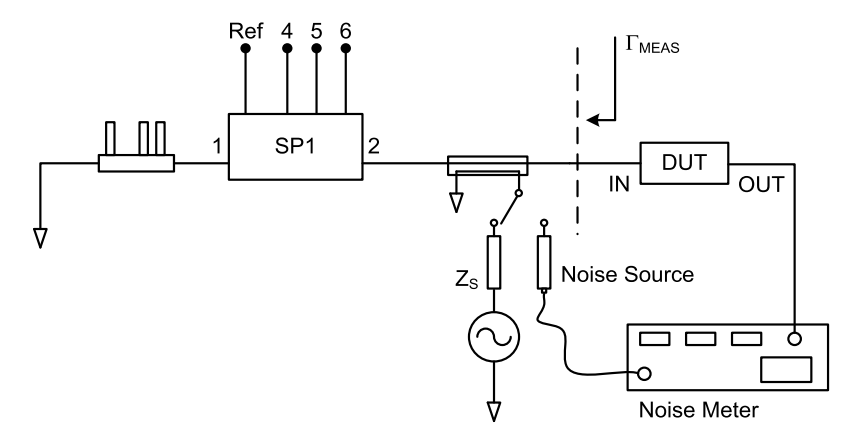


Fig. 4.10 A typical noise characterization setup based on reverse SP source-pull configuration [17], © IEEE 1995

the SP junction. In this arrangement, the SP reflectometer can simultaneously drive the input of the DUT and perform source-pull measurements.

4.7.1 Low Noise Amplifier Characterization

An important part of low noise amplifier design is the measurement of the transistor's noise figure and the determination of noise parameters. Figure 4.10 depicts a typical setup for noise characterization that is based on a reverse SP source-pull configuration [17].

The SP junction is calibrated at all test frequencies, so that it is capable of accurately measuring the source impedances seen by the DUT. During noise measurements, the microwave generator must be turned off when the noise source is on. The noise figure can be determined using the noise source, a noise meter and a standard measurement procedure [18, 19] and calculated using Eq. (4.38). It is important to note that the stability of the DUT is extremely important during characterization.

$$NF_{DUT} = 10\log\left\{\frac{G_{DUT}N_{in} + N_{added}}{G_{DUT}N_{in}}\right\}$$
(4.38)

where N_{added} is the difference between the measured output noise level and the noise level at the input of the device, G_{DUT} is the gain of the DUT, and N_{in} is the available noise power at the input of the DUT.

The advantage of SP source-pull based noise measurement and characterization is that the SP junction in reverse configuration gives the source impedance for any tuner position without any need to pre-calibrate the tuner using a network analyzer. In addition, this setup does not require a highly repeatable tuner.

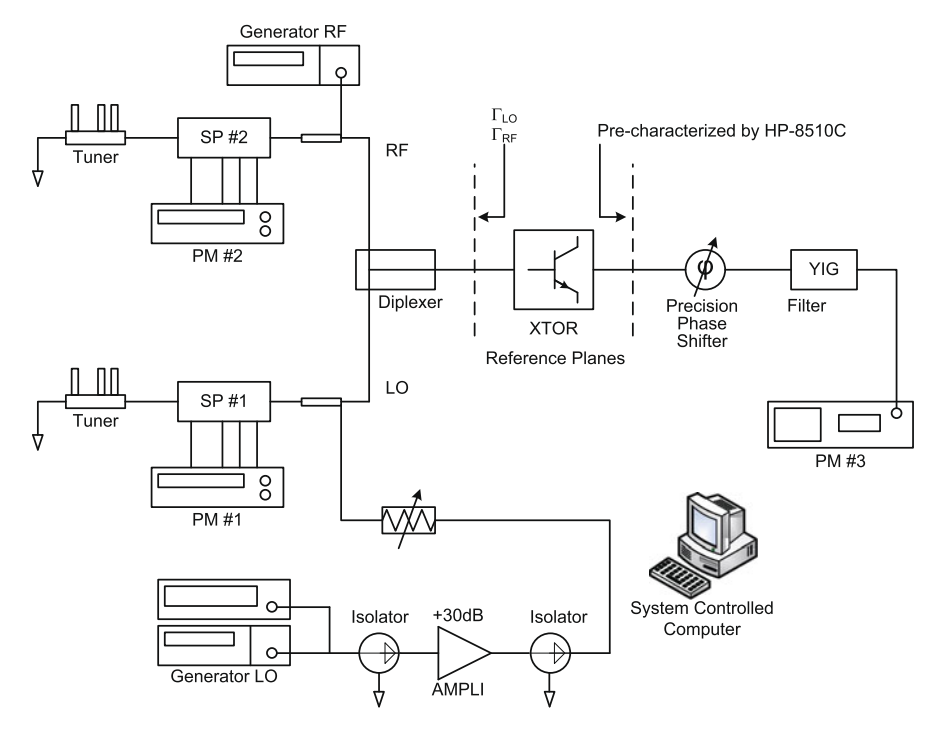


Fig. 4.11 Experimental setup for the source-pull characterization of a MESFET (metal semiconductor field effect transistor) gate mixer [13], © IEEE 1994

4.7.2 Mixer Characterization

The nonlinearity of the active device mainly contributes to the generation of intermodulation products in the mixers. In essence, the behavior of mixers depends strongly on the load and the local oscillator (LO) and RF source impedance terminations. Computer-aided design approaches using harmonic balance methods allow for the optimization of the input and output matching impedances, but the accuracy of the analysis relies on the nonlinear models of the device.

In practice, it is possible to experimentally optimize the input and output impedances simultaneously, by utilizing a reverse SP reflectometer to perform source-pull measurements at the input and a direct SP reflectometer to perform load-pull measurements at the output of the DUT [20] using the setup shown in Fig. 4.11 [13].

The mixer performance can be optimized by increasing its conversion gain, improving the return losses at its ports, and improving its linearity. The advantage of SP source-pull based mixer characterization is that the SP reflectometer in reverse configuration gives the source impedance for any tuner position without any need to pre-calibrate the tuner using a network analyzer. In addition, the tuner repeatability is not important in this setup.

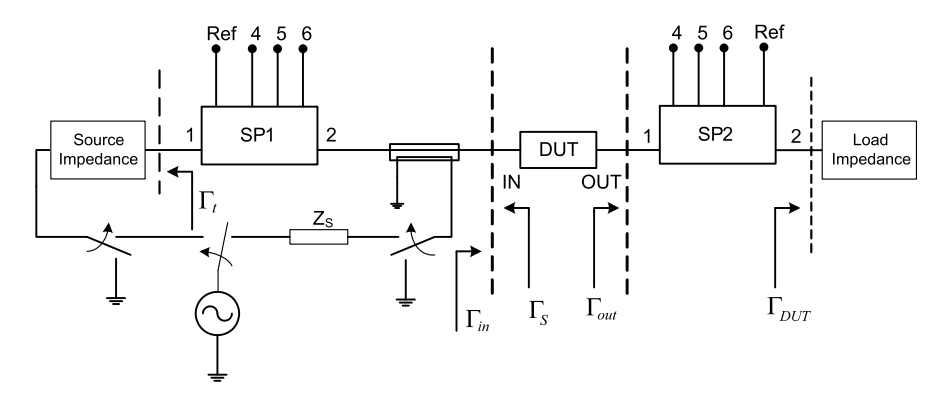


Fig. 4.12 A generic SP based setup for power amplifier characterization

4.7.3 Power Amplifier Characterization

Figure 4.12 shows a generic SP based setup for power amplifier characterization. The use of a reverse SP reflectometer allows for the measurement of the source and load impedances presented to the transistor by the input and output tuning. The measurement setup provides any designer with the ability to experimentally verify the transistor sensitivity in power gain versus termination impedances and, as a consequence, enables the designer to easily optimize the output power, amplifier gain, power-added efficiency (PAE) or the intercept point of the transistor [21].

The expressions given in Eqs. (4.39)–(4.42) are relevant during power amplifier characterization and optimization.

$$P_{out}(f) = |b_2|^2 \left(1 - \left| \Gamma_L(f) \right|^2 \right) \tag{4.39}$$

$$P_{in}(f) = |a_1|^2 \left(1 - \left| \Gamma_{in}(f) \right|^2 \right) \tag{4.40}$$

$$Power_gain = \frac{P_{out}}{P_{in}} \tag{4.41}$$

$$PAE = \frac{P_{out} - P_{in}}{P_{dc}} \tag{4.42}$$

where it is assumed that the dissipated DC power is known to calculate the PAE.

4.8 Oscillator Measurements

The characterization of active microwave devices is generally done by the measurement of S-parameters using automatic vector network analyzers (VNAs). The test port impedance of the VNA seen by the active DUT is the characteristic impedance of the measurement system (50 Ω). It must be noted that this test port impedance cannot normally be varied during measurements. This constraint is not convenient

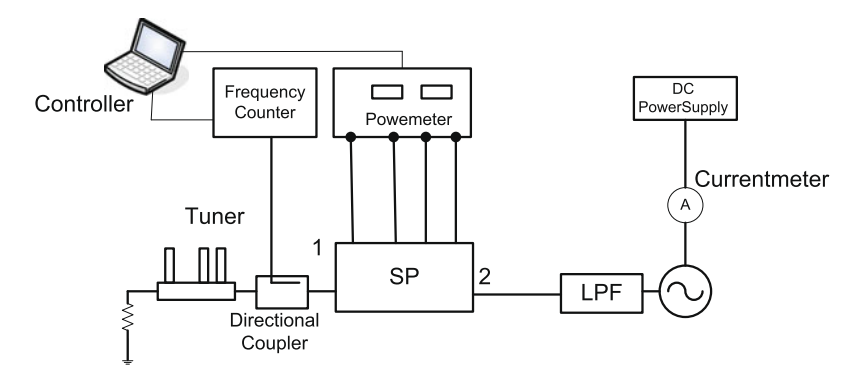


Fig. 4.13 Block diagram of the experimental set-up for source-/load-pull oscillator measurements [22], © IEEE 1992

when measuring active devices having negative resistance (e.g., diodes and transistors), because oscillations may occur during characterization whenever the negative resistance of the DUT exceeds 50 Ω . In such a situation, an SP reflectometer with variable test port impedance could be very effective. There has been a report of a specially designed SP junction that allows variation of the test port impedance over the entire Smith chart, which would find immediate use in large-signal active microwave device characterization, such as microwave source/load-pull oscillator measurements [22].

By using the transparent SP assumption from Eq. (4.4), it can be seen that, in order to obtain a variation of the test port impedance, it is sufficient to vary the internal impedance of the generator [22]. The variation of the test port impedance can be performed with a three-stub tuner inserted between the signal generator and the input port of the SP junction, as shown in Fig. 4.13. The generator and the three-stub tuner can be considered equivalent to a generator with variable test port impedance. Based on the above consideration and by using an appropriate calibration method that is insensitive to the source power level variation and internal source impedance [15], the calibration parameters of the SP reflectometer obtained for given tuner stub positions are valid for any position of the stubs.

Source/load-pull oscillator measurements monitor both the oscillator power and frequency as a function of the load impedance seen by the oscillator under test. The impedance seen by the oscillator can be changed and, at the same time, known over the quasi-entire Smith chart, by simultaneously changing and measuring the test port impedance of the SP junction of the experimental setup shown in Fig. 4.13.

The reflection coefficient associated with the load impedance, Z_{DUT} , seen by the oscillator is directly deduced from the measured reflection coefficient, Γ_{DUT} :

$$Z_{DUT} = Z_0 \frac{\Gamma_{DUT} + 1}{\Gamma_{DUT} - 1} \tag{4.43}$$

The available power, P_a , from the oscillator can be calculated using the SP calibration parameters and the power calibration parameter as follows [23]:

$$P_a(f) = \frac{k(f)P_3(f)|\Gamma_{DUT}(f)|^2}{|1 + c(f)\Gamma_{DUT}(f)|^2}$$
(4.44)

where c(f) is the de-embedding calibration parameter obtained by the SP error box calibration at oscillator frequency f, k(f) is a scalar parameter obtained by the power calibration at f, $P_3(f)$ is the power reading at port 3 of the SP junction at f, and $\Gamma_{DUT}(f)$ is the reflection coefficient measured by the SP reflectometer at oscillator frequency f.

The impedance seen by the oscillator can be simultaneously varied and measured over the quasi-entire Smith chart by changing the tuner stub positions and measuring the test port impedances of the SP junction in Fig. 4.13. The available power from the oscillator under test, P_a , is easily obtained at any tuner stub position and at any operating oscillator frequency using Eq. (4.44). The oscillator frequency is measured using a directional coupler and a frequency meter, as shown in Fig. 4.13. The SP reflectometer is calibrated at discrete frequency points centered around the nominal oscillator frequency. Measurement results of the oscillator characterization using SP based setup are presented in [22].

4.9 AM/AM and AM/PM Measurements

For an accurate and quick design of linear solid-state power amplifiers (SSPAs) and power limiters in hybrid microwave integrated circuit (HMIC) and monolithic microwave integrated circuit (MMIC) technologies, transistor characterization, in terms of phase distortion measurements, is highly recommended [24, 25]. The AM/PM distortion behavior can be described by the relative phase shift versus input power (ϕ vs P_{in}) and the AM/PM conversion coefficient, k, in degrees per dB.

Traditionally, ϕ vs P_{in} characteristics have been obtained using two-carrier stimuli [24, 25], which is a tedious and complex method. Therefore, another alternate method based on an SP active load-pull measurement system, which is less tedious and requires only a single-carrier stimulus to obtain the ϕ vs P_{in} characteristic, is more appropriate for microwave/millimeter wave amplifiers [5]. If needed, k can then be found by derivation of ϕ with respect to $P_{in}(d\phi/dP_{in})$. Actually, the measured ϕ vs P_{in} curve as a phase transfer function is more general for the characterization of the AM/PM distortion performance of microwave transistors and various power amplifiers. In addition, ϕ vs P_{in} characterization is especially useful for microwave limiters, where the variation range of the phase shift over given power ranges beyond saturation is the main concern [26].

This section utilizes a measurement setup that employs the principles of a dual SP network analyzer [5] and the active loading technique [3]. In comparison to heterodyne network analyzers based setups, the advantages of this measurement setup are [12]:

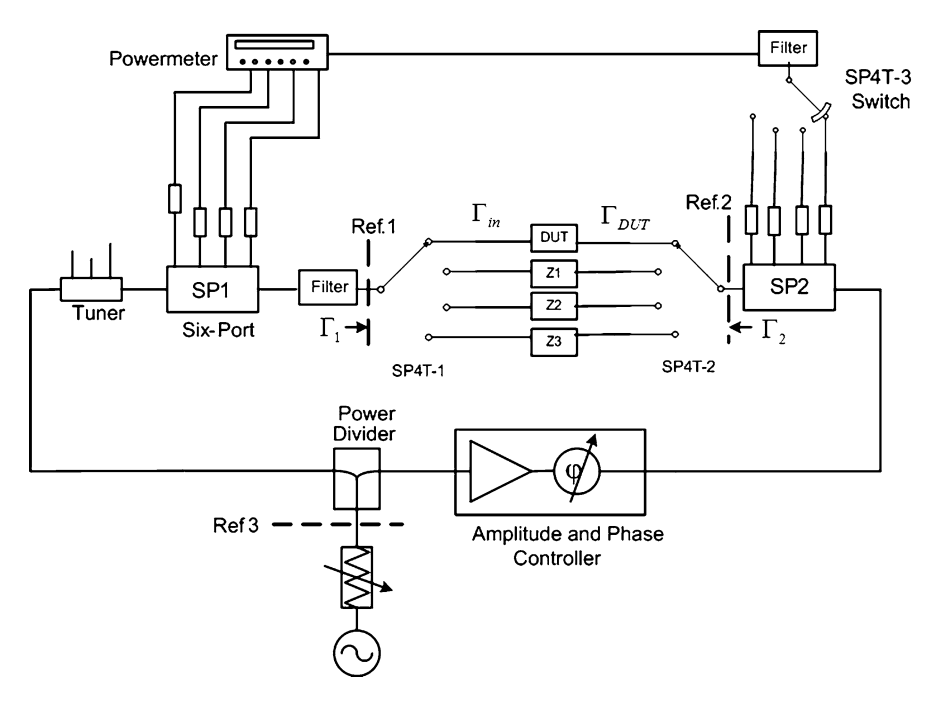


Fig. 4.14 Block diagram of load-pull stage of distortion measurement system [5], © IEEE 1995

- The impedance and power measurements are performed at the actual power level of the device: no extra attenuators are needed for power device characterization.
- The AM/PM characterizations are carried out at the input and output reference planes of the DUT, loaded by arbitrary impedances.
- The cost of this system is much lower than the cost of setups using two automatic network analyzers for AM/PM distortion load-pull measurements.

4.9.1 Principles of Operation

Figure 4.14 shows a block diagram of a distortion measurement system based on an SP reflectometer. As shown, two SP junctions associated with the amplitude and phase controllers are used for active load-pull techniques. Meanwhile, the measurement system can be viewed as a three-port network with reference planes 1, 2 and 3. In order to measure the input-output phase shift of the DUT, three two-port passive standards, Z1, Z2 and Z3, are introduced to obtain the calibration coefficients.

Due to the fact that the three-port network has fixed network S-parameters during the four measurements of the DUT, Z1, Z2 and Z3 for a fixed setting of the amplitude and phase controllers, we can obtain the following equations expressed in matrix format [14].

$$\begin{bmatrix} S_{12}(1) & \Delta(1) - \Gamma_1(1)S_{22}(1) & S_{12}(1)\Gamma_1(1) \\ S_{12}(2) & \Delta(2) - \Gamma_1(2)S_{22}(2) & S_{12}(2)\Gamma_1(2) \\ S_{12}(3) & \Delta(3) - \Gamma_1(3)S_{22}(3) & S_{12}(3)\Gamma_1(3) \end{bmatrix} \begin{bmatrix} x_1 \\ x_2 \\ x_3 \end{bmatrix} = \begin{bmatrix} \Gamma_1(1) - S_{11}(1) \\ \Gamma_1(2) - S_{11}(2) \\ \Gamma_1(3) - S_{11}(3) \end{bmatrix}$$
(4.45)

where

- x_i is related to the S-parameters of the three-port network for a given amplitude and phase setting;
- $\Delta(p) = S_{11}(p)S_{22}(p) S_{12}(p)S_{21}(p)$ and $S_{ij}(p)$, where p = 1, 2 and 3, are the known S-parameters of the three standards, Z1, Z2, and Z3;
- $\Gamma_1(p)$, where p = 1, 2 and 3, are measured by SP1, when the test path is connected to Z1, Z2, and Z3, respectively.

The three two-port standards, Z1, Z2, and Z3, are three coaxial transmission lines with different lengths. These standards have been chosen in such a way that the phase of $S_{12}(1)$, $S_{12}(2)$, and $S_{12}(3)$ deviate from each other by about 120° , in order to ensure a good condition for Eq. (4.45).

The following equation can also be derived [27] to calculate coefficient g, i.e., the ratio of the incident waves at reference planes 2 and 1, as shown in Fig. 4.15:

$$g = \frac{a_2'}{a_1'} = \frac{x_1 + x_3 \Gamma_1(T)}{1 + x_2 \Gamma_2(T)}$$
(4.46)

where x_i are complex constants [12], and $\Gamma_1(T)$ and $\Gamma_2(T)$ are measured by SP1 and SP2, respectively, when the test path is connected to the DUT. Coefficient g has to be de-embedded to the input and output ports of the DUT (reference planes T1 and T2), in order to transfer this parameter to the respective planes, T1 and T2.

Network M and N in Fig. 4.15 consist of single-pole four-throw switches, SP4Tl or SP4T2, bias tees and half parts (input or output) of the test fixture. For these networks, following expressions can be obtained [12]:

$$b_1' = S_{11}^m a_1' + S_{12}^m b_1 (4.47)$$

$$a_1 = S_{21}^m a_1' + S_{22}^m b_1 (4.48)$$

$$a_2 = S_{11}^n b_2 + S_{12}^n a_2' (4.49)$$

$$b_2' = S_{21}^n b_2 + S_{22}^n a_2' (4.50)$$

where S_{ij}^m and S_{ij}^n are the S-parameters of networks M and N, and $\Gamma_1(T) = b_1'/a_1'$ and $\Gamma_2(T) = b_2'/a_2'$.

From the above equations, a_2/a_1 can be deduced and related to coefficient g as given in Eq. (4.51).

$$\frac{a_2}{a_1} = g \cdot \frac{S_{12}^m}{S_{21}^n} \cdot \frac{\Gamma_2(T)S_{11}^n - \Delta^n}{\Gamma_1(T)S_{22}^m - \Delta^m}$$
(4.51)

where $\Delta^m = S_{11}^m S_{22}^m - S_{12}^m S_{21}^m$ and $\Delta^n = S_{11}^n S_{22}^n - S_{12}^n S_{21}^n$. Since switches SP4T1 and SP4T2 are operated under linear conditions, the S-parameters of networks M and N are constants when P_{in} is swept. These S-parameters can be obtained using a de-embedding method, such as the TRL (thru-reflect-line) technique [15].

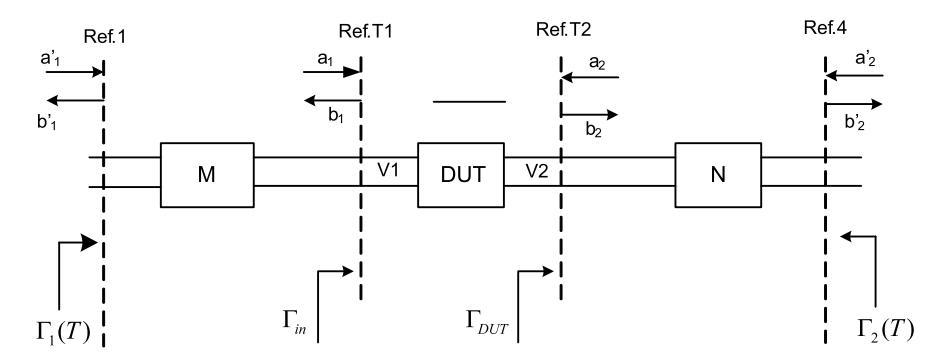


Fig. 4.15 Error box model for de-embedding procedures and computations

According to the definition of normalized waves a and b, the ratio of the voltages at the output and input ports of the DUT for any arbitrary load at a given P_{in} is determined as follows:

$$\frac{V_2}{V_1} = \frac{a_2 + b_2}{a_1 + b_1} = \frac{a_2}{a_1} \cdot \frac{1 + 1/\Gamma_{DUT}}{1 + \Gamma_{in}}$$
(4.52)

where a_2/a_1 is given by Eq. (4.51), Γ_{in} is the input reflection coefficient of the DUT, and Γ_{DUT} is the load reflection coefficient presented to the DUT.

In brief, by means of switches, $\Gamma_1(1)$, $\Gamma_1(2)$, $\Gamma_1(3)$ and $\Gamma_1(T)$, $\Gamma_2(T)$, can be measured when Z1, Z2, Z3 and the DUT are tested in turn for a fixed setting of the amplitude and phase controllers. Meanwhile, it is easy to obtain Γ_{in} , P_{in} , Γ_{DUT} and P_{DUT} with de-embedding techniques, when $\Gamma_1(T)$ and $\Gamma_2(T)$ are measured by SP1 and SP2 [5]. Therefore, the phase shift of the DUT can be determined by Eqs. (4.45)–(4.52). The filter in Fig. 4.14 is used to filter out the harmonics, which ensures that the signals detected by the power meter are only the fundamental components.

The phase distortion, ϕ , is defined as an input-output phase shift, relative to the reference phase shift value at a given lower input power, P_{in}^{ref} (small-signal operation mode), for a given load impedance. Thus, the pertinent relative phase shift corresponds to the change of the angle of V_2/V_1 , given in Eq. (4.52), when P_{in} increases. The measurement of ϕ vs P_{in} of the AM/PM distortion behavior followed by the calculation of the derivative $(d\phi/dP_{in})$ provides the AM/PM conversion coefficient (k).

Similarly, the AM/AM distortion is described by the deviation of the gain from its value at a small-signal input power level. Due to the fact that P_{DUT} and P_{in} are already measured, the operating power gain (G vs P_{in}) can be deduced; and, the AM/AM conversion coefficient can be determined by the derivative of dG_p/dP_{in} [5, 24].

4.9.2 Measurement Procedure

Traditionally, the load-pull measurement has to be carried out for each given P_{in} with variable Γ_{DUT} . This results in a large number of measurements and adjustments. However, the SP based setup given in Fig. 4.14 enables active load-pull measurements by fixing the positions of the amplitude and phase controllers and sweeping the input power. In such a condition, Γ_{DUT} does not change as P_{in} is swept. The amplitude and phase controllers are then adjusted at new positions, and the swept drive measurements are repeated. Finally, the load-pull contours for a given P_{in} can be extracted from the measured data [5].

In addition, characteristics P_{DUT} vs P_{in} and ϕ vs P_{in} for a given Γ_{DUT} can also be obtained from the measured result. The PAE and gain (G_{DUT}) can also be deduced.

In this method, there are mainly four error sources. First, the measurements are made by increasing the input power and not by amplitude modulation as in the actual operation mode. Therefore, the dynamic effect of the amplitude modulation, which becomes more significant by increasing the modulation bandwidth, is ignored. Second, the self-heating effect can introduce a drift in the electrical operational conditions. To minimize this effect, the temperature of the fixture of the transistor investigated needs to be maintained as almost constant by circulating a flux of air during measurements. Third, the measurement accuracy can also be diminished if the power level exceeds the operational range where the switches are linear. In order to circumvent this problem, it is preferable to use mechanical switches instead of solid-state switches when characterizing high-power devices. Fourth, the extraction of the pertinent data from the raw database and the post-measurement calculations using interpolation routines may introduce error. This effect can be reduced by increasing the amount of experimental data.

References

- F.M. Ghannouchi, R. Larose, R.G. Bosisio, Y. Demers, A six-port network analyzer load-pull system for active load tuning. IEEE Trans. Instrum. Meas. 39(4), 628–631 (1990)
- R. Hajji, F.M. Ghannouchi, R.G. Bosisio, Large-signal microwave transistor modeling using multiharmonic load-pull measurements. Microw. Opt. Technol. Lett. 5(11), 580–585 (1992)
- 3. F.M. Ghannouchi, R.G. Bosisio, An automated millimeter-wave active load-pull measurement system based on six-port techniques. IEEE Trans. Instrum. Meas. 41(6), 957–962 (1992)
- 4. F.M. Ghannouchi, F. Beauregard, A.B. Kouki, Large-signal stability and spectrum characterization of a medium power HBT using active load-pull techniques. IEEE Microw. Guided Wave Lett. 4(6), 191–193 (1994)
- F.M. Ghannouchi, G. Zhao, F. Beauregard, Simultaneous load-pull of intermodulation and output power under two tone excitation for accurate SSPA design. IEEE Trans. Microw. Theory Tech. 42(6), 943–950 (1994)
- F.M. Ghannouchi, F. Beauregard, R. Hajji, A. Brodeur, A de-embedding technique for reflection-based s-parameters measurements of HMICs and MMICs. Microw. Opt. Technol. Lett. 10(4), 218–222 (1995)
- R. Hajji, F. Beanregard, F.M. Ghannouchi, Multitone power and intermodulation load-pull characterization of microwave transistors suitable for linear Sspa's design. IEEE Trans. Microw. Theory Tech. 45(7), 1093–1099 (1997)

References 111

 D. Le, F.M. Ghannouchi, Multitone characterization and design of FET resistive mixers based on combined active source-pull/load-pull techniques. IEEE Trans. Instrum. Meas. 46(9), 1201–1208 (1998)

- G. Berghoff, E. Bergeault, B. Huyart, L. Jallet, Automated characterization of HF power transistors by source-pull and multiharmonic load-pull measurements based on six-port techniques. IEEE Trans. Microw. Theory Tech. 46(12), 2068–2073 (1998)
- 10. S. Jia, New application of a single six-port reflectometer. Electron. Lett. 20, 920–922 (1984)
- J.D. Hunter, P.I. Slomo, S-parameter measurements with a single six-port. Electron. Lett. 21, 157–158 (1985)
- 12. F.M. Ghannouchi, A. Mohammadi, *The Six-Port Technique* (Artech House, Norwood, 2009)
- D. Le, F.M. Ghannouchi, Source-pull measurements using reverse six-port reflectometers with application to MESFET mixer design. IEEE Trans. Microw. Theory Tech. 42, 1589–1595 (1994)
- 14. T.E. Hodgetts, G.J. Griffin, A unified treatment of the six-port reflectometer calibration using a minimum of standards, Royal Signals and Radar Establishment Rep. No. B3003, 1983
- G.F. Engen, Calibrating the six-port reflectometer by means of sliding terminations. IEEE Trans. Microw. Theory Tech. 26, 951–957 (1978)
- V. Teppati, A. Ferrero, U. Pisani, Recent advances in real-time load-pull systems. IEEE Trans. Instrum. Meas. 57, 2640–2646 (2008)
- 17. D. Le, F.M. Ghannouchi, Noise measurements of microwave transistors using an uncalibrated mechanical stub tuner and a built-in reverse six-port reflectometer. IEEE Trans. Instrum. Meas. 44(4), 847–852 (1995)
- 18. R.Q. Lane, Determination of device noise parameters. Proc. IEEE 57, 1461–1462 (1969)
- S.V. Bosch, L. Martens, Experimental verification of pattern selection for noise characterization. IEEE Trans. Microw. Theory Tech. 48(1), 156–158 (2000)
- F.M. Ghannouchi, R. Larose, R.G. Bosisio, A new multiharmonic loading method for largesignal microwave transistor characterization. IEEE Trans. Microw. Theory Tech. 39, 986–992 (1991)
- 21. G. Gonzalez, *Microwave Transistor Amplifiers Analysis and Design*, 2nd edn. (Prentice-Hall, Englewood Cliffs, 1996)
- F.M. Ghannouchi, R.G. Bosisio, Source-pull/load-pull oscillator measurements at microwave/mm wave frequencies. IEEE Trans. Instrum. Meas. 41, 32–35 (1992)
- 23. T. Yakabe, M. Kinoshita, H. Yabe, Complete calibration of a six-port reflectometer with one sliding load and one short. IEEE Trans. Microw. Theory Tech. **42**, 2035–2039 (1994)
- K. Koyama, T. Kawasaki, J.E. Hanely, Measurement of AM-PM conversion coefficients. Telecommun. 12(6), 25–28 (1978)
- J.F. Moss, AM-AM and AM-PM measurements using the PM null technique. IEEE Trans. Microw. Theory Tech. MTT-35(8), 780–782 (1987)
- T. Parra, X-band low phase distortion MMIC power limiter. IEEE Trans. Microw. Theory Tech. 41(5), 876–879 (1993)
- R.A. Soares, P. Gouzien, P. Legaud, G. Follot, A unified mathematical approach to two-port calibration techniques and some applications. IEEE Trans. Microw. Theory Tech. MTT-37, 1660–1674 (1989)

Chapter 5 High-Power Load-Pull Systems

This chapter presents the theory and critical issues associated with high reflection load-pull systems required for the characterization and measurement of high power transistor devices. Theory and analysis of the impedance transforming network between the device under test (DUT) and the load-pull system, which is needed to overcome problems encountered in high-power load-pull measurements, is discussed in detail. Finally, multi-tier calibration and de-embedding techniques, which are required for accurate data extraction during high-power DUT characterization, are also presented.

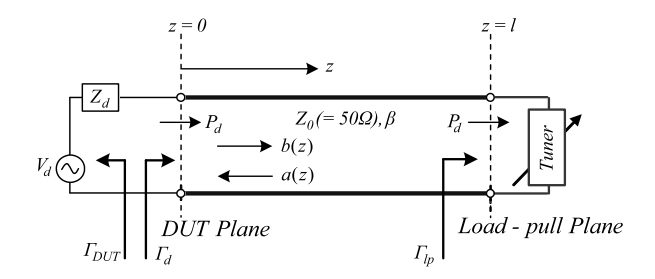
5.1 Introduction

Most high-power radio frequency (RF) transistor devices have extremely low output impedance, in the order of 1 Ω and, in some cases, even less than 1 Ω [1–3]. The measurement and characterization of such devices for optimal performance extraction, therefore, require load-pull systems capable of creating highly reflective loading environments, where the magnitude of the reflection coefficient, $|\Gamma_L|$, which is associated with the load presented to the transistor, approaches unity. The requirement to establish highly reflective environments puts severe constraints on traditional passive and active load-pull systems [4, 5]; and, as a result, these systems are limited in their use for the characterization and measurement of high-power devices.

5.2 Limitations of Existing Load-Pull Systems

The major drawback of the standard passive load-pull system is the limited maximum achievable reflection coefficient $|\Gamma_L|$ (maximum usually around 0.75–0.85), due to the inherent insertion losses in the load tuner, measurement network and test fixture [6]. Several developments, namely the quarter wave transformer technique,

Fig. 5.1 Generic model of a passive load-pull characterization setup



pre-matched tuning technique and active load-pull technique [7–14], have been incorporated to enhance the tuning range of the load-pull test benches to meet the demands of high-power device characterization. The probing couplers [15], which are used to sample and capture the incident and reflected traveling waves at the DUT plane, are primarily used in the characterization of on-wafer devices. Direct measurement of traveling waves at the DUT plane by probing couplers enables the enhancement in the tuning range of the load reflection coefficient.

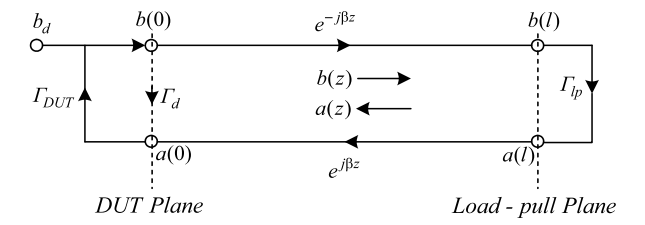
Tuning range enhancement is just one aspect in a high-power load-pull measurement technique. The large mismatch between the output impedance of the high-power DUT and the measurement system environment also creates a high voltage standing wave ratio (VSWR) in the measurement system. A high VSWR can generate very large voltage and current peaks in the measurement system that can damage the DUT and the measurement system. Furthermore, the load-pull power, P_{LP} , requirement in active load-pull systems increases manifold, due to the large impedance mismatch between the output impedance of DUT and the load-pull test set. The increase in P_{LP} limits the usefulness of active load-pull systems in practical applications due to increased cost.

In addition, the high impedance mismatch between the load-pull systems and the DUT also leads to increased measurement uncertainty [16], which is caused by the limitations of automatic vector network analyzers (VNAs) in characterizing "high-reflection low-loss" two-ports, such as tuners. According to the well known rule of thumb in metrology, the ratio between reference system impedance (usually $50~\Omega$) and DUT output should always remain less or equal to $10~(VSWR \le 10:1~or~|\Gamma_L| \le 0.8)$ in order to obtain reliable load-pull measurement data [16]. In highly reflective load-pull measurement systems, however, the required $|\Gamma_L|$ approaches unity, thereby leading to measurement uncertainty.

5.2.1 Problems Due to High Standing Waves

The impact of a high VSWR on the load-pull system performance, in passive as well as active systems, can be analyzed by considering a generic model of a passive load-pull system, as shown in Fig. 5.1, and the associated signal flow model, as depicted in Fig. 5.2. It can be observed that the DUT, which is represented by an equivalent

Fig. 5.2 Signal flow model representing a passive load-pull model



voltage source, V_d , and a series impedance, Z_d , is connected to the passive tuner via a 50 Ω lossless transmission path of length l.

In a standard load-pull characterization setup, a passive network that consists of measuring couplers is used for capturing the incident and reflected traveling waves at the DUT ports; therefore, it always has a transmission path between the DUT and the tuner. The terms Γ_d and Γ_{lp} represent the load reflection coefficients at the DUT and load-pull planes, respectively. The DUT output reflection coefficient is represented by Γ_{DUT} ; b_d is the maximum amplitude of the power wave generated by the DUT; β is the propagation constant along the transmission path; and, b(z) and a(z) are the incident and reflected waves, respectively.

Through the application of the standard transmission line theory, the relationship for the average available power from the DUT, P_{av} , transferred at the DUT plane can be expressed by Eq. (5.1), as follows:

$$P_{av} = \frac{|b_d|^2}{2} \left(1 - |\Gamma_{DUT} \Gamma_d| \right) \tag{5.1}$$

The DUT delivers the maximum available power, P_d , at the DUT plane when it is conjugately matched to the tuner transmission path, $\Gamma_{DUT} = \Gamma_d^*$.

$$P_d = P_{av}^{max} = \frac{|b_d|^2}{2} (1 - |\Gamma_d|^2)$$
 (5.2)

The voltage propagating on the transmission path, with the characteristic impedance, Z_0 , of 50 Ω , is related to the respective incident and reflected traveling waves as [17]:

$$V(z) = \sqrt{Z_0} (b(z) + a(z))$$
 (5.3)

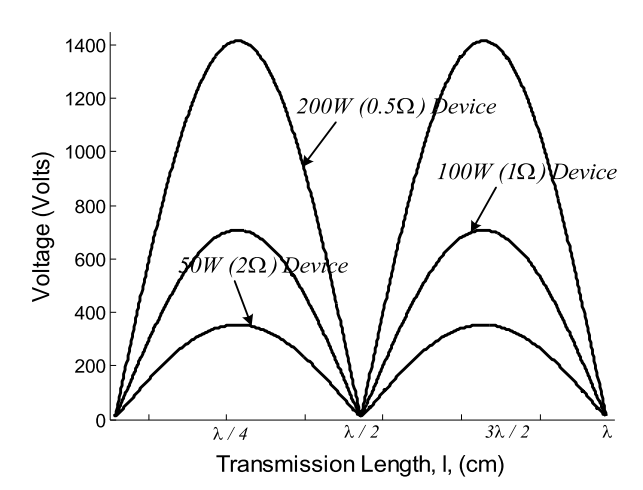
where the incident and reflected traveling waves, b(z) and a(z), are given by Eqs. (5.4) and (5.5).

$$b(z) = b(0)e^{-j\beta z} \tag{5.4}$$

$$a(z) = a(0)e^{j\beta z} \tag{5.5}$$

where b(0) and a(0) are the incident and reflected traveling waves at the DUT plane. The signal flow model in Fig. 5.2 can be used to derive the relationship between the power wave, b_d , and the incident wave, b(0), at the DUT plane, as given in Eq. (5.8).

Fig. 5.3 Propagating voltage on the transmission path for three DUTs with power ratings of 200 W, 100 W and 50 W



$$a(0) = b(0)\Gamma_d (5.6)$$

$$b(0) = b_d + a(0)\Gamma_{DUT}$$
 (5.7)

$$b(0) = \frac{b_d}{1 - |\Gamma_d|^2} \tag{5.8}$$

Equations (5.2) to (5.8), when solved and simplified, provide the voltage expression on the transmission path given in Eq. (5.9).

$$V(z) = \sqrt{\frac{2Z_0 P_d}{1 - |\Gamma_d|^2}} \left(1 + |\Gamma_d| e^{2j\beta z} \right) e^{-j\beta z}$$
 (5.9)

The propagating voltage, V(z), plotted using Eq. (5.9), along the transmission path for 200 W, 100 W and 50 W devices with the respective assumed low output impedances of 0.5 Ω , 1 Ω and 2 Ω and a characteristic system impedance, Z_0 , of 50 Ω is given in Fig. 5.3. It can be observed that massive voltage peaks, which are dependent on the power rating of the DUTs, are generated that can cause breakdowns between the transmission path and the ground, due to the "corona effect" [18]. This has the potential to damage the tuner, couplers or bias tees used in the measurement setup and/or the DUT itself. As a result, the load-pull setup in its standard configuration is not suitable for characterization and measurement of high-power DUTs with inherently low output resistance values.

The generated voltage peaks on the transmission path can be quantified by considering the magnitude of the voltage, V_{max} , in Eq. (5.10), which is derived from the expression of the propagating voltage in Eq. (5.9).

$$V_{max} = \sqrt{2P_d Z_0(VSWR)} \tag{5.10}$$

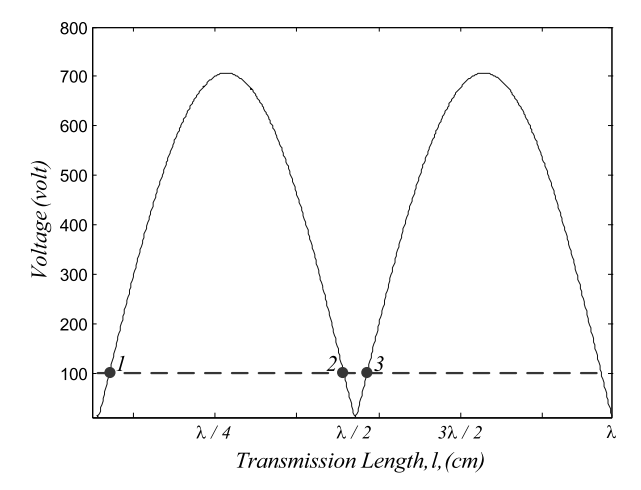
where

$$VSWR = \frac{1 + |\Gamma_d|}{1 - |\Gamma_d|} \tag{5.11}$$

Table 5.1 VSWR and maximum generated voltage for devices with low output impedances in the measurement system transmission path

Device output power (watts)	Assumed output impedance (Ω)	VSWR	V _{max} (volt)
50	2	24.974	353.37
100	1	49.891	706.34
200	0.5	99.503	1410.69
250	0.4	124.786	1766.25
400	0.25	199	2821.35
500	0.2	249	3528.46

Fig. 5.4 Propagating voltage in a passive load-pull measurement system when characterizing a $100 \text{ W} (1 \Omega)$ device at 2.1 GHz. Similar curves can be obtained for an active load-pull system

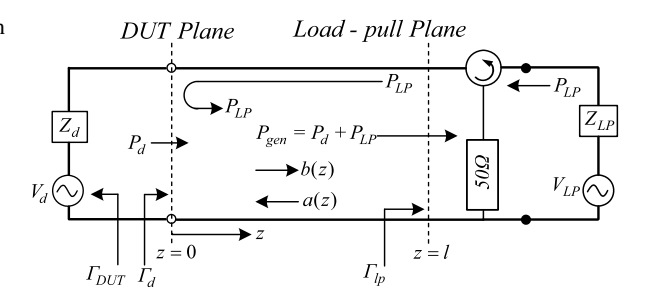


The data in Table 5.1 are the estimated peak voltages, V_{max} , along the measurement system transmission path obtained from Eq. (5.10) for transistor devices with arbitrarily assumed low impedances. For a simpler analysis, only real impedances have been assumed. It is apparent that a high VSWR in the load-pull setup used for characterization of high-power devices can generate very high voltages in the transmission path, which can damage the DUT and/or the measurement system.

It can be concluded from the above analysis that the tuner should be placed at the DUT port, in order to avoid high voltage peaks; however, this is not feasible in practical applications. For example, the propagating voltage, V(z), along the transmission path for a 100 W device at a frequency of 2.1 GHz (as shown in Fig. 5.4) can be as high as 707 V. To avoid this peak, the length of the transmission path between the DUT and the tuner should correspond to position 1 shown in Fig. 5.4, so that the peak voltage never goes above 100 V, which is assumed to be the maximum tolerable voltage for a DUT of 100 W with a 1 Ω output impedance.

The length of the transmission path corresponding to position 1 is, however, too small at 2.1 GHz; therefore, it is not feasible to place wave sampling apparatuses, such as directional couplers, between the DUT and the load tuner, if the length of the transmission path corresponding to position 1 is chosen. As a result, the closest the

Fig. 5.5 Generic model of an open-loop active load-pull measurement setup



tuner can be placed to the DUT corresponds to either to position 2 or 3 in Fig. 5.4, thus introducing at least one voltage peak. The increasing operating frequency increases the number of voltage peaks in the transmission path, due to decreasing wavelength. Therefore, the standard active or passive load-pull approaches that employ $50~\Omega$ transmission lines between the DUT and the load tuner are not suitable for high-power device characterization at high frequency.

5.2.2 Problem of Large Load-Pull Power

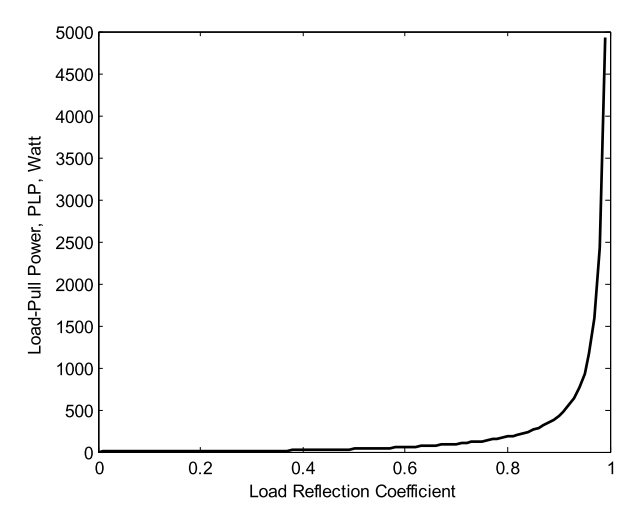
In an active load-pull technique, the reflected signal can be either from an external signal generator [19, 20] or a modified form of the DUT generated signal [21–23]. In both cases, the synthesis of the desired reflection coefficient at the DUT plane is dependent on the ability of the load-pull components to provide the necessary load-pull power, P_{LP} . In theory, active load-pull systems can synthesize reflection coefficients at and beyond the boundary of the Smith chart, but this requires the load-pull components to reflect a P_{LP} of high magnitude, which creates a bottleneck in the operation of the system.

The requirement of P_{LP} for desired reflection coefficient synthesis at the DUT plane can be analyzed through a generic model of an active load-pull setup, as shown in Fig. 5.5. The DUT is represented by an equivalent voltage source, V_d , and a series impedance, Z_d . The terms V_{LP} and Z_{LP} represent the voltage and the impedance of the active load-pull tuner, respectively. In this model, Z_{LP} is set to the system characteristic impedance, Z_0 , of 50 Ω , while the circulator isolates the DUT and the active load-pull tuner. The circulator should be as close as possible to the DUT in order to eliminate the occurrence of voltage peaks in the measurement system. In reality, the presence of a circulator requires an additional length to the transmission path, consequently leading to an increased possibility of voltage peak occurrence in the measurement system.

From the load-pull model in Fig. 5.5, one can derive the expression for the reflection coefficient at the load-pull plane, Γ_{lp} , which is given by the ratio of the reflected wave, a(z), to the incident wave, b(z), as:

$$\Gamma_{lp} = \frac{a(z)|_{z=l}}{b(z)|_{z=l}} = \sqrt{\frac{P_{LP}}{P_{gen}}}$$
(5.12)

Fig. 5.6 Load-pull power, P_{LP} , requirements as a function of the load reflection coefficient, Γ_{lp} , at the load-pull reference plane for a 100 W (1 Ω) device



where

$$P_{gen} = P_{LP} + P_d \tag{5.13}$$

The reflection coefficient at the DUT plane, Γ_d , is related to the reflection coefficient at the load-pull plane by the relationship given in Eq. (5.14).

$$\Gamma_{lp} = \Gamma_d e^{-2j\beta z} \tag{5.14}$$

Simplification of Eqs. (5.12), (5.13), (5.14) provides the relationship between the desired reflection coefficient at the DUT plane, Γ_d , and the required load-pull power, P_{LP} , to synthesize it.

$$P_{LP} = P_d \frac{|\Gamma_d|^2}{1 - |\Gamma_d|^2} \tag{5.15}$$

Fig. 5.6 is a plot of Eq. (5.15) and relates the load-pull power, P_{LP} , with the reflection coefficient at the DUT plane, $|\Gamma_d|$. It can be observed that the P_{LP} required for load-pulling of the assumed 100 W device having 1 Ω output impedance (i.e. load reflection coefficient of 0.96) is around 1175 W. The required P_{LP} of 1175 W is, however, impractical for load-pulling of a 100 W DUT, due to the cost involved in building such an active load-pull setup. It is these incurred costs that severely limit the use of active load-pull systems in their standard configuration [19–23] for the characterization of high-power DUTs in the order of 100 W.

5.3 High-Power Load-Pull

An appropriate load-pull for high-power device characterizations should be capable of synthesizing a high reflection factor and, at the same time, should possess some mechanism to minimize the VSWR. In the case of the active load-pull setup,

Fig. 5.7 Mechanical drawing of a pre-matched load-pull tuning setup [25] (diagram courtesy of Focus Microwaves)

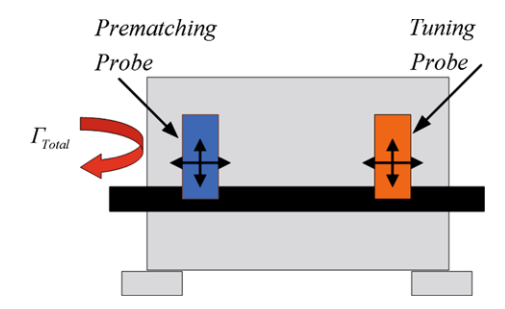
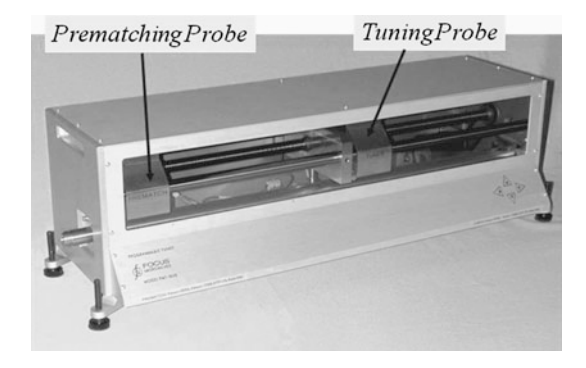


Fig. 5.8 Photograph of a commercial pre-matching load-pull tuner (photo courtesy of Focus Microwaves)



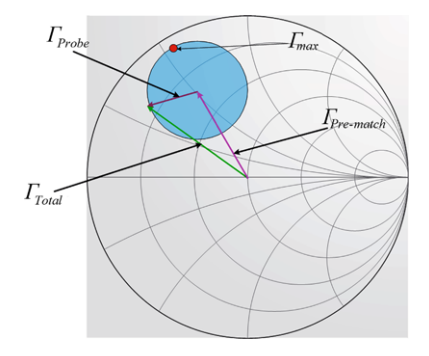
there is an additional requirement to minimize the load-pull power, P_{LP} , for the synthesis of the desired reflection coefficient. There is no generic approach to overcome these problems concurrently; however, techniques have been developed that are able to successfully fulfill the requirements of high-power device characterization and measurement problems. The pre-matched tuning technique [10, 11], the enhanced loop tuner [24], the quarter wave transformation technique [7] and the broadband impedance transformer technique [19] are the most common approaches in addressing the high-power device measurement and characterization problem.

5.3.1 Pre-matching Technique

Figure 5.7 shows a diagram of a pre-matched load-pull tuning setup. The pre-matched load-pull tuners consist of two independent RF probes, called pre-matching and tuning probes, respectively, placed side-by-side on a central conductor. These two probes are capable of individually generating smaller reflection coefficients, which combine together to enhance the maximum achievable reflection coefficient. Figure 5.8 depicts a photograph of a commercial pre-matching tuner.

In this technique, the reflection coefficients generated by the pre-matching probe, $\Gamma_{Pre-match}$, and the tuning probe, Γ_{Probe} , combine together to create the eventual load reflection coefficient, Γ_{Total} , given by Eq. (5.16).

Fig. 5.9 Smith chart demonstrating the concept of the total reflection coefficient, Γ_{Total} , generation by a pre-matching load-pull setup (diagram courtesy of Focus Microwaves)



$$\Gamma_{Total} = \Gamma_{Pre-match} + \frac{S_{12}S_{21}\Gamma_{Probe}}{1 - S_{22}\Gamma_{Probe}}$$
(5.16)

where S_{12} , S_{21} , and S_{22} are the S-parameters of the pre-matching tuner.

A practical pre-matched load-pull setup, however, utilizes a low-loss central conductor; therefore, it is reasonable to assume that $S_{21}S_{12}$ approaches unity. Furthermore, the term S_{22} can be assumed to be approaching zero, considering that there is no discontinuity in the central conductor. In such a situation, the reflection coefficient, Γ_{Total} , generated by the pre-matched load-pull setup is given as:

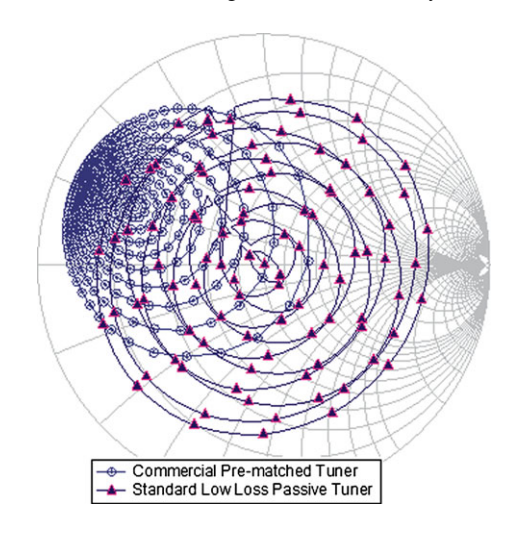
$$\Gamma_{Total} = \Gamma_{Pre-match} + \Gamma_{Probe}$$
 (5.17)

The concept of reflection coefficient synthesis by pre-matched load-pull setup using Eq. (5.17) is illustrated in Fig. 5.9. It can be observed that initially the pre-matching probe moves the matched condition from 50 Ω to some other desired region of the Smith chart. This position of the pre-matching probe defines the reflection coefficient of the pre-matching probe, $\Gamma_{Pre-match}$, as shown in the figure. The movement of the tuning probe in horizontal and vertical positions then generates the reflection coefficient of the tuning probe Γ_{Probe} , whose vector addition with $\Gamma_{Pre-match}$ results into the overall synthesized reflection coefficient, Γ_{Total} . For certain horizontal and vertical positions of the tuning probe, the overall synthesized reflection coefficient achieves the highest value, denoted by Γ_{max} .

It is evident from Fig. 5.9 that the overall synthesized reflection coefficient by the pre-matching load-pull setup can be significantly higher for some horizontal and vertical settings of the tuning probe. For example, pre-matched passive load-pull systems [10, 11] can synthesize reflection coefficients in the order of 0.90–0.92 magnitudes, which are higher than the maximum achievable reflection coefficient from a standard passive tuner, as can be seen in Fig. 5.10.

The pre-matching technique possesses an advantage over the quarter wave transformer and broadband impedance transformer techniques (described in Sects. 5.3.3 and 5.3.4, respectively), due to its capability of synthesizing any reflection coefficient within the maximum achievable value. As a result, this technique is better suited for high throughput load-pull measurement applications, in which a number of optimal reflection coefficients need to be synthesized without changing the measurement setup, such as the characterization and measurement of different DUTs

Fig. 5.10 Comparison of the achieved reflection coefficients using a standard passive tuner and a commercial pre-matched tuner at 2.425 GHz [37], © IEEE 2010



at varying frequencies. Additionally, the high bandwidth of the pre-matched loadpull setup, which is about one decade, makes it suitable for high-power harmonic load-pull applications.

The major drawback of this technique, however, is the strong dependence of the accuracy of the synthesized reflection coefficients on interpolation algorithms when the desired reflection coefficients lie farther from the calibration grid [26]. Prior characterization of the pre-matched tuner with a dense calibration grid improves the accuracy in the synthesized reflection coefficient. In some cases, separate prior characterizations of tuners for distinct DUTs or different operating frequencies also improve the accuracy in the synthesized reflection coefficients. However, in both these scenarios, the overall measurement throughput gets reduced. Additionally, the maximum achievable reflection coefficients get reduced, due to the adapters and the insertion loss of the fixture. For example, a 0.1 dB insertion loss reduces the reflection coefficient from 0.92 to 0.89, which is an increase in the synthesizable impedance from 2.08 Ω to 2.91 Ω [27].

5.3.2 Enhanced Loop Architecture

An enhanced loop load-pull setup consists of an impedance tuner and a passive loop cascaded together, as shown in Fig. 5.11 [24]. The impedance tuner, *Tuner2*, is a standard low-loss passive tuner, whereas the passive loop is built using a high directivity circulator and a coupler. In this technique, the passive loop first moves the matched point farther from 50 Ω by an amount Γ_{LOOP} , which is regulated by the length of the cable, L_2 , and the position of probes in the impedance tuner. The impedance tuner then adds its contribution to the reflection coefficient generated by the passive loop, in order to synthesize the high reflection coefficient at the DUT

Fig. 5.11 Block diagram of an enhanced loop load-pull tuner [24], © IEEE 2010

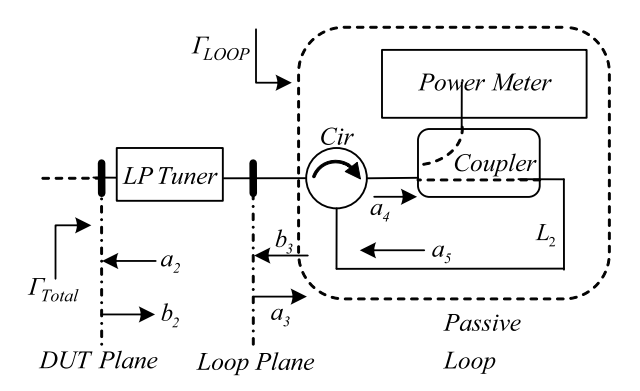
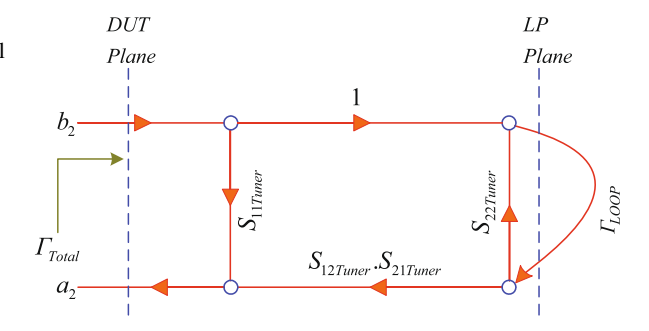


Fig. 5.12 Signal flow graph of an enhanced loop load-pull tuner [24], © IEEE 2010



plane. The signal flow graph in Fig. 5.12 illustrates the mechanism of reflection coefficient synthesis by this technique.

The signal flow graph clearly identifies the dependence of the reflection coefficient synthesized at the DUT plane, Γ_{Total} , on the contributions from the impedance tuner and the passive loop. The expression for Γ_{Total} derived from the above signal flow graph is given as:

$$\Gamma_{Total} = \frac{a_2}{b_2} = S_{11TUNER} + \frac{S_{12TUNER}S_{21TUNER}\Gamma_{LOOP}}{1 - S_{22TUNER2}\Gamma_{LOOP}}$$
(5.18)

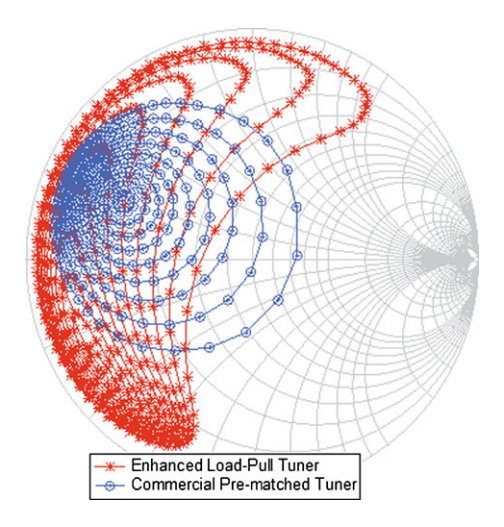
where

$$\Gamma_{LOOP} = \frac{b_3}{a_3} = |\Gamma_{LOOP}|e^{-2j\beta L_2}$$
(5.19)

where the term Γ_{LOOP} is the reflection coefficient generated by passive loop and is a complex term dependent on the loop component characteristics, i.e. the transmission factors of the coupler and the circulator, the phase velocity, β , of the traveling waves, and the length of the loop, L_2 .

The length of the loop and, hence, the reflection coefficient can be changed by employing cable of appropriate lengths. It has been found that cables of only three different lengths, L_2 , can cover the entire Smith chart [24]. The need for only three distinct cables results in reduced calibration and measurement time of the enhanced loop load-pull system, compared to the pre-matched load-pull techniques, where

Fig. 5.13 Comparison of achievable load reflection coefficient Γ_L using a commercial pre-matched tuner and the loop enhanced tuner [24] at 2.425 GHz, © IEEE 2010



separate pre-characterization of tuner is required for covering the desired Smith chart region for the specified DUT. Additionally, the maximum synthesizable reflection coefficients of 0.97 using the enhanced loop load-pull system is higher than the corresponding maximum values using the pre-matched load-pull system, as shown in Fig. 5.13.

In this technique, the insertion loss of the fixture also reduces the maximum synthesizable reflection coefficient, as in the pre-matched load-pull system [27]. Nonetheless, this technique is well suited for triplexer-based harmonic load-pull systems, when the insertion loss of the triplexer and fixture are small [28]. In such a situation, the all-passive harmonic load-pull setup can synthesize mutually independent high reflection coefficients at fundamental and harmonic frequencies.

5.3.3 Quarter Wave Transformer Technique

The pre-matching and enhanced loop techniques are limited in their application, due to two main reasons:

- The tuning ranges of these architectures are reduced by the adapters and the insertion loss of the associated fixture.
- The high loss between the DUT and the tuner makes the associated measurement error unpredictably high.

In many fundamental characterizations of high-power DUTs, the region of approximate optimal impedance lies is known. Therefore, in such applications, high reflection coefficient tuning architectures are an unnecessary expense. Instead, the inclusion of an impedance transforming network between the DUT and the tuner has a significant advantage in such applications, as it brings down the impedance mismatch to a level where the vector network analyzer (VNA) measurement uncertainty is low; and, consequently, the measurement accuracy is high [29].

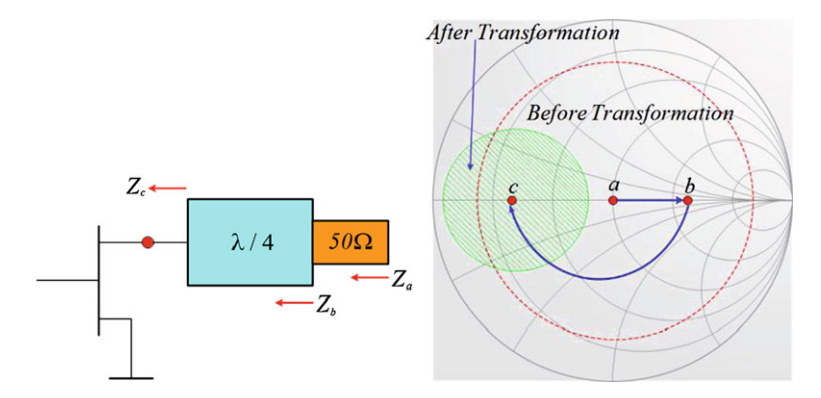


Fig. 5.14 Pictorial representation of the quarter wave transformation technique

In contrast to the pre-matched and enhanced loop load-pull techniques, impedance transforming network based load-pull setups do not experience drastic degradation in the tuning range and the measurement accuracy caused by the adapters and the insertion loss of the fixture. This is achieved due to the reduced Smith chart region in which the reflection coefficients need to be synthesized, thereby causing no or minimal error.

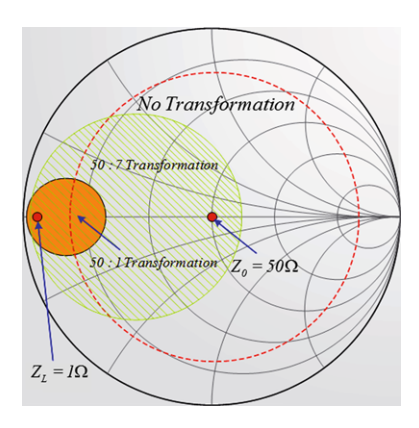
In principle, the quarter wave ($\lambda/4$) transformer technique is a special type of pre-matched load-pull system, where the enhancement in the reflection coefficient tuning range is obtained through the incorporation of a $\lambda/4$ impedance transformer between the DUT and the tuner. The quarter wave moves the matched impedance environment from 50 Ω to some other smaller value, as shown in Fig. 5.14.

It can be observed that the maximum achievable reflection coefficient before impedance transformation is smaller with the matched condition at point 'a' in the Smith chart; whereas, the incorporation of a $\lambda/4$ transformer transforms the matched condition to point 'c' in the Smith chart, which results in an enhanced tuning range, albeit with reduced Smith chart coverage. It should be noted that the 50 Ω line provides the match between the quarter wave transformer and the load-pull tuner.

The transformation of the measurement system's impedance to some smaller value results in a reduced impedance mismatch between the load-pull system and the DUT, which reduces the VSWR and, hence, any potential damage to the DUT, tuner and/or measurement system. The $\lambda/4$ transformer technique thus serves the dual purpose of VSWR reduction and tuning range enhancement [7, 8]. Additionally, the reduced impedance mismatch between the tuner and the DUT also significantly reduces the P_{LP} requirement (described in Sect. 5.5) in the case of active load-pull setups.

It must, however, be noted that the improvement in the tuning range and the reduction in the VSWR, which come at the cost of reduced Smith chart coverage, necessitates the replacement of the $\lambda/4$ transformer for the cases when the characterization of DUTs has to be carried out at multiple frequencies or when separate DUTs need to be characterized successively, so that required Smith chart regions are

Fig. 5.15 Reduction in Smith chart coverage with increase in the transformation ratio of the impedance transformer [18]



not precluded. This results into additional hardware and calibration, which eventually increases size, cost and measurement time. Further, the narrow band nature of a $\lambda/4$ transformer limits the usefulness of such systems in fundamental load-pull characterizations and measurements of high-power DUTs.

5.3.4 Broadband Impedance Transformer Technique

Limitations of the quarter wave impedance transforming network, whose bandwidth of only about 5 to 10 percent of the carrier frequency prevents harmonic load-pull applications, are overcome through the incorporation of a broadband impedance transformer, such as the "Klopfenstein" taper with bandwidth covering from a few 100 MHz to 12 GHz [30], between the DUT and the tuner [19]. The broadband impedance transformer does reduce Smith chart coverage with increasing impedance transformation ratios, as can be seen in Fig. 5.15, but this also results into increased accuracy in the load-pull measurements [29] due to reduced impedance mismatch between the DUT and the tuner. Furthermore, the broadband impedance transformer incorporation in the load-pull setup not only enhances the maximum achievable reflection coefficient, but also reduces the VSWR in both the active as well as passive load-pull systems and the required load-pull power, P_{LP} , in active load-pull systems [17, 18].

The reduced Smith chart coverage sometimes requires very careful selection of impedance transformers, because if the chosen impedance transformer precludes the Smith chart region where the optimal reflection coefficient for a specified DUT lies, then the very purpose of this whole exercise of impedance transformer incorporation gets negated. This is especially important for high impedance transformation ratios, because the smaller the impedance, the higher is the measurement sensitivity. It is, therefore, a standard practice to load-pull an unknown DUT without an impedance transformer, in order to determine the probable optimal impedance. It aids in the identification of the Smith chart region and, hence, in the selection of the impedance transformation ratio.

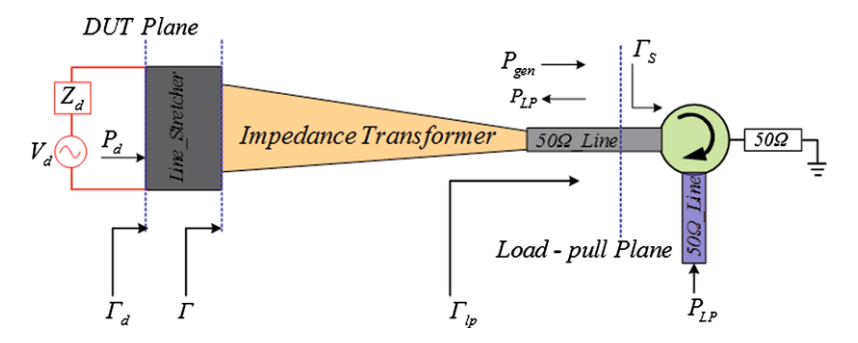


Fig. 5.16 Modified representation for an open-loop active load-pull system with incorporation of an impedance transformer [19], © IEEE 2005

5.4 Impact of a Transformation Network on P_{LP} and VSWR

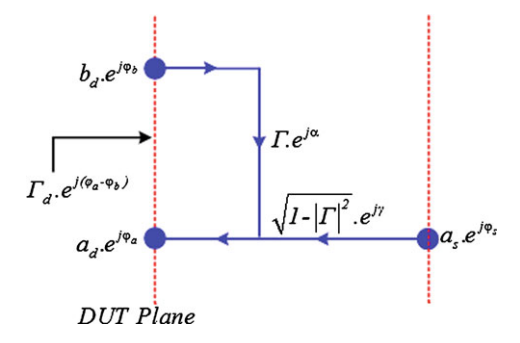
Impedance transformation networks between the DUT and the tuner enhance the reflection coefficient tuning range, as can be seen in Figs. 5.14 and 5.15, and reduce the generated VSWR and required P_{LP} in the load-pull systems [7, 8, 18, 19]. This section describes and quantifies the impact of Klopfenstein taper incorporation in an open-loop active load-pull setup, using a generic model that is depicted in Fig. 5.16. It is important to note that, although the analysis is based on an open-loop active load-pull system, it is equally valid for other load-pull approaches.

In the load-pull model, the DUT is represented by an equivalent voltage source, V_d , and a series impedance, Z_d , that is connected to the larger geometry and, hence, the smaller impedance of the impedance transformer. The circulator is connected to the smaller geometry having 50 Ω impedance. The line stretcher between the impedance transformer and the DUT adjusts the phase of the synthesized reflection coefficients. In several applications, the reflection coefficients phase adjustment is essential, in order to achieve the appropriate matching condition to minimize the required load-pull power, P_{LP} [18, 19, 22]. The parameter Γ_d represents the reflection coefficient at the DUT plane, Γ the transformation ratio of the impedance transformer, Γ_{lp} the synthesized reflection coefficient at the load-pull plane, and Γ_{Syst} the system reflection coefficient arising due to mismatch between the circulator and the smaller geometry of the impedance transformer.

Analysis of this load-pull model can be carried out using a simplified signal flow graph, as given in Fig. 5.17, which assumes that the impedance transformer is lossless and its high impedance end is perfectly matched to the circulator, thereby leading to a further assumption of Γ_{Syst} equaling zero.

In the signal flow graph, the term $a_s e^{j\varphi_s}$ stands for the signal injected at the load-pull plane (i.e. at the high impedance end of the impedance transformer) by the active load-pull source. The terms $b_d e^{j\varphi_b}$ and $a_d e^{j\varphi_a}$ represent the incident and reflected traveling waves at the DUT plane, respectively. Term α represents the phase associated with the line stretcher relating Γ to Γ_d , whereas $\sqrt{1-|\Gamma|^2}$ and γ represent the magnitude and phase of the transmission coefficient of the impedance

Fig. 5.17 Simplified signal flow graph representing an active load-pull setup with an impedance transformer between the DUT and the load-pull signal generator [38], © IEEE 2005



transformer. The synthesized reflection coefficient at the DUT plane, which is the ratio of the reflected and incident traveling wave, can be derived from the signal flow graph and expressed as:

$$\Gamma_d = \frac{a_d e^{j\varphi_a}}{b_d e^{j\varphi_b}} = |\Gamma_d| e^{j(\varphi_a - \varphi_b)}$$
(5.20)

It is evident from Eq. (5.20) that the load synthesized Γ_d at the DUT plane depends on the relative phase between the incident and reflected traveling waves. Therefore, the phase term φ_b can be taken as a reference and set to zero, in order to simplify Eq. (5.18), which is then modified to:

$$\Gamma_d = \frac{a_d e^{j\varphi_a}}{b_d e^{j\varphi_b}} = |\Gamma_d| e^{j\varphi_a} \tag{5.21}$$

The relationship given in Eq. (5.22) between the traveling waves present in the loadpull system can be deduced from the signal flow graph and can be simplified to determine the expression for the incident traveling wave, b_d , at the DUT plane given in Eq. (5.23).

$$a_d e^{j\varphi_a} = |\Gamma| e^{j\alpha} b_d e^{j0} + \sqrt{1 - |\Gamma|^2} e^{j\gamma} a_s e^{j\varphi_s}$$
 (5.22)

$$b_d = \frac{\sqrt{1 - |\Gamma|^2} a_s e^{j(\gamma + \varphi_s)}}{e^{j\alpha} (|\Gamma_d| e^{j(\varphi_d - \alpha)} - |\Gamma|)}$$

$$(5.23)$$

The net power, P_d , at the DUT plane is related to the reflected traveling wave, b_d , and the incident traveling wave, a_d , by Eq. (5.24).

$$P_d = |b_d|^2 - |a_d|^2 = |b_d|^2 (1 - |\Gamma_d|^2)$$
(5.24)

Substitution of Eq. (5.23) into Eq. (5.24) and simplification gives the expression for load-pull power, P_{LP} , injected at the load-pull plane by the active load-pull source.

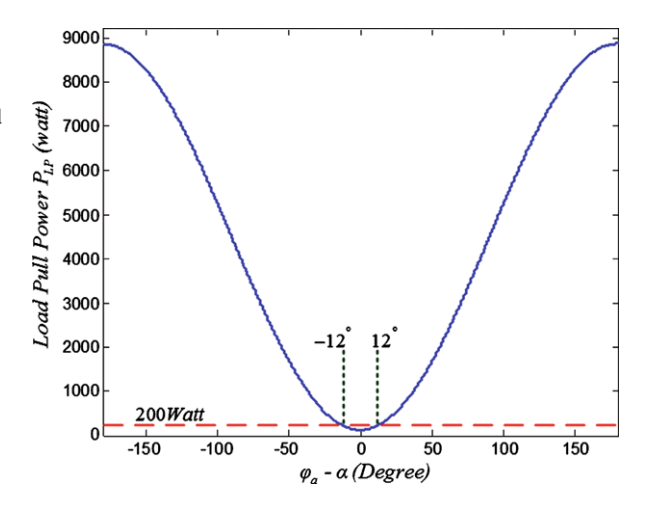
$$|a_s|^2 = |P_{LP}| = \frac{P_d(|\Gamma_d|^2 + |\Gamma|^2 - 2|\Gamma_d||\Gamma|\cos(\varphi_d - \alpha))}{(1 - |\Gamma_d|^2)(1 - |\Gamma|^2)}$$
(5.25)

Equation (5.25) relates P_{LP} to the transformation ratio of impedance transformer, $|\Gamma|e^{j\alpha}$, and the desired reflection coefficient, $|\Gamma_d|e^{j\varphi_a}$. Table 5.2 summarizes the

Transformation ratio	Required P_{LP} (watt)	Transformation ratio	Required P_{LP} (watt)
50:5	78	50:20	442
50:7	126	50:30	686
50:9	174	50:40	931
50:10	198	50:50	1175

Table 5.2 Impact of transformation ratio on the load-pull power for optimal synthesis of the load reflection coefficient, for a 100 W device with a 1 Ω output impedance

Fig. 5.18 Load-pull power requirements as a function of the relative phase difference between the phases of Γ_d and Γ for a 100 W (1 Ω) device by incorporating a 50:7 impedance transformer

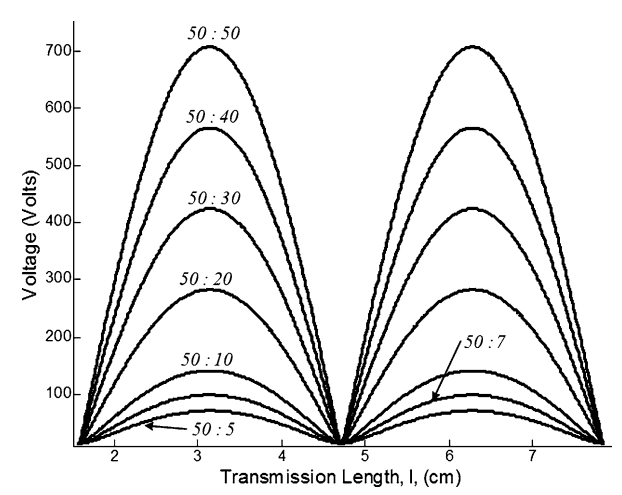


estimated P_{LP} for load-pulling of a 100 W device and clearly identifies the substantial reduction in P_{LP} for the synthesis of desired load reflection coefficients, Γ_d , with the increasing transformation ratio, Γ . In this case, it has been assumed that the phase terms φ_a and α are equal; thus, the cosine term in Eq. (5.25) is unity.

In practical situations, it is not always possible to perfectly align the phase terms φ_a and α . One can observe from Eq. (5.25) that the P_{LP} get smaller as the phase difference, $\varphi_a - \alpha$, approaches zero and reaches minimum when α equal φ_a . In order to visualize the impact of the term $\varphi_a - \alpha$ on P_{LP} , Eq. (5.25) can be plotted for the swept value of $\varphi_a - \alpha$ for a 100 W device and impedance transformer of 50:7, as shown in Fig. 5.18. It is apparent that a difference of 180° between φ_a and α results into a very high requirement of P_{LP} for the synthesis of a reflection coefficient to match the 1 Ω impedance of the 100 W device.

From Fig. 5.18, it is also evident that an active load-pull setup with 200 W of available P_{LP} requires the term $\varphi_a - \alpha$ to be below $\pm 12^{\circ}$. In a practical measurement setup, the phase difference, $\varphi_a - \alpha$, is minimized by adding a low impedance line or line stretcher between the DUT and the low impedance end of the transformer, as shown in Fig. 5.16. The inclusion of a line stretcher, however, requires an additional calibration step to remove any systematic error introduced by it [18, 31]. It is also important to note that the phase term α is a function of the transformation ratio of the

Fig. 5.19 Voltage standing wave for different transformation ratios in active and passive load-pull measurement systems when characterizing a 100 W (1 Ω) device at 2.1 GHz



impedance transformer; therefore, the selection of impedance transformer requires careful attention, so as to minimize the P_{LP} from the load-pull source.

The increasing transformation ratio also suppresses voltage peaks along the transmission path of the load-pull measurement system. It is evident from the voltage (obtained using Eq. (5.9)) plot in Fig. 5.19, which depicts the voltage variation along the transmission path for a 100 W (1 Ω) device for different transformation ratios of the impedance transformer.

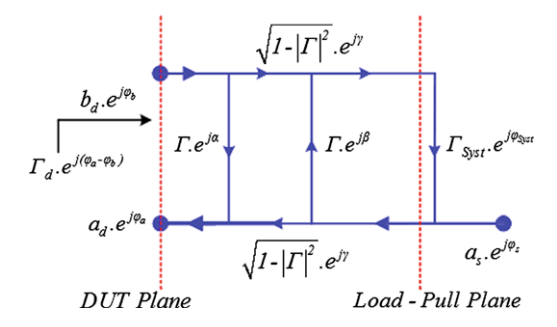
Fig. 5.19 and the data in Table 5.2 reveal that the higher the transformation ratio, the lower are the required P_{LP} and the VSWR within the measurement system. In practice, however, the highest transformation ratio is not the optimal choice, as it may preclude the desired Smith chart region. For an unknown device, the choice of the optimal transformation ratio is dictated by its output impedance [19]. Therefore, it is necessary to roughly estimate the output impedance of the DUT by measuring its large signal, S_{22} , in order to determine the approximate Smith chart region where the optimal reflection coefficient may lie. With this knowledge, an appropriate impedance transformer is then selected to simultaneously minimize P_{LP} demand and the VSWR.

5.5 Hybrid Load-Pull System

In the preceding section, it was assumed that the circulator and smaller geometry of impedance transformer in Fig. 5.16 were perfectly matched, due to both having a characteristic impedance of exact 50 Ω , thereby leading to Γ_{Syst} equaling zero. In practice, they do not possess perfect 50 Ω impedance, resulting in a non-zero Γ_{Syst} and modification in the signal flow graph that is shown in Fig. 5.20.

In this signal flow graph (Fig. 5.20), the additional terms $|\Gamma_{Syst}|e^{j\varphi_{Syst}}$ and $|\Gamma|e^{j\beta}$ represent the contributions of the impedance mismatch between the circulator and

Fig. 5.20 Signal flow graph for a load-pull model with an impedance transformer between the DUT and the tuner and with an unmatched circulator and impedance transformer [19], © IEEE 2005.



impedance transformer and the impedance transformer reflection coefficient at the high-impedance end of the impedance transformer, respectively. If it is assumed that the impedance transformer is lossless and reciprocal, according to lossless reciprocal network laws [30], its phase, β , can be related to its phase terms, α and γ , through the relationship expressed in Eq. (5.26)

$$\beta = 2\gamma - \alpha \pm n\pi \tag{5.26}$$

where n is an odd number.

The expression for P_{LP} in Eq. (5.30) can be obtained after the simplification of Eqs. (5.27) to (5.29), deduced from the signal flow graph in Fig. 5.20 and Eq. (5.24). Once again the reference phase, φ_b , has been set to zero for arriving at the expression for the P_{LP} .

$$a_d e^{j\varphi_a} = \Gamma_{in} b_d e^{j\varphi_b} + \Gamma_T a_s e^{j\varphi_s} \tag{5.27}$$

where

$$\Gamma_{in} = |\Gamma|e^{j\alpha} + \frac{(1 - |\Gamma|^2)|\Gamma_{Syst}|e^{j(\varphi_{Syst} + 2\gamma)}}{(1 - |\Gamma|)|\Gamma_{Syst}|e^{j(\varphi_{Syst} + \beta)}}$$
(5.28)

$$\Gamma_T = \frac{\sqrt{1 - |\Gamma|^2} e^{j\gamma}}{(1 - |\Gamma_{Syst}|) |\Gamma| e^{j(\beta + \varphi_{Syst})}}$$
(5.29)

$$P_{LP} = |a_{s}|^{2} = \frac{\begin{pmatrix} |\Gamma_{d}|^{2} + |\Gamma|^{2} + |\Gamma_{Syst}|^{2} + |\Gamma_{d}|^{2}|\Gamma|^{2}|\Gamma_{Syst}|^{2} \\ -2|\Gamma_{Syst}| \times |\Gamma| \times (1 + |\Gamma_{d}|^{2}) \times \cos(\beta + \varphi_{Syst}) \\ -2|\Gamma_{d}| \times |\Gamma| \times (1 + |\Gamma_{Syst}|^{2}) \times \cos(\varphi_{a} - \alpha) \\ +2|\Gamma_{d}| \times |\Gamma_{Syst}| \times |\Gamma|^{2} \times \cos(\beta + \varphi_{Syst} + \varphi_{a} - \alpha) \\ -2|\Gamma_{d}| \times |\Gamma_{Syst}| \times \cos(\varphi_{a} - 2\gamma - \varphi_{Syst}) \end{pmatrix}}{(1 - |\Gamma_{d}|^{2})(1 - |\Gamma|^{2})}$$
(5.30)

The impact of Γ_{Syst} on P_{LP} can be observed in Fig. 5.21, which depicts the plot of Eqs. (5.30) and (5.26) for two cases when $|\Gamma_{Syst}|$ equals 0 and 0.05, for a 100 W (1 Ω) DUT and an impedance transformer with a 50:7 transformation ratio. The phase terms φ_a , α , and γ have been set equal to π , as this provides the minimum P_{LP} ; whereas, the phase, φ_{Syst} , of the system reflection coefficient is swept from

Fig. 5.21 P_{LP} as a function of the phase of the system reflection coefficient with a 50:7 impedance transformer (for a 100 W (1 Ω) device)

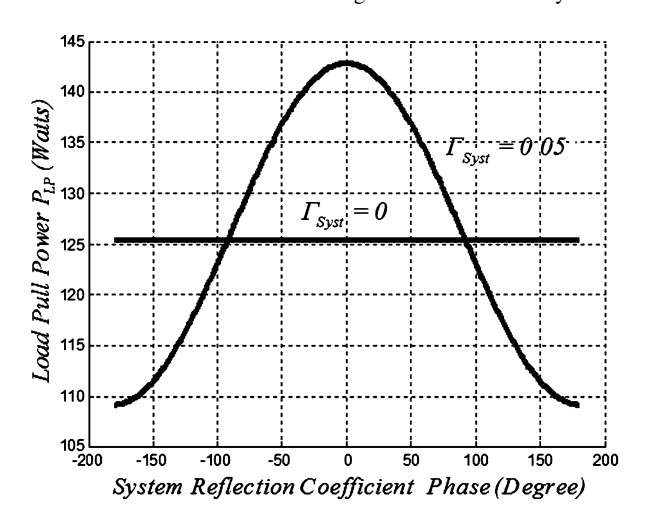
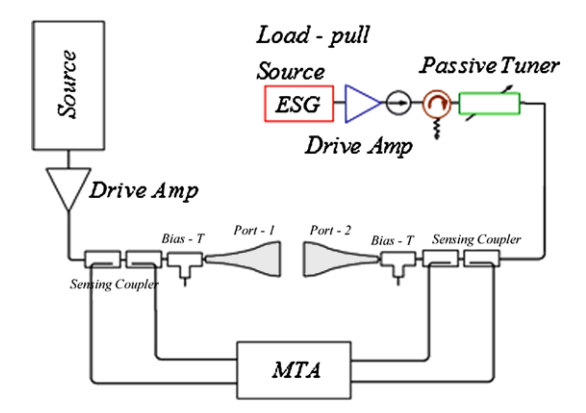


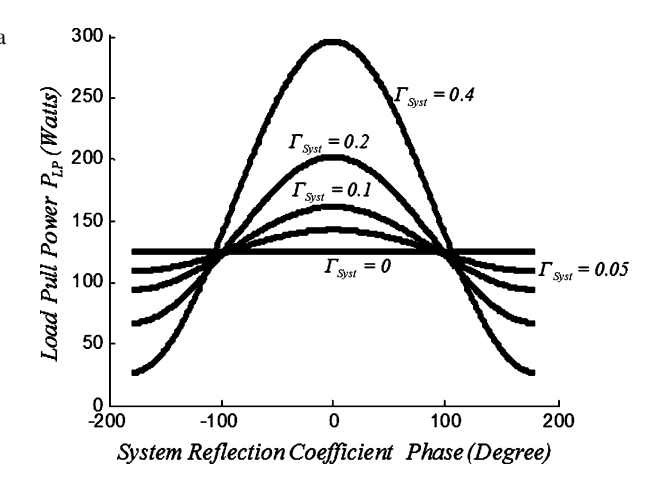
Fig. 5.22 Typical block diagram of a hybrid load-pull measurement setup that incorporates an impedance transformer, open-loop active load-pull components and a passive tuner



 $-\pi$ to π for plotting Eq. (5.30). It is evident from the plot in Fig. 5.21 that a small deviation in $|\Gamma_{Syst}|$ changes the P_{LP} required from the load-pull source drastically for the synthesis of a reflection coefficient to match the 100 W DUT.

The above plot also reveals a strong dependence of φ_{Syst} on P_{LP} . In this case of $|\Gamma_{Syst}| = 0.05$, the minimization of P_{LP} requires φ_{Syst} to be either smaller than -100° or larger than 100° . The dependence of P_{LP} on the mismatch between the circulator and impedance transformer is utilized as an advantage in hybrid load-pull systems [18, 22]. For example, a block diagram of a hybrid load-pull setup is illustrated in Fig. 5.22, which incorporates a passive tuner, in order to intentionally create a mismatch between the impedance transformer and the circulator to minimize P_{LP} from the load-pull source. Its optimal operation in any specified application requires the availability of an appropriate impedance transformer, a line stretcher between the DUT and the impedance transformer, and a tuning resolution of the passive tuner. Further, the available power from the active load-pull source plays a key role in the selection of the transformation ratio of the impedance transformer.

Fig. 5.23 Required P_{LP} as a function of the system reflection coefficient phase, φ_{Syst} , for varying system reflection coefficients when using a 50:7 impedance transformer (for a 100 W (1 Ω) device)



In measurement applications, the load-pulling of a device is initially carried out to identify the Smith chart region and then to select an appropriate impedance transformer for the DUT, as well as a line stretcher between the device and impedance transformer. Upon selection of the impedance transformer and the line stretcher, the system has two degrees of freedom, namely the passive tuner and the active load-pull source. In such a case, the passive tuner is first tuned appropriately to create a mismatch between the circulator and the impedance transformer; and, load-pull measurements are then performed using the load-pull source. The mismatch created by the passive tuner reduces the power demand from the load-pull source and, therefore, aids in the optimal operation of the hybrid load-pull system. For example, plot in Fig. 5.23 displays the dependence of P_{LP} on the phase and magnitude of Γ_{Syst} for load-pulling a 100 W (1 Ω) device using the hybrid load-pull setup with a 50:7 impedance transformer. The phase and magnitude of Γ_{Syst} are tuned by changing the setting of the passive tuner.

It can be observed in Fig. 5.23 that even a fine adjustment in the magnitude and phase of Γ_{Syst} significantly reduces P_{LP} . Thus, passive tuners with fine resolution in magnitude and phase variation are extremely important for reducing P_{LP} from the load-pull source. It can, therefore, be concluded that a hybrid load-pull system with an appropriate impedance transformer and a high-resolution passive tuner is very suitable for high-power DUT load-pull measurements, as it minimizes the P_{LP} demand from the load-pull source and also reduces the VSWR and, consequently, the voltage peaks in the measurement system.

5.6 Calibration and Data Extraction

Incorporation of an impedance transformer between the DUT and the tuner necessitates a two-tier calibration, in order for the high-power load-pull setup to function properly. For example, the load-pull setup in Fig. 5.22 requires two error adapters

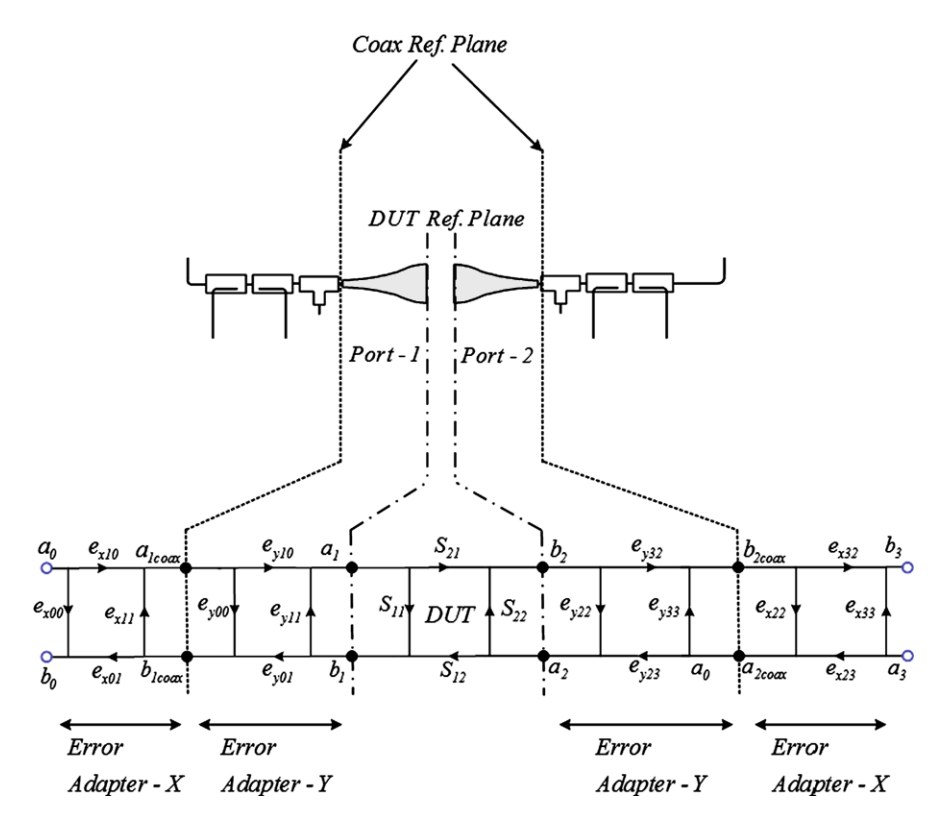


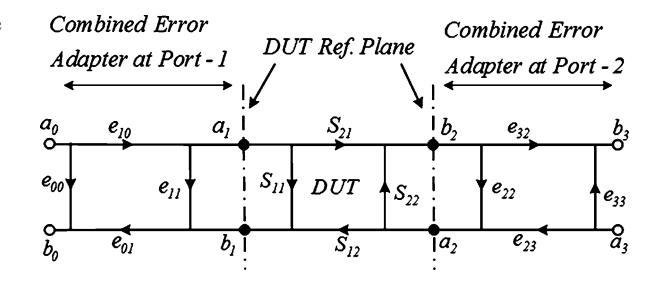
Fig. 5.24 Reference plane definition and error adapters at ports 1 and 2 of the DUT for removal of the imperfections in the components, connectors, board launchers and impedance transformers

at both ports 1 and 2 of the DUT, in order to account for the imperfections in the system components and the impedance transformation networks. As illustrated in Fig. 5.24, error adapters *X* account for the systematic errors introduced by the system components, as well as the connectors, and reset the reference plane at the coaxial connectors used for connecting the measurement setup and the impedance transformer. Error adapters *Y* remove the systematic errors contributed by the impedance transformer, launchers and test fixture and reset the reference plane at the DUT package.

The resetting of the error corrections and reference planes can be achieved by using either the measurement-based VNA error correction procedures, full wave analysis using numerical techniques or analytical methods based on approximate closed-form expressions [32–34]. The analytical method is based on approximations that have built-in uncertainty [34], as are the numerical techniques [33] in the form of material parameter uncertainty.

The VNA error correction techniques rely entirely on measurements and are regulated by well-defined mathematical expressions for the extraction of the error

Fig. 5.25 Flow graph of the combined error adapters at both the ports 1 and 2 of the DUT



terms for each half of the fixture [32]. The SOLT (Short-Open-Load-Thru) and TRL (Thru-Reflect-Line) techniques are the most popular calibration procedures for VNA error correction. SOLT standards, however, are difficult to implement for VNA measurements of microstrip and similar circuits [17]. The TRL technique, which relies only on the characteristic impedance of a short transmission, is simple and provides the highest calibration accuracy over a wide bandwidth [35] and, therefore, is preferred over the traditional SOLT technique.

The calibration of a high-power load-pull setup involves a first-tier calibration using coaxial TRL standards to determine the parameters of error adapters X, in order to reset the reference plane at the coaxial connectors shown in Fig. 5.24. The second-tier calibration for the determination of parameters of error adapters Y involves TRL calibration using in-fixture standards attached to the impedance transforming network, which then transfers the reference plane to the DUT ports.

The extraction of the measurement data at the DUT plane is a two-stage process. The first stage involves transformation of the parameters of error adapters X and Y to a common reference impedance [35]. It should be noted that, in practice, error adapters X are referenced to 50 Ω , which is the characteristic impedance of the calibration standards; whereas, error adapters Y are referenced to the characteristic impedance of the impedance transformer, which is usually smaller than 50 Ω , necessitating transformation of error adapters Y to 50 Ω . After transformation, the error adapters are combined to form combined error adapters at both ports of the DUT, as illustrated by the flow graph in Fig. 5.25. Equations (5.31) to (5.38), which are derived from Fig. 5.25, provide the error parameters of the combined error adapters.

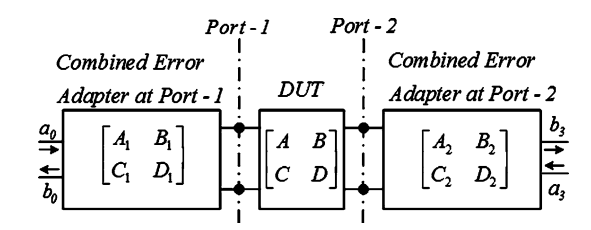
$$e_{00} = e_{x00} + \frac{e_{x01}e_{x10}e_{y00}^{50}}{1 - e_{x11}e_{y00}^{50}}$$
 (5.31)

$$e_{11} = e_{y11}^{50} + \frac{e_{y01}^{50} e_{y10}^{50} e_{x11}}{1 - e_{x11} e_{y00}^{50}}$$
 (5.32)

$$e_{10} = \frac{e_{y10}^{50} e_{x10}}{1 - e_{x11} e_{y00}^{50}}$$
 (5.33)

$$e_{01} = \frac{e_{y01}^{50} e_{x01}}{1 - e_{x11} e_{y00}^{50}}$$
 (5.34)

Fig. 5.26 Measurement system error adapters in terms of ABCD parameters



$$e_{22} = e_{y22}^{50} + \frac{e_{y23}^{50}e_{y32}^{50}e_{x22}}{1 - e_{y33}^{50}e_{x22}}$$
(5.35)

$$e_{33} = e_{x33} + \frac{e_{x23}e_{x32}e_{y33}^{50}}{1 - e_{y33}^{50}e_{x22}}$$
 (5.36)

$$e_{32} = \frac{e_{y32}^{50} e_{x32}}{1 - e_{y33}^{50} e_{x22}}$$
 (5.37)

$$e_{23} = \frac{e_{y23}^{50} e_{x23}}{1 - e_{y33}^{50} e_{x22}}$$
 (5.38)

where the terms with the superscript of 50 refer to the parameters of error adapters Y transformed to 50 Ω impedance.

In the second stage, all the S-parameter data, the parameters of error adapters and the corrected measured data required at the DUT plane are converted to ABCD parameters [36], as they are easy to manipulate in the cascaded structure shown in Fig. 5.26. For example, the actual measured data A_m , B_m , C_m and D_m at the VNA port is given by the cascade of the three ABCD matrices, according to Eq. (5.39).

$$\begin{bmatrix} A_m & B_m \\ C_m & D_m \end{bmatrix} = \begin{bmatrix} A_1 & B_1 \\ C_1 & D_1 \end{bmatrix} \begin{bmatrix} A & B \\ C & D \end{bmatrix} \begin{bmatrix} A_2 & B_2 \\ C_2 & D_2 \end{bmatrix}$$
(5.39)

Simplification of Eq. (5.39) then provides the desired corrected ABCD parameter of the DUT, as given in Eq. (5.40).

$$\begin{bmatrix} A & B \\ C & D \end{bmatrix} = \begin{bmatrix} A_1 & B_1 \\ C_1 & D_1 \end{bmatrix}^{-1} \begin{bmatrix} A_m & B_m \\ C_m & D_m \end{bmatrix} \begin{bmatrix} A_2 & B_2 \\ C_2 & D_2 \end{bmatrix}^{-1}$$
(5.40)

The ABCD parameters obtained from Eq. (5.40) are then converted to S-parameters, in order to determine the error corrected measured data of the DUT at the DUT plane [36]. This overall process of error corrected S-parameter extraction from the measured data at the VNA ports is also called the de-embedding technique [32].

References

D. Miller, M. Drinkwine, High voltage microwave devices, in *International Conference on Compound Semiconductor Manufacturing Digest* (2003), pp. 1–4

 M.H. Wong, S. Rajan, R.M. Chu, T. Palacios, C.S. Suh, L.S. McCarthy, S. Keller, J.S. Speck, U.K. Mishra, N-face high electron mobility transistors with GaN-spacer. Wiley InterScience 204(6), 2049–2053 (2007)

- 3. Maury Microwave Corporation, Pulsed-bias pulsed-rf harmonic load-pull for gallium nitride (GaN) and wide band gap (WBG), Application Note: 5A-043, Nov. 2009
- 4. B. Bonte, C. Gacquiere, E. Bourcier, G. Lemeur, Y. Crosnier, An automated system for measuring power devices in Ka-band. IEEE Trans. Microw. Theory Tech. **46**(1), 70–75 (1998)
- P. Bouysse, J. Nebus, J. Coupat, J. Villotte, A novel accurate load pull setup allowing the characterization of highly mismatched power transistors. IEEE Trans. Microw. Theory Tech. 42(2), 327–332 (1994)
- F. De Groote, J.-P. Teyssier, J. Verspecht, J. Faraj, Introduction to measurements for power transistor characterization. IEEE Microw. Mag. 9(3), 70–85 (2008)
- J. Sevic, A sub 1 Ω load-pull quarter wave prematching network based on a two-tier TRL calibration, in 52nd Automatic RF Techniques Group (ARFTG) Conference Digest, Rohnert Park, USA (1998), pp. 73–81
- S. Basu, M. Fennelly, J.E. Pence, E. Strid, Impedance matching probes for wireless applications, Application Note, AR126, Cascade Microtech, 1998
- 9. J. Hoversten, M. Roberg, Z. Popovic, Harmonic load pull for high power microwave devices using fundamental only load pull tuners, in *75th Automatic Radio Frequency Techniques Group (ARFTG) Conference Digest*, Anaheim, USA (2010), pp. 73–81
- Maury Microwave Corporation, Device characterization with harmonic load and source pull, Application Note: 5C-044, Dec. 2000
- Focus Microwaves, Load pull measurements on transistors with harmonic impedance control, Technical Note, August 1999
- P. Colantonio, A. Ferrero, F. Giannini, E. Limiti, V. Teppati, Harmonic load/source pull strategies for high efficiency PAs design, in *IEEE MTT-S International Microwave Symposium Di*gest (2003), pp. 1807–1810
- I. Yattoun, A. Peden, A new configuration to improve the active loop technique for transistor large signal characterization in the Ka-band. Microw. Opt. Technol. Lett. 49(3), 589–593 (2007)
- M.S. Hashmi, A.L. Clarke, S.P. Woodington, J. Lees, J. Benedikt, P.J. Tasker, An accurate calibrate-able multi-harmonic active load-pull system based on the envelope load-pull concept. IEEE Trans. Microw. Theory Tech. 58(3), 656–664 (2010)
- F. De Groote, J.-P. Teyssier, J. Verspecht, J. Faraj, High power on-wafer capabilities of a time domain load-pull setup, in *IEEE MTT-S International Microwave Symposium*, Atlanta, USA (June 2008), pp. 100–102
- Focus Microwaves, Accuracy and verification of load pull measurements, Application Note 18, Sept. 1994
- R. Ludwig, P. Bretchko, RF Circuit Design—Theory and Applications, 1st edn. (Prentice Hall, New York, 2000). ISBN 0-13-095323-7
- 18. Z. Aboush, Design, characterization and realization of thin film packaging for both broadband and high power applications, PhD Thesis, Cardiff University, 2007
- Z. Aboush, J. Lees, J. Benedikt, P.J. Tasker, Active harmonic load pull system for characterizing highly mismatched high power transistors, in *IEEE MTT-S International Microwave Symposium Digest*, vol. 3 (June 2005), pp. 1311–1314
- F.V. Raay, G. Kompa, Waveform measurements—the load-pull concept, in 55th Automatic Radio Frequency Techniques Group (ARFTG) Conference Digest, Boston, USA, vol. 37 (June 2000), pp. 1–8
- 21. F. De Groote, O. Jardel, J. Verspecht, D. Barataud, J.-P. Teyssier, R. Quere, Time domain harmonic load-pull of an AlGaN/GaN HEMT, in *66th Automatic Radio Frequency Techniques Group (ARFTG) Conference Proceedings*, Washington, USA (December 2005)
- 22. V. Teppati, A. Ferrero, U. Pisani, Recent advances in real-time load-pull systems. IEEE Trans. Instrum. Meas. **57**(11), (2008)

- M.S. Hashmi, A.L. Clarke, S.P. Woodington, J. Lees, J. Benedikt, P.J. Tasker, Electronic multi-harmonic load-pull system for experimentally driven power amplifier design optimization, in *IEEE MTT-S International Microwave Symposium Digest*, Boston, USA (June 2009), pp. 1549–1552
- F.M. Ghannouchi, M.S. Hashmi, S. Bensmida, M. Helaoui, Loop enhanced passive sourceand load-pull technique for high reflection factor synthesis. IEEE Trans. Microw. Theory Tech. 58(11), 2952–2959 (2010)
- 25. Focus Microwaves, Load-pull for power transistor characterization, Application Note, 2003
- C. Roff, J. Graham, J. Sirois, B. Noori, A new technique for decreasing the characterization time of passive load-pull tuners to maximize measurement throughput, in 72nd Automatic Radio Frequency Techniques Group (ARFTG) Conference Digest, Portland, USA (Dec. 2008), pp. 92–96
- Focus Microwaves, Using transformers in harmonic load pull, Technical Note TN-3-2008, Dec. 2008
- 28. Focus Microwaves, Comparing harmonic load-pull techniques with regards to power-added efficiency (PAE), Application Note 58, May 2007
- 29. M. Golio, J. Golio, *RF and Microwave Circuits, Measurements, and Modelling* (CRC Press, Boca Raton, 2008). ISBN 978-0-8493-7218-6
- D.M. Pozar, Microwave Engineering, 3rd edn. (Wiley, New York, 2005). ISBN 0-471-17096-
- 31. G.F. Engen, C.A. Hoer, Thru-reflect-line: an improved technique for calibrating the dual six-port automatic network analyzer. IEEE Trans. Microw. Theory Tech. 27, 987–993 (1979)
- 32. D. Rytting, Appendix to an analysis of vector measurement accuracy enhancement techniques, in *Hewlett-Packard RF Microwave Symposium Digest* (March 1982), pp. 1–42
- 33. EM User's Manual, v. 10, Sonnet Software Inc., Liverpool, NY, 2008
- 34. B. Wadell, *Transmission Line Handbook* (Artech House, Boston, 1991)
- 35. D. Williams, C.M. Wang, U. Arz, An optimal multiline TRL calibration algorithm, in *IEEE MTT-S International Microwave Symposium Digest*, vol. 3 (June 2003), pp. 1819–1822
- D.A. Fricky, Conversions between S, Z, Y, h, ABCD, and T parameters which are valid for complex source and load impedances. IEEE Trans. Microw. Theory Tech. 42(2), 205–211 (1994)
- M.S. Hashmi, F.M. Ghannouchi, P.J. Tasker, K. Rawat, Highly reflective load pull. IEEE Microw. Mag. 12(4), 96–107 (2011)
- 38. Z. Aboush, C. Jones, G. Knight, A. Sheikh, H. Lee, J. Lees, J. Benedikt, P.J. Tasker, High power active harmonic load-pull system for characterization of high power 100 Watt transistors, in *IEEE 35th European Microwave Conference*, vol. 1(4) (Oct. 2005), 4 pp.

Chapter 6 Envelope Load-Pull System

This chapter presents the fundamental concept of an active envelope load-pull (ELP) system. Subsequently, the realization and design, along with its characteristics, are presented and discussed. The calibration procedure of the ELP system, which is rapid and increases load-pull measurement throughput, is also described in detail. Finally, the harmonic ELP and its characteristics, which lead to valuable measurements and investigations, are presented.

6.1 Introduction

Both traditional passive and active load-pull techniques are commercially available [1–4]. In practice, however, most of these systems do not meet all the load-pull measurement requirements appropriately, such as in the design and optimization of harmonically tuned power amplifiers or high throughput radio frequency (RF) and microwave load-pull measurement applications. For example, the inability of the passive load-pull technique to synthesize harmonically independent reflection coefficients limits the use of such systems in the design of high-efficiency power amplifiers, such as class-F [5, 6]. Additionally, high load-pull measurement throughput requires pre-calibrated tuners at all tuner positions and settings, which can turn out to be lengthy and cumbersome procedures. Pre-calibration of passive tuners, albeit slow, are possible before their deployment in load-pull systems; however, the pre-calibration of classic active load-tuners is not possible.

An envelope load-pull (ELP) system can be calibrated rapidly and efficiently and is also capable of synthesizing harmonically independent reflection coefficients [7–9]. These two features make it most suitable for applications, such as semiconductor device characterization for broadband power amplifiers design and their optimization [10–12]. It is also suited for the evaluation of transistor devices for load- and supply-modulation applications [13], as well as the rapid experimental investigation of transistor devices for achieving high-efficiency and high-measurement throughput [7, 14]. Additionally, the ELP system is also capable of synthesizing drive- and

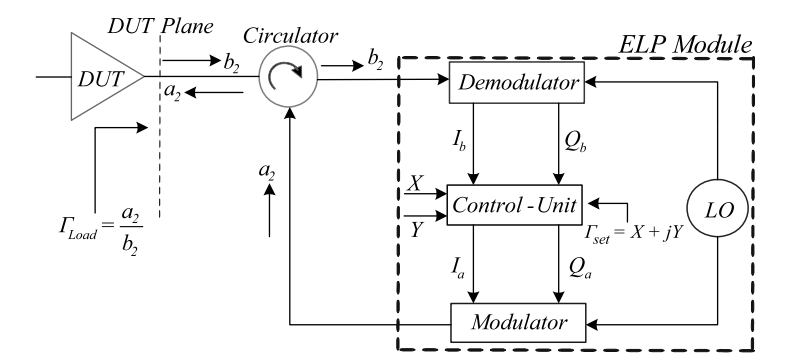


Fig. 6.1 Generic block diagram illustrating the concept of the ELP technique

bias-level independent reflection coefficients and, thus, can work better in several load-pull applications than other active load-pull methods. These applications may be nonlinear device modeling [15, 16], determination of solid-state device performance under varying drive and bias conditions [17–21], or waveform engineering [22].

6.2 Envelope Load-Pull Concept

The operating methodology of the ELP system is similar to the active closed-loop active load-pull technique. The major difference between the two techniques is the manner in which the traveling wave is modified before being fed back for the synthesis of the desired reflection coefficient at the DUT reference plane. The ELP utilizes external control variables, X and Y, for modifying the phase and amplitude of the reflected traveling wave, a_2 , as shown in Fig. 6.1. Furthermore, in ELP system, the modification in the forward traveling wave and then its feedback to the device takes place at the baseband or at an intermediate frequency, which shields the system from any oscillation at the carrier RF frequency.

6.2.1 Mathematical Formulation

Figure 6.1 depicts a generic block diagram of the ELP system. It consists of a quadrature demodulator that down-converts the incident traveling wave into baseband signals, a control unit that modifies the baseband signal components generated by the quadrature demodulator through external control variables X and Y, a quadrature modulator that up-converts the modified baseband signal components, and a local oscillator (LO) that provides the desired signal to the quadrature demodulator and modulator. In principle, the circulator works as a perfect three-port component with the ability to transfer signals only one way between two respective

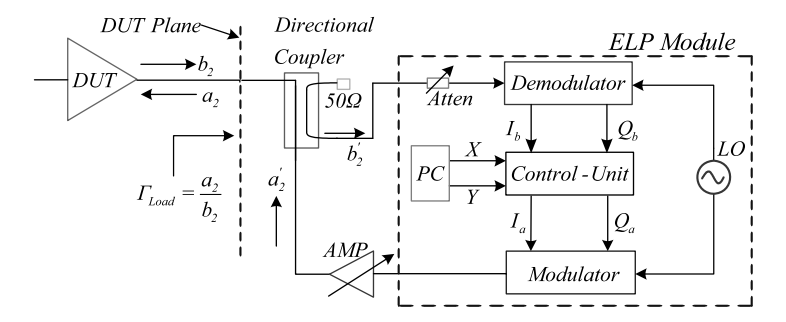


Fig. 6.2 Block diagram illustrating a realized ELP setup [8], © IEEE 2010

ports. As shown in Fig. 6.1, this helps in completely directing the incident traveling wave, b_2 , to the quadrature demodulator and the up-converted reflected traveling wave, a_2 , to the DUT plane for the synthesis of the reflection coefficient given by Eq. (6.1).

$$\Gamma_{Load} = \frac{a_2}{b_2} \tag{6.1}$$

The synthesized reflection coefficient at the DUT plane is regulated by the control function, F(X, Y), given in Eq. (6.2). The control function is also called the reflection coefficient, Γ_{set} , formulated by the control unit.

$$F(X,Y) = \Gamma_{set} = X + jY \tag{6.2}$$

According to the ELP concept [23, 24], in an ideal situation, the synthesized reflection coefficient at the DUT plane, Γ_{Load} , should be equal to the control function, F(X, Y); therefore, Eq. (6.3) can be written as:

$$X + jY = \frac{a_2}{b_2} \tag{6.3}$$

Equations (6.4) and (6.5) give the incident and reflected waves, b_2 and a_2 , in terms of their respective quadrature baseband components, I_b , Q_b , I_a and Q_a .

$$b_2(t) = I_b(t) + j Q_b(t)$$
(6.4)

$$a_2(t) = I_a(t) + jQ_a(t)$$
 (6.5)

Equations (6.3), (6.4), (6.5) can be simplified to obtain the ELP equations given in Eqs. (6.6) and (6.7).

$$I_a = I_b X - Q_b Y \tag{6.6}$$

$$Q_a = Q_b X + I_b Y (6.7)$$

The ELP equations relate control variables X and Y to the quadrature baseband components of traveling waves b_2 and a_2 .

6.3 Practical Realization

Figure 6.2 shows a block diagram of a realized ELP system. It can be observed that the realization of the system requires one quadrature demodulator, one quadrature modulator, a control unit, one loop amplifier and some passive components, such as cables, connectors, directional coupler or circulator, and attenuators.

Either an active or a passive demodulator can be used for the realization of the system. An active direct conversion demodulator provides in principles a wider bandwidth and higher operating dynamic range, compared to the passive demodulator, but also suffers from a bias-dependent inherent DC offset. The presence of varying DC offsets degrades the overall performance of the system [7, 8]. Ideally, the complete removal of DC offsets is essential for the calibration of the setup. In order to remove the DC offsets, the ELP system needs to be operated in a heterodyne mode [9].

The control unit is an electronic circuit with the functionality to perform multiplication and addition/subtraction. It takes computer-generated control variables X and Y, which act on the baseband components, I_b and Q_b , in order to synthesize the active Γ_{Load} using the ELP equations (Eqs. (6.6) and (6.7)). A directional coupler or circulator can be employed as a three-port component for directing the incident and reflected waves in the desired direction. For example, the realized setup employs a directional coupler, as it provides better isolation between the incident and reflected waves compared to a circulator.

Better isolation is key in achieving accurate calibration, as described in Sect. 6.4. A circulator, however, can be used in place of the directional coupler in measurement applications where the desired accuracy in the synthesized reflection coefficients is not too stringent.

The quadrature modulator used in the system can be either active or passive and should be chosen according to the required measurement bandwidth, as an active quadrature modulator provides higher bandwidth than that of a passive modulator. A loop amplifier, AMP, is used to boost the amplitude of the reflected traveling wave, in order to enhance the tuning range of the synthesized reflection coefficient at the DUT plane; whereas, the attenuator, Atten, controls the level of the incident traveling wave in the feedback loop of the system. The ELP system stability is heavily dependent on the settings of AMP and Atten [8]; therefore, it is essential to choose appropriate settings, in order to achieve and guarantee a stable operation over the whole dynamic range and bandwidth of the system.

6.3.1 Design of Control Unit

The control unit processes the ELP equations (Eqs. (6.6) and (6.7)) consisting of four multiplication, one addition and one subtraction terms. In an analogue technique, four multipliers, one adder and one subtractor are required, as shown in Fig. 6.3.

6.3 Practical Realization 143

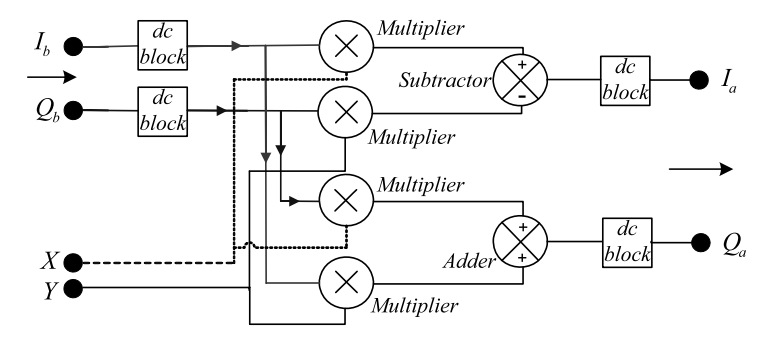


Fig. 6.3 Generic configuration of a control unit for the processing of the ELP equations

The control unit requires DC blocks at the input to suppress the DC offset if an active demodulator is used for the design of the ELP setup. The DC blocks at the output of the control unit discard any DC offsets generated by the multiplier or adder/subtractor units, while passing only the useful information contained in the baseband intermediate frequency (IF) signal to subsequent next stages for further processing.

In the heterodyne mode, as expressed below, the quadrature demodulator down-converts the incident traveling wave, given in Eq. (6.8), by mixing it with an LO signal, given in Eq. (6.9), and generates the baseband signal components, given in Eqs. (6.10) and (6.11). The higher mixing components are filtered out by low-pass filters, LP

$$b_2(t) = R\cos(\omega_s t - \alpha) \tag{6.8}$$

$$LO = S\cos(\omega_S t + \delta\omega_S t) \tag{6.9}$$

$$I_b(t) = LP\left\{ \left(\frac{RS}{2} \right) 2\cos(\omega_s t - \alpha)\cos(\omega_s t + \delta\omega_s t) \right\}$$

= $A\cos(\delta\omega_s t + \alpha)$ (6.10)

$$Q_b(t) = LP\left\{ \left(\frac{RS}{2} \right) 2\cos(\omega_s t - \alpha)\sin(\omega_s t + \delta\omega_s t) \right\}$$

$$= A\sin(\delta\omega_s t + \alpha)$$
(6.11)

where A = (RS/2) and α represent the magnitude and phase of the baseband signals, ω_s is the stimulus frequency, and $\delta\omega_s$ is the frequency offset between the stimulus and the LO.

In practical realizations, however, there can be imbalances in the magnitude and phase of the baseband components, I_b and Q_b . For example, Eqs. (6.12) and (6.13) are the quadrature baseband components, with the terms L and K representing the amplitudes of I_b and Q_b , respectively, when there is a magnitude imbalance between the two.

$$I_b(t) = L\cos(\delta\omega_s t + \alpha) \tag{6.12}$$

$$Q_b(t) = K \sin(\delta \omega_s t + \alpha) \tag{6.13}$$

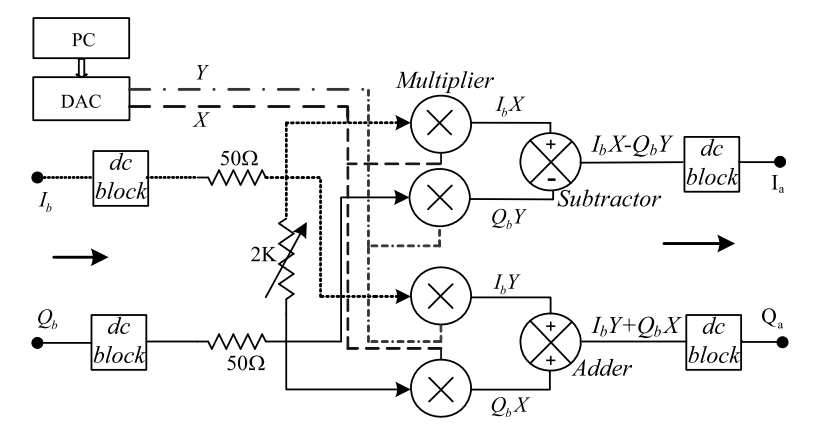


Fig. 6.4 Analogue domain implementation of a modified control unit to suppress the image creation in the ELP feedback loop [9], © IOP Measurement Science and Technology 2010

The processing of these baseband components in the control unit, through the use of control variables X and Y, and then up-conversion by the quadrature modulator using the LO signal in Eq. (6.9) produces the reflected traveling wave, a_2 , given in Eq. (6.14).

$$a_{2}(t) = \left(\left\{ \left(\frac{L+K}{2} \right) \cos(\omega_{s}t - \alpha) \right\} + \left\{ \left(\frac{L-K}{2} \right) \cos(\omega_{s}t - \alpha + 2\delta\omega_{s}t) \right\} \right) |\Gamma_{set}| e^{j\theta}$$
 (6.14)

where $|\Gamma_{set}| = \sqrt{X^2 + Y^2}$ is the magnitude and $\theta = \tan^{-1}(Y/X)$ is the phase of the control function F(X, Y).

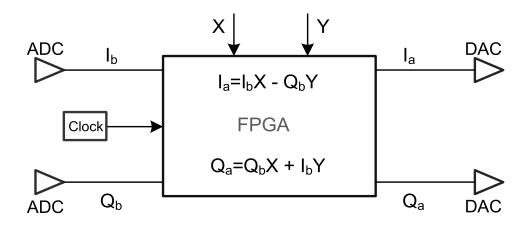
The reflected traveling wave in Eq. (6.14) contains two components—one is useful, whereas the other is its image. The image generation is the result of an imbalance in the magnitudes of baseband signals I_b and Q_b . An imbalance in the phase of I_b and Q_b also creates an image signal in the system [9]. The image due to a phase imbalance, however, falls far away from the carrier signal and, therefore, does not affect the performance of the ELP system. However, the image due to an amplitude imbalance lies very close to the carrier signal and, as a result, greatly affects the performance of the system [9]. As a consequence, the imbalances between I_b and Q_b must be corrected, in order to suppress the image and attain good load-pull performance from the system [7–9]. This can be achieved by balancing the magnitude imbalance of I_b and Q_b generated by the demodulator through the incorporation of a balance bridge, as shown in Fig. 6.4.

The balancing in the amplitude of the baseband components suppresses the image in the up-converted signal given in Eq. (6.15) and, therefore, creates the required reflected traveling wave for the synthesis of a desired reflection coefficient at the DUT plane.

$$a_2(t) = (A\cos(\omega_s t - \alpha))|\Gamma_{set}|e^{j\theta}$$
(6.15)

6.4 ELP Calibration 145

Fig. 6.5 FPGA-based implementation of the control unit



The control unit can also be designed using a digital platform, such as a field-programmable gate array (FPGA), as shown in Fig. 6.5 [25]. Analogue-to-digital converters (ADCs) transform the baseband I_b and Q_b into digital bit streams, which are then modified by on-board generated variables X and Y. The modified bit streams are then transformed into the analogue domain by digital-to-analogue converters (DACs). DC offsets from I_b and Q_b are removed using digital filtering, while the balancing is done on-board using different scaling for the I and Q paths. The on-board global clock synchronizes the whole baseband processing required for the implementation of the ELP equations (Eqs. (6.6) and (6.7)).

6.4 ELP Calibration

The purpose of ELP system calibration is the correction of the imperfections introduced by the components, demodulator, control unit, modulator, directional coupler, cables and connectors, in order for it to function properly. After calibration, the reflection coefficients at the DUT plane can be precisely synthesized through the variation of control variables *X* and *Y*.

6.4.1 Error Flow Model Formulation

The first step in ELP calibration is the formulation of the error flow model for the system, which requires identification of the sources of systematic errors, as illustrated in Fig. 6.6. These errors in the system are introduced, due to the non-ideal nature of demodulator and modulator, imperfect feedback effect caused by the directional coupler, and delays and losses in the cables. The term T_D accounts for the demodulator conversion gain and the losses and delays associated with the physical setup on the demodulator side; and, the term T_M refers to the modulator conversion gain and the losses and delays associated with the cables and connectors on the modulator side. The term Γ_0 is the passive impedance of the network, while the error term, Γ_F , accounts for the imperfections in the feedback and system isolation.

The impact of systematic errors in the ELP system can be analyzed using the error flow model illustrated in Fig. 6.7. The error model assumes that an active demodulator has been used and, therefore, includes error terms D and M caused by the DC offset present in the baseband signal components. Error terms D and M are

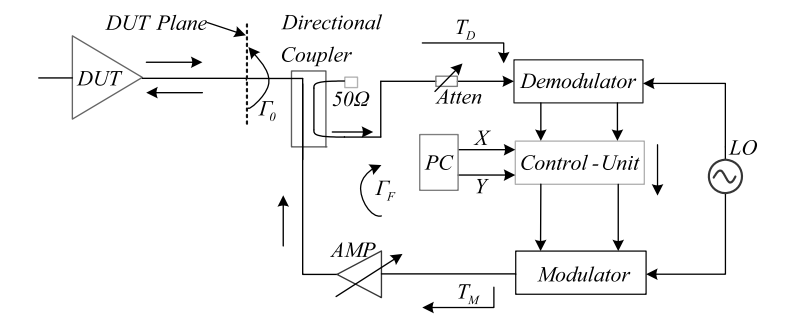
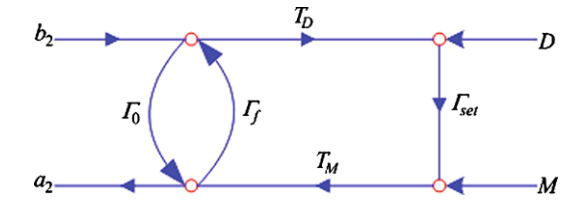


Fig. 6.6 Block diagram of an ELP system depicting the sources of systematic errors [8], © IEEE 2010

Fig. 6.7 Error flow model accounting for the errors introduced by the components used in the design of the ELP system [8], © IEEE 2010



absent from the error flow model in case a passive demodulator is employed in the design of the system. The term $\Gamma_{set} = X + jY$ refers to the required load reflection coefficient established by control variables X and Y.

6.4.2 Simplification of the Error Flow Model

The error flow model can be simplified in five steps, using the flow graph reduction technique [26] shown in Fig. 6.8.

Equation (6.16), which relates traveling waves a_2 and b_2 , can be deduced from the last stage of the simplification process.

$$a_2 = \left(b_2 + \frac{1}{T_D} \left(D + \frac{M}{\Gamma_{set}}\right)\right) \left(\frac{\Gamma_{set} T_D T_M}{1 - \Gamma_F (\Gamma_{set} T_D T_M)} + \Gamma_0\right)$$
(6.16)

The presence of DC offset terms D and M does not allow for the determination of the direct ratio of the traveling waves a_2 and b_2 and, hence, the reflection coefficient at the DUT plane, which prevents the straightforward calibration of the ELP system. In order to discard the DC offset terms and to achieve a calibrated ELP system, a passive demodulator should be used or an active demodulator and DC blocks should be employed. The removal of terms D and M from Eq. (6.16) enables a direct relationship between a_2 and b_2 (Eq. (6.17)) and, therefore, provides the ELP

6.4 ELP Calibration 147

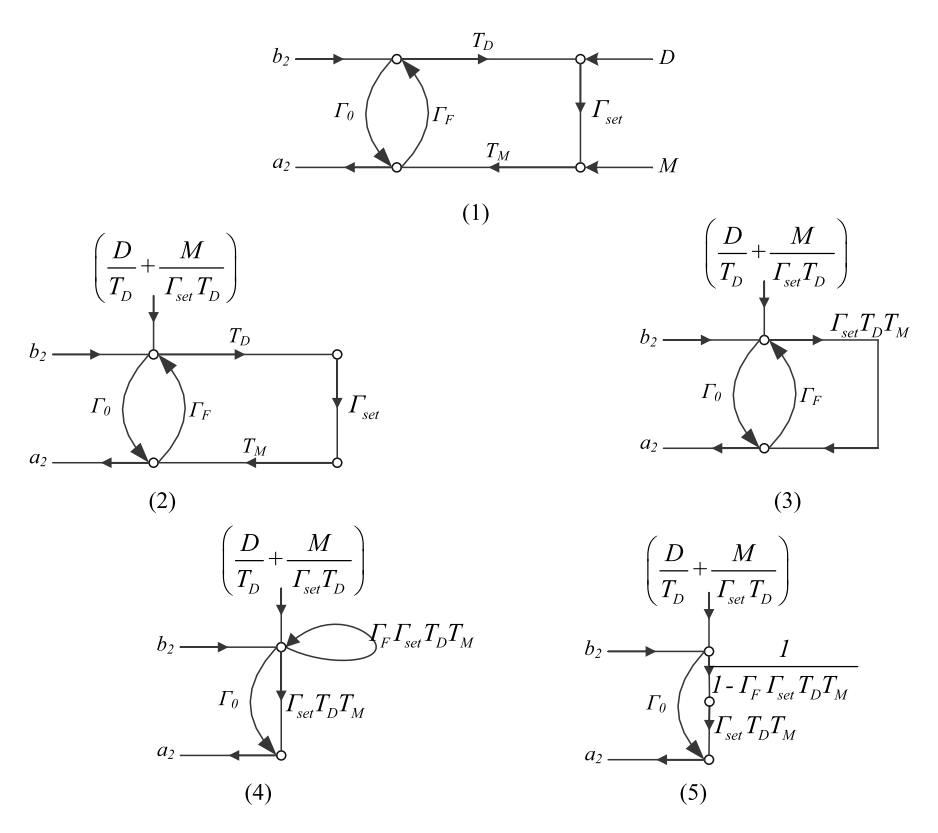


Fig. 6.8 Simplification of the error flow model of the ELP system

system with the ability to directly relate the synthesized reflection coefficient, Γ_{Load} , to the parameters of the error model.

$$\frac{a_2}{b_2} = \Gamma_{Load} = \left(\frac{\Gamma_{set} T_D T_M}{1 - \Gamma_F (\Gamma_{set} T_D T_M)} + \Gamma_0\right) \tag{6.17}$$

Equation (6.17), which is a first-order control equation describing the behavior of the ELP setup, can be simplified to obtain a linear equation, as given in Eq. (6.20).

$$\Gamma_{Load} = \left(\frac{\Gamma_{set}G}{1 - \Gamma_{E}(\Gamma_{set}G)} + \Gamma_{0}\right) \tag{6.18}$$

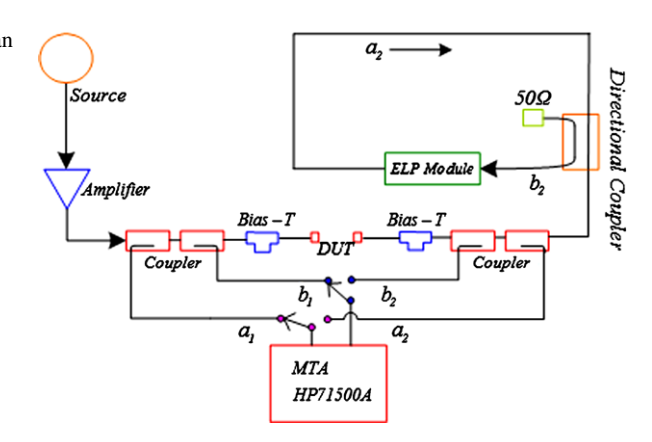
$$\Gamma_{Load} - \Gamma_{Load}\Gamma_{set}(\Gamma_F G) = \Gamma_0 + \Gamma_{set}[G(1 - \Gamma_0 \Gamma_F)]$$
(6.19)

$$\Gamma_{Load} = A + B\Gamma_{Load}\Gamma_{set} + C\Gamma_{set}$$
 (6.20)

where G represents the factor $T_D T_M$ and is termed as the gain of the ELP loop, and $A = \Gamma_0$, $B = \Gamma_F G$ and $C = G(1 - \Gamma_0 \Gamma_F)$.

It can be observed that the simplified equation (Eq. (6.20)), which is analogous to the 1-port error model calibration equation of any standard vector network analyzer (VNA) [27], relates the measured reflection coefficient at the DUT plane to the

Fig. 6.9 Block diagram of an ELP setup integrated in a waveform measurement system for the purpose of calibration [9], © IOP Measurement Science and Technology 2010



reflection coefficient set by the ELP system and the error terms introduced by the imperfect system components.

6.4.3 Calibration Technique

The three unknown terms, A, B and C, in Eq. (6.20) need to be determined, in order to calibrate the ELP system. In theory, calibration measurements on three distinct values of reflection coefficients, which are called ELP calibration standards and are defined through control variables X and Y, can enable the determination of the unknowns, A, B and C. In practice, however, it is preferable to perform calibration measurements on a higher number of calibration standards, in order to minimize random errors, and then to use the least squares method [28] to determine the unknowns, A, B and C. The ELP calibration standards can be increased just by varying variables X and Y.

Determination of the unknowns, A, B and C, enable the extraction of the error terms, Eqs. (6.21) to (6.23), of the error flow model.

$$\Gamma_0 = A \tag{6.21}$$

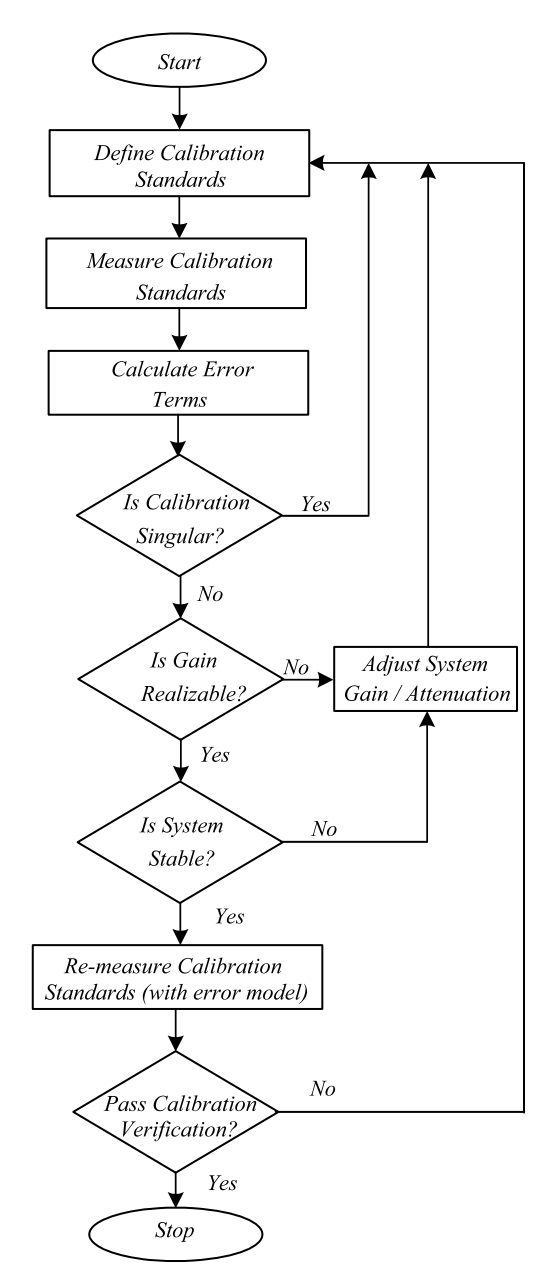
$$G = T_D T_M = C + BA \tag{6.22}$$

$$\Gamma_F = \frac{B}{G} \tag{6.23}$$

Finally, substitutions of the above equations into Eq. (6.17) allow for the prediction of the precise values of X and Y needed for the synthesis of any reflection coefficient, Γ_{Load} , at the DUT plane. Calibration of the ELP setup requires a vector corrected network analyzer, such as a waveform measurement system [29–35], an example of which is the two-channel, pre-calibrated, time-domain waveform measurement system shown in Fig. 6.9, and a step-by-step calibration procedure, as outlined in Fig. 6.10.

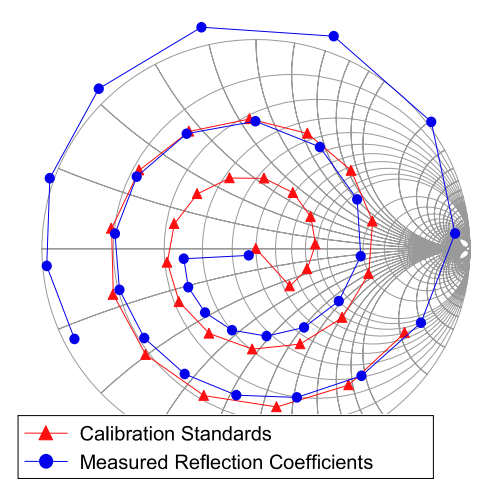
6.4 ELP Calibration 149

Fig. 6.10 Flow chart outlining the steps for systematically calibrating the ELP system [8], © IEEE 2010



As a first step, distinct calibration standards of thirty points, which are obtained by varying variables X and Y, are defined and measured. The calibration standards and the measured reflection coefficients shown in Fig. 6.11 do not match up and, therefore, experimentally verify the need for ELP calibration. Error terms are

Fig. 6.11 Uncalibrated performance of an ELP system over a 30-point data set [8], © IEEE 2010



calculated using Eqs. (6.18) to (6.23), and the system checks if the gain, G, is realizable. G is dependent on the attenuator and loop amplifier settings (Fig. 6.6), which need to be changed appropriately until the check returns positive confirmation.

With a positive result for the gain check, the system is checked for stability by considering the denominator of Eq. (6.18). In order to pass the stability test, the error terms must satisfy Eq. (6.24).

$$\left| \Gamma_F(\Gamma_{set}G) \right| < 1 \tag{6.24}$$

In case the stability test returns a negative result, the components of the system (Fig. 6.6) need to be readjusted suitably and re-measured until the test returns positive confirmation, by satisfying the stability condition in Eq. (6.24). The readjustment may be in the settings of the attenuator and/or loop amplifier, in the power level of the LOs feeding the modulator and demodulator, or in the chosen calibration standards. In the worst case, a directional coupler with better isolation between its coupled and through ports may be required to achieve stability.

With a positive stability check, the calibration standards need to be re-measured, but with a modified set given by Eq. (6.25), in order to verify the calibration procedure.

$$\Gamma_{set} = \frac{1}{G} \left(\frac{(\Gamma_{Load})_{meas} - \Gamma_0}{\Gamma_F(\{(\Gamma_{Load})_{meas} - \Gamma_0\} + 1)} \right)$$
(6.25)

The results, as illustrated in Fig. 6.12, show a perfect match between the calibration standards and the measured reflection coefficients and, therefore, verify the calibration procedure.

6.4.4 Evaluation of the Calibration Technique

The accuracy of the calibration can be quantified in terms of percentage error, e, using Eq. (6.26), where N is the number of calibration standards. It is important

6.4 ELP Calibration 151

Fig. 6.12 Measured reflection coefficients after incorporation of error terms over a 30-point data set [8], © IEEE 2010

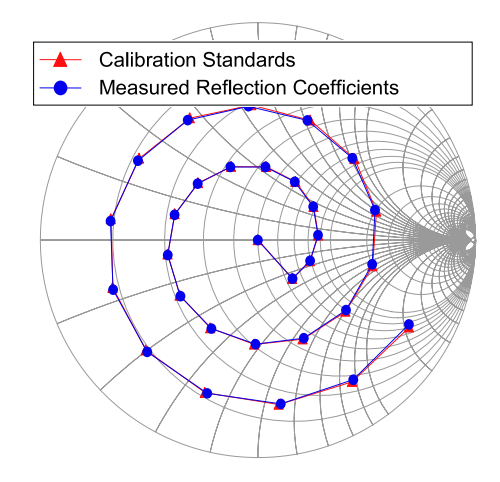


Table 6.1 Average difference between the calibration standards and the measured reflection coefficients after calibration and verification [8], © IEEE 2010

No. of calibration standards, N	e (%)	No. of calibration standards, <i>N</i>	e (%)
3	0.0456	12	0.0258
8	0.0337	20	0.0239
10	0.0271	30	0.0224

to note that a minimum of three calibration standards are needed to determine the terms of the ELP error model; therefore, Eq. (6.26) starts from N = 3.

$$e = \left(1/N\sum_{3}^{N} \frac{|(\Gamma_{Load})_{meas} - \Gamma_{set}|}{|\Gamma_{set}|}\right) \times 100$$
 (6.26)

The percentage errors for different numbers of calibration standards are listed in Table 6.1, which shows a substantial improvement in accuracy with the increasing number of calibration standards. As a compromise between the measurement speed and the calibration accuracy, it is reasonable to assume that a calibration procedure utilizing 12–20 calibration standards provides suitably accurate results [7].

Table 6.2, which provides information about the ELP calibration at varying frequencies, shows that the calibration accuracy is independent of the operating frequency.

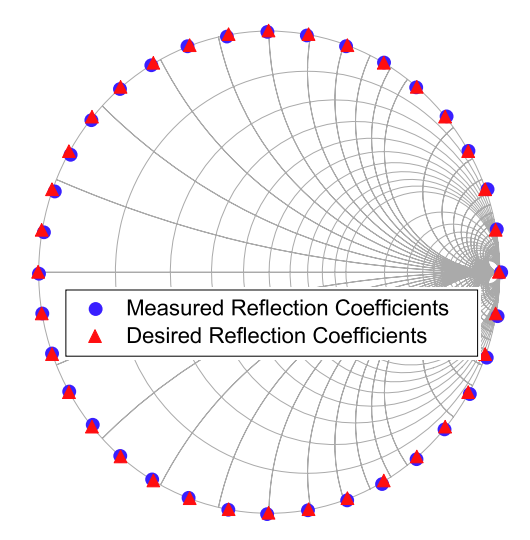
Figure 6.13 illustrates the comparison between the calibrated measured reflection coefficients and the desired reflection coefficients at the extreme edge of the Smith chart. This is a stringent measure to test the calibration accuracy; and, in this case, the two sets of reflection coefficients overlay each other, thereby demonstrating good calibration accuracy.

It can, therefore, be concluded that the ELP calibration, which is independent of the operating frequency, the number of calibration standards, or the location of the

Table 6.2 Average difference between the 12 calibration standards and the respective measured reflection coefficients [8], © IEEE 2010

Carrier frequency (MHz)	e (%)	Carrier frequency (MHz)	e (%)
850	0.0252	1800	0.0258
900	0.0255	2100	0.0259

Fig. 6.13 Evaluation of the ELP calibration process over a 36-point data set [16], © IEEE 2010



desired reflection coefficients, is accurate and versatile and, thus, helps in designing a reliable active load-pull measurement system as compared to open-loop active load-pull systems [13, 14].

The ELP calibration speed is another key parameter in improving the load-pull measurement throughput and speeding up of power amplifier design/optimization [7]. For example, an ELP system that integrated into a two-channel waveform measurement setup [33] takes 15 minutes when subjected to 30 point calibration standards; whereas, the calibration evaluation over 36 points takes a further 18 minutes [7, 8]. Therefore, on average, an ELP system can be calibrated, evaluated and then employed in load-pull measurement applications in just over 30 minutes. As a comparison, passive load-pull systems typically need pre-characterization of tuners over hundreds of points, covering all frequency ranges, thus requiring significantly more time [36].

The key features of ELP system calibration can be summarized in the following points:

- The equation representing the error flow model of an ELP setup is similar to 1-port error flow model equation of any standard vector network analyzer.
- The calibration can be carried out with as low as three calibration standards.

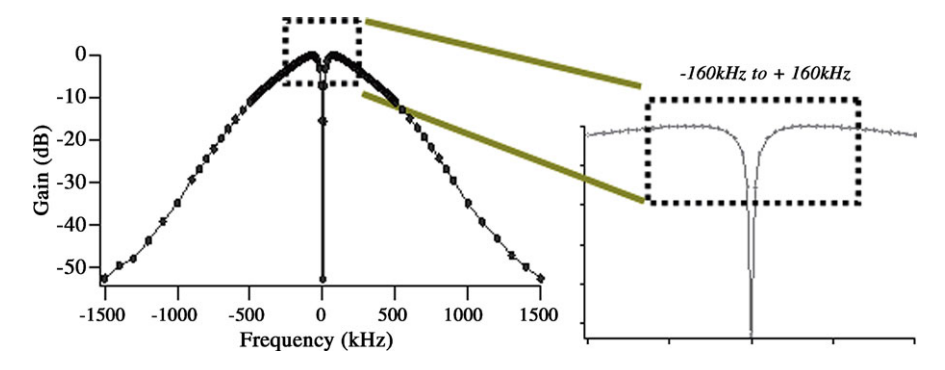


Fig. 6.14 Frequency response of the control unit of a prototype ELP setup

- Calibration accuracy can be improved by increasing the number of calibration standards. The standards are not physical, but can be created through variations of control variables, X and Y.
- The accuracy of calibration is not dependent on the operating frequency.
- The calibration is rapid and, therefore, improves the load-pull measurement throughput.

6.5 Stability Analysis

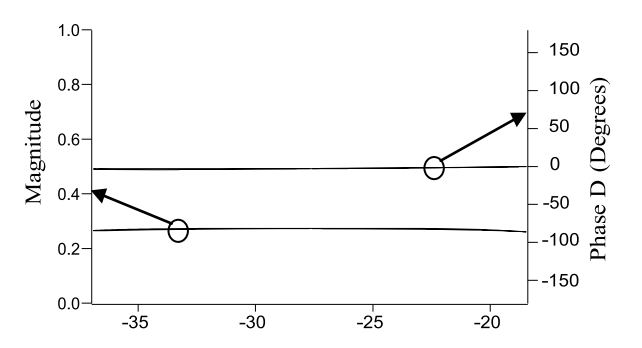
The ELP system is based on a closed-loop feedback concept and, thus, has the potential of creating instability in the measurement setup [37]. Equation (6.18) can be analyzed to address the stability issues in the ELP system. The system is free from oscillations if the denominator in Eq. (6.18) satisfies the following relationship:

$$\left|\Gamma_F(\Gamma_{set}G)\right| < 1 \implies \left|\Gamma_{set}\right| < \frac{1}{\left|\Gamma_F G\right|}$$
 (6.27)

From Eq. (6.27), it can be deduced that the ELP system never goes into oscillation as long as the magnitude of the desired reflection coefficient, Γ_{set} , synthesized through the variation of X and Y does not go beyond the product of the error terms Γ_F and G. In order to achieve this condition, the directional coupler must have a high-isolation capability and the gain/attenuation in the loop must be appropriately regulated through the adjustment of Atten and AMP in Fig. 6.6, so as to obtain a higher product of Γ_F and G.

Alternatively, the frequency response of the baseband section of the system can be monitored to identify and mitigate any oscillation in the loop. For example, Fig. 6.14 illustrates the baseband frequency response of a typical prototype ELP system [39]. It can be observed that the response rolls off beyond $-160~\rm kHz$ and $+160~\rm kHz$, without any peaking characteristics beyond this range. There is also a stop band in the response, due to the DC blocks used in the ELP prototype. The setup must be calibrated and operated in the maximum gain region, in this case between $-160~\rm kHz$ and $+160~\rm kHz$, in order to ensure that the oscillation never occurs.

Fig. 6.15 Measured magnitude and phase of the reflection coefficient on a THRU standard at a carrier frequency of 1.8 GHz for a constant value of the control variables *X* and *Y*, as drive power is swept from —38 dBm to —18 dBm [23], © IEEE 2005



On a side note, the baseband section in the ELP setup functions as a default bandpass filter, removing the need for any additional highly selective filters to achieve stability, which are normally required in the traditional closed loop active load-pull system [38].

6.6 Features of the Envelope Load-Pull System

Load-pull measurements and characterizations often involve input power, P_{in} , sweeps at several load reflection coefficients, Γ_{Load} , in order to either extract optimal performance from transistor devices or validate nonlinear transistor models at varying drive levels. Any load-pull system exhibiting drive-level independent reflection coefficients synthesis capability is, therefore, appropriate for such applications, as they can perform measurements in a rapid manner. An ELP system also fulfills this criterion, as illustrated in Fig. 6.15, and, thus, satisfies the requirements of swept power load-pull measurement applications. This result has been achieved using the ELP configuration of Fig. 6.10; and, in this particular case, the setup synthesizes non-varying reflection coefficients over a drive level from -38 to -18 dBm and, thus, exhibits a dynamic range of 20 dB [23]. The dynamic range of the ELP system, is dependent on the dynamic range of the components used to assemble the system and can be enhanced by employing components that possess higher dynamic ranges and better performance.

The ELP system can be easily reconfigured to meet the requirements of high-power device measurements and characterizations. The required baseband processing for reflection coefficient synthesis at the DUT plane for any device is the same, except that with distinct devices it will require appropriate readjustment of the attenuator and loop amplifier at the ELP module plane, as illustrated in Fig. 6.16. However, it is important to note that any change in the settings of the attenuator and/or loop amplifier invalidates the current calibration, necessitating recalibration of the ELP setup.

Some applications, such as class-F mode power amplifier design [6], require a load-pull system capable of synthesizing bias-level independent reflection coefficients. The ELP system, like the traditional passive load-pull systems, has the ability to synthesize bias-level independent reflection coefficients [39].

Fig. 6.16 Block diagram depicting the ELP module plane, which needs to be reconfigured appropriately for meeting the requirements of high-power devices

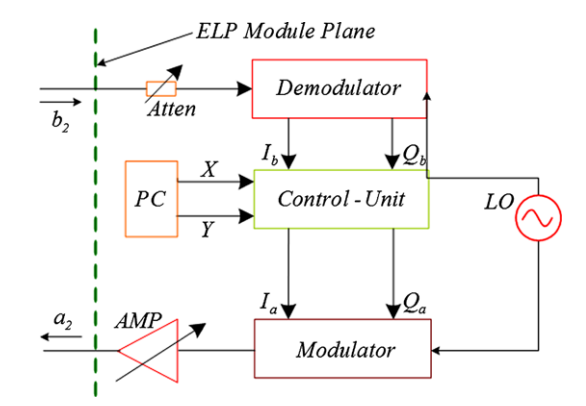
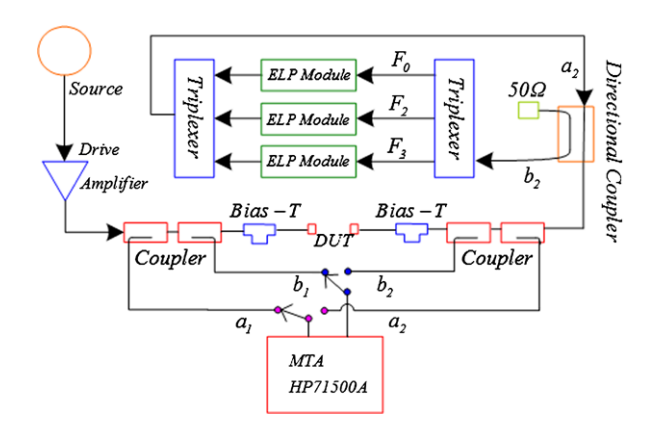


Fig. 6.17 Configuration of the 3-harmonic ELP system within the two-channel time-domain waveform measurement system [8], © IEEE 2010



6.7 Harmonic Envelope Load-Pull System

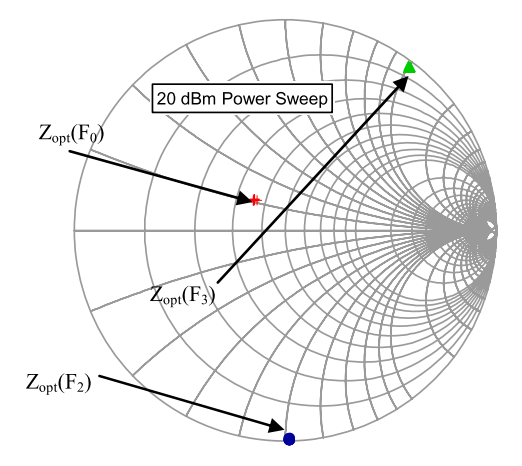
The ELP system can be easily extended for multi-harmonic applications. The ELP approach is an active technique; therefore, a triplexer-based harmonic architecture, as shown in Fig. 6.17, is preferred, since it provides better isolation between the synthesized reflection coefficients at the fundamental and harmonic frequencies. The three-harmonic ELP setup is similar to the fundamental setup, with additional triplexers before and after the bank of three ELP modules to separate and then recombine the frequency components of the incident and reflected traveling waves, b_2 and a_2 respectively.

The utilization of a harmonic ELP system in measurement applications requires calibration of each of the ELP modules based on the calibration technique described in Sect. 6.4. Table 6.3 provides the calibration data for the three ELP modules. It can be observed that the accuracy of the calibration is independent of the harmonic power and frequency. This result, thus, conveys that the ELP calibration technique is independent of the frequency and the power level of the traveling waves a_2 and b_2 .

Table 6.3 Average difference between the calibration standards and the measured reflection coefficients at each harmonic frequency, after calibration and verification at a fundamental frequency of 850 MHz [8], © IEEE 2010

No. of Fundamental Second Third calibration (F_0) harmonic harmonic standards, N (F_2) (F_3) 0.0258 12 0.0252 0.0276 20 0.0237 0.0243 0.0259 10 0.0271 30 0.0224

Fig. 6.18 Measurement data depicting drive and harmonically independent reflection coefficient emulation capability of the harmonic ELP system [7], © IEEE 2009



In principle, harmonic load-pull applications require the capability of synthesizing harmonically independent reflection coefficients. This feature is essential for accurate performance estimation of transistor devices. In practice, however, with the exception of the traditional closed-loop active load-pull architecture, none of the load-pull systems possess this capability. On the other hand, the ELP can readily synthesize harmonically independent reflection coefficients [7, 8], as illustrated in Fig. 6.18. This figure depicts measured harmonic load reflection coefficients on a 1 W gallium arsenide (GaAs) field-effect transistor (FET) for the 20 dB drive power sweep at the fundamental frequency of 850 MHz and shows that the harmonic impedance does not move during the power sweep. This characteristic of the harmonic ELP technique is unique and extremely useful in accurate, rapid and reliable harmonic load-pull measurement applications, such as the harmonic load-pull optimization of the transistor device illustrated in Fig. 6.19.

The results in Fig. 6.19 show ELP harmonic load-pull measurement data for a 1 W GaAs FET device when the fundamental impedance has been swept over a 4×4 impedance grid; whereas, for each fundamental, the phase of the second-harmonic impedance has been varied in steps of 45 degrees around the extreme edge of the Smith chart, and the third-harmonic impedance has been held at 50 Ω . It can be observed that the harmonic impedances are uncoupled and unaffected by each other.

In this investigation, the whole sweep involved capturing only 128 measurements using the harmonic ELP technique, which with an open-loop active harmonic load-

Fig. 6.19 Measurement data illustrating the independent harmonic reflection coefficient synthesis capability of the harmonic ELP system [8], © IEEE 2010

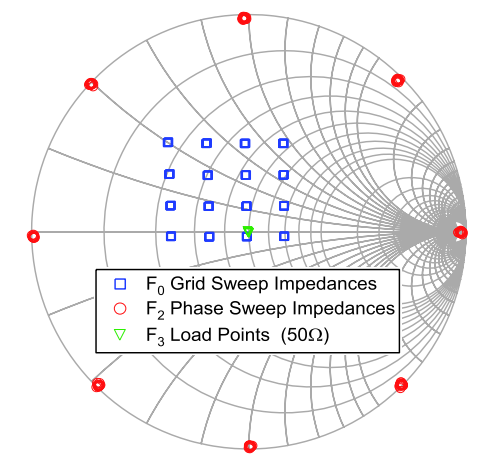
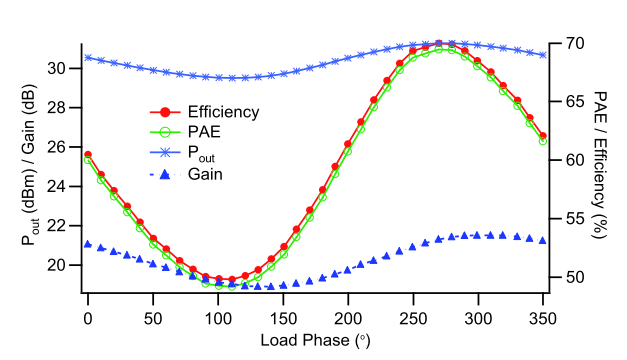


Fig. 6.20 Measurement of PA design parameters by sweeping the phase of the second-harmonic reflection coefficient, $\Gamma(F_2)$, while maintaining constant $\Gamma(F_0)$ and $\Gamma(F_3)$ [9], © IOP Measurement Science and Technology 2010



pull system would require at least 15 times more (1920) measurements, due to the system needing to iterate and converge on the harmonic impedances [22]. This feature of the ELP system results, in most cases, reduced characterization time and, hence, increased measurement throughput.

6.8 Unique Measurement Applications

The independent harmonic reflection coefficient synthesis capability of the ELP system enables investigation into the impact of harmonic terminations and their precise effects on the power amplifier (PA) design parameters, in order to optimize the transistor devices for PA design applications. For example, the impact of a second-harmonic termination on a 1 W GaAs FET device that has been subjected to its optimal fundamental reflection coefficient, $\Gamma(F_0)$, and matched third-harmonic reflection coefficient, $\Gamma(F_3)$, into 50 Ω is illustrated in Fig. 6.20. In this investigation, the phase of the second-harmonic reflection coefficient, $\Gamma(F_2)$, has been swept every 10 degrees for $|\Gamma(F_2)| = 1$; and, data has been collected on a two-channel waveform

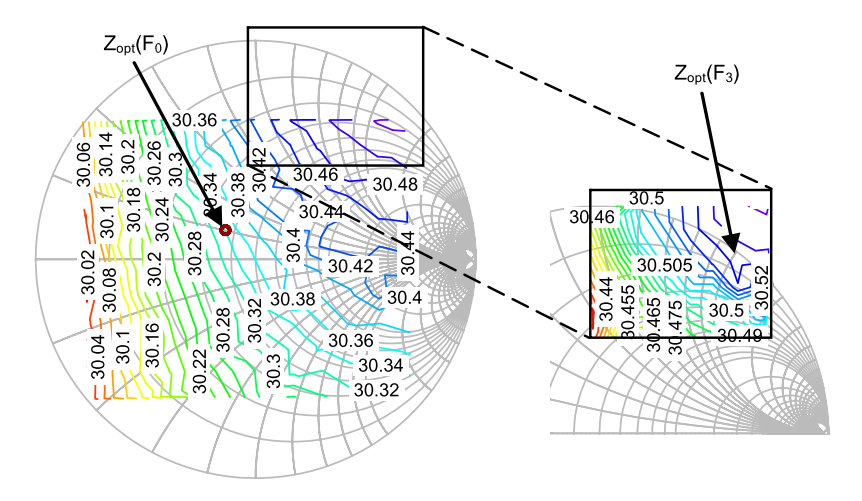


Fig. 6.21 Output fundamental power contours from sweeping third-harmonic reflection coefficients, $\Gamma(F_3)$, over 12×12 and 6×4 grids, holding $Z_{opt}(F_0) = 36.3 + j9.9 \Omega$ [7], © IEEE 2009

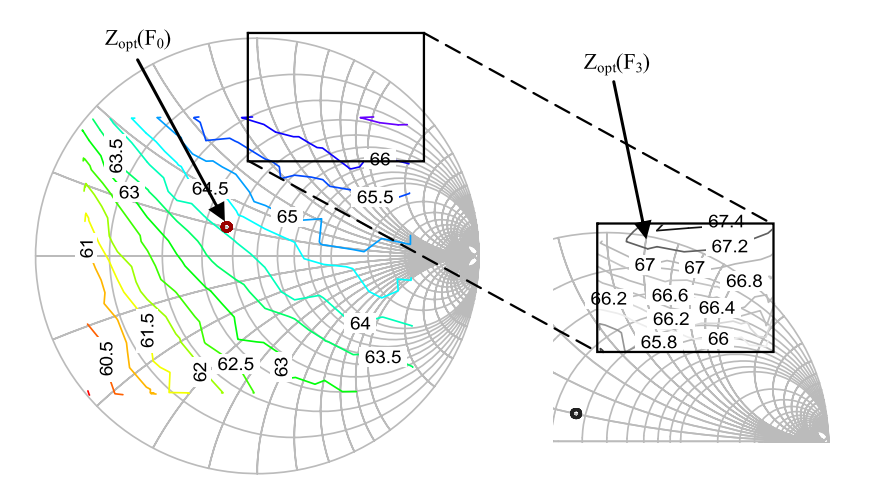


Fig. 6.22 Drain efficiency contours from sweeping third-harmonic reflection coefficients, $\Gamma(F_3)$, over 12×12 and 6×4 grids, holding $Z_{opt}(F_0) = 36.3 + j9.9 \Omega$ [7], © IEEE 2009

measurement setup. It can be observed that the PA design parameters are highly sensitive to variations of the phase of the second-harmonic reflection coefficient.

In practice, this investigation can be carried out using traditional active and passive load-pull systems; however, the accuracy and reliability in the measurement data remain questionable, considering the inability of these systems to synthesize harmonically independent reflection coefficients. Furthermore, this type of investigation usually requires significantly more time (tenfold) on a similar open-loop harmonic active load-pull system compared to the harmonic ELP system [39].

The rapid and harmonically independent reflection coefficient synthesis capability of the ELP system can be employed in measurements where the effect of a large number of impedances on a device needs to be investigated for their optimization in PA design applications. Figures 6.21 and 6.22, for example, illustrate the effect of third-harmonic reflection coefficient variation on the output power and drain efficiency, respectively, of a 1 W GaAs FET device at a fundamental frequency of 850 MHz.

In this investigation, fundamental and second-harmonic reflection coefficients remain fixed to their optimal values and 50 Ω , respectively. The measurements involve a 12 × 12 third-harmonic reflection coefficient grid on a broader area of Smith chart, in order to check the sensitivity of its variation on the output power and drain efficiency and to determine the Smith chart region where the optimal position of third-harmonic reflection coefficient may be. The measurement required a further 6 × 4 reflection coefficient grid sweep to find the precise location of $\Gamma_{opt}(F_3)$ for the optimal output power and drain efficiency.

The determination of optimal third-harmonic reflection coefficients and, therefore, the respective third-harmonic impedances of $1.3+j100~\Omega$ and $0.6+j60.4~\Omega$ for optimal output power and drain efficiency, which requires 168 measurements, take just over 75 minutes for the measurements on an ELP system integrated into a two-channel waveform measurement setup [39]. This type of measurement and investigation is not usually possible through traditional passive and active load-pull systems. Furthermore, an open-loop harmonic active load-pull system, irrespective of its inability to synthesize independent harmonic reflection coefficients, would require 10 times more measurement time on a similar setup.

The multi-harmonic ELP system can also be used to conduct load-pull measurements to discover the continuous high efficiency and output power from a device, through the control of fundamental and harmonic reflection coefficients in a precisely controlled manner [10, 12]. These measurements are essential in the design of PAs, such as class-J and class-J* [40].

One such investigation, illustrated in Fig. 6.23, requires measurements of 15 specific fundamental and second-harmonic reflection coefficients at the package plane of a 2 W gallium nitride (GaN) device. This measurement needs the fundamental and second-harmonic reflection coefficients to be directly related, with the reactive components of fundamental and second-harmonic impedances being in a ratio of 1:2 for fixed real components of the fundamental and harmonic impedances, in order to obtain constant output power and drain efficiency from the device, as shown in Fig. 6.24.

The results in Fig. 6.24 show the achieved contours of constant efficiency and output power, with less than 1 % deviation in a drain efficiency around 70 % and only 0.1 dB deviation in the 34.5 dBm output power over the selected range of fundamental and harmonic reflection coefficient variation. This type of investigation to achieve a highly efficient linear mode PA, using experimental device probing and design, can only be carried out by employing an ELP system as other load-pull systems are either incapable or too slow for this purpose.

Fig. 6.23 Depiction of robust harmonic load reflection coefficient control by employing the developed harmonic envelope load-pull system [8], © IEEE 2010

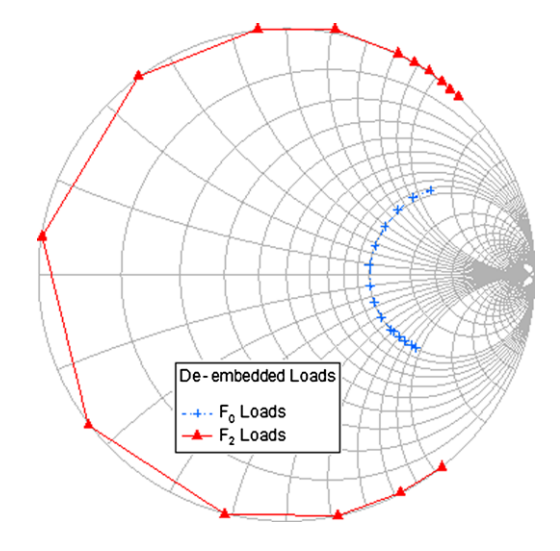
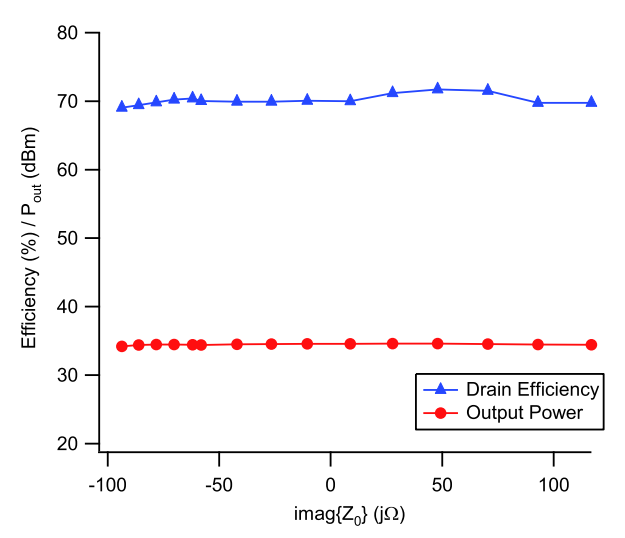


Fig. 6.24 Demonstration of constant power output and efficiency with respect to changing reactance through the use of an envelope load-pull system [8], © IEEE 2010



References

- Focus Microwaves, Product catalogue, http://www.focus-microwaves.com/template.php? unique=4. Accessed Oct. 2010
- Maury Microwave Corporation, Product catalogue, http://www.maurymw.com/mmc_catalog/ mmccatalog06.htm. Accessed Oct. 2010
- 3. Mesuro, Product catalogue, http://www.mesuro.com/products.htm. Accessed Oct. 2010
- Real Time Passive Source/Load Pull Systems, PAF product, http://www.se-group.com/doc/ paf.pdf. Accessed Oct. 2010
- R. Negra, F.M. Ghannouchi, W. Bachtold, Study and design optimization of multiharmonic transmission-line load networks for class-E and class-F K-band mmic power amplifiers. IEEE Trans. Microw. Theory Tech. 55(6), 1390–1397 (2007)

References 161

 C. Roff, J. Benedikt, P.J. Tasker, Design approach for realization of very high efficiency power amplifiers, in *IEEE MTT-S International Microwave Symposium Digest* (June 2007), pp. 143– 146

- M.S. Hashmi, A.L. Clarke, S.P. Woodington, J. Lees, J. Benedikt, P.J. Tasker, Electronic multiharmonic load-pull system for experimentally driven power amplifier design optimization, in *IEEE MTT-S International Microwave Symposium*, Boston, USA, vols. 1–3 (June 2009), pp. 1549–1552
- 8. M.S. Hashmi, A.L. Clarke, S.P. Woodington, J. Lees, J. Benedikt, P.J. Tasker, An accurate calibrate-able multi-harmonic active load-pull system based on the envelope load-pull concept. IEEE Trans. Microw. Theory Tech. **58**(3), 656–664 (2010)
- M.S. Hashmi, A.L. Clarke, J. Lees, M. Helaoui, P.J. Tasker, F.M. Ghannouchi, Agile harmonic envelope load-pull system enabling reliable and rapid device characterization. IOP Meas. Sci. Technol. 21(055109), 1–9 (2010)
- S.C. Cripps, P.J. Tasker, A.L. Clarke, J. Lees, J. Benedikt, On the continuity of high efficiency modes in linear RF power amplifiers. IEEE Microw. Wirel. Compon. Lett. 19(10), 665–667 (2009)
- P. Wright, J. Lees, J. Benedikt, P.J. Tasker, S.C. Cripps, A methodology for realizing high efficiency class-J in a linear and broadband PA. IEEE Trans. Microw. Theory Tech. 57(12), 3196–3204 (2009)
- F.M. Ghannouchi, M.S. Hashmi, Experimental investigation of the uncontrolled higher harmonic impedances effect on the performance of high-power microwave devices. Microw. Opt. Technol. Lett. 52(11), 2480–2482 (2010)
- H.M. Nemati, A.L. Clarke, S.C. Cripps, J. Benedikt, P.J. Tasker, C. Fager, J. Grahn, H. Zirath, Evaluation of a GaN HEMT transistor for load- and supply-modulation applications using intrinsic waveform measurements, in *IEEE MTT-S International Microwave Symposium Digest* (May 2010), pp. 509–512
- A.L. Clarke, M. Akmal, J. Lees, J. Benedikt, P.J. Tasker, Investigation and analysis into device optimization for attaining efficiencies in-excess of 90 % when accounting for higher harmonics, in *IEEE MTT-S International Microwave Symposium Digest* (May 2010), pp. 1114–1117
- R. Hajji, F.M. Ghannouchi, R.G. Bosisio, Large-signal microwave transistor modeling using multiharmonic load-pull measurements. Microw. Opt. Technol. Lett. 5(11), 580–585 (1992)
- H. Qi, J. Benedikt, P.J. Tasker, Nonlinear data utilization: from direct data lookup to behavioral modeling. IEEE Trans. Microw. Theory Tech. 57(6), (2009)
- 17. P. Berini, F.M. Ghannouchi, R.G. Bosisio, Active load characterization of a microwave transistor for oscillator design, in *IEEE Instrumentation & Measurements Technology Conference*, Ottawa, Canada (May 1997), pp. 668–673
- 18. F.M. Ghannouchi, F. Beauregard, A.B. Kouki, Power added efficiency and gain improvement in MESFETs amplifiers using an active harmonic loading technique. Microw. Opt. Technol. Lett. **7**(13), 625–627 (1994)
- 19. G. Zhao, S. El-Rabaie, F.M. Ghannouchi, The effects of biasing and harmonic loading on MESFET tripler performance. Microw. Opt. Technol. Lett. **9**(4), 189–194 (1995)
- E. Bergeault, O. Gibrat, S. Bensmida, B. Huyart, Multiharmonic source-pull/load-pull active setup based on six-port reflectometers: influence of the second harmonic source impedance on RF performances of power transistors. IEEE Trans. Microw. Theory Tech. 52(4), 1118–1124 (2004)
- 21. Y.Y. Woo, Y. Yang, B. Kim, Analysis and experiments for high efficiency class-F and inverse class-F power amplifiers. IEEE Trans. Microw. Theory Tech. **54**(5), 1969–1974 (2006)
- J. Benedikt, R. Gaddi, P.J. Tasker, M. Goss, M. Zadeh, High power time domain measurement system with active harmonic load-pull for high efficiency base station amplifier design, in *IEEE/MTT-S International Microwave Symposium*, Boston, USA (June 2000), pp. 1459–1462
- T. Williams, J. Benedikt, P. Tasker, Experimental evaluation of an active envelope load-pull
 architecture for high speed device characterization, in *IEEE/MTT-S International Microwave Symposium*, vol. 3, Long Beach, USA (June 2005), pp. 1509–1512

- 24. T. Williams, J. Benedikt, P.J. Tasker, Application of a novel active envelope load-pull architecture in large signal device characterization, in *IEEE 35th European Microwave Conference Digest*, Paris, France (Oct. 2005), 4 pp.
- S.J. Hashim, M.S. Hashim, T. Williams, S. Woodington, J. Benedikt, P.J. Tasker, Active envelope load-pull for wideband multi-tone stimulus incorporating delay compensation, in 38th IEEE European Microwave Conference, Amsterdam, The Netherlands (Oct. 2008), pp. 317–320
- D.M. Pozar, Microwave Engineering, 3rd edn. (Wiley, New York, 2005). ISBN 0-471-17096-
- R. Ludwig, P. Bretchko, RF Circuit Design: Theory and Applications, 2nd edn. (Pearson, Upper Saddle River, 2008). ISBN 13-978-013-13555-07
- E. Kreyszig, Advanced Engineering Mathematics, 8th edn. (Wiley, New York, 2000). ISBN 13-9780471488859
- M. Sipila, K. Lehtinen, V. Porra, High-frequency periodic time-domain waveform measurement system. IEEE Trans. Microw. Theory Tech. 36(10), 1397–1405 (1988)
- U. Lott, Measurement of magnitude and phase of harmonics generated in nonlinear microwave two-ports. IEEE Trans. Microw. Theory Tech. 37(10), 1506–1511 (1989)
- 31. F. van Raay, G. Kompa, A new on-wafer large-signal waveform measurement system with 40 GHz harmonic bandwidth, in *IEEE MTT-S International Microwave Symposium Digest*, vol. 3 (June 1992), pp. 1435–1438
- 32. D. Barataud, C. Arnaud, B. Thibaud, M. Campovecchio, J.-M. Nebus, J.P. Villotte, Measurements of time-domain voltage/current waveforms at RF and microwave frequencies based on the use of a vector network analyzer for the characterization of nonlinear devices-application to high-efficiency power amplifiers and frequency-multipliers optimization. IEEE Trans. Instrum. Meas. 47(5), 1259–1264 (1998)
- 33. D.J. Williams, P.J. Tasker, An automated active source and load-pull measurement system, in 6th IEEE High Frequency Student Colloquium Digest (Sep. 2001), pp. 7–12
- 34. S. Bensmida, P. Poire, R. Negra, F.M. Ghannouchi, G. Brassard, New time-domain voltage and current waveform measurement setup for power amplifier characterization and optimization. IEEE Trans. Microw. Theory Tech. **56**(1), 224–231 (2008)
- 35. W.S. El-Deeb, M.S. Hashmi, S. Bensmida, N. Boulejfen, F.M. Ghannouchi, Thru-less calibration algorithm and measurement system for on-wafer large-signal characterization of microwave devices, in *IET Microwaves, Antenna and Propagation* (2010)
- C. Roff, J. Graham, J. Sirois, B. Noori, A new technique for decreasing the characterization time of passive load-pull tuners to maximize measurement throughput, in 72nd Automatic Radio Frequency Techniques Group (ARFTG) Conference Digest, Portland, USA (Dec. 2008), pp. 92–96
- K. Ogata, Modern Control Engineering, 5th edn. (Prentice Hall, New York, 2009). ISBN 13-978-013-6156734
- 38. A. Ferrero, V. Teppati, G.L. Madonna, U. Pisani, Overview of modern load-pull and other non-linear measurement systems, in *Automatic RF Techniques Group Conference (ARFTG) Digest* (June 2001), pp. 1–5
- M.S. Hashmi, Analysis, realization and evaluation of envelope load-pull system both for CW and multi-tone applications, PhD Thesis, Cardiff University, 2009
- J.D. Rhodes, Output universality in maximum efficiency linear power amplifiers. Int. J. Circuit Theory Appl. 31, 385–405 (2003)

Chapter 7

Waveform Measurement and Engineering

In this chapter, techniques to develop high-frequency nonlinear time-domain waveform measurement systems are discussed along with critical issues related to these systems. The description entails two aspects, namely the development of a test set and the subsequent calibration mechanism for determining the absolute values of magnitudes and phases of the individual harmonic components when the transistor devices are operated in the nonlinear region. Finally, the waveform engineering technique along with some of its applications in the context of power amplifiers is discussed.

7.1 Introduction

The study of nonlinear semiconductor devices for obtaining the best insight into the device behavior often requires detailed consideration of the time-varying current and voltage waveforms on the terminals of such devices. For example, the operation mode of radio frequency power amplifiers (RFPAs) can be effectively identified by looking at the time-domain current and voltage (I-V) waveforms at the output terminal of transistor devices. Figure 7.1 depicts such a scenario for a current-mode class-D amplifier.

When active microwave devices are subjected to periodic nonlinear operation, there is high harmonic content in the I-V waveforms. If these waveforms are measured in such a manner that they contain all the relevant associated harmonics, valuable information would be obtained for the understanding and modeling of these devices. For example, if the terminal voltages and currents waveforms of an RFPA are measured, it can be optimized for optimal design parameters, such as output power, direct current (DC) to RF (radio frequency) power conversion efficiency, gain [1–4]. In addition, these terminal waveforms also enable appropriate nonlinear device models for RFPA applications [5].

As a result, it is suggested that, for an RFPA, the terminal I-V waveforms are the unifying theoretical link between transistor technology, circuit design and system

Fig. 7.1 Current mode class-D amplifier schematic and the ideal respective current and voltage waveforms across each transistor

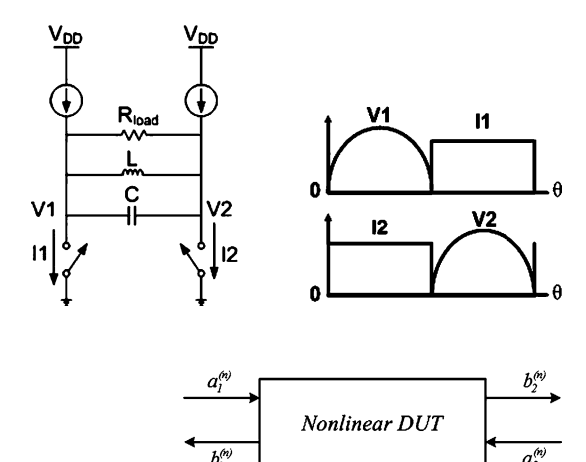


Fig. 7.2 Depiction of traveling waves at a nonlinear two-port DUT

performance [6, 7]. The investigation of such a hypothesis requires an appropriate measurement system that can measure I-V waveforms at high frequencies. It should be understood that the time-domain waveforms at low frequencies can be easily measured using any standard oscilloscope. At RF and microwave frequencies, however, the scenario is completely different.

The difficulty in measuring high-frequency I-V waveforms stems not just from the inability of the standard scopes to measure all the harmonic components due to the limitation of the bandwidth of the scopes: the problem mainly occurs from the generic technological limitations that are very common at high frequencies. The standard probes at microwave frequencies generate reflections, due to the comparable size of probe and the wavelength of the waves being measured, which have the potential to damage the device under test (DUT) and the measurement system due to high VSWR that can occur in the transmission line of the system resulting from the reflections.

High-speed sampling oscilloscopes can fulfill the bandwidth requirements; however, in the microwave region, there are systematic errors that are introduced by the frequency response of the measurement system, mismatches, multiple reflections and other factors. As a consequence, appropriate calibration algorithms are employed to correct for these errors [8–10] at fundamental frequency and the relevant harmonics present in the I-V waveforms.

7.2 Theoretical Formulation

The periodic current and voltage waveforms at the terminals of the DUT consist of fundamental and harmonic waves $a_k^{(n)}$ and $b_k^{(n)}$, as depicted in Fig. 7.2, with k and n representing the number of ports and harmonics, respectively.

The normalized traveling waves are defined by Eqs. (7.1) and (7.2):

$$a_k^{(n)} = \frac{V_k^{(n)} + I_k^{(n)}}{2\sqrt{2Z_0}} \tag{7.1}$$

$$b_k^{(n)} = \frac{V_k^{(n)} - I_k^{(n)}}{2\sqrt{2Z_0}} \tag{7.2}$$

where Z_0 is the reference impedance (usually 50 Ω for all harmonics); and, $V_k^{(n)}$ and $I_k^{(n)}$ are the *n*th Fourier coefficients that need to be measured, which are given in Eqs. (7.3) and (7.4), for the construction of the voltage and current waveforms at the DUT's terminals.

$$V_k^{(n)} = \sqrt{2Z_0} \left(a_k^{(n)} + b_k^{(n)} \right) \tag{7.3}$$

$$I_k^{(n)} = \sqrt{2/Z_0} \left(a_k^{(n)} - b_k^{(n)} \right) \tag{7.4}$$

Once these Fourier coefficients are known, the time-domain voltage and current waveforms at the DUT's terminals can be obtained by employing Eqs. (7.5) and (7.6), respectively.

$$v_k(t) = V_k^{(0)} + \sum_{n=1}^{N_h} V_k^{(n)} \cos(2\pi n f t - \varphi_k^{(n)})$$
 (7.5)

where $V_k^{(0)}$ is the direct current component at kth port, $V_k^{(n)}$ is the magnitude of the nth harmonic at kth port, N_h is the number of harmonics, f is the fundamental frequency, and $\varphi_k^{(n)}$ is the phase of the nth harmonic.

$$i_k(t) = I_k^{(0)} + \sum_{n=1}^{N_h} I_k^{(n)} \cos(2\pi n f t - \theta_k^{(n)})$$
 (7.6)

where $I_k^{(0)}$ the direct current component at kth port is, $I_k^{(n)}$ is the magnitude of the nth harmonic at kth port, N_h is the number of harmonics, f is the fundamental frequency, and $\theta_k^{(n)}$ is the phase of the nth harmonic.

It is evident from Eqs. (7.5) and (7.6) that the construction of time-domain current and voltage waveforms at the DUT's terminals requires absolute values of the magnitude and phase of each harmonic component. Therefore, the most appropriate time-domain waveform measurement system is the one that can accurately provide the phase and magnitude information at the harmonic component of interest.

7.3 Historical Perspectives

At low frequencies, the terminal voltage can be directly measured using a highimpedance probe, and the current through a node can be measured using a lowimpedance probe in series. At high frequencies, the high and low impedances of the probes can only be maintained across a narrow bandwidth, and conditionally stable circuits can become unstable during the measurement. In order to address this problem, non-intrusive measurement techniques are employed in which the incident and reflected energy of traveling voltage waveforms is measured [11–13]. This allows a constant measurement impedance environment ($Z_0 = 50~\Omega$) across a broad frequency bandwidth. These traveling waves are measured in terms of scattering parameters (S-parameters) [14] using a vector network analyzer (VNA) [15], which can then be converted to impedance and admittance using conversion matrices. The impedance and admittance matrices relate the sum of the voltage and current to the measurement ports.

Despite the valuable information gained from S-parameter data, the measurement technique can only be applied when the superposition principle holds true [16]. This principle prevents energy being transferred from the stimulus frequency to other harmonic frequencies. Therefore, the measurements are performed by exciting the DUT with a number of sine waves, one frequency at a time, in order to detect the response of the DUT at each stimulus frequency. This produces limitations when dealing with nonlinear networks containing active devices operating at high power levels, where the superposition principle cannot be applied, as nonlinear behavior produces additional harmonic frequency and intermodulation components.

These nonlinear effects have traditionally been measured in the frequency domain using spectrum analyzers (SAs) to estimate and assess the device performance at the fundamental and harmonic frequencies. The SA is a scalar instrument and can measure a broad spectrum in real time, while achieving very high dynamic range. In cases where modulated signals are used, an SA can measure the magnitudes of the fundamental and harmonic frequencies and the intermodulation components. However, the main limitation of such instruments is the inability to measure the phase information, thus limiting their usefulness in nonlinear device modeling applications. Nonetheless, the real-time broadband behavior of the SA provides the capability for detecting and measuring spurious signals that result from device instabilities and oscillations. All these measurements can be carried out without calibration or prior knowledge of the circuit behavior, making the SA an ideal instrument for evaluating the performance of circuits and devices operating in a nonlinear mode of operation.

The nonlinear behavior of a device or circuit can be obtained from the direct measurement of the voltage and current waveforms in the time domain using a conventional oscilloscope. The Fourier transformation of the measured time-domain waveforms gives both the magnitude and phase information for the fundamental frequency and each harmonic component. The absolute phase information gives additional information for estimating the DUT's behavior.

At high frequencies, limitations are introduced by the restricted sampling rates of the analog-to-digital converter (ADC) employed in the oscilloscope. This results in a reduced bit resolution at high frequencies, which reduces the dynamic range of the oscilloscope. Additionally, the measurement system must be fully error corrected, in terms of magnitude and phase, in order to achieve the error coefficients at each harmonic of interest before reconstruction of the I-V waveforms can be achieved at the DUT's terminals.

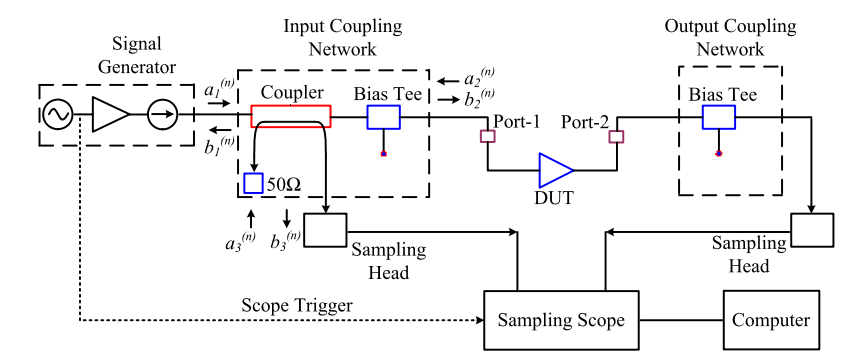


Fig. 7.3 Waveform measurement system developed using a two-channel sampling scope [17], © IEEE 1988

The first nonlinear I-V waveform measurement system that was capable of providing the absolute values of the magnitude and phase of each harmonic content of the waveform was reported in 1988 [17]. The measurement system, as depicted in Fig. 7.3, uses a two-channel high-frequency sampling oscilloscope and collects two of the four traveling waves: the reflected input wave, b_1 , and the transmitted output wave, b_2 . Using knowledge of the S-parameters of the linear input and output coupling networks at the fundamental and harmonic frequencies, the terminal current and voltage (I-V) waveforms are determined.

In this system, the calibration is performed by measuring the S-parameters of the whole system, in order to remove the error introduced by losses, mismatches and imperfect directivities in the system. The measured traveling waves are converted into the frequency domain for vector error correction, and the inverse transform is then performed to retrieve the corrected traveling waves. This approach is seen as important in the development of large-signal measurement systems, as it allows for the adoption of calibration procedures akin to those developed for the more established VNA technology.

The disadvantages of this system include the requirement to measure the S-parameters of the input and output coupling networks, leading to an increased likelihood of error in measurements. The system also suffers from noise introduced by trigger jitter, reducing the dynamic range compared to the mixer based approach adopted in VNAs. These errors become quite large at frequencies above 5 GHz, limiting the application of this system to frequencies of less than 2 GHz when accurate information up to the third harmonic component is required.

An alternate system, as depicted in Fig. 7.4, that utilizes a modified VNA architecture for the capture of time-domain I-V waveforms was reported in 1989 [18]. The most important component in the system is the calibrated VNA that measures the magnitude and phase of a constant wave signal at each frequency of interest.

This system utilizes a high-frequency Schottky diode as a reference for the purpose of determining the absolute phase of *n*th harmonic component with respect to the fundamental signal. The Schottky diode produces a calibration reference for the

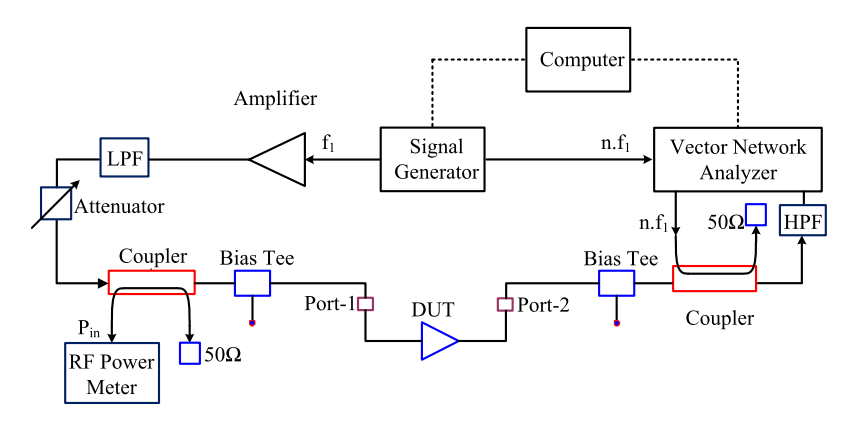


Fig. 7.4 VNA based time-domain waveform measurement system presented in [18], © IEEE 1989

absolute magnitude and phase required for reconstructing the output waveforms in the time domain.

This measurement technique offers greater dynamic range compared to that achieved using an oscilloscope, due to the use of a VNA. This system, however, is limited in its application, as it allows construction of time-domain waveforms only at the output of the DUT.

A significantly improved system based on this concept was reported in 1998 [19]. It enables the measurement of time-domain I-V waveforms at both the input and output ports of the DUT. The system employs a step recovery diode (SRD) for producing a fixed reference signal. In this system, the amplitude calibration can be achieved by attaching known calibration standards to the measurement ports; and, the SRD facilitates phase calibration, as it produces a signal with very well behaved and known phase relationship at the fundamental and harmonic frequencies.

This system, however, is inherently slow, due to presence of a VNA, considering that a frequency sweep has to be carried out for each harmonic to be measured. In addition, accurate phase coherence is difficult to achieve for fundamental and harmonic frequencies. However, it is worth mentioning that the concept employed in this system has led to the development of more advanced VNAs and is commercially available in the form of PNA-X [20].

The microwave transition analyzer (MTA) operates as a wideband, time-domain sampling oscilloscope in its main mode of operation and has the capability to conduct narrowband swept frequency measurements and acts as a VNA to measure S-parameters with a very high dynamic range. It is advantageous over other sampling oscilloscopes for two main reasons. Firstly, the sample-and-hold trigger employed in conventional sampling oscilloscopes is replaced with a mixing process in the MTA, which uses a local oscillator (LO) signal that is phase locked to one of the input signals.

The MTA is, therefore, immune to the errors introduced by trigger jitter, and time-base error is defined only by the quality of the LO signal. Thus, measurement using an MTA is significantly better than that of the sampling oscilloscopes. Several

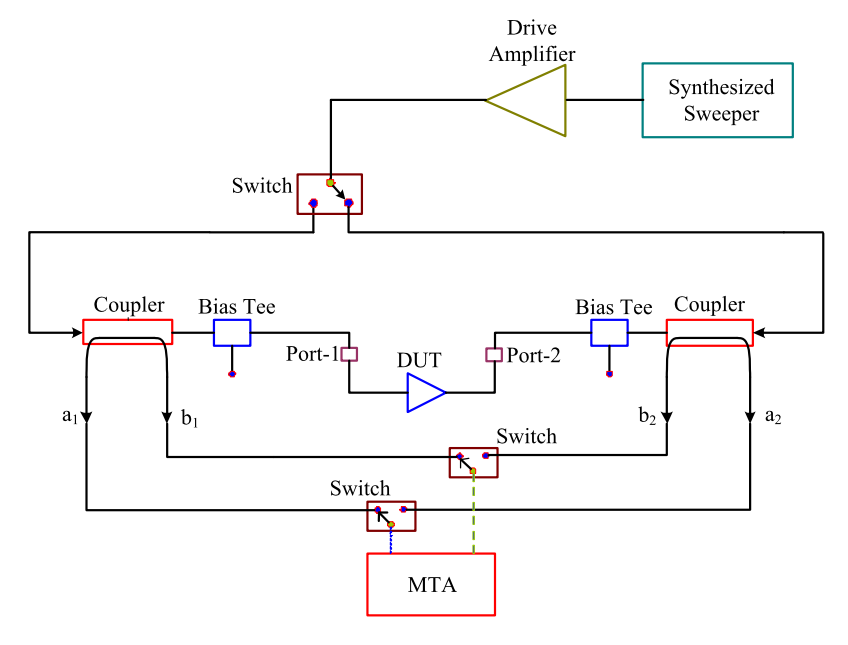


Fig. 7.5 A typical time-domain waveform measurement system built around a microwave transition analyzer (MTA)

I-V waveform measurement systems with an MTA as the main instrument have been reported [21–25] in the past two decades. One such system, as depicted in Fig. 7.5, utilizes the MTA as a multi-harmonic receiver (MHR).

As can be seen, a multiplexing network converts the two-channel MTA into a four-channel receiver, allowing measurement of all the four traveling waves in one shot. Recent advances employ more advanced MTA type receivers, such as a nonlinear vector network analyzer (NLVNA) [26] that consists of four channels and reduces the complexity of the measurement setup.

An alternative approach for determining time-domain I-V waveforms at the DUT's ports is the six-port based waveform correlator [27]. In such a system, the concept of frequency-domain reflectometry is employed; therefore, such setups when appropriately configured can also be useful for linear measurements [28].

7.4 Practical Waveform Measurement System

A typical waveform measurement setup is depicted in Fig. 7.6. The system consists of an MTA used as a complex MHR from DC to 40 GHz [29], an RF generator, four RF two-way (single pole, double throw, i.e., SPDT) switches, a control circuit for the switches, a power supply, one power divider, and two directional couplers. The entire system is controlled by a personal computer (PC) via general purpose interface bus (GPIB).

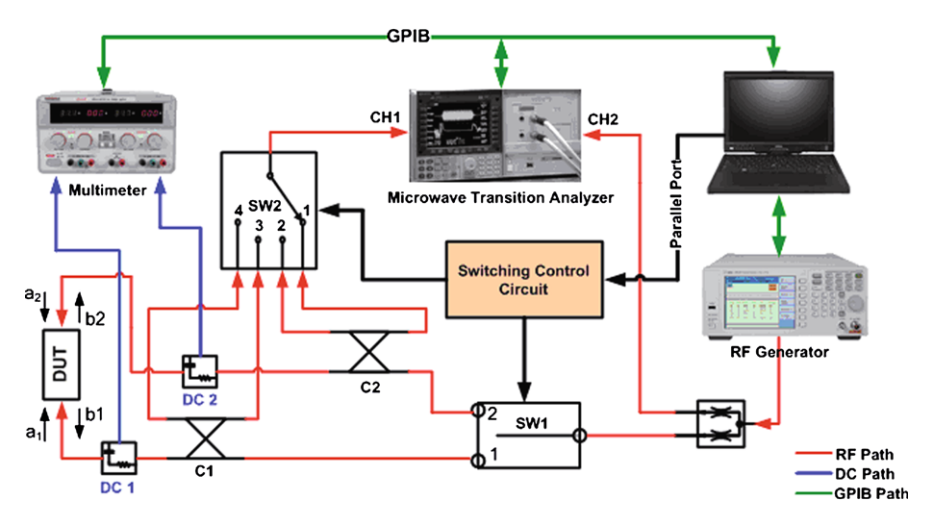


Fig. 7.6 Block diagram of a typical MTA based measurement system

A harmonic receiver operates in a similar way to a conventional super heterodyne receiver; the main difference is in the mixing process. In a harmonic receiver, the LO signal is first passed through a comb generator prior to being applied to the mixer. This effectively generates multiple harmonics of the LO signal, meaning that multiple sections of the RF spectrum can be captured simultaneously. The MTA works on a similar principle. In this setup, the power divider splits the signal from the generator into two parts. The first part excites the DUT's ports, depending on the position of switch 1 (SW1); and, the second part is fed to channel 2 (CH2) of the MTA for a reference signal. Channel 1 (CH1) of the MTA serves as the measuring port in this setup, although there have been measurement setups based around an MTA in which the channels have been used differently [21–23]. This particular setup provides measurements as ratios between CH1, as the receiver of the incident and reflected waves to be measured, and CH2, as a reference channel.

To fully exploit the capability of any high-frequency I-V waveform measurement system, full vector error correction needs to be carried out, in order to remove the systematic errors introduced by mismatches, losses, and imperfect components.

7.5 System Calibration

For the accurate large-signal waveforms measurements, the error terms of the error flow model between the MHR measuring plane and the DUT's terminals, described for the *n*th harmonic frequency and depicted in Fig. 7.7, need to be fully determined. This is a simplified version of the error model: more extensive details can be found in [23].

As a general rule, if there is no error introduced by the system imperfections and mismatches, the traveling waves at the DUT's ports are exactly the same as

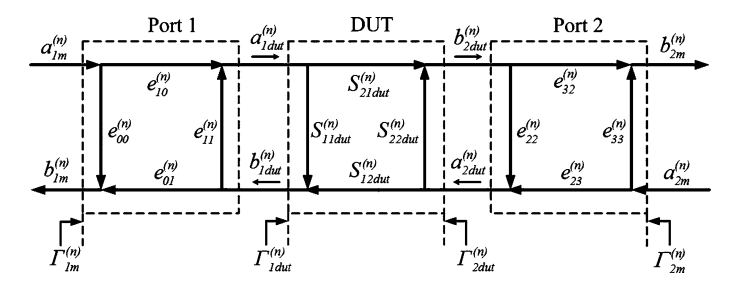


Fig. 7.7 Error flow graph depicting the error terms between the DUT and MHR ports

measured at the MHR port. In such an ideal scenario, the I-V waveforms can be directly extracted by employing Eqs. (7.3) and (7.4). However, in practical situations, the error terms between the DUT and MHR's ports change this direct relationship. For example, the traveling waves at the first port of DUT and MHR ports are related by Eqs. (7.7) and (7.8).

$$a_{1dut}^{(n)} = \left(\left(e_{01}^{(n)} e_{10}^{(n)} - e_{00}^{(n)} e_{11}^{(n)} \right) a_{1m}^{(n)} + e_{11}^{(n)} b_{1m}^{(n)} \right) / \left(e_{01}^{(n)} \right)$$
(7.7)

$$b_{1dut}^{(n)} = \left(\left(-e_{00}^{(n)} \right) a_{1m}^{(n)} + b_{1m}^{(n)} \right) / \left(e_{01}^{(n)} \right) \tag{7.8}$$

It is apparent from the above equations that the extraction of terminal I-V waveforms requires determination of individual error terms separately, thereby necessitating a different calibration process from the standard VNA calibration. In essence, the calibration approach for the waveform extraction is a three-step process where one of the steps is conventional VNA calibration. The three steps are discussed in the following three subsections.

7.5.1 First Step: Power Flow Calibration

The purpose of this step is to relate the power at the DUT port to the power sampled at the MHR port through a power scaling factor, α . This factor takes into account the losses incurred in the cabling and all other peripheral components employed in the measurement setup. The correct scaling factor changes the Fourier coefficient Eqs. (7.3) and (7.4) to a new set of equations, i.e., Eqs. (7.9) and (7.10), and consequently helps in determining the exact magnitude of the voltage and current waveforms.

$$V_1^{(n)} = \sqrt{2Z_0} \left(a_{1dut}^{(n)} + b_{1dut}^{(n)} \right) = \alpha V_1^{(n)}$$
 (7.9)

$$I_1^{(n)} = \sqrt{2/Z_0} \left(a_{1dut}^{(n)} - b_{1dut}^{(n)} \right) = \alpha I_1^{(n)}$$
 (7.10)

Fig. 7.8 Error flow graph depicting the error terms between the DUT and MHR ports

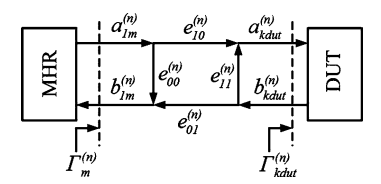


Figure 7.8 depicts the power flow at the MHR plane, P_m , and the DUT plane, P_{dut} . They are related to the error parameters, the reflection coefficient at coaxial plane, Γ_{dut} , and the power scaling factor, α , as follows [30]:

$$P_{kdut} = \frac{1}{2} \left| a_{kdut}^{(n)} \right|^2 = \frac{\alpha P_m}{\left| 1 + \left(-e_{11}^{(n)} \right) \Gamma_{kdut}^{(n)} \right|^2}$$
(7.11)

The power flow calibration factor, α , is obtained by connecting a power meter to the DUT port [31]. The power measured by the power meter, P_{PWM} , is related by:

$$P_{PWM} = \frac{1}{2} \left| a_{kdut}^{(n)} \right|^2 \left(1 - \left| \Gamma_{kdut}^{(n)} \right|^2 \right) = \frac{\alpha P_m (1 - \left| \Gamma_{kdut}^{(n)} \right|^2)}{\left| 1 + \left(-e_{11}^{(n)} \right) \Gamma_{kdut}^{(n)} \right|^2}$$
(7.12)

Simplification of Eqs. (7.11) and (7.12) gives the power calibration factor (α).

$$\alpha = \frac{P_{PWM}|1 + (-e_{11}^{(n)})\Gamma_{kdut}^{(n)}|^2}{P_m(1 - |\Gamma_{kdut}^{(n)}|^2)}$$
(7.13)

7.5.2 Second Step: S-Parameter Calibration

The second step is the conventional VNA type calibration for the determination of error terms $e_{00}^{(n)}$, $e_{11}^{(n)}$ and $e_{01}^{(n)}e_{10}^{(n)}$ for first port and $e_{22}^{(n)}$, $e_{33}^{(n)}$ and $e_{23}^{(n)}e_{32}^{(n)}$ for the second port, as shown in Fig. 7.7.

For the first port, Fig. 7.7 can be simplified to derive an expression for the measured reflection coefficient at the MHR port, $\Gamma_{1m}^{(n)}$, in terms of error parameters and the reflection coefficient at the first port of DUT, $\Gamma_{1dut}^{(n)}$.

$$\Gamma_{1m}^{(n)} = e_{00}^{(n)} + \frac{e_{01}^{(n)} e_{10}^{(n)} \Gamma_{1dut}^{(n)}}{1 - e_{11}^{(n)} \Gamma_{1dut}^{(n)}} = \frac{-\Delta e_{1}^{(n)} \Gamma_{1dut}^{(n)} + e_{00}^{(n)}}{-e_{11}^{(n)} \Gamma_{1dut}^{(n)} + 1}$$
(7.14)

where

$$\Delta e_1^{(n)} = \left(e_{00}^{(n)} e_{11}^{(n)} - e_{01}^{(n)} e_{10}^{(n)} \right). \tag{7.15}$$

For determining the three unknowns $e_{00}^{(n)}$, $e_{11}^{(n)}$ and $e_{01}^{(n)}e_{10}^{(n)}$ in Eq. (7.14), the simplest method is to measure the open-short-load (OSL) standards [32] at the first port

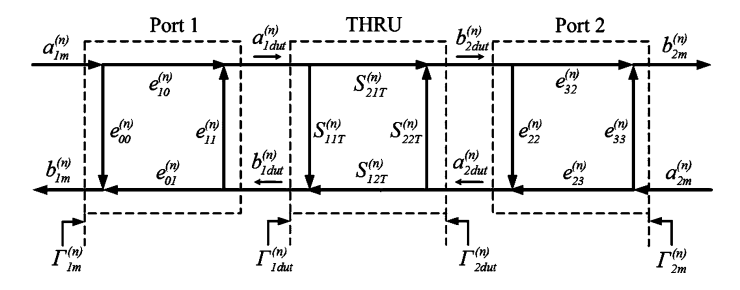


Fig. 7.9 Error flow graph depicting the error terms between the DUT and MHR ports

of the DUT. These measurements provide three sets of linear equations, which are summarized in matrix form in Eq. (7.16).

$$\begin{bmatrix} e_{00}^{(n)} \\ e_{11}^{(n)} \\ \Delta e_{*}^{(n)} \end{bmatrix} = \begin{bmatrix} 1 & (\Gamma_{1dut})_{O}(\Gamma_{m1})_{O} & -(\Gamma_{1dut})_{O} \\ 1 & (\Gamma_{1dut})_{S}(\Gamma_{m1})_{S} & -(\Gamma_{1dut})_{S} \\ 1 & (\Gamma_{1dut})_{L}(\Gamma_{m1})_{L} & -(\Gamma_{1dut})_{L} \end{bmatrix}^{-1} \times \begin{bmatrix} (\Gamma_{m1})_{O} \\ (\Gamma_{m1})_{S} \\ (\Gamma_{m1})_{L} \end{bmatrix}$$
(7.16)

where the terms with subscript O, S and L are the quantities for the calibration standards open, short and load, respectively.

Equation (7.16) once solved gives the error terms $e_{00}^{(n)}$, $e_{11}^{(n)}$ and $e_{01}^{(n)}e_{10}^{(n)}$ between port 1 of the DUT and the MHR, while the determination of error terms $e_{22}^{(n)}$, $e_{33}^{(n)}$ and $e_{23}^{(n)}e_{32}^{(n)}$ between port 2 and the MHR requires a thru standard between port 1 and port 2, as shown in Fig. 7.9. The simplification of error flow model in Fig. 7.9 gives expressions for error terms $e_{22}^{(n)}$, $e_{33}^{(n)}$ and $e_{23}^{(n)}e_{32}^{(n)}$ as a function of the measured S-parameters of the thru standard given in Eqs. (7.17)–(7.20).

$$e_{33}^{(n)} = \frac{S_{11T}^{(n)} - e_{00}^{(n)}}{t_{11}^{(n)} + e_{11}^{(n)}(S_{11T}^{(n)} - e_{00}^{(n)})}$$
(7.17)

$$e_{22}^{(n)} = S_{22T}^{(n)} - \frac{t_{22}^{(n)} e_{11}^{(n)}}{1 - e_{11}^{(n)} e_{22}^{(n)}}$$
(7.18)

$$t_{11}^{(n)} = e_{01}^{(n)} e_{10}^{(n)} = e_{00}^{(n)} e_{11}^{(n)} - \Delta e_{1}^{(n)}$$

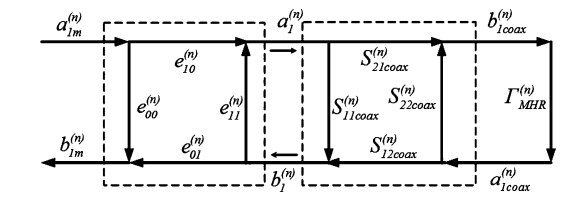
$$(7.19)$$

$$t_{22}^{(n)} = e_{32}^{(n)} e_{23}^{(n)} = S_{12T}^{(n)} S_{21T}^{(n)} \frac{(1 - e_{11}^{(n)} e_{33}^{(n)})^2}{t_{11}^{(n)}}$$
(7.20)

where $S_{11T}^{(n)}$, $S_{12T}^{(n)}$, $S_{21T}^{(n)}$ and $S_{22T}^{(n)}$ are the measured S-parameters of the thru standard connected between ports 1 and 2, and $t_{11}^{(n)}$ and $t_{22}^{(n)}$ are the reflection tracking parameters representing ports 1 and 2, respectively.

Equations (7.16)–(7.20) allows the calculation of error terms $e_{00}^{(n)}$, $e_{11}^{(n)}$, $e_{01}^{(n)}e_{10}^{(n)}$, $e_{22}^{(n)}$, $e_{33}^{(n)}$ and $e_{23}^{(n)}e_{32}^{(n)}$ of the error model between the MHR and DUT ports and is, therefore, referred as the S-parameter calibration stage. However, this step does not allow for the determination of individual terms $e_{01}^{(n)}$, $e_{10}^{(n)}$, $e_{23}^{(n)}$, and $e_{32}^{(n)}$ and,

Fig. 7.10 Error flow graph of the setup with coaxial cable between the MHR and port 1 of the DUT



consequently, does not provide enough information for accurate determination of the traveling waves at the DUT's ports, e.g., the traveling waves at the first port of DUT given by Eqs. (7.7) and (7.8), and hence for the extraction of terminal I-V waveforms.

7.5.3 Third Step: Enhanced Calibration

This calibration step is necessary to separate the individual terms from the tracking error parameters, $e_{01}^{(n)}e_{10}^{(n)}$ and $e_{23}^{(n)}e_{32}^{(n)}$. It is an enhancement of the second step and, as a result, is called enhanced calibration.

In this step, with the thru standard connected between ports 1 and 2, as shown in Fig. 7.9, the error flow model when solved gives two possible values of $e_{10}^{(n)}e_{32}^{(n)}$ through following expressions [33]:

$$S_{21T}^{(n)} \left(e_{10}^{(n)} e_{32}^{(n)} \right)^2 - S_{12T}^{(n)} \left(e_{01}^{(n)} e_{10}^{(n)} \right) \left(e_{32}^{(n)} e_{23}^{(n)} \right) = 0$$
 (7.21)

$$e_{10}^{(n)}e_{32}^{(n)} = \pm \sqrt{\frac{S_{12T}^{(n)}(e_{01}^{(n)}e_{10}^{(n)})(e_{32}^{(n)}e_{23}^{(n)})}{S_{21T}^{(n)}}}$$
(7.22)

The appropriate solution for the transmission tracking between the first and second DUT ports, $e_{10}^{(n)}e_{32}^{(n)}$, is dependent on the length of the thru standard and it is given by [33]:

$$\operatorname{Re}\left[\frac{(e^{-\gamma l})^{(n)}}{S_{21T}^{(n)}}\right] > 0 \tag{7.23}$$

where γ is the propagation constant, l is the length of the thru standard and $S_{21T}^{(n)}$ is the measured S-parameter of the thru standard connected between first and second ports of the DUT.

Next, the thru standard is replaced by a coaxial cable and its S-parameters, $S_{11coax}^{(n)}$, $S_{12coax}^{(n)}$, $S_{21coax}^{(n)}$ and $S_{22coax}^{(n)}$, are measured. Subsequently, the end of coaxial cable connecting the second port of DUT is disconnected and connected to first channel of the MHR, the error flow model of which is shown in Fig. 7.10, in order to measure the traveling wave, $b_{coax}^{(n)}$.

Simplification of the error flow model in Fig. 7.10 provides an expression for the error term $e_{10}^{(n)}$ given in Eq. (7.24) [25]

$$\begin{split} e_{10}^{(n)} &= \left(\frac{b_{coax}^{(n)}}{a_{1m}^{(n)}}\right) \left(\frac{(1 - e_{11}^{(n)} S_{11coax}^{(n)})(1 - \Gamma_{MHR}^{(n)} S_{22coax}^{(n)})}{S_{21coax}^{(n)}}\right) \\ &- \left(\frac{b_{coax}^{(n)}}{a_{1m}^{(n)}}\right) \left(\frac{(e_{11}^{(n)} \Gamma_{MHR}^{(n)} S_{21coax}^{(n)} S_{12coax}^{(n)})}{S_{21coax}^{(n)}}\right) \end{split} \tag{7.24}$$

The determination of the absolute value of individual term $e_{10}^{(n)}$ enables the calculation of error parameters $e_{01}^{(n)}$, $e_{23}^{(n)}$ and $e_{32}^{(n)}$ from Eqs. (7.25), (7.26), (7.27), which are directly deduced from Eqs. (7.19), (7.20) and (7.22).

$$e_{01}^{(n)} = \frac{e_{01}^{(n)}e_{10}^{(n)}}{e_{10}^{(n)}} = \frac{t_{11}^{(n)}}{e_{10}^{(n)}}$$
(7.25)

$$e_{32}^{(n)} = \frac{e_{10}^{(n)}e_{32}^{(n)}}{e_{10}^{(n)}} \tag{7.26}$$

$$e_{23}^{(n)} = \frac{e_{23}^{(n)} e_{32}^{(n)}}{e_{32}^{(n)}} = \frac{t_{22}^{(n)}}{e_{32}^{(n)}}$$
(7.27)

The determination of the absolute values of error parameters enables accurate measurements of incident and reflected traveling waves, given by Eqs. (7.28)–(7.31), at the DUT's ports.

$$a_{1dut}^{(n)} = \left(\frac{e_{01}^{(n)}e_{10}^{(n)} - e_{00}^{(n)}e_{11}^{(n)}}{e_{01}^{(n)}}\right)a_{1m}^{(n)} + \left(\frac{e_{11}^{(n)}}{e_{01}^{(n)}}\right)b_{1m}^{(n)}$$
(7.28)

$$b_{1dut}^{(n)} = \left(\frac{-e_{00}^{(n)}}{e_{01}^{(n)}}\right) a_{1m}^{(n)} + \left(\frac{1}{e_{01}^{(n)}}\right) b_{1m}^{(n)}$$
(7.29)

$$a_{2dut}^{(n)} = \left(\frac{e_{32}^{(n)}e_{23}^{(n)} - e_{33}^{(n)}e_{22}^{(n)}}{e_{23}^{(n)}}\right)a_{2m}^{(n)} + \left(\frac{e_{33}^{(n)}}{e_{23}^{(n)}}\right)b_{2m}^{(n)}$$
(7.30)

$$b_{2dut}^{(n)} = \left(\frac{-e_{33}^{(n)}}{e_{23}^{(n)}}\right) a_{2m}^{(n)} + \left(\frac{1}{e_{23}^{(n)}}\right) b_{2m}^{(n)}$$
(7.31)

The measured incident and traveling waves along with the power calibration factor, α , obtained from power calibration in the first step gives complete information for the extraction of time-domain current and voltage waveforms at the DUT's ports given by Eqs. (7.9) and (7.10).

7.5.4 Calibration Evaluation

The fully calibrated system, when used to measure terminal voltage waveform at the output port of a Mini-Circuits ZHL-42 W power amplifier biased at 17 V and excited

Fig. 7.11 Output voltage waveforms of the ZHL-42 W power amplifier operating in linear mode

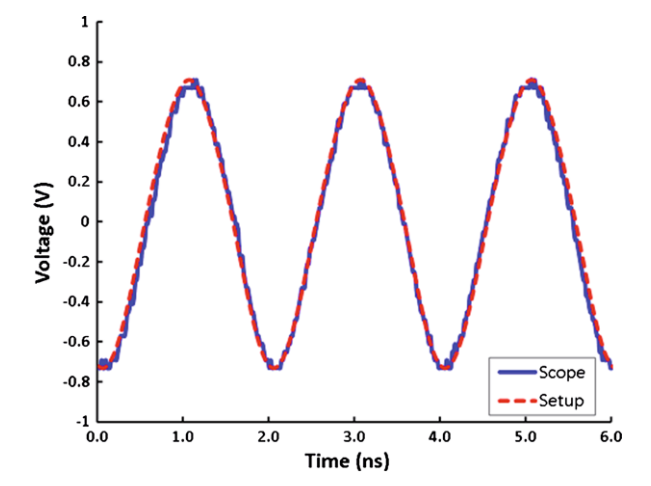
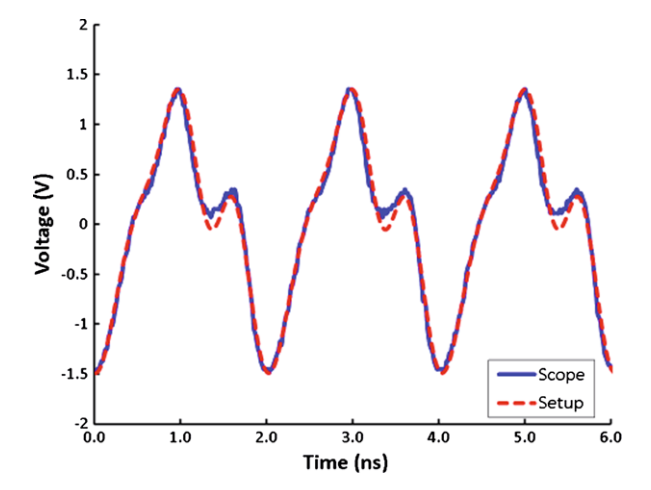


Fig. 7.12 Output voltage waveforms of the ZHL-42 W power amplifier operating in nonlinear mode



by a 0.5 GHz signal, gives the results shown in Fig. 7.11 during linear operation, while considering up to five harmonics.

It is also evident that the voltage waveforms measured using the system and a standard commercial scope, i.e., 4 Gbps digital oscilloscope (Tektronix TDS 794D) [34], show good agreement. However, the output voltage waveform is distinct even when the amplifier is pushed into slightly nonlinear region, as shown in Fig. 7.12. The difference is due to the fact that the system captured all the spectral components of the voltage waveform, whereas the commercial scope could capture spectral lines only up to four harmonics for the chosen excitation of 500 MHz, due to limited bandwidth of the commercial scope.

7.6 Six-Port Based Waveform Measurement System

By accurately determining the magnitude of the DC component $(V^{(0)}, I^{(0)})$, as well as the magnitude and phase of the fundamental frequency $(V^{(1)}, I^{(1)})$ and harmonic components $(V^{(n)}, I^{(n)})$, the time-domain voltage and current waveforms can be calculated at the port of the DUT according to Eqs. (7.32) and (7.33).

$$v(t) = \text{Re}\left\{\sum_{n=0}^{m} V^{(n)} e^{(j2\pi n f_0 t)}\right\}$$
(7.32)

$$i(t) = \text{Re}\left\{\sum_{n=0}^{m} I^{(n)} e^{(j2\pi n f_0 t)}\right\}$$
(7.33)

where n denotes the harmonic order, f_0 is the fundamental frequency, and m is the total number of harmonics included in the measurement.

The DC components, $V^{(0)}$ and $I^{(0)}$, are routinely measured directly with a biasing instrument; however, the measurement of the complex Fourier coefficients, $V^{(n)}$ and $I^{(n)}$, for $n \ge 1$ is more difficult. A traditional setup developed using a multi-harmonic receiver (MHR) has evolved in the form of a large-signal network analyzer (LSNA) [35, 36], which shows promise.

Alternatively, a deliberately modified six-port (SP) reflectometer, which works as homodyne VNA, can also determine the complex Fourier coefficients of the waves in the frequency domain [27]. To be able to determine waveforms v(t) and i(t), complex voltage traveling waves, also called pseudowaves [37], at least at the fundamental frequency (f_0) and second ($2f_0$), and third ($3f_0$) harmonic frequencies should be measured. At a given reference plane, $V^{(n)}$ and $I^{(n)}$ in Eqs. (7.32) and (7.33) are related to the incident traveling wave, $a^{(n)}$, and reflected traveling wave, $b^{(n)}$, by [37, 38]:

$$V^{(n)} = a^{(n)} + b^{(n)} (7.34)$$

$$I^{(n)} = \frac{a^{(n)} - b^{(n)}}{Z_c} \tag{7.35}$$

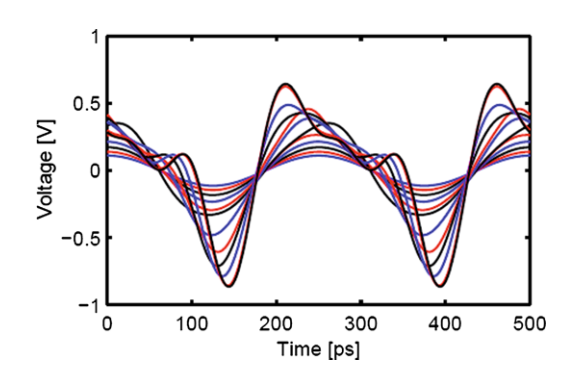
where Z_c is the characteristic impedance of the system (typically 50 Ω).

By measuring the pseudo reflection coefficients, $\Gamma^{(n)} = a^{(n)}/b^{(n)}$, at a given plane using an SP reflectometer, the magnitude and phase of traveling wave $a^{(n)}$ can be easily determined if traveling wave $b^{(n)}$ is from a reference generator, i.e., whose magnitude and phase is known. We propose to measure pseudo reflection coefficient $\Gamma^{(n)}$ at a given plane by means of an SP reflectometer. In the proposed source/load-pull setup, the reflection coefficient measured by the SP reflectometer is equal to $\Gamma^{(n)}$, since the reference impedance used to define the traveling waves is equal to the characteristic impedance of the system [37]. Subsequently, the voltage and current frequency components, $V^{(n)}$ and $I^{(n)}$, can be deduced according to Eqs. (7.34) and (7.35).

Fig. 7.13 Schematic of the used SRD based multi-harmonic reference generator [27], © IEEE 2008

RF NDS RF Output FET FLC091 WF SRD

Fig. 7.14 Measured multi-harmonic reference generator voltage waveforms for different input levels [27], © IEEE 2008



7.6.1 Multi-harmonic Reference Generator

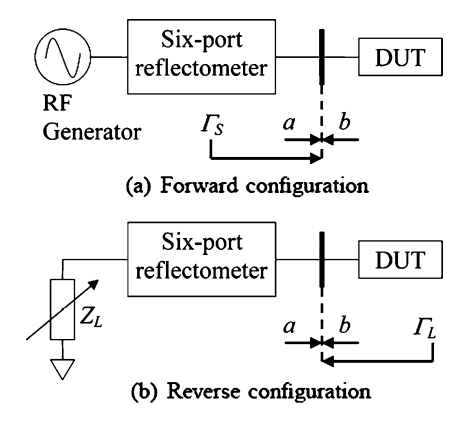
The multi-harmonic generator shown in Fig. 7.13 generates the harmonic-rich voltage wave, $b^{(n)}$, with known magnitude and phase components and has been employed as a reference signal generator for time-domain waveform measurements. It consists of an SRD excited by a continuous wave RF signal at the fundamental frequency, f_0 , of 4 GHz. A high-gain amplifier is used to enhance the signal level to the extent that the output of the SRD is a harmonic-rich RF signal with spectral components at f_0 and its higher harmonics. It is evident from the waveforms are spectrally rich at the output of the SRD, as shown in Fig. 7.14, measured using an LSNA for input drive levels from -10 dBm to 12 dBm.

7.6.2 SP Reflectometer Principle

The SP reflectometer is an interferometric circuit with six ports. Measurements are performed by connecting a generator to Port 1, also called the generator port, and an unknown load to Port 2, denoted as the measurement port. In this configuration, the RF powers detected at Ports 3–6 are related to the reflection coefficient, Γ , presented by the unknown load.

An SP reflectometer can be used to determine both the source and the reflection coefficients, as illustrated in Fig. 7.15. Referring to Fig. 7.15(a), the SP reflectometer operates in the forward configuration, i.e., it is driven by an RF source at Port 1 and

Fig. 7.15 Typical setup for reflection coefficient measurement using an SP reflectometer in (a) forward configuration and (b) reverse configuration [27], ⊚ IEEE 2008



measures the source reflection coefficient, Γ_S , as given in Eq. (7.36), of the DUT connected to Port 2

$$\Gamma_S = \frac{b}{a} \tag{7.36}$$

In the reverse configuration, as shown in Fig. 7.15(b), the SP reflectometer measures the load reflection coefficient, Γ_L , as given in Eq. (7.37), at the DUT plane, presented by the impedance seen through the SP reflectometer

$$\Gamma_L = \frac{a}{b} \tag{7.37}$$

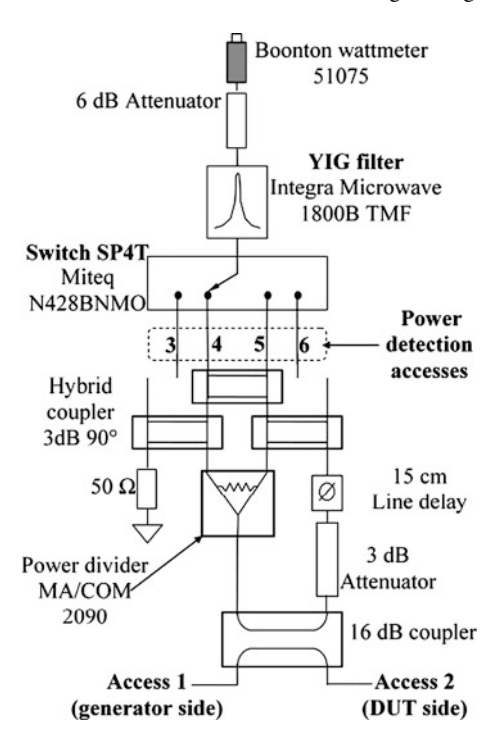
Moreover, the SP reflectometer is able to measure the incident power, P_{OUT} , delivered to a load connected to the measurement port and is related to the detected power at Port 3 [39, 40].

7.6.3 Multi-harmonic SP Reflectometer Architecture

Typical broadband SP architectures based on branch-line couplers and a power divider are available for several octaves of bandwidth. However, the detection block of a conventional SP reflectometer is not able to discriminate between the different spectral components, because it only detects the total power at the detection ports. Time-domain waveform measurements, however, require the measurement of a few complex Fourier coefficients of the signal. To be able to perform this measurement, the power detection block of the SP reflectometer is modified, as shown in Fig. 7.16, to become frequency selective and, hence, allow for multi-harmonic measurements.

The power detection block consists of a single pole, four through (SP4T) switch, a tunable yttrium-iron-garnet (YIG) filter, and a power meter. For harmonic measurements, the YIG filter is adjusted to pass only one harmonic frequency component at a time from the output of the SP4T switch to the power meter. Using the SP4T switch to switch successively from Port 3 to Port 6 and detect the powers, the

Fig. 7.16 Multi-harmonic SP reflectometer topology [27], © IEEE 2008



magnitude and phase of reflection coefficient $\Gamma = b/a$ can be measured through the procedure described in the following paragraph.

The YIG filter is centered at f_0 . Port 3 is selected by means of the S4PT switch, and the power is measured. Before tuning the YIG filter to $2f_0$, the powers at Port 4, 5 and 6 are measured. In the next measurement cycle, the filter is adjusted to $2f_0$, and the powers at Ports 3, 4, 5 and 6 are measured. Finally, the filter is set to $3f_0$, and the power detection steps are repeated. Before every measurement, the repeatability of the YIG filter adjustment and the switch contact quality has to be verified. The multi-harmonic SP reflectometer is calibrated at f_0 , $2f_0$ and $3f_0$.

The relationships between the measured powers at Port 4, 5 and 6, $P_3^{(n)}$, $P_4^{(n)}$, $P_5^{(n)}$, and $P_6^{(n)}$, and the output power, $P_{OUT}^{(n)}$, and the reflection coefficient, $\Gamma_L^{(n)}$, are given by:

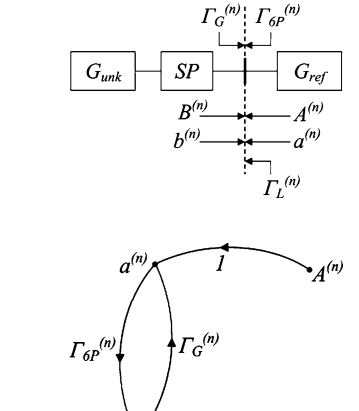
$$\frac{P_{in}}{P_3^{(n)}} = k_{in} \left| \frac{1 + A_{in} \Gamma_S^{(n)}}{1 + A_3^{(n)} \Gamma_S^{(n)}} \right|^2$$
 (7.38)

$$\Gamma_S^{(n)} = \frac{1}{\Gamma_I^{(n)}} \tag{7.39}$$

$$P_{OUT}^{(n)} = k_P^{(n)} \frac{P_3^{(n)}}{1 + A_3^{(n)} \Gamma_S^{(n)}} \left(1 - \left|\Gamma_S^{(n)}\right|^2\right)$$
 (7.40)

Fig. 7.17 Definition of the calibration principle of the SP reflectometer for time-domain voltage and current waveform measurements [27], © IEEE 2008

Fig. 7.18 Flow graph of the calibration principle of the SP reflectometer [27], © IEEE 2008



where *n* is the harmonic order, constants k_{in} and system related constants A_{in} (for i = 4, 5, 6) are determined by the SP calibration procedure, and constants $k_p^{(n)}$ are determined by an absolute power calibration method using a reference power meter.

7.6.4 Multi-harmonic SP Reflectometer Calibration

Figure 7.17 shows a block diagram of the SP reflectometer calibration principle for time-domain voltage and current waveform measurements in a source/load-pull environment. The Fourier coefficients of the harmonic-rich reference voltage wave, $A^{(n)}$, which is injected by reference G_{ref} , is known in both magnitude and phase. Unlike $A^{(n)}$, the spectral content of $B^{(n)}$, generated by an unknown generator G_{unk} , does not have to be known. Therefore, G_{unk} can be any arbitrary multi-harmonic generator.

In Fig. 7.17, G_{unk} consists of three active branches that form the load impedance tuning system [41]. $a^{(n)}$ and $b^{(n)}$ are total traveling waves that travel toward the SP and G_{ref} , respectively, in the measurement reference plane. $a^{(n)}$ is the sum of the reference signal, $A^{(n)}$, for each harmonic generated by G_{ref} and any reflected waves. The same relation is valid for $B^{(n)}$ and $b^{(n)}$. $\Gamma_G^{(n)}$ represents the reflection coefficient presented by the source impedance of G_{ref} when $A^{(n)} = 0$, and $\Gamma_{6P}^{(n)}$ represents the reflection coefficient presented by the source impedance of the SP reflectometer when G_{unk} is off, i.e., $B^{(n)} = 0$. Finally, $\Gamma_L^{(n)}$ is the reflection coefficient presented by the load impedance at the respective fundamental and harmonic frequencies, synthesized by G_{unk} at the measurement plane and measured by the SP reflectometer.

Since G_{ref} delivers wave $A^{(n)}$ with a known magnitude and phase, the SP reflectometer should be calibrated to determine the magnitude and phase of $B^{(n)}$ for extraction of the time-domain waveform. The error flow model, as shown in Fig. 7.18,

of the SP reflectometer calibration setup can be used to deduce the expression for $B^{(n)}$ through the following steps.

If the source delivering $B^{(n)}$ is turned off, then:

$$a^{(n)} = A^{(n)} + b^{(n)} \Gamma_G^{(n)}$$
(7.41)

$$b^{(n)} = a^{(n)} \Gamma_{6P}^{(n)} \tag{7.42}$$

Combining Eqs. (7.41) and (7.42) leads to:

$$a^{(n)} = \frac{A^{(n)}}{1 - \Gamma_{6P}^{(n)} \Gamma_{G}^{(n)}}$$
 (7.43)

In the same way, if the source delivering $A^{(n)}$ is off, then $a^{(n)}$ can be written as:

$$a^{(n)} = \frac{\Gamma_G^{(n)} B^{(n)}}{1 - \Gamma_{GP}^{(n)} \Gamma_G^{(n)}}$$
(7.44)

The superposition of Eqs. (7.43) and (7.44) for the coexistence of $A^{(n)}$ and $B^{(n)}$ results in:

$$a^{(n)} = \frac{A^{(n)} + \Gamma_G^{(n)} B^{(n)}}{1 - \Gamma_{GP}^{(n)} \Gamma_G^{(n)}}$$
(7.45)

Similarly, the expression for $b^{(n)}$ given in (7.46) can also be derived from:

$$b^{(n)} = \frac{B^{(n)} + \Gamma_{6P}^{(n)} A^{(n)}}{1 - \Gamma_{6P}^{(n)} \Gamma_{G}^{(n)}}$$
(7.46)

The measured reflection coefficient, $\Gamma_L^{(n)}$, provided by the synthesized load of G_{unk} is obtained from the ratio of Eqs. (7.46) and (7.45):

$$\Gamma_L^{(n)} = \frac{b^{(n)}}{a^{(n)}} = \frac{B^{(n)} + \Gamma_{6P}^{(n)} A^{(n)}}{A^{(n)} + \Gamma_G^{(n)} B^{(n)}}$$
(7.47)

Rearrangement of Eq. (7.47) gives the expression for unknown quantity $B^{(n)}$:

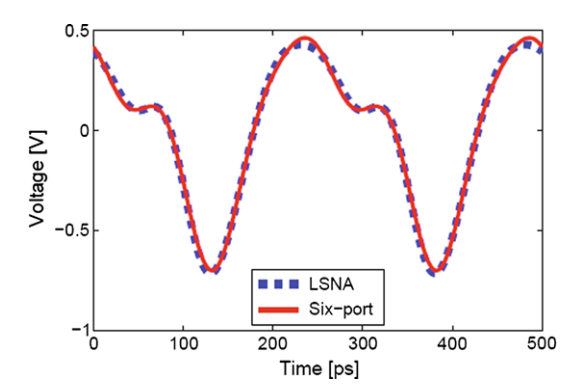
$$B^{(n)} = A^{(n)} \frac{(\Gamma_{6P}^{(n)} - \Gamma_L^{(n)})}{(\Gamma_G^{(n)} \Gamma_I^{(n)} - 1)}$$
(7.48)

In Eq. (7.48), since $A^{(n)}$ is the known wave generated by G_{ref} , only $\Gamma_{6P}^{(n)}$, $\Gamma_{G}^{(n)}$ and $\Gamma_{L}^{(n)}$ need to be measured. $\Gamma_{6P}^{(n)}$, and $\Gamma_{G}^{(n)}$ can be measured by an SP reflectometer or a VNA, whereas $\Gamma_{L}^{(n)}$ can be measured as a pseudo reflection coefficient by means of an SP reflectometer in the reverse configuration, as shown in Fig. 7.15(b).

7.6.5 Calibration Verification

The multi-harmonic calibration of the SP reflectometer can be verified by measuring reference signals $A^{(n)}$ at a different power level from the one used to determine

Fig. 7.19 Comparison between SP reflectometer and LSNA measurements of the time-domain waveform at the output of the harmonic generator [27], © IEEE 2008



 $B^{(n)}$ during the calibration procedure. Since the SP reflectometer measures $\Gamma_L^{(n)}$, traveling waves $A^{(n)}$ can be extracted using Eq. (7.48).

The voltage waveforms deduced from the SP reflectometer measurements are then compared with the waveforms previously measured with an LSNA, as depicted in Fig. 7.14. The measured voltage waveforms at the output of the harmonic generator obtained by the calibrated SP reflectometer and an LSNA are shown in Fig. 7.19. Although the SP takes into account only the first three harmonic components of the signal $(f_0, 2f_0 \text{ and } 3f_0)$, the relative error compared to the LSNA measurement based on a total of five harmonics is less than 2.5 %. This result shows the accuracy and efficiency of the SP reflectometer calibration procedure.

7.7 Waveform Engineering

The coupling of the waveform measurement setup with impedance controlling elements results into a typical waveform engineering system, such as the one depicted in Fig. 7.20. These systems are capable of measuring high-frequency waveforms in variable impedance environments at the terminals of the DUT.

In principle, waveform engineering is the technique in which the current and voltage waveforms at the DUT's terminals can be modified in a quantified manner to optimize the performance of the DUT [42]. Through theoretical and experimental investigations, it has been established that the terminal current and voltage waveforms are the unifying link between transistor technology, circuit design and RFPA performance [3, 4]. Therefore, it is imperative to consider engineering of the waveform as fundamental force driving both the measurement and mathematical methods in the overall RFPA design process, i.e., transistor optimization, circuit design, and system integration.

The waveform engineering technique can be applicable in the design investigation/evaluation loop of either power transistor technology or power amplifiers [42]. This eliminates the black box design process and allows for new intelligent design processes that are completely founded on theoretical waveform analysis. Alternatively, it can also indirectly support the amplifier investigation/evaluation loop by

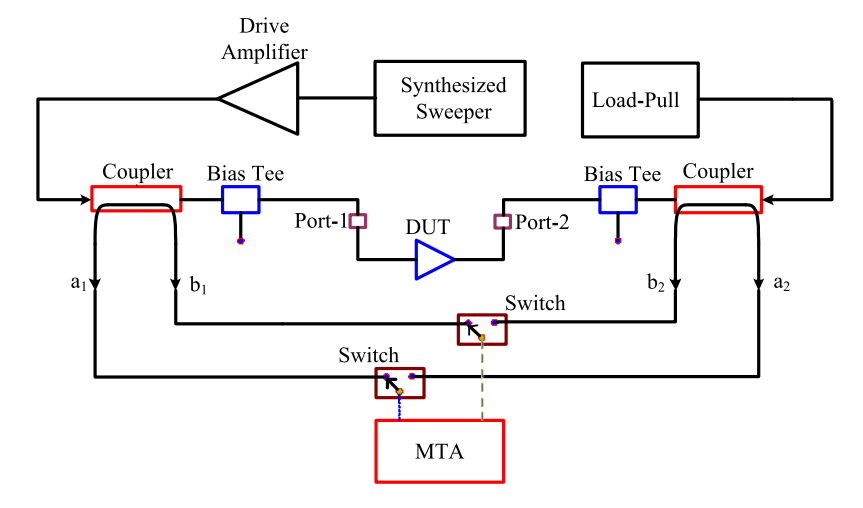


Fig. 7.20 Block diagram of a typical waveform engineering system

supporting the development or improving the accuracy of nonlinear transistor models or by providing computer-aided design (CAD) accessible behavioral or behavioral model parameter datasets [42].

7.8 Applications of Waveform Engineering

7.8.1 Transistor Characterization

RF waveform engineering systems find extensive use in the determination of non-linear dynamic responses of transistor devices. For example, such a system can be used in the investigation of RF power performance of a gallium nitride (GaN) heterojunction field effect transistor (HFET). The poor performance of GaN HFETs is often associated with knee walkout or current collapse problems. Knee walkout is defined as the condition when the knee voltage (minimum drain voltage at maximum drain current) is increased under RF excitation over that determined under DC excitation. On the other hand, the current collapse is the condition in which the maximum drain current under an RF excitation is reduced compared to that observed under DC excitation. Traditional microwave measurements, linear or non-linear, are unable to provide visual observations; rather, they can only measure the consequences, e.g., transconductance and output conductance dispersion, RF power loss, and/or decreased efficiency [42].

However, RF waveform measurement and engineering systems [43] help in overcoming such problems and readily allow observation of the knee walkout and current collapse problem, as shown in Fig. 7.21. The plot in this figure shows the engineered waveforms obtained by varying the RF fundamental load impedance from

Fig. 7.21 One GHz fan diagrams, showing measured observation of both knee walkout and poor pinch-off [43], © IEEE 2006

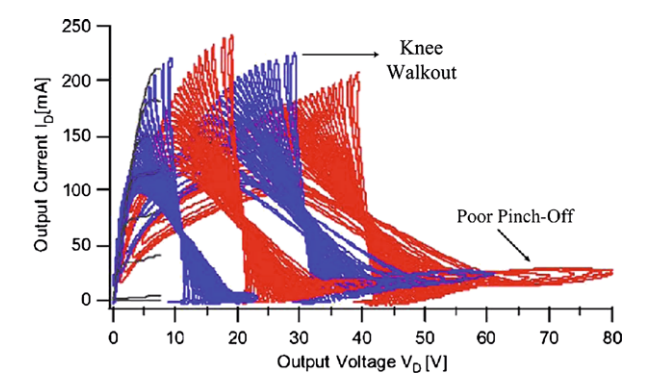
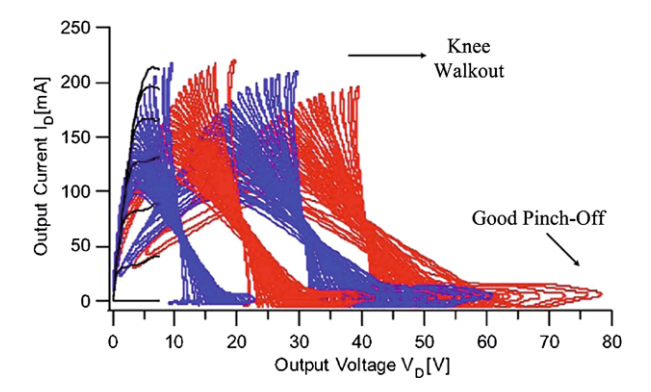


Fig. 7.22 One GHz fan diagrams, showing measured knee walkout and optimized pinch-off [43], © IEEE 2006



a low (short) to a high (open) impedance for four different drain bias voltages, increasing the values of the DC quiescent (10, 20, 30 and 40 V). The RF knee walkout and its extension with increased drain voltage are evident in these measured results.

The results in Fig. 7.21 also provide an indication that this particular technology also suffers from poor pinch-off (minimum drain current was not zero at high drain voltages). On the contrary, Fig. 7.22 shows similar sets of measurements with identical knee walkout problems, but no pinch-off issues. Through these plots, one can easily identify the role of iron doping the buffer on the dynamic transistor response. Thus, in this case the RF waveform and engineering aided in technology optimization, i.e., iron doped buffer design [43].

Other applications of RF current and voltage waveform measurement and engineering systems in the transistor characterization domain include technology selection, reliability investigations, and engineered RF stress testing.

7.8.2 CAD Incorporation

RF waveform measurement systems are also considered a tool for the optimization of nonlinear transistor models: therefore, they can also support nonlinear CAD.

Waveform engineering systems further advance the nonlinear model development and nonlinear CAD. These systems enable the full device I-V plane to be dynamically investigated without the previous requirement of DC bias point variations. Therefore, these systems can generate more robust data for either the extraction of a transistor's nonlinear state functions [44] or the validation of conventional analytical models [45].

Furthermore, engineered current and voltage waveforms measured as functions of load impedance can be used within the CAD tool that is relevant for PA design or behavior modeling of transistor devices [46]. The incorporation of measured data directly into a CAD environment provides an accurate alternative to the traditional solution requiring a nonlinear device model. This concept is analogous to the direct use of measured S-parameter datasets rather than, for example, small-signal equivalent transistor circuit models in linear CAD.

7.8.3 Power Amplifier Design

Waveform measurement and engineering systems are very useful in determining the appropriate matching impedance required at device ports to achieve the required performance. This performance is directly linked to the mode of operation (voltage and current waveforms) realized, which can be directly obtained. Through the independent control of bias and drive, one can engineer the shape of current waveforms; whereas, the voltage waveforms can be engineered by varying the impedance through a load-pull system. Therefore, these systems can be utilized to achieve the target current and voltage waveforms obtained from theoretical analysis, in order to reach the theoretically predicted performance. Once the desired performance is achieved, linear CAD tools can then be employed to design a suitable matching network.

As an example, let us consider the first-pass design of a class-J high-efficiency broadband PA based on GaN HFET technology. Class J is defined as a mode in which the voltage has harmonic components that make it behave asymptotically towards a half-wave rectified sine wave. This, in practice, can be usefully approximated by a suitably phased second harmonic component. Therefore, a class-J amplifier can be realized by engineering the waveforms using appropriate fundamental and second harmonic terminations. In this way, a higher fundamental component can significantly outweigh the loss in power implied by the reactive load. Consequently, class J displays approximate half-wave rectified sinusoidal output current and voltage waveforms with a phase overlap between the two, as shown in Fig. 7.23 [47].

The engineered waveforms achieved after systematic waveform optimization clearly demonstrate that the transistor can support the class-J mode of operation and, hence, deliver the expected RF output power along with very high power-added efficiency (PAE) across a broad bandwidth [47]. In addition, once the targeted waveforms are achieved, the system provides the designer with the desired input and output matching circuit impedances necessary at the fundamental frequency and second and third harmonic frequencies.

References 187

Fig. 7.23 Measured typical class-J waveforms on a 10 W GaN HEMT [47], © IEEE 2009

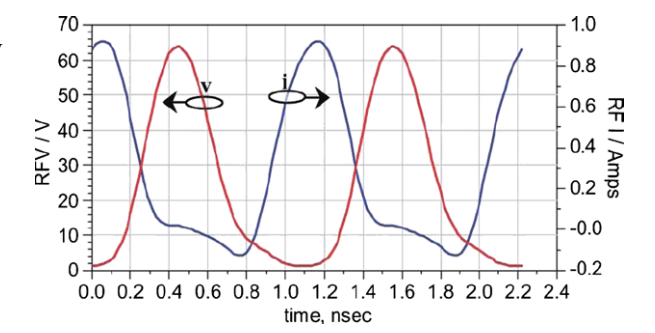
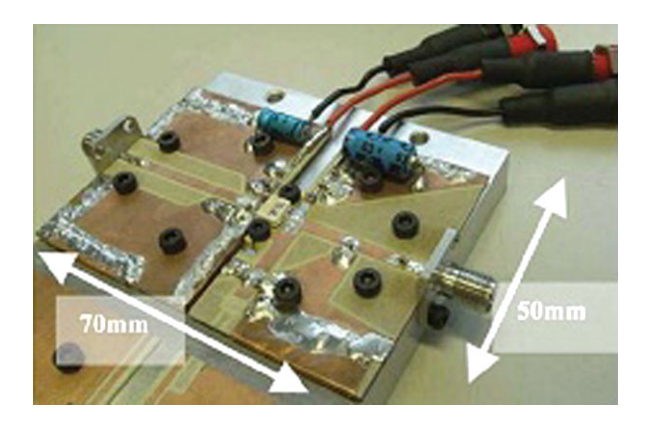


Fig. 7.24 Realized class-J amplifier [47], © IEEE 2009



The designer now has all the information necessary to design an appropriate microwave matching circuit and assemble the amplifier shown in Fig. 7.24. Once assembled and measured, the amplifier gives a measured performance that is identical to that predicted, i.e., a first-pass design success [47].

References

- A. Ramadan, A. Martin, T. Reveyrand, J.-M. Nebus, P. Bouysse, L. Lapierre, J.-F. Villemazet, S. Forestier, Efficiency enhancement of GaN power HEMTs by controlling gate-source voltage waveform shape, in 39th European Microwave Conference Digest, Rome, Italy (Sept. 2009), pp. 1840–1843
- 2. Y.Y. Woo, Y. Yang, B. Kim, Analysis and experiments for high efficiency class-F and inverse class-F power amplifiers. IEEE Trans. Microw. Theory Tech. **54**(5), 1969–1974 (2006)
- H.M. Nemati, A.L. Clarke, S.C. Cripps, J. Benedikt, P.J. Tasker, C. Fager, J. Grahn, H. Zirath, Evaluation of a GaN HEMT transistor for load- and supply-modulation applications using intrinsic waveform measurements, in *IEEE Microwave Theory and Techniques Society's International Microwave Symposium Digest*, Anaheim, USA (May 2010), pp. 509–512
- C.J. Wei, P. DiCarlo, Y.A. Tkachenko, R. McMorrow, D. Bartle, Analysis and experimental waveform study on inverse class-F mode of microwave power FETs, in *IEEE Microwave Theory and Techniques Society's International Microwave Symposium Digest*, Boston, USA (June 2000), pp. 525–528

- W. Grabinski, B. Nauwelaers, D. Schreurs (eds.), Transistor Level Modeling for Analog/RF IC Design (Springer, Dordrecht, 2006)
- 6. D.M. Snider, A theoretical analysis and experimental confirmation of the optimally loaded and overdriven RF power amplifier. IEEE Trans. Electron Devices, 851–857 (1967)
- J.D. Rhodes, Output universality in maximum efficiency linear power amplifiers. Int. J. Circuit Theory Appl. 31, 385–405 (2003)
- 8. K.A. Remley, D.F. Williams, Sampling oscilloscope models and calibrations, in *IEEE Microwave Theory and Techniques Society's International Microwave Symposium Digest*, Philadelphia, USA (June 2003), pp. 1507–1510
- 9. T.S. Clements, P.D. Hale, D.F. Williams, C.M. Wang, A. Dienstfrey, D.A. Keenan, Calibration of sampling oscilloscopes with high-speed photodiodes. IEEE Trans. Microw. Theory Tech. **54**(8), 3173–3181 (2006)
- 10. J. Verspecht, P. Debie, A. Barel, L. Martens, Accurate on-wafer measurement of phase and amplitude of the spectral components of incident and scattered voltage waves at the signal ports of a nonlinear microwave device, in *IEEE Microwave Theory and Techniques Society's International Microwave Symposium Digest*, Orlando, USA (May 1995), pp. 1029–1032
- 11. J. Fitzpatrick, Error models for systems measurement. Microw. J. May, 63–66 (1978)
- R.S. Tucker, P.D. Bradley, Computer-aided error correction of large-signal load-pull measurements. IEEE Trans. Microw. Theory Tech. 32(3), 296–300 (1984)
- W.R. Scott Jr., G.S. Smith, Error corrections for an automated time-domain network analyzer. IEEE Trans. Instrum. Meas. 35, 300–303 (1986)
- 14. D.M. Pozar, Microwave Engineering, 3rd edn. (Wiley, New York). ISBN 0-471-44878-8
- Understanding the fundamental principles of vector network analysis, Application Note, Agilent AN 1287-1
- 16. S.A. Mass, Nonlinear Microwave Circuits, 2nd edn. (Artech House, Norwood, 2003)
- M. Sipila, K. Lehtinen, V. Porra, High-frequency periodic time-domain waveform measurement system. IEEE Trans. Microw. Theory Tech. 36(10), 1397–1405 (1988)
- 18. U. Lott, Measurement of magnitude and phase of harmonics generated in nonlinear microwave two-ports. IEEE Trans. Microw. Theory Tech. **37**(10), 1506–1511 (1989)
- D. Barataud, C. Arnaud, B. Thibaud, M. Campovecchio, J.-M. Nebus, J.P. Villotte, Measurements of time-domain voltage/current waveforms at RF and microwave frequencies based on the use of a vector network analyzer for the characterization of nonlinear devices—application to high-efficiency power amplifiers and frequency multipliers. IEEE Trans. Instrum. Meas. 47(5), 1259–1264 (1998)
- Agilent Technical Data Sheet, PNA-X series network analyzer, http://cp.literature.agilent. com/litweb/pdf/N5242-90007.pdf (Online)
- 21. F. van Raay, G. Kompa, A new on-wafer large signal waveform measurement system with 40 GHz harmonic bandwidth, in *IEEE Microwave Theory and Techniques Society's International Microwave Symposium Digest*, Albuquerque, USA (June 1992), pp. 1435–1438
- 22. M. Demmler, P.J. Tasker, M. Schlechtweg, A vector corrected high power on-wafer measurement system with a frequency range for the higher harmonics up to 40 GHz, in *24th European Microwave Conference*, Cannes, France (Sept. 1994), pp. 1367–1372
- 23. J. Benedikt, R. Gaddi, P.J. Tasker, M. Goss, High-power time-domain measurement system with active harmonic load-pull for high-efficiency base-station amplifier design. IEEE Trans. Microw. Theory Tech. **48**(12), 2617–2624 (2000)
- W.S. El-Deeb, M.S. Hashmi, S. Bensmida, N. Boulejfen, F.M. Ghannouchi, Thru-less calibration algorithm and measurement system for on-wafer large-signal characterization of microwave devices. IET Microw. Antenna Propag. 4(11), 1773–1781 (2010)
- W.S. El-Deeb, M.S. Hashmi, N. Boulejfen, F.M. Ghannouchi, Small-signal, complex distortion and waveform measurement system for multiport microwave devices. IEEE Instrum. Meas. Mag. 14(3), 2833 (2011)
- Agilent Technical Data Sheet, Agilent nonlinear vector network analyzer, http://cp.literature.agilent.com/litweb/pdf/5989-8575EN.pdf (Online)

27. S. Bensmida, P. Poire, R. Negra, F.M. Ghannouchi, New time-domain voltage and current waveform measurement setup for power amplifier characterization and optimization. IEEE Trans. Microw. Theory Tech. **56**(1), 224–231 (2008)

- 28. F.M. Ghannouchi, A. Mohammadi, *The Six-Port Technique with Microwave and Wireless Applications* (Artech House, Norwood, 2009)
- The Microwave Transition Analyser, Measure 25 ps transitions in switched and pulsed microwave components, Hewlett Packard Product Note 70820-2, 1991
- W.S. El-Deeb, S. Bensmida, N. Boulejfen, F.M. Ghannouchi, An impedance and power flow measurement system suitable for on-wafer microwave device large-signal characterization. Int. J. RF Microw. Computer-Aided Eng. 4(11), 306–312 (2010)
- 31. W.S. El-Deeb, S. Bensmida, F.M. Ghannouchi, A de-embedding technique for on-wafer simultaneous impedance and power flow measurements, in *IEEE Instrumentation and Measurement Technology Conference*, Victoria, Canada (May 2008), pp. 58–61
- 32. J.R. Juroshek, D.X. LeGolvan, Correcting for systematic errors in one-port calibration standards, in *62nd ARFTG Microwave Measurement Conference*, Boulder, USA (Dec. 2003), pp. 119–126
- 33. P.S. Blockley, J.G. Rathmell, Towards generic calibration, in 65th ARFTG Measurement Conference, Long Beach, USA (June 2005), pp. 1–4
- 34. Tektronix, TDS794D user's manual, http://www2.tek.com/cmswpt/psdetails.lotr?ct=PS&cs=psu&ci=13446&lc=EN
- J.G. Lecky, A.D. Patterson, J.A.C. Stewart, A vector corrected waveform and load line measurement system for large signal transistor characterization, in *IEEE Microwave Theory and Techniques Society's International Microwave Symposium Digest*, Orlando, USA (May 1995), pp. 1243–1246
- 36. D.J. Williams, P.J. Tasker, An automated active source- and load-pull measurement system, in 6th IEEE High Frequency Student Colloquium, Cardiff, UK (Sept. 2001), pp. 7–12
- R.B. Marks, D.F. Williams, A general waveguide circuit theory. J. Res. Natl. Inst. Stand. Technol. 97(5), 533–562 (1992)
- 38. J. Verspecht, Large signal network analysis. IEEE Microw. Mag. 6(4), 82–92 (2005)
- 39. S. Bensmida, P. Poire, F.M. Ghannouchi, Source-pull/load-pull measurement system based on RF and baseband coherent active branches using broadband six-port reflectometers, in *37th European Microwave Conference*, Munich, Germany (Oct. 2007), pp. 953–956
- E. Bergeault, B. Huyart, G. Geneves, L. Jallet, Accuracy analysis for six-port automated network analyzers. IEEE Trans. Microw. Theory Tech. 38(3), 492–496 (1990)
- F.M. Ghannouchi, R. Larose, R.G. Bosisio, A new multiharmonic loading method for largesignal microwave and millimeter-wave transistor characterization. IEEE Trans. Microw. Theory Tech. 39(6), 986–992 (1991)
- 42. P.J. Tasker, Practical waveform engineering. IEEE Microw. Mag. 10(7), 65–76 (2009)
- C. Roff, P. McGovern, J. Benedikt, P.J. Tasker, R.S. Balmer, D.J. Wallis, K.P. Hilton, J.O. Maclean, D.G. Hayes, M.J. Uren, T. Martin, Detailed analysis of dc-RF dispersion in Al-GaN/GaN HFETs using waveform measurements, in 1st European Microwave Integrated Circuits Conference, Manchester, UK (Sept. 2006), pp. 43–45
- 44. R. Gaddi, J.A. Pla, J. Benedikt, P.J. Tasker, LDMOS electro-thermal model validation from large-signal time-domain measurements, in *IEEE Microwave Theory and Techniques Society's International Microwave Symposium Digest*, Phoenix, USA (May 2001), pp. 399–402
- D.G. Morgan, G.D. Edwards, A. Phillips, P.J. Tasker, Full extraction of PHEMT state functions using time domain measurements, in *IEEE Microwave Theory and Techniques Society's International Microwave Symposium Digest*, Phoenix, USA (May 2001), pp. 823–826
- 46. G. Simpson, J. Horn, D. Gunyan, D.E. Root, Load-pull + NVNA = enhanced X-parameters for PA designs with high mismatch and technology-independent large-signal device models, in 72nd ARFTG Microwave Measurement Conference, Portland, USA (Dec. 2008), pp. 88–91
- P. Wright, J. Lees, J. Benedikt, P.J. Tasker, S.C. Cripps, A methodology for realizing high efficiency class J in a linear and broadband PA. IEEE Trans. Microw. Theory Tech. 57(12), 3196–3204 (2009)

Chapter 8 Advanced Configurations and Applications

This chapter presents some advanced applications of load-pull and source-pull systems. The major emphasis of this chapter is on multi-tone and modulated load-pull systems and their applications. Subsequently, a noise characterization system is described. Finally, a description of a mixer characterization technique is presented.

8.1 Introduction

Radio frequency power amplifiers (RFPAs) are generally characterized using load-pull measurement techniques to determine the parametric values of efficiency, power-added efficiency (PAE), gain, power output, etc., of the power amplifier (PA). In these measurements, various complex load conditions are presented to the device, in order to determine the optimal loading condition for the desired parameters. In the majority of applications, the signals used are single continuous-wave (CW) signals. However, in practical situations, such as load-pull measurements for optimal intermodulation (IMD) components, broadband matching impedance synthesis and device characterization under digitally modulated stimulus, are extremely difficult to carry out using standard load-pull setups.

The major problem in traditional load-pull setups when employing a multi-tone and modulated stimulus stems from the different delays caused by individual tones in the spectrum of the stimulus in the measurement setup, while transmitting and reflecting the modulated traveling waves [1–3]. In order to overcome such problems, requirement/application-driven load-pull setups have been developed [4–12]. These setups have proven to be highly effective in characterizing devices for the determination of optimal parametric values for the desired application.

8.2 Multi-tone Load-Pull Technique

Intermodulation distortion (IMD) analysis is a good way to assess the nonlinear behaviors of RF and microwave amplifiers [5, 13]. IMD analysis is relatively well

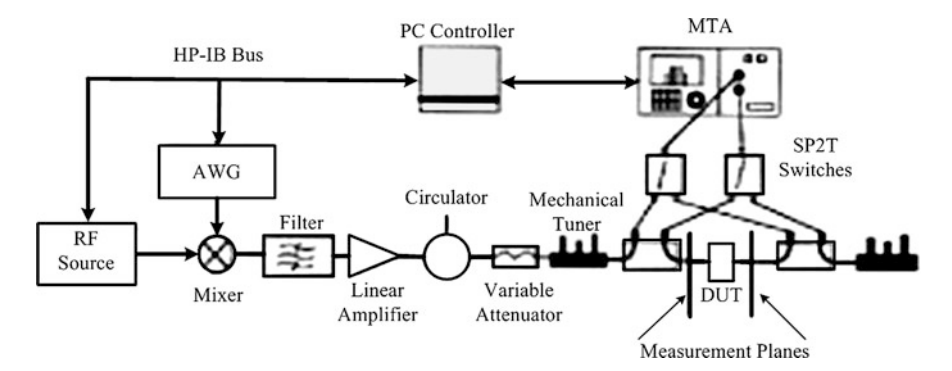


Fig. 8.1 Diagram of the multi-tone load-pull measurement setup developed by Ghannouchi et al. [4], © IEEE 1997

studied, theoretically and experimentally, under two-tone excitations [14, 15]. However, IMD characterization and analysis under multi-tone excitations have not yet been well investigated in open literature [16].

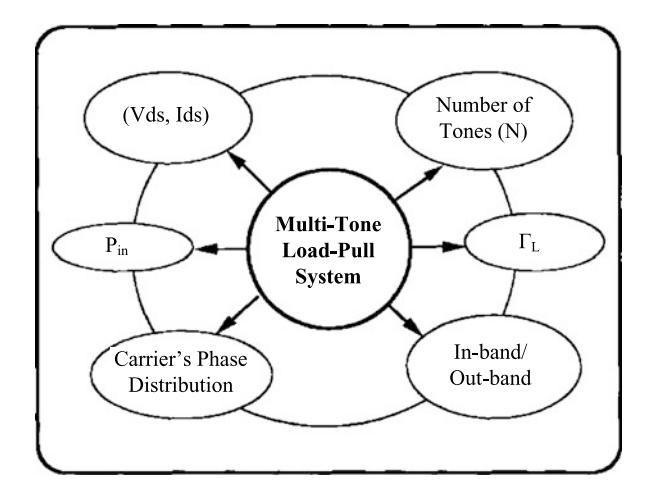
Theoretical postulations about IMD are available [15, 16], but those Ghannouchi et al. [4, 17] were among the first to develop multi-tone signal test setups to experimentally evaluate those theoretical postulations. The setup in [17] focuses on multi-tone device characterization when the tones have an optimal phase relationship [18]; whereas the setup reported in [4] and shown in Fig. 8.1 is capable of IMD characterization with different multi-tone phase distributions.

For multi-tone load-pull measurements, it is important to first generate a very clean spectrum of the multi-tone excitation to be applied to the transistor. In Fig. 8.1, the arbitrary waveform generator (AWG) generates the desired number of tones with the desired frequency spacing, power level and phase distribution. The phase distribution of the tones can be random, uniform, or fixed by the user. Using an AWG reduces the complexity of the system as the number of tones increases, and the synchronization problem between the tones is avoided. The other indispensable instrument used in the setup is the microwave transition analyzer (MTA, e.g., HP70820), which acts as a network analyzer with its home-designed test set.

The mixer up-converts the baseband signal generated by the AWG to around the microwave operating signal available from the microwave synthesizer connected to the other input of the mixer. The highly selective narrowband filter placed at the output of the mixer is used to pass only the principal N-tone spectrum, where N is the number of tones. The multi-tone signal at the output of the filter is obtained with an intermodulation rejection (IMR) of 55 dBc. The filtered spectrum gets amplified by a linear amplifier to reach the desired power level. The variable attenuator performs a power sweep, and the mechanical tuner adjusts the input reflection coefficient for maximum power transfer to the transistor.

The incident and reflected waves at the input and output of the transistor are sampled by two dual couplers with small coupling factors (20 dB). These sampled waves are received and measured by the MTA via a switching stage. The output

Fig. 8.2 Various parameter variation options in the setup developed by Ghannouchi et al. [4], © IEEE 1997

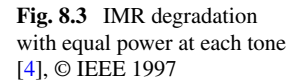


mechanical tuner passively tunes the load. The insertion losses in the tuner limit the maximum achievable reflection coefficient magnitude to 0.9. However, use of recently developed load-pull configurations in this setup can improve the maximum achievable reflection coefficient [19]. A Hewlett-Packard interface bus (HP-IB) controlled through a personal computer (PC) aids in the data acquisition from the MTA, system calibration, and the control of single pole, double throw (SPDT) switches. De-embedding of the measured raw data taken by the MTA to the reference measurement planes of the transistor can be achieved by carrying out short-open-load-thru (SOLT) [20] or thru-reflect-line (TRL) [21] techniques. For power corrections, the measuring ports can be calibrated with an independent power meter.

Overall, the setup in Fig. 8.1 is appropriate for both packaged and on-wafer devices. In addition, it is essential to note that the measurement systems [5, 13] are only useful for two-tone excitations where two separate signal generators are employed. These systems have severe limitations, due to the increasing complexity if the number of tones increases, as one signal generator is required for each tone. However, the Ghannouchi technique overcomes this problem by using an AWG and a simple mixer to generate the spectrum of any desired tones; therefore, it eliminates the need for a large number of signal generators and the associated problem of signal synchronization in those setups.

This configuration enables several kinds of multi-tone measurements, as shown in Fig. 8.2, through the variation of independent parameters of the system. It is evident that this setup allows for the characterization of DUTs in terms of most of the common parameters, such as input power, number of tones, carrier phase distribution, biasing conditions, load impedance and IMR measurement mode (inband/out-band). By varying various parameters, these measurements can generate a complete database that could be useful in the development of different charts for a given DUT in terms of nonlinear characteristics.

To demonstrate the usefulness of such a setup, a metal semiconductor field effect transistor (MESFET, i.e., SCK0151P) exhibiting a 1 dB compression point (P_{1dB})



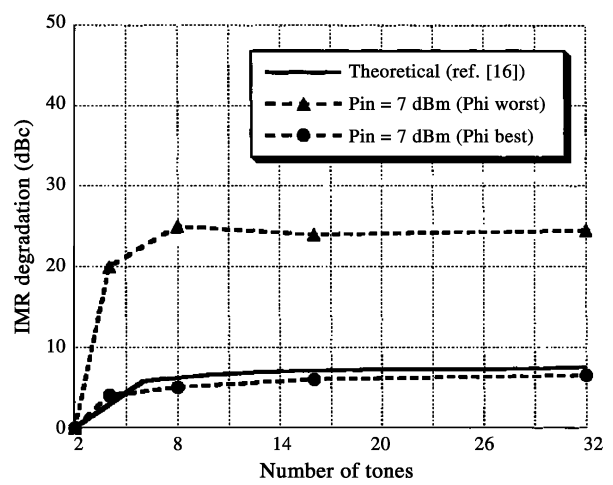
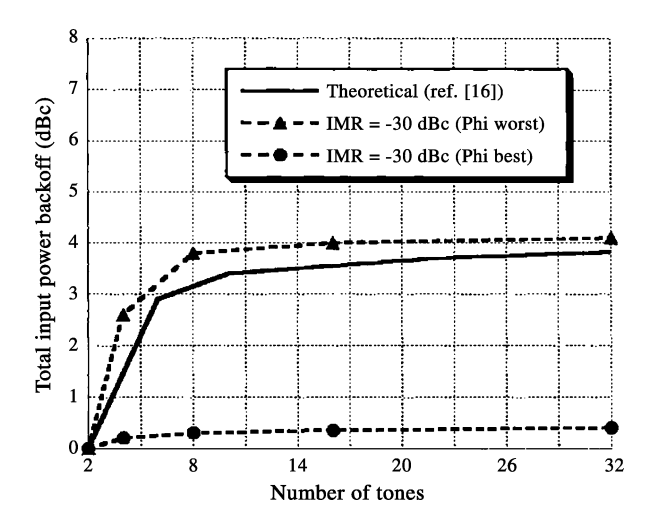


Fig. 8.4 Required power backoff to maintain constant IMR [4], © IEEE 1997



of 23 dBm was characterized for assessing the effect of various parameters on the overall IMR and validation of the theoretical intermodulation distortion analysis [16]. The device was biased at $V_{ds}=10~{\rm V}$ and $I_{ds}=100~{\rm mA}$ for class-A operation.

The first experiment constituted the evaluation of IMR degradation as the number of tones increases, as well as the required backoff level in the input power to maintain a certain constant IMR. All the measurements were carried out for input signals having 2, 4, 8, 16 and 32 tones, with spacing of 100 kHz between tones. The load was set at its optimal value of $\Gamma_L = 0.58 \angle 172^\circ$, which was obtained from load-pull measurement data.

Using the MTA, the input reflection coefficient, absorbed input power per tone, output reflection coefficient, output power per tone, and third-order IMR of the transistor were measured. For each number of tones, the IMR parameter was measured for an input power sweep up to the 1 dB compression region of the transistor. Such

measurement was repeated for ten random phase distributions of the carriers. The experimental results, as shown in Figs. 8.3 and 8.4 [4], correspond to the two extreme cases of the phased distribution among the ten cases considered: one is the best case, and the other is the worst case.

Figure 8.3 illustrates a comparison between the measured and theoretical [16] IMR degradation as a function of the number of tones for the same total input power level ($P_{in/total} = 7 \text{ dBm}$). The total input power in dB is calculated from Eq. (8.1).

$$P_{in/total} = P_{in/tone} + 10\log(N) \tag{8.1}$$

where N is the number of tones in the input signal.

It is apparent that the theoretical IMR degradation falls in the range defined between the best and worst cases of the carriers' phase distribution. This result proves that the phase distribution of the carriers has a strong influence on the IMR; and, in this particular example, the difference is up to 20 dBc between the IMR degradation values of the two extreme cases. Thus, it supports the hypothesis that the power characteristics of amplifiers in a multichannel operation strongly depend on the behavior of the carrier signal of each channel.

Figure 8.4 shows the measured and theoretical [16] total input power backoff required to maintain a constant IMR. Again, the theoretical results fall in the range bounded by the best and worst cases. It is also important to note that, for a certain phase distribution of the carriers, a backoff in the total input power is not needed to maintain a constant IMR, as it can be seen for the best case scenario where the power backoff required is very small (around 0.2 to 0.4 dB). This is very important in the design of highly efficient linear amplifiers, where the transistor has to be operated near its compression region to achieve the desired high power-added efficiency.

In the second experiment, the effect of amplifier class on the IMR was measured. In this measurement, the carriers' phase distribution was kept uniform for all performed operating classes (i.e., identical absolute phase for each tone). The transistor was loaded with the optimal impedance for maximum output power ($\Gamma_L = 0.58 \angle 172^\circ$). The IMR measurements were performed at seven bias points, from 30 % I_{dss} to 70 % I_{dss} with a 10 % step, where I_{dss} is the saturation current. The measurement results were obtained by carrying out an input power sweep at each bias point for N=2 and 8 tones.

It can be observed from the experimental result that the IMR slope, as a function of drain current, varies at a certain bias point depending on the applied input power. This experimental result is not readily explainable. To further investigate this experimental observation, multi-tone harmonic-balance simulations [22] were performed using Agilent's Advanced Design System (ADS) software on a MESFET model extracted from the measured DC and scattering parameter (S-parameter) data by applying using the cubic model [23].

The comparison of the measured and simulated results, as shown in Figs. 8.5 and 8.6, for values of N of 2 and 8, respectively, reveals that there is an acceptable agreement in terms of the IMR levels, mainly with respect to the IMR variation slope. Discrepancies between the measurement and simulation results increase when the transistor moves toward its pinch-off region. This may be attributed to limitations of the model extracted from the measured data.

Fig. 8.5 Effects of changing the saturation current (I_{dss}) on IMR for N=2 [4], © IEEE 1997

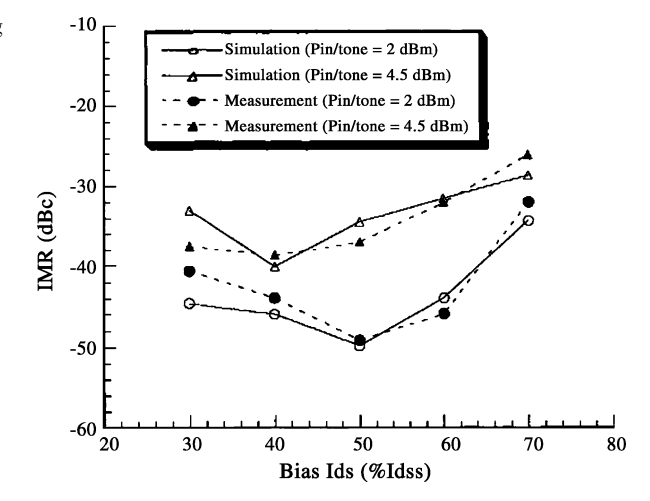
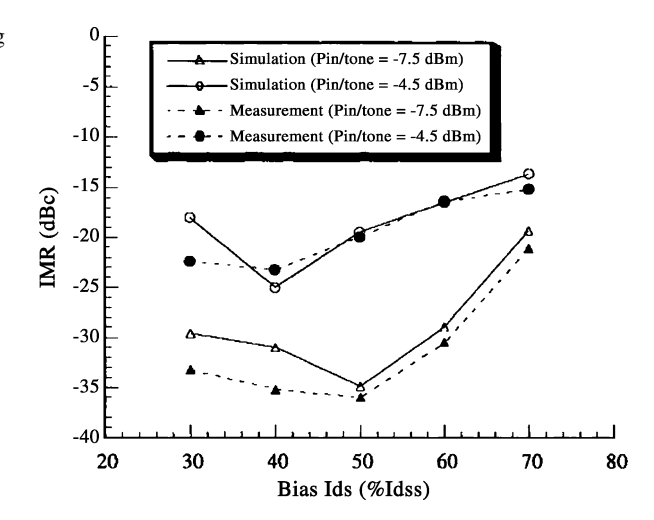


Fig. 8.6 Effects of changing the saturation current (I_{dss}) on IMR for N=8 [4], © IEEE 1997



It can be observed that the IMR is optimal in class-A operation (50 % I_{dss}) in small-signal operating mode (low-input power level), whereas the IMR worsens toward the clipping and pinch-off regions. In the large-signal operating mode (near or in the compression region), the IMR degradation increases with the increase in drain current and tends to become constant at high I_{dss} . The multi-tone setup developed by Ghannouchi et al. [4], therefore, enables the optimization of power and linearity performances of amplifiers through biasing conditions.

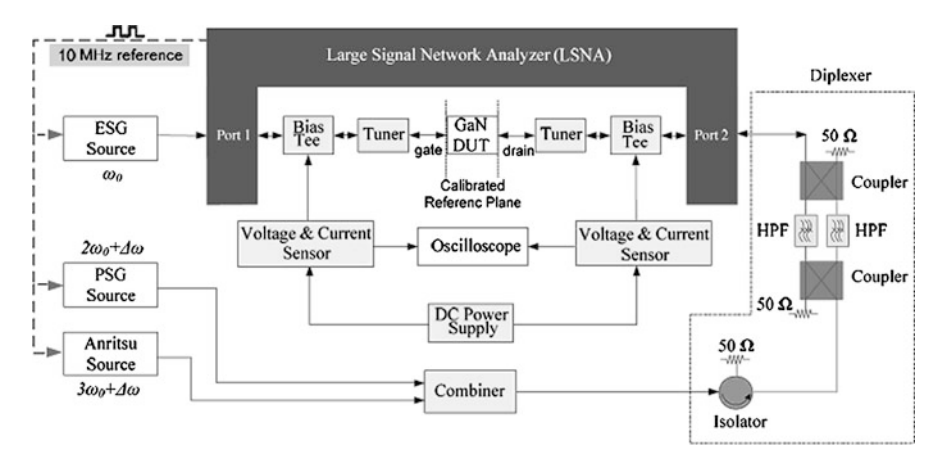


Fig. 8.7 Real-time multi-harmonic load-pull setup developed by Cui et al. [24], © IEEE 2006

8.3 Real-Time Multi-harmonic Load-Pull Technique

Cui et al. [24] developed an efficient real-time open-loop multi-harmonic load-pull system, as shown in Fig. 8.7, based on the large signal network analyzer (LSNA). The system is capable of rapidly synthesizing a wide range of fundamental and harmonic impedances without the usual stability problem associated with traditional active closed-loop load-pull systems [25] and the slowness inherent in the conventional open-loop load-pull system [26]. In essence, this setup is an advanced version of the systems reported in [27]. Roblin et al. [28] developed a further advancement on this system.

In Fig. 8.7, Ports 1 and 2 are used for the gate and drain of the DUT, respectively. The bias tees and DC power supplies set the quiescent operating point of the DUT. The voltage and current sensors detect the time variations of the device bias voltage and current, which gets displayed on the oscilloscope. A group-delay calibration procedure is needed to synchronize the RF envelope measured by the LSNA with the time dependence of the acquired bias current signal (with a period of $\Delta\omega$). The ESG generates a fundamental signal (ω_0) used to excite the DUT input. The two harmonic sources (PSG and Anritsu) inject $2\omega_0 + \Delta\omega$ and $3\omega_0 + \Delta\omega$ in the real-time tuning case (i.e., swept phase measurement case) or generate $2\omega_0$ and $3\omega_0$ in the constant phase measurement scenario. The 10 MHz reference signals are tied together for phase synchronization. The diplexer provides $50~\Omega$ termination at Port 2 for the fundamental frequency, while offering a path for the injected second and third harmonics at the DUT output. The LSNA acquires incident and reflected waves in the frequency domain at the de-embedded calibration planes. The LSNA is operated in the modulation mode to deal with the modulation effects brought about by $\Delta\omega$.

This system employs a real-time approach in which the tuning at the *n*th harmonic utilizes a CW tone $a_2(n\omega_0 + \Delta\omega)$ with a frequency offset $\Delta\omega$ (see Fig. 8.7) from the targeted *n*th harmonic frequency injected at the device output, so that the phase of the harmonic load reflection coefficient is continuously swept in a single

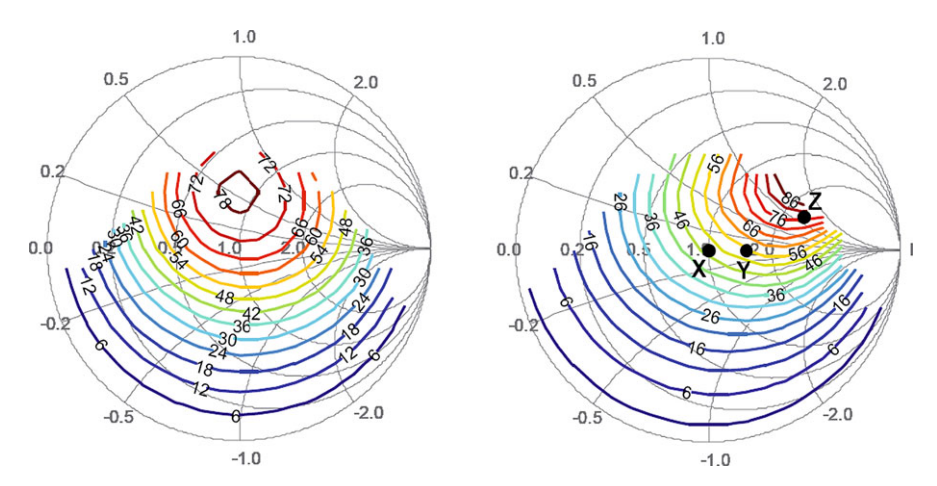


Fig. 8.8 Output power contour (*left*) and PAE contour (*right*) in $\Gamma_L(\omega_0)$ plane, obtained from the $\omega_0 + \Delta \omega$ real-time swept phase measurements [24], © IEEE 2006

LSNA measurement [24]. The power of the CW tone $|a_2(n\omega_0 + \Delta\omega)|^2$ can be swept using a computer via a general purpose interface bus (GPIB). It aids in varying the radius of the reflection coefficient loci, which in turn can produce a large set of harmonic reflective load coefficients with amplitudes smaller or larger than unity mapping of the extended Smith chart.

As an example to demonstrate the capability of this setup, a GaN HEMT (gallium nitride high electron mobility transistor) device was considered with a quiescent DC bias of $V_{GS}=-2.77$ V, $V_{DS}=4.25$ V and $I_{DS}=1.7$ mA for the interactive design of a high-efficiency PA operating in class F. The LSNA was used to acquire frequency domain data up to the fourth harmonic (N=4). In principle, before carrying out real-time second and third harmonic tuning, it is imperative to run the real-time active load-pull measurement at the fundamental frequency, so that an optimal load at ω_0 can be obtained. This optimal load at ω_0 eventually forms the basis for subsequent harmonic tuning.

In the fundamental load-pull case, the ESG provides a 2 GHz fundamental signal (ω_0), and the PSG source injects a $\omega_0 + \Delta\omega$ [$\Delta\omega = 200$ KHz] signal at the DUT's output. The obtained fundamental output power and PAE contours given in Fig. 8.8 show a strong dependence on the loading condition. It is also apparent that the optimal loading for this device for both the PAE and output power lie in the same region of Smith chart.

Case Z marked in Fig. 8.8 represents the impedance point for achieving a high PAE while keeping a large output power. Although both the PAE and output power show progressive trends in the first quadrant of Smith chart, one can identify that there are some termination impedances, which are potentially unstable because the corresponding magnitude of $|\Gamma_{in}(\omega_0)|$ is greater than one, as shown in Fig. 8.9. This situation indicates negative input impedances, which potentially could lead to unstable operation.

Fig. 8.9 $|\Gamma_{in}(\omega_0)|$ contour obtained from the $\omega_0 + \Delta \omega$ real-time swept phase measurements [24], © IEEE 2006

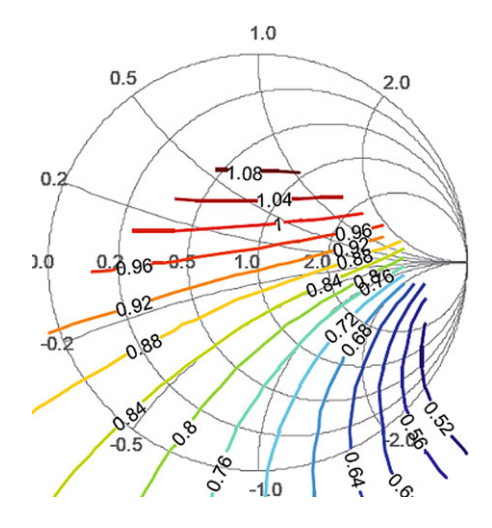


Table 8.1 Comparison of three typical cases in Fig. 8.8: cases X, Y and Z [24], © IEEE 2006

$\Gamma_L(\omega_0)$	PAE (%)		Output power (mW)	
	Swept phase	Constant phase	Swept phase	Constant Phase
Case X: 0	47.9	49.1	69.9	72.8
Case Y: 0.2∠0°	55.4	57.6	67.1	72.4
Case Z: 0.53∠19.3°	80.0	70.6	53.0	56.2

In this situation, study terminations with only positive input impedances are investigated; therefore, three typical cases (X, Y and Z) are selected from the PAE contour plot in Fig. 8.9 for efficiency comparison as shown in Table 8.1. For these cases, the PAE and output power data extracted from the real-time swept phase measurement correlates to the results obtained from the constant phase measurement. Note that in the constant phase measurement the ESG source injects 2 GHz fundamental signal at the drain output without any frequency offset.

It can be observed in Table 8.1 that, in case Z, a higher PAE is extracted from the swept phase measurement than is obtained from the constant phase measurement, due to the large swept power at $(\omega_0 + \Delta \omega)$. For cases X or Y, the PAE difference is less between the swept and constant phase measurements, because smaller power at $(\omega_0 + \Delta \omega)$ is applied. Due to the high PAE (70.6 %) and stability consideration, the load reflection coefficient of case Z was chosen as the optimal fundamental impedance for further analysis at the second and third harmonics.

For load-pulling the harmonic, the PSG source injects $(2\omega_0 + \Delta\omega)$ at the DUT's output, whereas the ESG source provides the 2 GHz (ω_0) excitation at the DUT's input. In this case, the fundamental impedance is kept to the previously identified optimal impedance corresponding to point Z, whereas the third harmonic is left arbitrarily terminated. The sensitivity of the second harmonic termination on the obtained PAE and output power is given in Fig. 8.10.

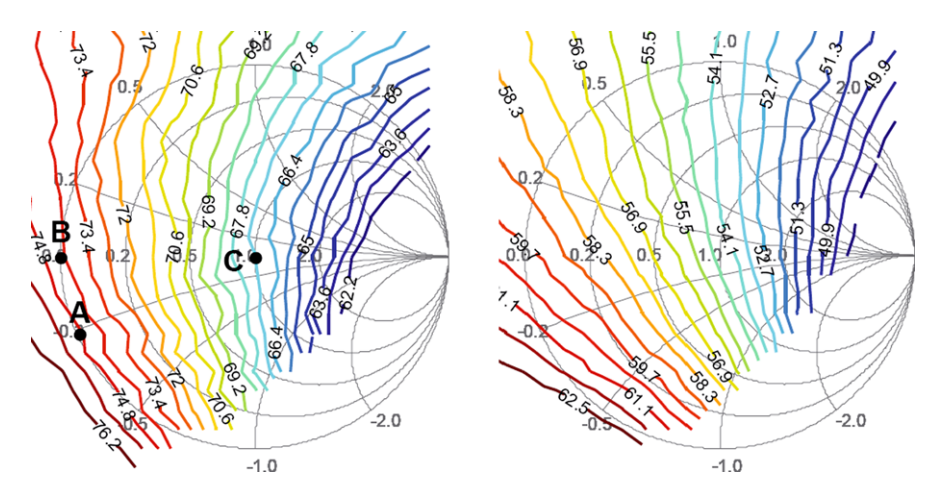


Fig. 8.10 PAE contour (*left*) and output power contour (*right*) in the $\Gamma_L(2\omega_0)$ plane, obtained from the $2\omega_0 + \Delta\omega$ real-time swept phase measurements [24], © IEEE 2006

 Table 8.2
 Comparison of three typical cases in Fig. 8.10: cases A, B and C [24], © IEEE 2006

$\Gamma_L(\omega_0)$	PAE (%)		Output power (mW)	
	Swept phase	Constant phase	Swept phase	Constant phase
Case A: 0.985∠ −156°	74.95	72.03	61.15	57.7
Case B: 0.976∠ −180°	74.18	71.82	59.79	57.6
Case C: 0	67.13	66.47	54.6	53.4

It is evident from Fig. 8.10 that the second harmonic termination with the highest PAE (case A) is close to the short circuit condition and is in agreement with the class-F PA design theory. This high PAE can be further verified from the constant phase measurement, which turns out to be 72.03 %. The corresponding output power using the developed real-time load-pull system and using standard constant phase measurements are 61.15 mW and 57.7 mW, respectively, as given in Table 8.2.

In Table 8.2, the PAEs for three typical cases (A, B, C) are picked from the PAE contours in Fig. 8.10 for the sake of comparison. For the constant phase measurement, the PSG source simply injects a $2\omega_0$ signal to the DUT's output. In each of these three cases, both the PAE and output power results calculated from the real-time swept phase measurement are consistent with those from the constant phase measurement. The degradations of PAE and output power from the swept phase to the constant phase are much less than those in Table 8.1. This fact indicates that the memory effect brought about by the 200 kHz frequency is prominent only at the fundamental frequency, rather than in the second harmonic [24].

The third harmonic real-time load-pull measurement utilizes the optimized load conditions acquired from the tests at the fundamental frequency and harmonic (points Z and A in Figs. 8.8 and 8.10, respectively). In this case, the ESG gives

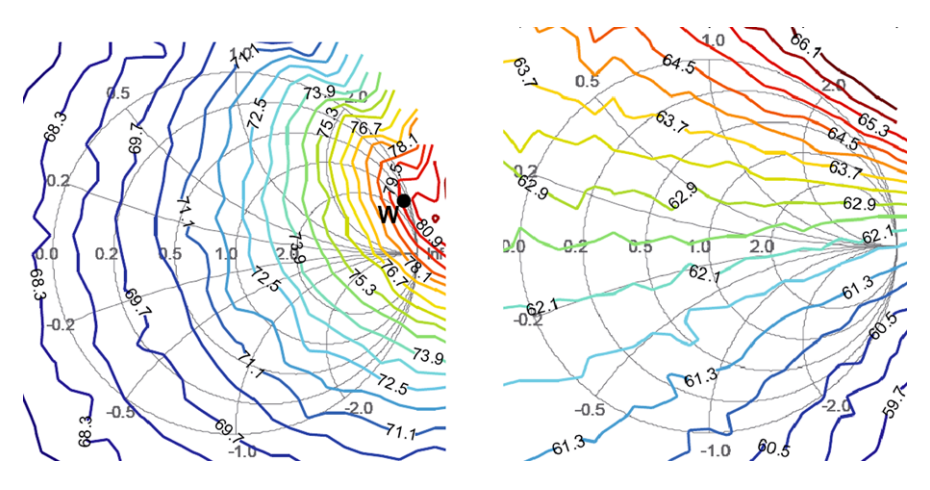


Fig. 8.11 PAE contour (*left*) and output power contour (*right*) in the $\Gamma_L(3\omega_0)$ plane, obtained from the $3\omega_0 + \Delta\omega$ real-time swept phase measurements [24], © IEEE 2006

the 2 GHz (ω_0) excitation at the DUT's input, while the second harmonic ($2\omega_0$) and the third harmonic with frequency offset ($3\omega_0 + \Delta\omega$) are injected by the two harmonic sources to the DUT's output. The load tuner is properly adjusted to the optimal fundamental termination. The PAE and output power obtained from the swept phase measurements in the $\Gamma_L(3\omega_0)$ plane are given in Fig. 8.11.

In Fig. 8.11, the high PAE (around 80 %) contour lines are mainly distributed around the rightmost part (nearer to the open circuit condition) of the Smith chart, which is in close agreement with class-F PA theory. In this particular case, the optimum for class F turns out to be case W with $\Gamma_L(3\omega_0)$ of $0.97\angle17.3^\circ$, which is close to the edge of Smith chart.

The setup developed by Cui et al. [24] thus enables device characterization for high-efficiency PA design. It offers great potential in expediting the device characterization and, therefore, minimizing the power amplifier design time.

8.4 Modulated Signal Load-Pull Technique

Load-pull measurements have been generally limited to single- and two-tone signals for optimizing the output power and third-order intermodulation products (IMD3) performances of transistors. However, with the advancement in modulation techniques, traditional figures of merits, such as the one dB compression point (P_{1dB}) and third-order inception point (IP_3), obtained from one and two-tone stimuli can no longer be used to fully predict the behavior and performance of the transceiver. This is due to the fact that signals represented by discrete spectra do not reflect the complex digitally modulated signals. Furthermore, it has been thoroughly studied and found that the performance of a transistor is strongly dependent on the type of excitation used during characterization and measurement [29, 30]. In order to address

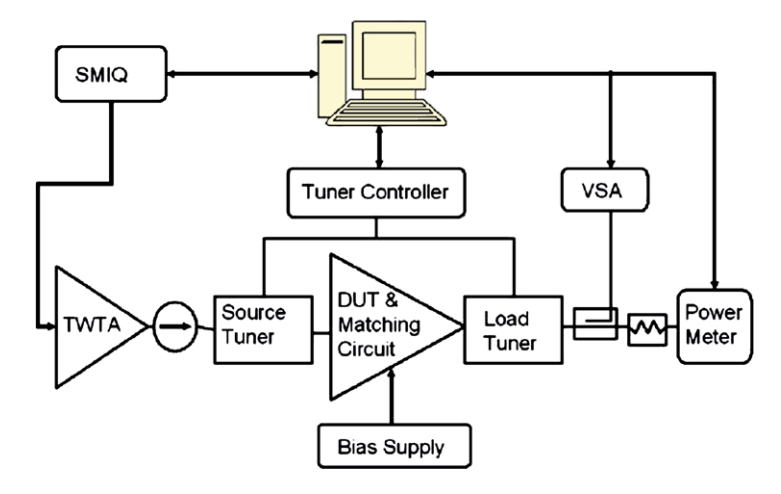


Fig. 8.12 Illustration of a load-pull setup developed by Ghanipour et al. [6], © IEEE 2007

these concerns and investigate the device performance under digitally modulated stimuli, Ghanipour et al. [6] developed a load-pull setup using standard equipment, as shown in Fig. 8.12.

The load-pull system illustrated in Fig. 8.12 utilizes an automatic tuner system (ATS) from Maury Microwave [29]. A vector signal generator (VGS) (Rohde and Schwarz SMIQ03B) uploads and generates the desired digitally modulated stimuli. A traveling wave tube amplifier (1277H) amplifies the stimuli, whereas power meters (HP437B) measure the output and reflected powers. The vector signal analyzer (VSA) (Rohde and Schwarz FSQ8) measures the adjacent channel power ratio (ACPR) and IMD3 of the signals. The ATS software controls all the instruments in the measurement setup.

To show the usefulness of this setup, a high-power laterally diffused metal oxide semiconductor (LDMOS) device (MRF21030LR3) with a typical P_{1dB} output power of 44.6 dBm was selected. The experiment was carried out at 2.14 GHz using WCDMA (wideband code division multiple access) modulated signals (peak-to-average power ratio (PAPR) values of 9.4, 8.6, 7.6, 7.6, 6.5 and 6.1 dB), OFDM (orthogonal frequency division multiplexing) signals (PAPR values of 9.4 and 6.1 dB), and a two-tone signal. In order to resemble the bandwidth of a single-carrier WCDMA signal, the OFDM signal had a 5 MHz bandwidth, and the two-tone signal generated had tone spacing of 5 MHz. For each type of source signal, the average output power was adjusted, so that the peak output power for all eight signals was 40.4 dBm at 4 dB backoff.

Power gain and lower channel ACPR (ACLR)/IMD3 contours, as shown in Fig. 8.13, for the WCDMA signal with a PAPR of 9.1 dB and a two-tone excitation reveal that the size and shape of the contours are very much dependent on the type of stimuli used during the load-pull measurement.

It is apparent that the optimal loading conditions for two-tone and WCDMA stimuli are quite different. To quantify the difference, the optimal impedance

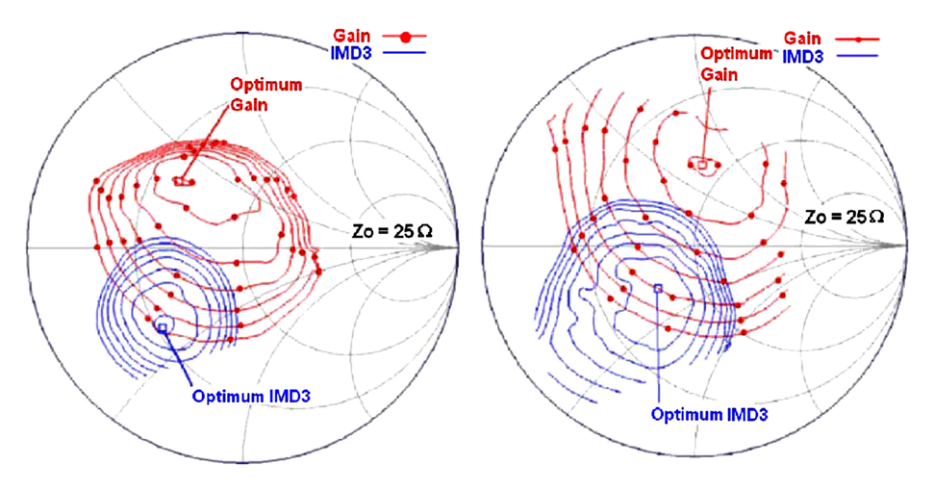
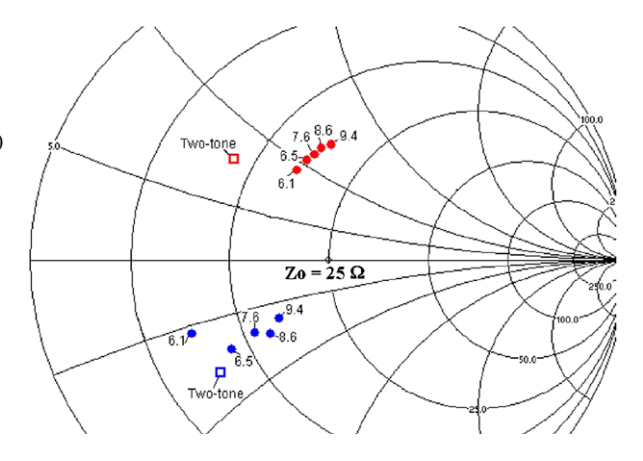


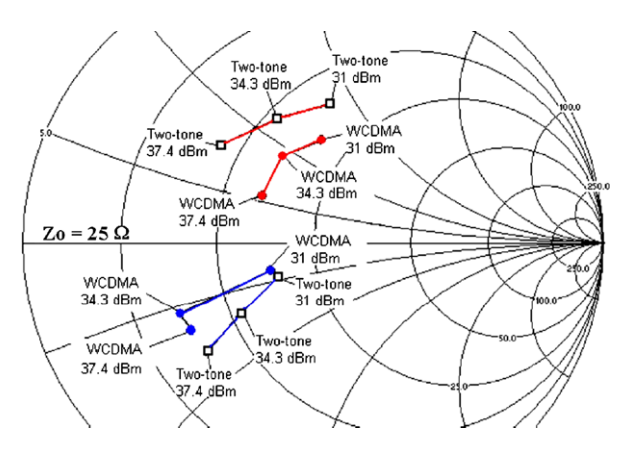
Fig. 8.13 Gain and IMD3 contours for an MRF21030 device with a two-tone source (left) and gain and ACLR contours for an MRF21030 device with a WCDMA (PAR = 9.4 dB) source (right) [6], © IEEE 2007

Fig. 8.14 Optimal gain (shown in the *upper half* of the Smith chart) and optimal ACLR/IMD3 (shown in the *lower half* of the Smith chart) impedances for two-tone and WCDMA (with PAPR values of 9.4, 8.6, 7.6, 6.5 and 6.1 dB) signals [6], © IEEE 2007



obtained from all the stimuli under consideration, as shown in Fig. 8.14, can be analyzed. In this figure, the optimal gain impedances are located in the upper part of the Smith chart, while the optimal ACLR and IMD3 impedances are located in the lower section. It can be seen that the reactance of the optimal gain impedance decreases as the average power of the excitation signal is increased (to compensate for the decreasing PAPR). Similarly, the resistance of the optimal ACLR impedance for WCDMA signals tends to increase as the average power is increased. The ACLR and gain contours and the location of the respective optimal impedances for OFDM signals (not shown here) also matched those for WCDMA signals with similar PAPR values.

Fig. 8.15 Optimal gain (shown in the *upper half* of the Smith chart) and optimal ACLR/IMD3 (shown in the *lower half* of the Smith chart) impedances for two-tone and WCDMA (PAPR = 6.1 dB) signals at various output power levels [6], © IEEE 2007



It can, therefore, be concluded that device performance is predominately dependent on stimuli's power, PAPR and bandwidth and are largely independent of the type of excitation, i.e., OFDM or WCDMA signal.

To enhance the understanding of whether the shift in the optimal gain and ACLR impedances was due to an increase in the average power or due to a decrease in PAPR, another experiment was performed, in which load-pull measurements of the WCDMA signal with a PAPR of 6.1 dB were performed with the average output power at 31, 34.3 and 37.4 dBm and compared to two-tone load-pull measurements with the same average power.

The results in Fig. 8.15 show that, even though the optimal impedances for a two-tone signal are significantly different from the optimal impedances for a modulated signal, both are similarly affected by an increase in output power. As the required output power is increased, the reactance of the optimal gain impedance tends to decrease and is in agreement with theoretical results [32]. This experiment also revealed a new insight: there is increased resistance of the optimal ACLR impedance as the output power is increased, which can be very useful in the optimization of devices for PA design applications.

8.5 Multi-tone Envelope Load-Pull Technique

As mobile communications have become more complex with the transmission of huge volumes of data, the modulation schemes used to transmit the information have also become more complex often requiring transmission over very wide bandwidths. In order to fully characterize and design the required PA properly, it is vital that large-signal measurement systems adapt to accommodate these complex modulations.

The ideal way to predict the performance of a designed PA for modern communication system is a priori characterization of devices under modulated excitations. A load-pull setup capable of synthesizing constant impedance over a modulation bandwidth and beyond is a logical requirement for characterizing devices

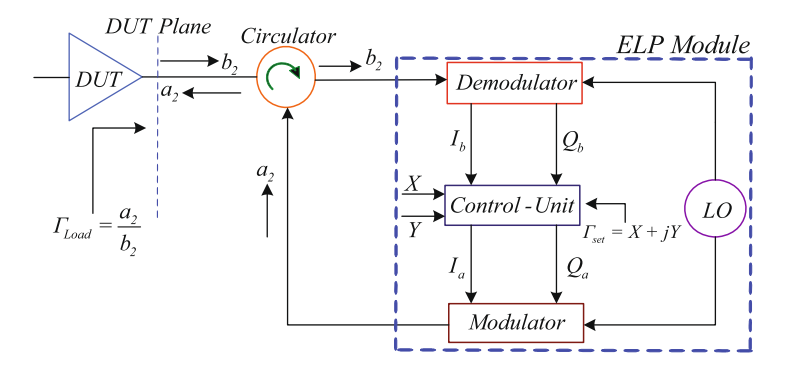


Fig. 8.16 Generic block diagram illustrating the concept of the ELP technique

for such applications. Hashmi et al. [33] proposed a concept to emulate broadband impedance, and the technique has been further enhanced [11, 34] and shown to provide significant characterization data [35].

The envelope load-pull (ELP) system (a block diagram of which is illustrated in Fig. 8.16) explained in Chap. 6 emulates reflection coefficient given by Eq. (8.2). However, for a modulated signal of modulation frequency ω_m with n tones, this relationship changes to Eq. (8.3) [11].

$$\Gamma_{load}(\omega) = \frac{a_2(\omega)}{b_2(\omega)} = X + jY \tag{8.2}$$

$$\Gamma_{load}(\omega_c - n\omega_m) = \frac{a_2(\omega)}{b_2(\omega)} = (X + jY)e^{jn\omega_m\tau}$$
(8.3)

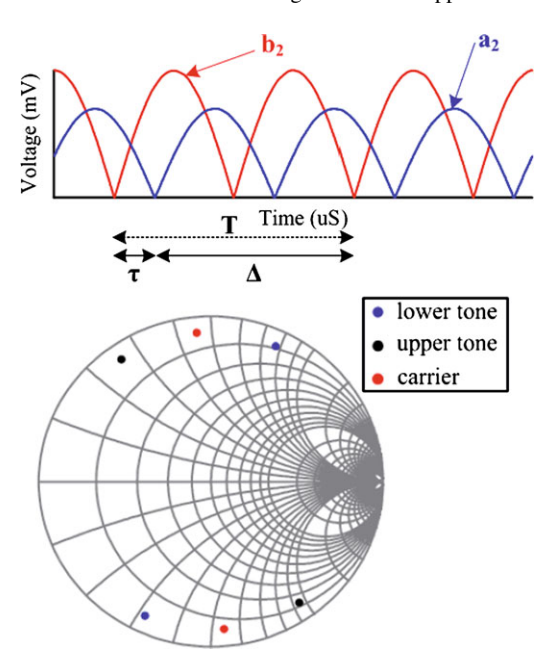
Parameter τ in Eq. (8.3) is the group delay around the loop of the load-pull system. It is apparent from Eq. (8.3) that the load reflection coefficient becomes dependent on the modulation frequency through a phase operator, $e^{jn\omega_m\tau}$, and that it leads to phase spread between the loads at $\omega_c - n\omega_m$ and $\omega_c + n\omega_m$ frequency pairs, respectively. This spread can be alternatively attributed to the delayed envelope of a_2 (reflected traveling wave) at the reference plane when it traverses through the feedback loop. Equation (8.4) gives the envelope domain expression for a CW signal, whereas the envelope domain expression changes to Eq. (8.5) for a modulated signal.

$$I_a(t) + jQ_a(t) = (X + jY)(I_b(t) + jQ_b(t))$$
 (8.4)

$$I_a(t) + jQ_a(t) = (X + jY)(I_b(t - \tau) + jQ_b(t - \tau))$$
 (8.5)

Experimentally, the effect of group delay can be observed in Fig. 8.17, which was measured using a time-domain modulated waveform system [36]. These results are from an experiment carried out on a thru line in place of a DUT with three-tone excitation (on a 1.8 GHz carrier) having a tone spacing of 100 kHz for emulation of the reflection coefficients of $0.9 \angle 90^{\circ}$ and $0.9 \angle 270^{\circ}$. It is evident that the loss of synchronization between the envelopes of transmitted traveling wave, b_2 , and reflected traveling wave, a_2 , cause spread in the synthesized reflection coefficient and thus agree perfectly with Eqs. (8.3) and (8.5).

Fig. 8.17 Measured three-tone envelope (*top*) and two emulated reflection coefficients in the Smith chart (*bottom*) [11], © IEEE, 2008



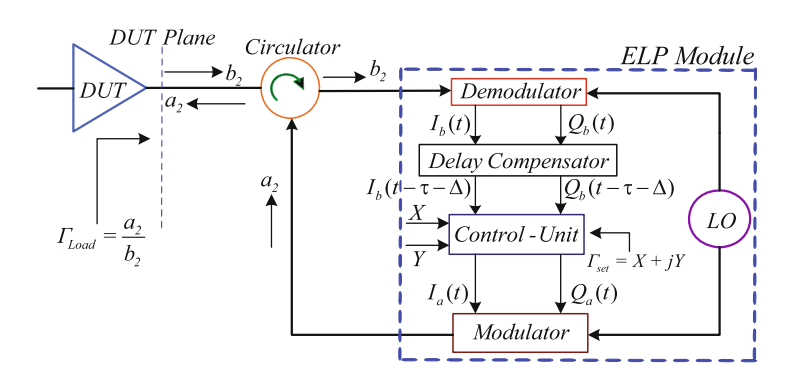


Fig. 8.18 Block diagram of the envelope load-pull system with a delay compensator developed by Hashmi et al. [33] for synchronizing the second cycle of the transmitted traveling wave, b_2 , with the first cycle of the reflected traveling wave, a_2

In general, time-domain waveform measurement systems utilized in nonlinear device characterization employ repetitive signals. Therefore, Hashmi et al. [33] identified that a delay compensator in the feedback loop of ELP system, as shown in Fig. 8.18, can be incorporated in such a way that the envelope domain expressions for transmitted traveling wave, b_2 , and reflected traveling wave, a_2 , are related by Eq. (8.6) [11, 33].

$$I_a(t) + jQ_a(t) = (X + jY) \left(I_b(t - \tau - \Delta) + jQ_b(t - \tau - \Delta) \right)$$

$$(8.6)$$

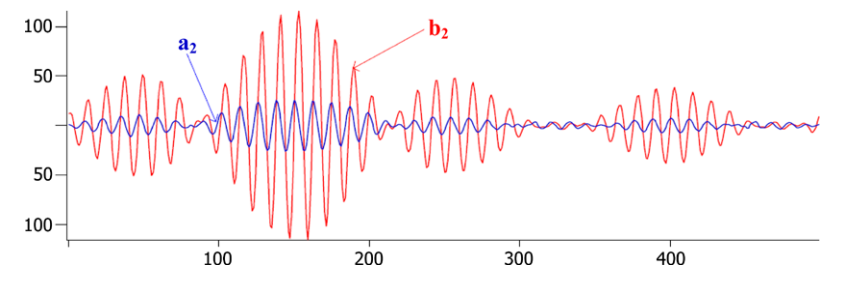
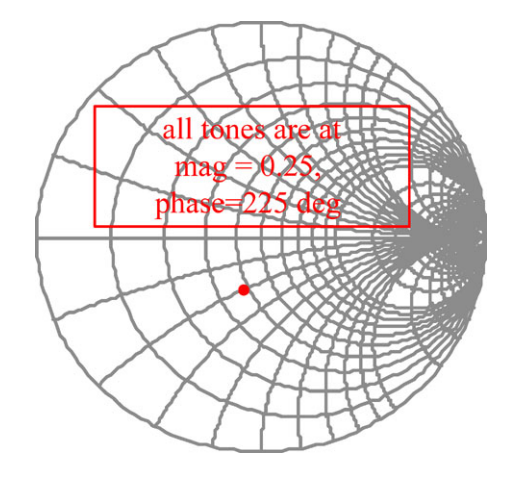


Fig. 8.19 Reflected traveling wave (a_2) and transmitted traveling wave (b_2) and a clear depiction of their synchronized envelopes [34], © IEEE 2008

Fig. 8.20 Measured six-tone reflection coefficient over a 6 MHz bandwidth after delay compensation in the envelopes (i.e., synchronization of the transmitted and reflected traveling waves) [34], © IEEE 2008



where $\Delta = T - \tau$ is the additional delay provided by the delay compensator to synchronize the envelope of the transmitted traveling wave, b_2 , and the reflected traveling wave, a_2 ; and, T is the time period of the excitation signal.

This compensation technique works equally well with any excitation, as can be seen in Fig. 8.19 [34]. It is evident that the transmitted and reflected traveling waves are synchronized as a result of delay compensation in their envelopes. The stimulus in this case was a six-tone signal with a tone separation of 1.2 MHz, and the target reflection coefficient was $0.25 \angle 225^{\circ}$. This enabled the synthesis of the constant reflection coefficient (i.e., constant load impedance), as shown in Fig. 8.20, around the 6 MHz bandwidth of the six-tone stimulus.

As an example, this setup finds immediate use in the investigation of the effect of RF impedance variation around the fundamentals on PA distortion characteristics [35]. Such an experiment allows for the determination of device behavior in terms of linearity when subjected to variable impedances or constant impedance around a specific bandwidth and also aids in the associated trade-off between linearity and efficiency.

8.6 Wideband Load-Pull Technique

The use of signals with high peak-to-average power ratios (PAPRs) for increased spectral efficiency in modern wireless systems results in the requirement that PAs have both good linearity and efficiency. Traditionally, class-AB (where all higher harmonics are shorted) or inverse class-AB operation (where all higher harmonics are open [49]) are used and operated in backoff, until an acceptable linearity performance is obtained. However, this approach is suboptimal, as it results in poor design for signals with high PAPRs.

Alternatively, linearization techniques that utilize out-of-band terminations at the baseband and second harmonic frequencies are used to improve the in-band linearity of transistor devices employed in the design of PAs [51, 52]. To evaluate device technologies for their linearity, a dedicated large-signal characterization setup is required that must provide:

- Calibrated testing of highly linear devices at all frequencies of interest (e.g., f_0 , $2f_0$, $3f_0$, and third- and fifth-order intermodulation frequencies).
- Flexible and independent control of the baseband, fundamental and second harmonic terminations at both the DUT's input and output over the full Smith chart.
- Constant impedance for all frequency components.

Unfortunately, commercially available passive load-pull systems [52, 53] cannot control the baseband (BB) impedance and do not cover the complete Smith chart. On the other hand, most of the active load-pull systems can cover the entire Smith chart, but are not appropriate for linearity characterization with wideband signals, due to the inherent electrical delay associated with these systems that causes spread in the phase of synthesized reflection coefficients. To overcome these problems, Spirito et al. [7] developed an active load-pull setup, which was further improved by Marchetti et al. [9].

The setup possesses a high dynamic range and also provides a solution that overcomes the losses, electrical delay, power handling and linearity limitations present in traditional passive and active load-pull systems. The setup is based on wideband data acquisition and wideband signal injection of the incident and device generated power waves at the frequencies of interest.

By monitoring and controlling the spectral content of these waves in the fundamental and harmonic frequency bands, it is possible to synthesize user defined reflection coefficients at the DUT's reference planes. This allows emulation of any matching network based on its frequency scattering parameters (S-parameters). Furthermore, the monitoring and control of the spectral content of the waves at the DUT's reference planes enables the automatic compensation of the signal distortion resulting from the loop amplifier nonlinearities [9]. In theory, the elimination of amplifier nonlinearities and the electrical delay allows this setup to characterize devices under wideband stimuli.

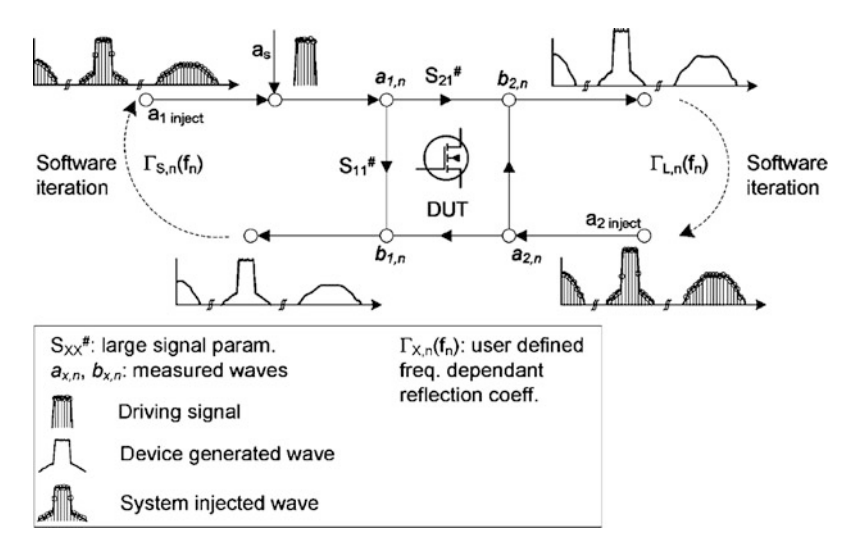


Fig. 8.21 Principle of the wideband open-loop active load-pull approach. [9], © IEEE 2008

8.6.1 Wideband Load-Pull Approach

As the reflection coefficients represent the ratio of waves, there is a requirement to control the linear ratios of the incident and device generated waves of the DUT in the BB, fundamental and harmonic frequency bands described in Fig. 8.21.

When the nonlinear DUT is excited with a user defined modulated signal, a_s , it generates signals in the baseband, fundamental and higher harmonic frequency bands. By measuring the device's generated waves $(b_{1,n} \text{ and } b_{2,n})$ as well as the incident waves, the waves to be injected are estimated at every iteration. When the required reflection coefficient versus frequency (at every controlled band) is achieved, the iteration has converged, and the large signal parameters (e.g., power-added efficiency, output power, intermodulation distortion) are measured.

The only wave known prior to the iteration procedure is the source signal (a_s) , whereas the device generated waves (b waves) are the result of the interaction of a_s with the unknown nonlinear properties of the device. It is important to note that the spectral content of the generated waves include not only the fundamental frequency band, but also BB, higher order harmonics, and intermodulation distortion. However, the accurate measurement of the spectral content of the device generates waves along with the knowledge of user defined reflection coefficient and allows for the estimate of the spectral content of all the injected waves (a waves) at the DUT's port. The expression in Eq. (8.7) relates the a and b waves and the user defined reflection coefficient [9].

$$a_{x,n}(f_n) = b_{x,n}(f_n)\Gamma_{x,n}(f_n)$$
(8.7)

where x is an index to indicate source (s) or load (l); n indicates the frequency band, e.g., BB (0), fundamental (1) and harmonic (2 and up); and, $\Gamma_{x,n}(f_n)$ is the

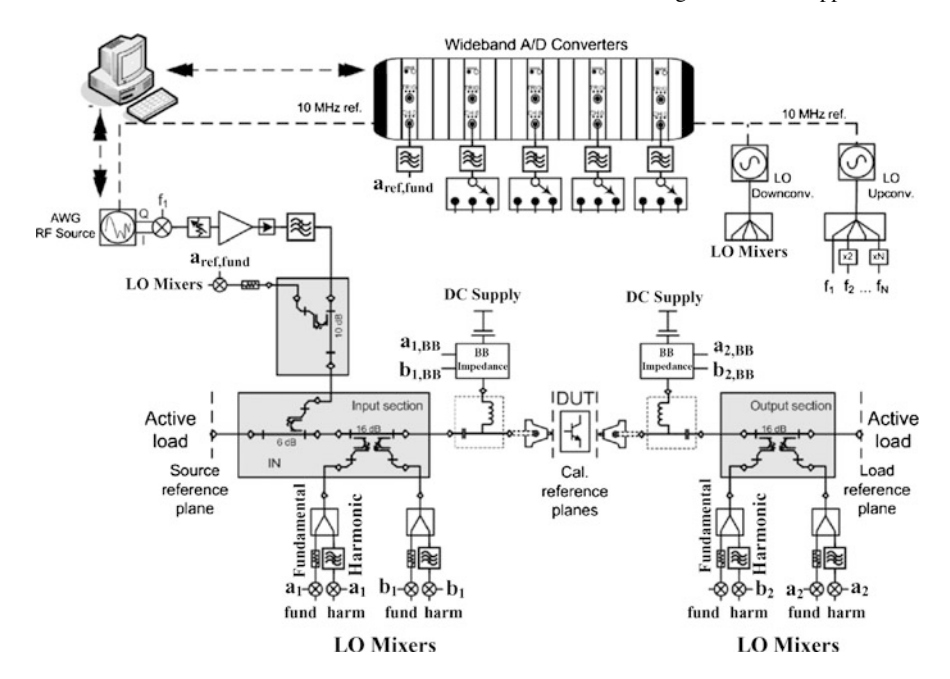


Fig. 8.22 Simplified block diagram of the wideband active harmonic load-pull system developed by Marchetti et al. [9], © IEEE 2008

user defined reflection coefficient of the source or load versus frequency at the BB, fundamental or harmonic frequency.

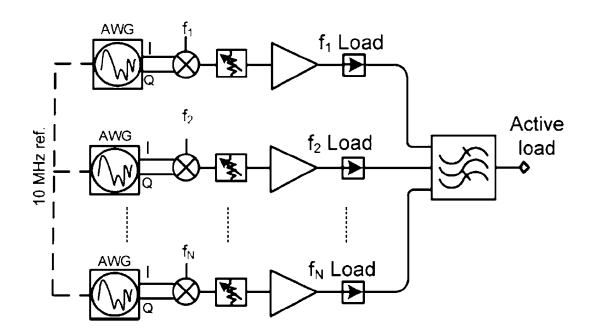
It is imperative to understand that, although this load-pull technique seems simple, in practice, it requires attention to a few issues. First of all, it requires very fast data acquisition with high linearity and dynamic range, in order to handle the spectral content of the complex modulated signals with their related distortion products. Secondly, the a waves need to be generated with a high dynamic range and must be optimized for their spectral content, in order to satisfy Eq. (8.7). Both these requirements place high demands on the capabilities of the hardware configuration, as well as on the related software [9].

8.6.2 Setup Description

A simplified block diagram of the measurement setup is shown in Fig. 8.22. The S-parameter test set, which is based on a five-coupler configuration [54], allows for simultaneous measurement of the source, input and load reflection coefficients at the DUT's reference planes.

Wideband analog-to-digital (A/D) converters (or ADCs) with a sampling frequency of 100 MHz are used to acquire the down-converted waveforms, facilitating the measurement of the device reflection coefficients over a wide bandwidth in a

Fig. 8.23 Simplified block diagram of the wideband active loads with phase coherent frequency up-conversion [9], © IEEE 2008



single data acquisition. Custom bias tees with low inductance are placed directly at the wafer probe, in order to minimize the electrical delay of the BB impedance. They are implemented as a passive impedance switch bank [55]. The BB circuit also includes the low-frequency test set for the calibrated BB impedance measurement.

The source signal and all injection signals needed to create the user defined reflection coefficients at the DUT's reference planes, originate from fully synchronized (200 MS/s) AWGs having same the time base. Based on the phase coherency requirement between fundamental and harmonic injection signals, the in-phase/quadrature (IQ) up-conversion is preferred over digital intermediate frequency (IF) techniques [56]. This allows for the use of a single local oscillator (LO) to generate the high-frequency signals at fundamental and harmonic frequencies by means of multipliers (e.g., 32 for the second harmonic) in the LO path, as depicted in Fig. 8.23. This guarantees that the active loads and driving signal are phase coherent, since this LO does not need to be swept. Consequently, the source and all injection signals are up-converted to the fundamental and harmonic frequencies and fed to the DUT to establish the driving signal and reflection coefficients [9].

Another advantage of the IQ approach, compared to other known signal generation techniques, is the relative limited length of the data records needed to fulfill the standard model requirements of complex modulated signals (e.g., WCDMA [57]), yielding a significant speed advantage in practical measurement situations.

In Fig. 8.23, computer controlled attenuators and high power amplifiers are placed in the signal path, in order to control the level the power of the injection signals. This allows for the utilization of the maximum dynamic range of the AWGs at all times, something that proves to be essential for meeting the spectral requirements of modern communication signals.

In this method, the accurate representation of the spectral content of the RF waves at fundamental and harmonic frequencies can be obtained if the measured power waves are down-converted to a lower frequency prior to data acquisition. This is also a common technique used in vector network analyzers (VNAs) and allows the highest possible dynamic range achievable.

For modulated signals, it is very important that the detection path is free from nonlinear errors that cannot be corrected by linear calibration techniques. The detection dynamic range of the harmonic frequency components are optimized through the use of power splitters and high-pass filters at the detection ports of the couplers in the input and output sections, as shown in Fig. 8.22 [7, 9].

By high-pass filtering the higher harmonic components, the mixer used for the down-conversion in the signal path is protected from the high power of the fundamental signal. This drastically relaxes the mixer linearity requirements for the second and higher harmonics, improving the quality of the acquired signals. By stepping the LO frequency, the frequency band centered on the harmonic of interest is down-converted to its low IF representation for data acquisition.

The detection dynamic range of the system in the fundamental frequency band is maximized by using variable attenuators in the RF path and high-power high-linearity mixers. Note that DUT nonlinearities also give rise to BB signals, which do not need frequency conversion prior to the data acquisition. The resulting low IF signals and BB signals from the DUT are fed to high-speed multiplexing switches to reduce the required number of high-performance wideband ADCs [9].

Finally, the system calibration can be carried out using the combination of the techniques described in [54, 55, 58]. In the first step, the combination of standards at the source and DUT input reference planes allows for simultaneous measurement of the source and DUT input reflection coefficients [54]. At the same time, use of an open-short-load (OSL) standard at the DUT's input and output reference planes enables the calibrated measurement of the BB impedance [55].

In the second step, use of a OSL standard at the load reference plane, when a thru line is in place of a DUT, allows for the measurement of the DUT's load reflection coefficient. Finally, connection of power meter at the load reference plane aids in absolute power calibration [58]. IQ modulators can be calibrated for leakage minimization through the use of DC offsets, while balance and quadrature errors can be corrected through digital pre-compensation [59].

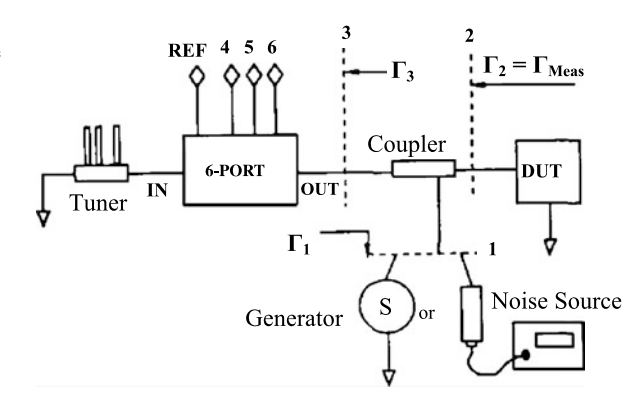
8.7 Noise Characterization

Noise parameter determination methods have evolved in order to cater to the requirements of emerging low-noise transistor technology. In principle, noise characterization always requires a highly repeatable electronic or automated mechanical tuner along with a VNA. Ghannouchi et al. [37] developed a noise characterization setup that removes the need of a repeatable impedance tuner and discards the requirement for a VNA. It employs a reverse six-port (SP) reflectometer and a standard spectrum analyzer and.

8.7.1 Noise Parameter Measurement

The measurement of the noise parameter consists of measuring the noise factor of the DUT for several different noise source impedances. The noise factor of a network, as defined by Friis, is the ratio of the input signal-to-noise ratio (SNR) to the output SNR. The output signal is equal to the input signal multiplied by the gain of

Fig. 8.24 Block diagram of source-pull setup in a reverse six-port configuration for the measurement of noise source impedance [37], © IEEE 1995



the device; therefore, the noise factor (F) can be expressed as per Eq. (8.8) and the noise figure (NF) can be expressed as per Eq. (8.9).

$$F = \frac{N_{out}}{G.N_{in}} \tag{8.8}$$

$$NF = 10\log(F) \tag{8.9}$$

with $N_{in} = kT_0B$ and $N_{out} = GkT_0B + N_{add}$, where k is Boltzman's constant, and B is the measurement bandwidth in hertz.

In a 1 Hz bandwidth for a reference temperature, T_0 , defined as 290 K, the reference noise level, kT_0B , is equal to -174 dBm. N_{add} represents the noise contribution of the DUT and is independent of the noise power injected to the input of the DUT. When measuring the noise factor with an available input noise, N_{in} , different from -174 dBm, the obtained noise factor given by Eq. (8.8) is wrong. However, for a known input noise power level, appropriate corrections help in reaching the true noise factor of the device [37].

The measurement of the noise figure using a non-repeatable tuner experiences two critical issues. The first relates to the determination of an accurate impedance of a noise source for each position of the uncalibrated tuner, while the other corresponds to the accurate evaluation of the available noise power at the input of DUT associated with the impedance of a noise source. A SP reflectometer in reverse configuration, as shown in Fig. 8.24, can measure its own test port measurement (Γ_2) as described in Chap. 4.

Experimental verification shows that the reflection coefficient (Γ_2) measured by a reverse SP reflectometer is identical to that measured by a VNA connected at plane 2 in Fig. 8.24. The advantage of the reverse SP configuration is that it can measure the source impedance's reflection coefficient (Γ_2) at plane 2, under any experimental condition. As a consequence, the repeatability and calibration of the tuner are not required. For a transparent SP reflectometer (i.e., $S_{11} \approx S_{22} \approx 0$ and $S_{12} \approx S_{21} \approx 1$), the tuner and SP junction can cover a wide area of the Smith chart [38]. Noise can be injected to the DUT by switching alternatively between the signal generator and a commercial 50 Ω noise source.

The available signal or noise power at plane 2 can be determined once the reflection coefficient (Γ_2) and the scattering matrix ($S[3 \times 3]$) of the directional coupler are known. Scattering matrix $S[3 \times 3]$ can be reduced to matrix $S'[2 \times 2]$ in such a way that its entries are functions of the reflection coefficient (Γ_3) at plane 3 in Fig. 8.24 [37]. This reflection coefficient (Γ_3) can be obtained from the measured reflection coefficient (Γ_2) and the scattering matrix $S[3 \times 3]$ of the coupler. Matrix $S'[2 \times 2]$ represents the tuner, SP and coupler as an equivalent two-port network defined between planes 1 and 2. The available power (P_1) of the generator connected at plane 1 is related to the available power at plane 2 (P_2) by the expression given in Eq. (8.10) [37]. The term G_{21} in this expression represents the available power gain in the two-port network between planes 1 and 2.

$$P_2 = G_{21}P_1 = \frac{1 - |\Gamma_1|^2}{|1 - S'_{11}\Gamma_1|^2} |S'_{21}| \frac{1}{1 - |\Gamma_2|^2} P_1$$
(8.10)

where Γ_1 is the reflection coefficient of the generator connected at plane 1, Γ_2 is measured by the reverse SP junction at plane 2, and:

$$S'_{11} = S_{11} + \frac{S_{13}S_{31}}{(1/\Gamma_3) - S_{33}}$$

$$S'_{21} = S_{21} + \frac{S_{23}S_{32}}{(1/\Gamma_3) - S_{33}}$$

$$\Gamma_3 = \frac{\Gamma_2 - S_{22}}{S_{23}S_{32} + (\Gamma_2 - S_{22})S_{33}}$$

The available noise power at plane 2 can be expressed as a function of the component noise temperature given in Eq. (8.11). It is assumed that the noise contribution from the directional coupler, SP junction and tuner are maintained at the same constant physical temperature (T_c).

$$N_2 = (T_S \alpha + (1 - \alpha)T_c)kB \tag{8.11}$$

where T_S is the noise temperature of the noise source with $kT_SB = N_1$; and, α is the coupling loss between planes 1 and 2 and is equal to available gain G_{21} given by Eq. (8.10).

As the power available at the input of the DUT is not at -174 dBm, the noise factor cannot be determined from Eq. (8.8). Instead, a comparison of the measured output noise (N_{out}) and the calculated input noise (N_2G_{DUT}) yields the noise contribution, N_{add} , of the DUT. G_{DUT} represents the gain of the DUT.

$$N_{add} = (N_{out})_{measured} - N_2 G_{DUT}$$
(8.12)

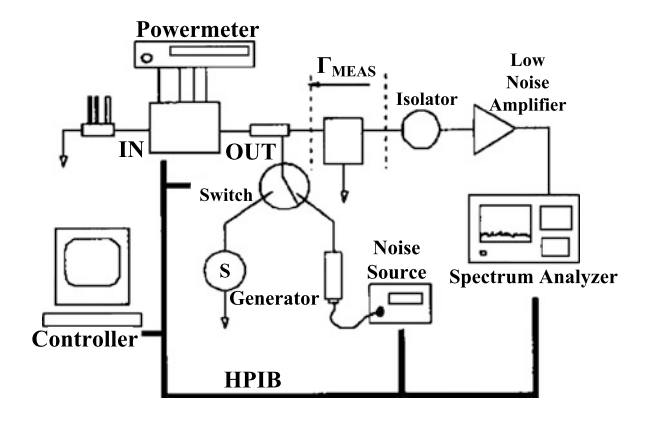
Equations (8.8), (8.9) and (8.12) can be simplified at reference temperature T_0 to obtain the expression for the noise figure (NF) of the DUT as:

$$NF_{DUT} = 10 \log \left(\frac{N_{out} + N_{add}}{G_{DUT}kT_0B} \right)$$

$$= 10 \log \left(\frac{(N_{out})_{measured} + G_{DUT}(kT_0B - N_2)}{G_{DUT}kT_0B} \right)$$
(8.13)

where $N_{out} = G_{DUT}N_{in} = G_{DUT}kT_0B$.

Fig. 8.25 Noise parameter test setup using an uncalibrated tuner [37], © IEEE 1995



Equation (8.13) requires measurements at only one noise temperature; therefore, a noise receiver with high measurement accuracy is needed. In the absence of such a quality noise receiver, an alternative approach is to use Y factor for the noise figure calculation, which given in Eq. (8.14).

$$NF_{DUT} = 10\log\frac{(\frac{T_H}{T_0} - 1) - Y(\frac{T_C}{T_0} - 1)}{Y - 1}$$
(8.14)

 T_H and T_C are deduced from N_2 , and Y is deduced from N_{out} as follows:

$$T_H = \frac{N_2(H)}{kB}; \qquad T_C = \frac{N_2(C)}{kB}; \qquad Y = \frac{N_{out}(H)}{N_{out}(C)}$$
 (8.15)

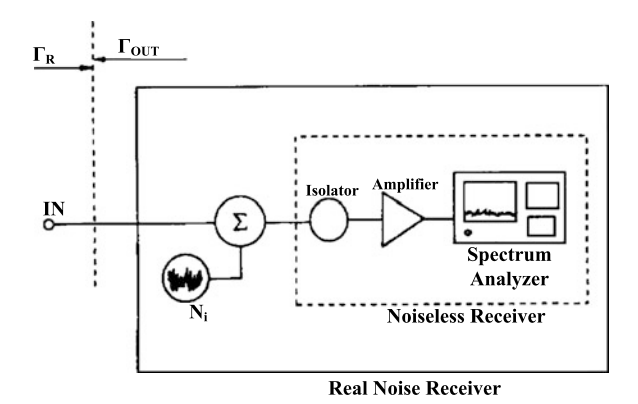
8.7.2 Noise Parameter Test Setup

Dedicated noise receivers are the most suitable instrument for measuring noise, but they often require costly converters for high-frequency measurements. Furthermore, noise receivers use a fixed measurement bandwidth of a few MHz; and, this may become a problem when measuring narrowband devices. In such circumstances, a multipurpose spectrum analyzer offers variable measurement bandwidth and performs noise measurements with acceptable accuracy. Figure 8.25 shows a block diagram of an experimental setup that utilizes a multipurpose spectrum analyzer in the noise characterization of microwave transistors.

In this setup, a spectrum analyzer, with a 2 MHz resolution bandwidth centered on the test frequency, measures the available noise power. The noise level is relatively low at the DUT's output; therefore, a low-noise pre-amplifier is necessary to increase the sensitivity of the spectrum analyzer. The isolator, with $|S_{12}|$ smaller than $-30 \, \mathrm{dB}$, helps in maintaining a constant noise figure of the noise receiver (comprising of the isolator, pre-amplifier, and spectrum analyzer shown in Fig. 8.26).

A 2–8 GHz transparent SP reflectometer in reverse configuration measures the source reflection coefficient, Γ_{meas} , presented by the non-repeatable mechanical stub

Fig. 8.26 Model of spectrum analyzer based noise receiver [37], © IEEE 1995



tuner seen at the reference plane. Power at the four detection ports of the SP junction is measured using a four-channel power meter. This task can also be performed by the spectrum analyzer with computer-controlled switches. The losses in the SP junction, 10 dB directional coupler and test fixture limit the source impedance coverage up to a radius circle of 0.75 on the Smith chart, but this is sufficient for noise parameter measurement. Microwave signals and white noise are injected alternatively into the SP reflectometer and into the DUT using a PC-controlled switch.

To determine the gain and noise figure of the noise receiver, a conventional calibration technique consists of measuring two noise standards, which correspond to the hot and cold states of the noise source. An alternative technique for spectrum analyzer based noise receivers, as shown in Fig. 8.26, discards the use of noise standards [39]. However, in this technique, the gain and noise figure of the pre-amplifier must be known; and, if the input mismatch factor is taken into account the noise power available at the reference plane is given by Eq. (8.16) [37].

$$N_{Receiver} = \left(\frac{(P_{SA})_{measured}}{G_{amplifier}} - N_i\right) \frac{|1 - \Gamma_R \Gamma_{out}|^2}{1 - |\Gamma_{out}|^2}$$
(8.16)

where Γ_R and Γ_{out} are the reflection coefficients at the input of the noise receiver and output of the DUT, respectively; and, N_i is the noise contribution of the receiver given by:

$$N_i = (10^{0.1NF_R(dB)} - 1)kT_0B (8.17)$$

The power measured by the spectrum analyzer, $(P_{SA})_{measured}$, and Eq. (8.15) can then be utilized to evaluate the noise at plane 2 (N_2) given in Eq. (8.11) as detailed in the following paragraph.

The available noise power of the noise source connected at plane 1 is premeasured (see Fig. 8.24). The available noise power at plane 2 is then calculated as a function of the tuner position during measurement according to Eqs. (8.10) and (8.11) and measured using the receiver according to Eq. (8.16). As an example, Table 8.3 lists the measured and calculated values for eight different tuner settings for an experimented carried out on a GaAs MESFET device operated in low noise amplifier mode. Both the values agree well with only a slight discrepancy that can be

Table 8.3 Comparison between the calculated and measured noise power [37], © IEEE 1995

Γ_S	Calculated	Measured
Amplitude/phase	dBm	dBm
0.6710/ -102.5°	-73.82	-73.42
0.6739/+152.2°	-73.12	-72.91
$0.4308/+161.0^{\circ}$	-75.05	-74.45
0.7433/ -131.9°	-72.88	-72.62
0.1293/+152.9°	-75.92	-75.72
$0.1722/-155.8^{\circ}$	-75.76	-75.69
0.2236/ +088.8°	-75.64	-75.54
$0.0966/-012.2^{\circ}$	-75.97	-75.82

attributed to the measurement uncertainty of the SP reflectometer and noise receiver. This offset in the measured results can be reduced by taking measurements at two different noise temperatures.

8.8 Mixer Characterization

In-band intermodulation (IBIM) is an essential characteristic of microwave/millimeter-wave front-end mixers. In modern wireless systems, IBIM products generated by the mixer can significantly deteriorate the main IF signal. The field effect transistor (FET) resistive mixers [40] substantially overcome this problem, as they exhibit good performance, in terms of conversion loss, higher operating frequency, and a low level of intermodulation products [41–44]. These performances are usually evaluated using setups that are complex and difficult to operate [5, 13, 45]. Ghannouchi et al. [8], therefore, developed a mixer characterization setup that is simple to operate and enables measurement and design of wide dynamic range (linear) FET resistive mixers.

8.8.1 Measurement Setup

The mixer characterization setup, given in Fig. 8.27, makes use of an active source-pull measurement (ASPM) system [46], as shown in Fig. 8.28. In the ASPM system, a part of the input signal that is well controlled in phase and magnitude is injected as a reflected wave to synthesize the reflection coefficient, Γ_S , at the DUT port. The advantage of ASPM over the traditional passive tuner lies in the fact that a truly unitary Γ_S , which is often needed for mixer characterization, can be generated using ASPM, whereas a passive tuner fails to do so.

Figure 8.27, which depicts a multi-frequency test setup, is a dual SP network analyzer appropriately modified to simultaneously carry out ASPM and load-pull

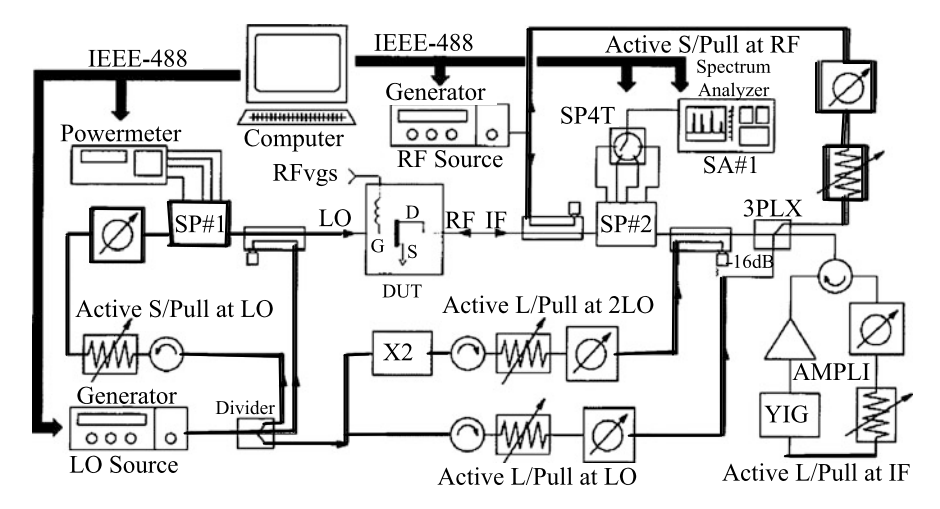
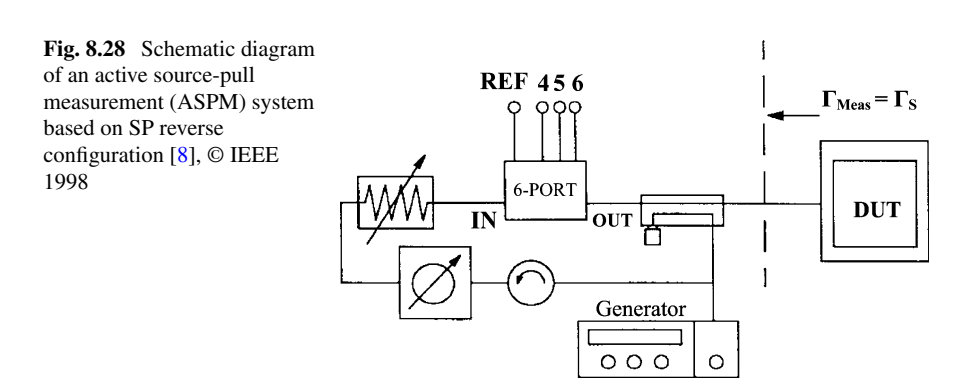


Fig. 8.27 Schematic diagram of multi-frequency test setup for characterization of mixers [8], © IEEE 1998



measurements on a FET resistive mixer. The test setup is built such that the LO and RF signals are received by the gate and drain, respectively. The IF signal gets extracted from the drain. It is imperative to note that the drain is not biased; therefore, the transistor works as a time-varying resistance controlled by the LO signal.

The power at four detection side arms of SP#1 is measured by a four-channel power meter. A computer-controlled SP4T (single pole, four through) switch allows successive measurements of the powers at the four detection ports of SP#2. Since many frequencies are simultaneously present at the output, there are two possible ways to take power readings at the ports of SP#2: either by a power probe along with a computer-controlled yttrium iron garnet (YIG) filter or by a pre-calibrated spectrum analyzer controlled via an IEEE-488 bus. The measurement by the first technique has advantages in terms of accuracy and speed, but suffers from three following problems:

- The stability regulation of the computer-controlled YIG filter versus the variations in the temperature and polarized current, although possible, is tedious and complex.
- In a two-tone test, the third- and fifth-order IBIM products remain inside the 30 MHz pass band of the YIG filter and, therefore, cause problems in measurements.
- The characterization of low-power nonlinear devices, such as FET resistive mixers, often requires detection of signals below -50 dBm, which can be overwhelmed by the noise of the YIG filter and power sensor. The dynamic range of detection (i.e., the variation of power at each detection port of SP#2) with a power meter and YIG filter may be as low as 15 dB, which is insufficient for practical needs.

The pre-calibrated spectrum analyzer (SA#1 in Fig. 8.27) can circumvent these problems. A very weak signal becomes measurable when a high-resolution bandwidth is used. The dynamic range of SP#2 can be increased to 60 dB, which enables measurements over the frequencies of the intermodulation products of interest. In addition, the presence of a spectrum analyzer in SP#2 allows for observation of any higher order products of the LO and RF signals (spurious responses). Furthermore, it has been demonstrated that an appropriate setting of the spectrum analyzer could give both reasonable accuracy and speed of measurement [39].

SP#1 performs LO active source-pulling at the transistor gate, while SP#2 simultaneously holds ASPM at the input RF frequency and active load-pull measurements at the output LO, 2LO and IF frequencies, both at the drain of the transistor. The power available from the source and the power absorbed by the load can be evaluated by SP#1 and SP#2, respectively, according to the expressions given in Eqs. (8.18) and (8.19) [37, 48].

$$(P)_{SP\#1} = \frac{1 - |\Gamma_S|^2}{|1 - S_{11}\Gamma_S|^2} S_{21} \frac{1}{|1 - \Gamma_S|^2} P_{Source}$$
(8.18)

$$(P_{Absored})_{SP\#1} = \frac{k(P_{Ref-port})_{SP\#2}}{|1 - c\Gamma_L|^2}$$
 (8.19)

where S_{ij} are the S-parameters of the two-port network defined between the generator and the measurement plane of SP#1. Γ_S and Γ_L are the reflection coefficients measured by SP#1 and SP#2, respectively, k is a real power calibration constant, and c is the complex error box constant.

A triplexer separates the LO, RF and IF frequencies into three branches, while the 2LO active load-pull branch is realized by injecting the 2LO signal via a wide-band 16 dB directional coupler. The IF active load-pulling is performed by a closed loop, in order to ensure the frequency coherence of the IF re-injected signal. The insertion of a computer-controlled YIG filter in this closed loop eliminates any risk of oscillation. In practice, a quasi-unitary reflection coefficient can be emulated at the DUT plane by increasing the synthesized signals to compensate for the combined insertion loss of the triplexer, SP junction, 16 dB directional couplers, bias tee, and test fixture.

The whole system is PC controlled via a HPIB controller. The YIG filter and SP4T switch are controlled directly by a digital-to-analog 16-channel converter card. This setup can be configured to provide fully automatic measurements by replacing the manual phase shifters and variable attenuators with electronic vector modulators.

8.8.2 Experimental Procedure

To carry out experiments, SP junctions SP#1 and SP#2 need to be calibrated using any appropriate technique, such as the conventional six-to-four-port reduction technique [47]. For a transistor mounted on a microstrip line test fixture, a thrureflection-line (TRL) method can be employed to de-embed the measurements at the input and output (I/O) planes.

Since only the LO signal is injected into the gate and several signals are present at the drain of the transistor, it is necessary to calibrate the SP junctions for a set of frequencies. For example, during the design of a C-band mixer, the required frequencies are SP#1 at 2.225 GHz (LO frequency), SP#2 at 2.225 GHz, SP#2 at 3.600–3.900–4.200 GHz (IF frequencies), SP#2 at 4.450 GHz (2LO frequency), snf SP#2 at 5.825–6.125–6.425 GHz (RF frequencies) [8].

The setup contains two 2–18 GHz signal generators, which provide +15 dBm and -4 dBm powers for the respective LO and RF signals, which need to be measured when the source impedance is set to $50~\Omega$, in order to be matched to the $50~\Omega$ power probe. A quick measurement can then be performed to verify that the measured reflection coefficient of a fixed impedance remains quasi-constant when the source powers (LO and RF) are swept from $-35~\mathrm{dBm}$ to their maximum available values, in order to identify the dynamic range of the setup.

In the design and characterization of mixers, usually the target is the optimization of the linearity as a function of termination impedances, while maintaining a typical conversion loss. The overall measurement involves a series of measurements that involves sweeping of different parameters with the most important parameters first and the less significant ones last. The optimization starts with a biasing point and input power levels (LO and RF), followed by LO and RF source impedances, and finally by the load impedances. These load impedances, in turn, are in order of importance: the load at the IF, the load at the LO, and finally, at the second harmonic 2LO frequencies of the output signal.

Once the effects of the termination impedances at a single-tone RF excitation are known, a two-tone RF excitation can then be applied to determine the IBIM performance of the transistor. However, it is imperative to understand that there is a need of some hardware modifications to adapt the test set to two-tone measurements, as shown in Fig. 8.29. First, the second harmonic 2LO load-pull branch is replaced by a second spectrum analyzer, SA#2. It is connected to the DUT output via a 16 dB directional coupler and detects a higher magnitude signal than that detected by SA#1.

In two-tone measurements, the terminating impedances are fixed as $(Z_S)_{RF1} \cong (Z_S)_{RF2}$ and $(Z_S)_{IF1} \cong (Z_S)_{IF2}$ obtained in single-tone characterization, since the

References 221

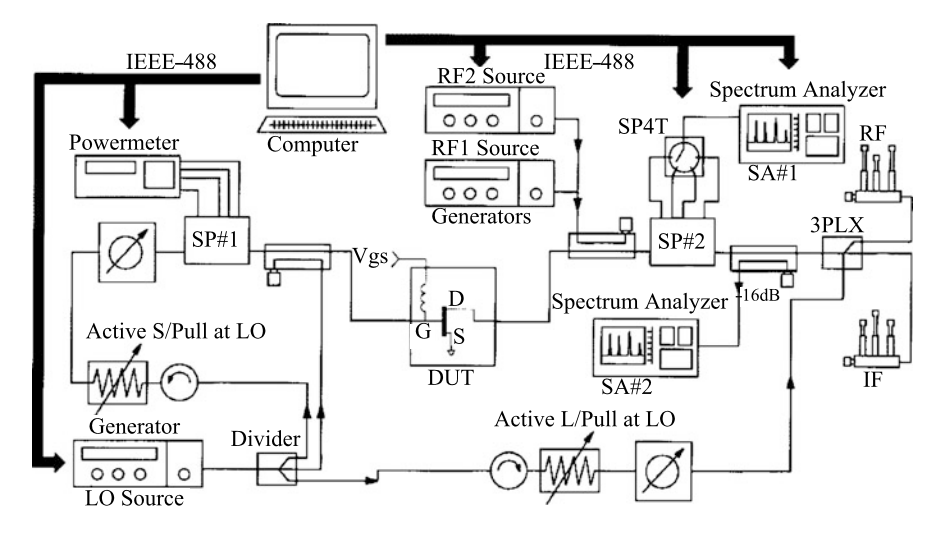


Fig. 8.29 Modified setup for two-tone measurements [8], © IEEE 1998

variation in frequency is very small. In theory, the active loop can still be used for the synthesis of IF impedances, but this setup (Fig. 8.29) utilizing mechanical tuners is simpler and sufficient for measurement requirements, considering that the range of optimal IF impedances are now known from the single-tone measurements. A detailed description of a mixer characterization and design example is available in [8].

References

- M.J. Pelk, L.C.N. de Vreede, M. Spirito, J.H. Jos, Base-band impedance control and calibration for on-wafer linearity measurements, in 63rd ARFTG Conference (June 1994), pp. 35–40
- H. Arthaber, M.L. Mayer, G. Mageri, An active load-pull setup for broadband signals using digital baseband processing for the active loop. Int. J. RF Microw. Computer-Aided Eng. 18(6), 574–581 (2008)
- 3. M.S. Hashmi, J. Benedikt, P.J. Tasker, Impact of group delay on the load emulation in multitone active envelope load-pull system. Aust. J. Electr. Electron. Eng. 7(1), 83–88 (2010)
- R. Hajji, F. Beauregard, F.M. Ghannouchi, Multi-tone power intermodulation load-pull characterization of microwave transistors suitable for linear SSPA's design. IEEE Trans. Microw. Theory Tech. 45(7), 1093–1099 (1997)
- F.M. Ghannouchi, G. Zhao, F. Beauregard, Simultaneous load-pull of intermodulation and output power under two-tone excitation for accurate SSPAs design. IEEE Trans. Microw. Theory Tech. 42(6), 929–934 (1994)
- P. Ghanipour, S. Stapleton, J. Kim, Load-pull characterization using different digitally modulated stimuli. IEEE Microw. Wirel. Compon. Lett. 17(5), 400–402 (2007)
- M. Spirito, M.J. Pelk, F. van Rijs, S.J.C.H. Theeuwen, D. Hartskeeri, L.C.N. de Vreede, Active harmonic load-pull for on-wafer out-of-band device linearity optimization. IEEE Trans. Microw. Theory Tech. 54(12), 4225–4235 (2006)

- 8. D. Le, F.M. Ghannouchi, Multitone characterization and design of FET resistive mixers based on combined active source-pull/load-pull techniques. IEEE Trans. Microw. Theory Tech. **46**(9), 1201–1208 (1998)
- 9. M. Marchetti, M.J. Pelk, K. Buisman, W. Neo, M. Spirito, L. de Vreede, Active harmonic load-pull with realistic wideband communications signals. IEEE Trans. Microw. Theory Tech. **56**(12), 2979–2988 (2008)
- B. Noori, P. Hart, J. Wood, P.H. Aaen, M. Guyonnet, M. Lefevre, J.A. Pla, J. Jones, Load-pull measurements using modulated signals, in 36th European Microwave Conference, Paris, France (2005), pp. 1594–1597
- M.S. Hashmi, S.J. Hashim, S. Woodington, T. Williams, J. Benedikt, P.J. Tasker, Active envelope load pull system suitable for high modulation rate multi-tone applications, in 3rd International Microwave Monolithic Integrated Circuit Workshop, Malaga, Spain (Nov. 2008), pp. 93–96
- Maury Microwave Corporation, Active harmonic load-pull with realistic wideband communications signals, Application Note 5A-044, June 2010
- 13. C. Tsironis, Two-tone intermodulation measurements using computer controlled microwave tuner. Microw. J. 32, 161 (1989)
- 14. J. Jacobi, IMD still unclear after 20 years, in Microwaves & RF (Nov. 1986), pp. 119-126
- J.G. Freed, Equations provide accurate third-order IMD analysis, in *Microwaves & RF* (Aug. 1992), pp. 75–84
- M. Leffel, Intermodulation distortion in a multi-signal environment, in RF Design (June 1995), pp. 78–83
- 17. R. Hajji, F. Beauregard, F.M. Ghannouchi, Multi-tone characterization for intermodulation and distortion analysis, in *IEEE Microwave Theory and Techniques Society's International Microwave Symposium Digest*, San Francisco, CA (June 1996), pp. 1691–1694
- 18. L. Cellai, A. Greco, Optimal phase relationship aids IM testing, in *Microwaves & RF* (July 1996), pp. 56–61
- M.S. Hashmi, F.M. Ghannouchi, P.J. Tasker, K. Rawat, Highly reflective load-pull. IEEE Microw. Mag. 12(4), 96–107 (2011)
- G.P. Locatelli, De-embedding techniques for device characterization. Alta Freq. 57(5), 267– 272 (1988)
- M.A. Maury Jr., S.L. Mar, G.R. Simpson, TRL calibration of vector automatic network analyzers. Microw. J. 30(5), 382–387 (1987)
- K.S. Kundert, A.S. Vincentelli, Simulation of nonlinear circuits in the frequency domain. IEEE Trans. Computer-Aided Des. 5, 521–535 (1986)
- W.R. Curtice, GaAs MESFET modeling and nonlinear CAD. IEEE Trans. Microw. Theory Tech. 36, 220–230 (1988)
- 24. X. Cui, S.J. Doo, P. Roblin, G.H. Jessen, J. Strahler, Real-time active load-pull of the 2nd and 3rd harmonics for interactive design of non-linear power amplifiers, in *68th ARFTG Conference*, Colorado, USA (Nov. 2006), pp. 29–42
- G.P. Bava, U. Pisani, V. Pozzolo, Active load technique for load-pull characterization at microwave frequencies. IET Electron. Lett. 18(4), 178–180 (1982)
- Y. Takayama, A new load-pull characterisation method for microwave power transistors, in IEEE Microwave Theory and Techniques Society's International Microwave Symposium Digest (1976), pp. 218–220
- 27. F. Verbeyst, M.V. Bossche, Real-time and optimal PA characterization speeds up PA design, in 34th European Microwave Conference, Amsterdam, Netherlands (2004), pp. 431–434
- P. Roblin, Seok Joo Doo, Xian Cui, G.H. Jessen, D. Chaillot, J. Strahler, New ultra-fast realtime active load-pull measurements for high speed RF power amplifier design, in *IEEE Mi*crowave Theory and Techniques Society's International Microwave Symposium Digest, Honolulu, USA (June 2007), pp. 1493–1496
- J. Sevic, M.B. Steer, A.M. Pavio, Large-signal automated load-pull of adjacent-channel power ratio for digital wireless communication systems, in *IEEE Microwave Theory and Techniques* Society's International Microwave Symposium Digest (1996), pp. 763–766

References 223

 C. Clark, Time-domain envelope measurement technique with application to wideband power amplifier modelling. IEEE Trans. Microw. Theory Tech. 46(12), 2351–2540 (1998)

- 31. O. Väänänen, J. Vankka, K. Halonen, Effect of Clipping in Wideband CDMA System and Simple Algorithm for Peak Windowing (Helsinki University of Technology, Helsinki, 2002)
- 32. D.E. Stoneking, R.J. Trew, J.B. Yan, Load pull characteristics of GaAs MESFETs calculated using an analytic, physics based large signal device model, in *IEEE Microwave Theory and Techniques Society's International Microwave Symposium Digest* (1998), pp. 1057–1060
- 33. M.S. Hashmi et al., Active envelope load pull solution addressing the RF device multi-tone characterization problem, in *IEEE MTT-11 Design Competition*, Atlanta, USA (June 2008). http://www.mtt.org/mtt11/ims_award.htm
- 34. S.J. Hashim, M.S. Hashmi, T. Williams, S. Woodington, J. Benedikt, P.J. Tasker, Active envelope load-pull for wide-band multi-tone stimulus incorporating delay compensation, in *34th European Microwave Conference*, Amsterdam, Netherlands (2008), pp. 317–320
- S.J. Hashim, M.S. Hashim, J. Benedikt, P.J. Tasker, Effect of impedance variation around the fundamental on pa distortions characteristics under wideband stimuli, in *IEEE Asia Pacific Conference on Circuits and Systems*, Kuala Lumpur, Malaysia (Dec. 2010), pp. 1115–1118
- T. Williams, O. Mojon, S. Woodington, J. Lees, M.F. Barciela, J. Benedikt, P.J. Tasker, A robust approach for comparison and validation of large signal measurement systems, in *IEEE Microwave Theory and Techniques Society's International Microwave Symposium Digest*, Atlanta, USA (June 2008), pp. 257–260
- 37. D. Le, F.M. Ghannouchi, Noise measurements of microwave transistors using an uncalibrated mechanical stub tuner and a built-in reverse six-port reflectometer. IEEE Trans. Instrum. Meas. **44**(4), 847–852 (1995)
- 38. F.M. Ghannouchi, R.G. Bosisio, Source-pull/load-pull oscillator measurements at microwave/MMwave frequencies. IEEE Trans. Instrum. Meas. 41(1), 32–35 (1992)
- 39. B. Peterson, Spectrum analysis basics, Hewlett-Packard Application Note 150, p. 2634, and pp. 38–40
- S.A. Maas, A GaAs MESFET mixer with very low intermodulation. IEEE Trans. Microw. Theory Tech. 35, 429–435 (1987)
- 41. H.H.G. Zirath, C.-Y. Chi, N. Rorsman, G.M. Rebeiz, A 40 GHz integrated quasi-optical slot HFET mixer. IEEE Trans. Microw. Theory Tech. 42, 2492–2497 (1994)
- 42. K. Yhland, N. Rorsman, H.H.G. Zirath, Novel single device balanced resistive HEMT mixers. IEEE Trans. Microw. Theory Tech. 43, 2863–2867 (1995)
- R.S. Virk, S.A. Maas, Modeling MESFET for intermodulation analysis of resistive FET mixers. in *IEEE Microwave Theory and Techniques Society's International Microwave Sympo*sium Digest, Orlando, USA, vol. 3 (May 1995), pp. 1247–1250
- E.W. Lin, W.H. Ku, Device considerations and modeling for the design of an INP-based MOD-FET millimeter-wave resistive mixer with superior conversion efficiency. IEEE Trans. Microw. Theory Tech. 43(Aug.), 1951–1959 (1995)
- L. Ricco, G.P. Locatelli, F. Calzavara, Constant intermodulation Loci measure for power devices using HP-8510 network analyzer, in *IEEE Microwave Theory and Techniques Society's International Microwave Symposium Digest*, New York, USA (May 1988), pp. 221–224
- D. Le, P. Poire, F.M. Ghannouchi, Six-port based active source-pull measurement technique. IOP Meas. Sci. Technol. 9, 1336–1342 (1998)
- J.D. Hunter, P.I. Somlo, Explicit six-port calibration method using five standards. IEEE Trans. Microw. Theory Tech. MTT-39, 69–72 (1985)
- F.M. Ghannouchi, R. Larose, R.G. Bosisio, A new multiharmonic loading method for large signal microwave transistor characterization. IEEE Trans. Microw. Theory Tech. 39(June), 986–992 (1991)
- 49. F. van Rijs, R. Dekker, H.A. Visser, H.G.A. Huizing, D. Hartskeer, P.H.C. Magnee, R. Dondero, Influence of output impedance on power added efficiency of si-bipolar power transistors, in *IEEE Microwave Theory and Techniques Society's International Microwave Symposium Digest*, Boston, USA (June 2000), pp. 1945–1948

- S. Liwei, L.E. Larson, An Si-SiGe BiCMOS direct-conversion mixer with second-order and third-order nonlinearity cancellation for WCDMA applications. IEEE Trans. Microw. Theory Tech. 51(11), 2211–2220 (2003)
- 51. V. Aparin, C. Persico, Effect of out-of-band terminations on intermodulation distortion in common-emitter circuits, in *IEEE Microwave Theory and Techniques Society's International Microwave Symposium Digest*, Anaheim, USA (June 1999), pp. 977–980
- 52. Maury Microwave Corporation, http://www.maurymw.com/
- 53. Focus Microwaves, http://www.focus-microwaves.com/
- 54. G.L. Madonna, M. Pirola, A. Ferrero, U. Pisani, Testing microwave devices under different source impedance values—a novel technique for on-line measurement of source and device reflection coefficients. IEEE Trans. Instrum. Meas. **49**(2), 285–289 (2000)
- M.J. Pelk, L.C.N. de Vreede, M. Spirito, J.H. Jos, Base-band impedance control and calibration for on-wafer linearity measurements, in 63rd ARFTG Conference, Forth Worth, USA (June 2004), pp. 35–40
- W.C.E. Neo, J. Qureshi, M.J. Pelk, J.R. Gajadharsing, L.C.N. de Vreede, A mixed-signal approach towards linear and efficient N-way Doherty amplifiers. IEEE Trans. Microw. Theory Tech. 55(5), 866–879 (2007)
- 3G TS 25.141 base station conformance testing (FDD), Tech. specification group radio access networks, 3rd generation partnership project, Valbonne, France, Tech. Spec., Rev. V3.1.0, 2000
- 58. A. Ferrero, U. Pisani, An improved calibration technique for on-wafer large-signal transistor characterization. IEEE Trans. Instrum. Meas. **42**(2), 360–364 (1993)
- 59. R. Marchesani, Digital precompensation of imperfections in quadrature modulators. IEEE Trans. Commun. **48**(4), 552–556 (2000)

Authors

Fadhel M. Ghannouchi is professor and AITF/CRC Chair in the Department of Electrical and Computer Engineering, Schulich School of Engineering, University of Calgary, Canada, and Director of the Intelligent RF Radio Laboratory. He has held numerous invited positions at several academic and research institutions in Europe, North America and Japan. He has provided consulting services to a number of microwave and wireless communications companies. His research interests are in the areas of microwave instrumentation and measurements, nonlinear modeling of microwave devices and communications systems, design of power and spectrum efficient microwave amplification systems and design of intelligent RF transceivers and software-defined radio systems for wireless and satellite communications. His research activities have led to over 500 publications and 14 US patents (6 pending) and two books. He is Fellow of IEEE and he has been a distinguished microwave lecturer of IEEE MTT-S since 2009.

Mohammad S. Hashmi received MS degree from Darmstadt University of Technology, Germany and PhD degree from Cardiff University, UK. He is now an adjunct researcher at the iRadio Lab, University of Calgary, Canada and Assistant Professor at IIIT Delhi, India. He was previously associated with Philips Semiconductors and Thales Electronics in Germany during which time he was involved in the field of RF circuits and systems. His current research interests are related to nonlinear microwave instrumentation, microwave device characterization, and linearization of power amplifiers for mobile and satellite applications. He was the recipient of 2008 Automatic Radio Frequency Techniques Group (ARFTG) Microwave Measurement Fellowship, and 3rd place winner in the novel and creative instrument design competition organized by IEEE MTT-11 for the year 2008. His research has led to over 40 publications and 3 US patents (pending).

About the Book

This first book on load-pull systems is intended for readers with a broad knowledge of high frequency transistor device characterization, nonlinear and linear microwave measurements, RF power amplifiers and transmitters. It fulfills the demands of users, designers, and researchers both from industry and academia who have felt the need of a book on this topic. It presents a comprehensive reference spanning different load-pull measurement systems, waveform measurement and engineering systems, and associated calibration procedures for accurate large signal characterization. Besides, this book also provides in-depth practical considerations required in the realization and usage of load-pull and waveform engineering systems. In addition, it also provides procedure to design application specific load-pull setup and includes several case studies where the user can customize architecture of load-pull setups to meet any specific measurement requirements. Furthermore, the materials covered in this book can be part of a full semester graduate course on microwave device characterization and power amplifier design.

0-9	С
1-port error flow model, 147, 152	CAD-based PA Design, 14, 15
	CAD incorporation, 185
A	Calibration, vii, viii, 21, 29, 35, 37, 38, 40–42,
ABCD Parameter, 136	55, 87–93, 95, 97, 99–101, 105–107,
Accurate calibration, 142	113, 122, 123, 126, 129, 133, 135, 139,
Active Impedance Tuner, 17	142, 145–156, 163, 164, 166–168,
Active load-pull, viii, 18, 20, 22, 55-62, 64,	170–175, 181–183, 193, 197, 211–213,
67, 69–71, 75, 76, 78, 83, 96, 98, 99,	216, 219, 227
106, 107, 110, 113, 114, 117–119,	Cascaded Tuner, 49, 51
125–129, 132, 133, 139, 140, 152, 154,	CDMA, 1
156, 158, 159, 198, 208, 209, 219	Characteristic impedance, 17, 32, 55, 94, 104,
Active Source-Pull, 95	115, 118, 130, 135, 177
Active Tuner, 40	Characterization, vii, viii, 14, 17–22, 35, 37,
Adjacent Channel Power Ratio (ACPR), 5, 8,	38, 42, 47, 49, 50, 55, 57, 62, 63, 70,
9, 87, 202	72, 83, 101–107, 113–122, 124, 125,
AM/AM, viii, 87, 106, 109	139, 152, 157, 184, 185, 191–193, 201,
AM/AM Measurement, viii, 87, 106	204–206, 208, 212, 215, 217–221, 225,
AM/PM, viii, 87, 106, 107, 109	227
AM/PM Measurement, viii, 87, 106, 107	C/IMD3, 87
Arbitrary waveform generator (AWG), 192,	Class-A, 10–12, 194, 196
193	Class-AB, 208
Attenuator, 56–61, 68, 76, 83, 95, 99, 142,	Class-B, 82
150, 154, 192	Class-C, 10, 12
Automatic tuner system (ATS), 202	Class-D, 12, 13, 163, 164
	Class-E, 12, 13
В	Class-F, 13
Baseband, 140-145, 153, 154, 192, 208, 209	Class-J, 13, 159, 186, 187
signal, 140, 143, 145, 192	Closed-loop Load Pull, 62
Bias Current, 3, 10, 12, 13, 197	Coaxial environment, 32
Bias Voltage, 3, 13, 197	Common Reference, 76, 77, 135
Blocking Capacitor, 3	Communication, vii, 1, 2, 7, 9, 204, 211
Breakdown Voltage, 4	Complex Load, 4, 191
Broadband Impedance, 120, 121, 126, 205	Computer-Aided Design (CAD), 14, 15, 18,
Broadband matching, 191	103, 184–186

F.M. Ghannouchi, M.S. Hashmi, Load-Pull Techniques with Applications to Power Amplifier Design, Springer Series in Advanced Microelectronics 32

Coplanar waveguide (CPW), 99 ESG, 197–200 Current waveform, 10, 181 Extraction, 14, 17, 99, 110, 113, 133–136, 148 171, 174, 175, 181, 186
DC Power, 1, 104, 197 F
De-embed, 97, 220 Fan-diagram, 185
De-embedding, 35, 36, 41, 90, 91, 93, 94, 97, Feed-Forward, 68, 69, 71, 74, 78
99, 101, 106, 108, 109, 113, 136, 193 Feed forward Active Load Pull, viii, 55, 69, 70
Device Characterization, 18, 19, 21, 22, 35, 42, Feedback, 55, 56, 58, 60–64, 66, 140, 142,
47, 49, 105, 107, 114, 118, 120, 139, 144, 145, 153, 205, 206
191, 192, 201, 206, 225, 227 Feedback Loop, 56, 58, 61–64, 66, 142, 144,
Device Under Test, 16, 17, 29, 55, 87, 113, 164 Digital, 1, 145, 166, 176, 210–212, 220 Feedback Network, 58, 60
Direct SP Configuration, 94 First-order, 147
Directivity, 38–41, 50, 59, 61, 62, 122 Flow Graph, 39, 62, 70–72, 80, 123, 127, 128
Doherty, 2 130, 131, 135, 146, 171–174, 181
Drain Efficiency, 4–6, 11–14, 38, 158, 159 Fourier coefficient, 171
DUT, 17, 20, 22, 29, 30, 32, 34–41, 44, 45, 47, 48, 50, 51, 55–59, 61, 62, 65, 66, 68–70, 72, 76, 77, 79, 87–89, 91, 92, 94-99, 101–110, 113–119, 122–136, 140–142, 144–148, 154, 164–166, 168–175, 177, 179, 183, 193, 197–201, 205, 208–217, 219, 220 plane, 38, 40, 51, 55-059, 65, 68, 69, 72,
76, 79, 114, 115, 118, 119, 123, 127, G
128, 135, 136, 141, 142, 144–148, 154, GaAs, 42, 82, 156, 159, 216
172, 179, 219 GPIB, 34, 169, 198
Dynamic range, 7, 83, 142, 154, 166–168, 208,
210–212, 217, 219, 220 H
Harmonic
E Active Open-Loop Load-Pull, 77 Efficiency, 1, 2, 4–6, 10–16, 30, 38, 42, 63, 80, Closed-Loop Load-Pull, 63, 64
Efficiency, 1, 2, 4–6, 10–16, 30, 38, 42, 63, 80, Closed-Loop Load-Pull, 63, 64 83, 87, 104, 139, 158–160, 163, 183, Harmonic Distortion, 4, 6–8, 78
184, 186, 191, 195, 198, 199, 201, Harmonic ELP, 139, 155–159
207–209 Harmonic Feed-Forward Load-Pull, 74
Electromehanical tuner (EMT), vii, 29–32, 34, Harmonic frequency, 37, 48, 78, 156, 166, 170
35 179, 197, 208–211
Electronic circuit, 33, 142 Harmonic Index, 75, 78
Electronic Load Module (ELM), 75 Harmonic Load-Pull, 42, 44–47, 197 Electronic Typing (ETS), viii 20, 22, 25 Harmonic Typing 12, 47, 40, 82, 108
Electronic Tuner (ETS), vii, 29, 33–35 Harmonic Tuning, 13, 47, 49, 83, 198 ELP viii, 130, 150, 205, 206 HEMT, 82, 187, 108
ELP, viii, 139–159, 205, 206 HEMT, 82, 187, 198 equations, 141–143, 145 Heterodyne receiver, 170
Enhanced calibration, 174 High Frequency, 22, 118, 227
Enhanced Loop, 49, 50, 120, 122–125 High-power DUT, 113, 114, 133

High Power Load Pull, 18, 19, 113, 114, 122,	Linear Network, 2, 186
133, 135	Linearity, 1, 2, 6, 7, 12, 18, 35, 50, 87, 103,
Hybrid Load-Pull, 130	196, 207, 208, 210, 212, 220
	Load Impedance, 4, 11, 13, 22, 87, 97, 105,
I	109, 181, 184, 186, 193, 207
Impedance grid, 83, 156	Load Line, 3, 4, 11
Impedance sweep, 156	Load-Pull, 1, 17, 18, 22, 29, 30, 35, 36, 42,
Impedance Synthesis, 191	44–47, 55, 56, 62, 64, 68, 71, 74, 76,
Impedance Transformer, 120, 121, 125–135	78, 83, 87, 96, 97, 99, 113, 118, 119,
•	
IMR, 192–196	130, 140, 154, 155, 191, 197, 201, 204,
In-band intermodulation, 217, 219, 220	208, 209, 225
Incident, 17, 29, 30, 36–39, 56, 63, 65, 66, 69,	Load-Pull Gain, 15, 69, 70
79, 94, 108, 114, 115, 118, 127, 128,	Load-Pull Head, 66, 67
140–143, 155, 166, 170, 175, 177, 179,	Load-pull power, 114, 118–120, 126–129
192, 197, 208, 209	Load Reflection Coefficient, 17, 51, 69, 109,
Incident Traveling Wave, 56, 63, 65, 66, 69,	114, 119, 120, 124, 129, 146, 160, 179,
128, 140–143, 177	197, 199, 205, 212
Injected, 29, 40, 41, 69, 72, 89, 91, 93–95, 98,	Load Resistance, 10
127, 128, 181, 197, 201, 209, 213, 216,	Local Model, 80–82
217, 219, 220	Local Oscillator (LO), 103, 140, 168, 211
Injected Traveling Wave, 127	Loop, viii, 49-51, 55-68, 70-84, 99, 118, 120
Input Impedance, 87, 95, 96	122–125, 127, 132, 140, 142, 144, 147,
Input noise, 213, 214	150, 152-154, 156, 158, 159, 183, 197,
Insertion Loss, 20, 34, 35, 41, 48, 49, 91, 122,	205, 206, 208, 209, 219, 221
124, 125, 219	Loop Amplifier, 56–60, 62–68, 70, 73, 76, 77,
Intermodulation Distortion (IMD), 4, 7, 8, 87,	83, 99, 142, 150, 154, 208
191, 192, 194, 201–204, 209	Low Impedance Line, 129
IQ demodulator, 140–143	Low Loss Passive Tuner, 66
IQ Modulator, 75	Low-pass filter, 143
Isolation, 43, 46–50, 57, 59, 61, 68, 70, 142,	Low pass litter, 143
	M
145, 150, 153, 155 Itarativa Praeses, 14, 20, 70, 78	Magnitude, 5, 9, 30, 31, 41, 42, 44–47, 56, 57,
Iterative Process, 14, 30, 70, 78	59, 60, 68, 70, 72, 75–79, 83, 87, 95,
I-V	113, 116, 118, 127, 133, 143, 144, 153,
plane, 186	
waveform, 167, 169, 170	154, 165–168, 171, 177, 178, 180, 181,
***	193, 198, 217, 220
K	Matching Circuit, 4, 19, 186, 187
Kahn, 2	Matching Impedance, 17, 186, 191
Klopfenstein, 126, 127	Matching Network, 5, 19, 186, 208
Knee Voltage, 4, 12, 184	Measurement, vii, viii, 1, 9, 14–16, 18, 20–22,
	29, 34–42, 47–49, 55, 57, 62, 63, 66,
L	67, 70–72, 79, 80, 83, 87–90, 94–99,
Large Periphery, viii	101, 102, 104, 106, 107, 109, 110, 113,
Large-Signal, vii, 2, 3, 11, 14–16, 37, 69, 76,	114, 116–118, 120–126, 129, 130,
87, 96, 105, 167, 170, 177, 196, 204,	132–136, 139, 142, 144, 148, 151–159,
208	163–172, 174, 176–186, 191–195,
Large-Signal Model, 14, 170, 196	197–202, 204, 206, 209–213, 215–221,
Large Signal Network Analyzer (LSNA), 177,	225, 227
178, 183, 197, 198	Measurement-based PA Design, 16
Large-signal waveform, 16	Measurement plane, 181, 219
Least Squares Method, 148	Measuring port, 39, 88, 89, 93, 170
LINC, 2	Memory effect, 200
Line Stretcher, 127, 129, 132, 133	MESFET, 103, 193, 195, 216
Linear mode PA, 159	Microstrip, 34, 35, 41, 135, 220
,,	· r/- // //

Microwave, vii, viii, 14, 18, 30, 37, 39, 51, 89,	Oscillator Measurements, 104, 105
91, 93, 99, 101, 102, 104–106, 139,	Oscilloscope, 164, 166–168, 176, 197
163, 164, 168, 169, 184, 187, 191, 192, 202, 215–217, 225, 227	Output Impedance, 113, 114, 117, 119, 129, 130
Microwave Transition Analyzer (MTA),	Output noise, 102, 214
168–170, 192–194	Output Power, 2, 3, 5, 6, 11–14, 18, 20, 29, 39.
Mismatch, 11, 30, 31, 38, 39, 51, 60, 80, 114,	41, 42, 50, 64–67, 73, 75, 77, 78, 99,
124–127, 130, 132, 133, 216	104, 117, 159, 163, 180, 186, 194, 195,
Mixer, vii, viii, 75, 103, 167, 170, 191–193,	198–202, 204, 209
212, 217, 218, 220, 221	170 202, 204, 207
Modulated, viii, 8, 9, 18, 21, 166, 191, 201,	P
202, 204, 205, 209–211	Passive demodulator, 142, 146
Modulated Load Pull, viii, 191, 201, 202	Passive Impedance Tuner, 22, 88, 122, 132,
Multi-harmonic Load-pull, 197	133
Multi-harmonic Receiver (MHR), 169–174,	Passive Load-Pull, 29, 30, 96
177	Passive Source-Pull, 95, 96
Multi-harmonic SP Reflectometer, 179–181	Passive Tuner, 20, 29, 36, 40, 50, 64–66, 88,
Multi-tone, viii, 191–193, 195, 196, 204	115, 121, 122, 132, 133, 217
Multi-tone Load-Pull, 191	Peak Voltage, 13, 117
Multipurpose Tuner (MPT), 46–48	Phase, 30, 31, 42, 44–47, 49, 51, 56-61, 68, 70
	72–79, 83, 87, 95, 97–99, 106–110,
N	123, 127–129, 131–133, 140, 143, 144,
Network analyzer, 19, 29, 36–40, 97, 99, 100,	154, 156–158, 165–168, 177, 178, 180,
102, 103, 106, 124, 147, 148, 152, 166,	181, 186, 192, 193, 195, 197–201, 205,
169, 177, 192, 197, 217	208, 211, 217, 220
Newton-Raphson, 78, 83	Phase Shifter, 56–61, 68, 76, 83, 95, 99
Noise	PHD, 78, 79, 81–83
meter, 102	model, 78, 79, 81–83
parameter, 212, 215, 216	PIN diode, 30, 33–35
source, 102, 212–214, 216	PNA-X, 168
Noise Characterization, viii, 102, 191, 212,	Poly Harmonic Distortion Modeling, 78
215	<i>P_{out}</i> , 5–7, 12, 29, 30, 38, 41, 65, 66, 104, 179
Noise Measurement, viii, 34, 102	Power Added Efficiency (PAE), 4–6, 18, 20,
Nonlinear device modeling, 140, 166	30, 38, 87, 104, 110, 186, 191, 198–201
Nonlinear I-V waveform, 167	Power Amplifier (PA), vii, 1–7, 10–16, 18, 29,
Nonlinear network, 2	42, 49, 55, 63, 65–68, 101, 104, 113,
Nonlinear Vector Network Analyzer (NLVNA), 169	152, 154, 157–159, 163, 175, 176, 186, 191, 198, 200, 201, 204, 207, 227
N-port network, 88	Power Amplifier Characterization, 104
Numerical method, 79	Power meter, 29, 36, 37, 39–41, 50, 99–101,
Numerical method, 79	109, 172, 179, 181, 193, 212, 216, 218,
0	219
On-wafer, 18, 21, 32, 33, 35, 49, 87, 99-101,	Pre-match, 120, 121
114, 193	Pre-matching, 120, 121, 124
Open-Loop Active Load-Pull, viii, 55, 76, 81,	Pre-matching Probe, 120, 121
82	Probe, 21, 22, 30–32, 36, 120, 121, 164, 165,
Open-loop harmonic, 158, 159	211, 218, 220
Open-short-load (OSL), 40, 99–101, 172, 212	Pseudowave, 177
Optimal second-harmonic, 157, 159	
Optimal third-harmonic, 159	Q
Optimization, vii, 2, 42, 72, 80, 81, 103, 104,	Quadrature Demodulator, 140-143
139, 152, 156, 159, 183, 185, 186, 196,	Quadrature Modulator, 140, 142, 144
204, 220	Quarter wave Transformer, 113, 121, 124, 125
Oscillation, 57, 59, 62, 63, 140, 153, 219	Quiescent Point, 4

R	Source Impedance, 87, 88, 95–97, 102, 103,
Radio Frequency (RF), vii, 1-4, 6, 12, 36-39,	105, 181, 213, 216, 220
75, 88, 103, 113, 120, 139, 140, 163,	Source-Pull, 95, 101
164, 169, 170, 178, 184–186, 191, 197,	SP, 87–99, 101–110, 177–183, 212–220
207, 211, 212, 218–220, 225, 227	SP Calibration, 89, 97, 106, 181
Reciprocal Network, 131	SP Junction, 88–95, 101, 102, 105, 106, 213,
Reference	214, 216, 219
port, 88	SP Network Analyzer, 97, 106, 217
signal, 76, 168, 170, 178, 181	SP Reflectometer, 88–91, 93–96, 98, 101–107,
Reference Plane, 30–32, 38, 40, 41, 66, 89–91,	177–183, 213, 215–217
93–95, 101, 119, 134, 135, 140, 177,	SP1, 96, 108, 109
181, 205, 212, 216	SP2, 96–98, 108, 109
Reflected, 17, 29, 30, 36, 38, 39, 42–44, 55,	S-Parameter, 172
56, 63, 65, 66, 69, 73–76, 78–81, 91,	S-parameter calibration, 172, 173
94, 114, 115, 118, 127, 128, 140–142,	Spectrum analyzer, 36, 212, 215, 216, 218–220
144, 155, 166, 167, 170, 175, 177, 181,	Spurious Free Dynamic Range, 7
192, 197, 202, 205–207, 217	Stability, 56, 62, 70, 77, 102, 142, 150, 153,
Reflected Traveling Wave, 43, 44, 55, 56, 63,	154, 197, 199, 219
66, 69, 74-76, 79, 128, 140–142, 144,	analysis, 153
177, 205–207	Step Recovery Diode (SRD), 168, 178
Reflection Coefficient, 17, 19, 22, 29, 31–33,	Switched-Mode Power Amplifier, 13
37, 39, 40, 42, 45, 47, 50, 51, 56–60,	Switching Amplifier, 13, 14
62, 63, 65, 66, 68–73, 76–81, 83,	Synthesized reflection coefficient, 59, 70, 72,
88–99, 101, 105, 106, 109, 113–115,	121, 122, 127, 128, 141, 142, 147, 205
118–133, 140–142, 144, 146–148, 153,	T
154, 156–160, 172, 177–182, 192–194,	T
197–199, 205, 207, 209, 210, 212–215,	Test Frequency, 215 Third harmonic 42, 78, 156, 150, 167, 186
217, 219, 220 Perfection Feator 10, 20, 22, 24, 25, 43, 48	Third-harmonic, 42, 78, 156–159, 167, 186, 198–201
Reflection Factor, 19, 30–32, 34, 35, 43, 48,	Third order
50, 51, 119 Reflectometer, viii, 88–91, 93–96, 98,	mixing, 79
101–107, 177–183, 212, 213, 215–217	model, 79
Reverse Configuration, 89–91, 93, 95, 97, 98,	Third-order Intercept (IP3), 7, 201
101–103, 179, 182, 213, 215	Third-order Intermodulation (IMD3), 7, 87,
RF Power, 1, 2, 4, 38, 39, 184, 227	201–204
RFPA, 1, 163, 183	Three-port, 56, 61, 64, 107, 108, 140, 142
Ki 1A, 1, 105, 165	component, 56, 61, 64, 140, 142
S	Thru-Reflect-Line (TRL), 135
Sampling	Time-domain waveform, viii, 148, 155, 163,
oscilloscope, 167, 168	165, 168, 169, 178, 179, 181, 183, 206
rate, 166	Total Efficiency, 6
Second-harmonic, 42, 43, 81, 156-159, 186,	Total Harmonic Distortion (THD), 7
199–201, 208, 211, 220	Transconductance, 10, 12, 13, 184
Short-Open-Load-Thru (SOLT), 135, 193	Transistor characterization, 20, 106, 184, 185
Signal Flow Graph, 62, 72, 123, 127, 128, 130,	Transmission line, vii, 30, 32, 33, 115, 164
131	Traveling Wave, 30, 43, 44, 55, 56, 63, 65, 66,
Signal Flow Model, 40, 50, 57, 58, 71, 114,	68, 69, 74–76, 79, 128, 140–144, 174,
115	177, 202, 205–207
Single-stub, 30	Triplexer, 43–45, 47–49, 63, 77, 124, 155, 219
Six-Port, 87, 177	TRL Standard, 135
Six-Port Load-Pull, 87	Tuner Bandwidth, 21
Sliding-Short, 72–74	Tuner Resolution, 20
Small-Signal, 11, 109, 186, 196	Tuner Size, 21, 34
Small-signal Model, 186, 196	Tuning Accuracy, 21, 35

Tuning Probe, 120, 121 Voltage waveform, 12, 13, 175, 176, 185 Tuning Range, viii, 19, 20, 32, 48-50, 57, 114, 125, 127, 142 Tuning Speed, 20, 33 Waveform, vii, viii, 9, 10, 12, 13, 16, 140, 148, Two-port network, 88, 89, 97, 214, 219 152, 155, 157, 159, 163–172, 174–186, Two-tone, 7, 192, 193, 201-204, 219-221 192, 205, 206, 227 U engineering, vii, viii, 140, 163, 183, 184, Uncertainty, 38, 39, 114, 124, 134, 217 186, 227 Unique measurement, viii, 157 measurement, 16, 148, 152, 155, 159, 163, 165, 167–170, 177, 183–186, 206, 227 WCDMA, 1, 202-204, 211 Vector Network Analyzer (VNA), 19, 29, 36, Wide Bandwidth, 135, 210 38-41, 97, 101, 104, 124, 134-136, Wideband, 1, 43, 46, 168, 202, 208–212, 219 147, 152, 166-169, 171, 172, 177, 182, 212, 213 Wideband Load-Pull, 208, 209 VNA Wireless, vii, 1, 7, 208, 217, 225 error correction, 134, 135 Wireless Communication, 1, 7 plane, 40 Voltage Standing Wave Ratio (VSWR), 11, 32, Y 39, 48, 114, 116, 117, 119, 125–127, 129, 130, 133, 164 YIG Filter, 63, 179, 180, 219, 220